



ADVERTIMENT. L'accés als continguts d'aquesta tesi queda condicionat a l'acceptació de les condicions d'ús establertes per la següent llicència Creative Commons:  <https://creativecommons.org/licenses/?lang=ca>

ADVERTENCIA. El acceso a los contenidos de esta tesis queda condicionado a la aceptación de las condiciones de uso establecidas por la siguiente licencia Creative Commons:  <https://creativecommons.org/licenses/?lang=es>

WARNING. The access to the contents of this doctoral thesis it is limited to the acceptance of the use conditions set by the following Creative Commons license:  <https://creativecommons.org/licenses/?lang=en>



Polypyrrole nanoparticles & composites:
Cardiac arrhythmia treatment evaluated in cells &
Caenorhabditis elegans

Sumithra Yasaswini Srinivasan

Doctoral thesis

Doctoral studies in Materials Science

Supervisor and Tutor: Dr. Anna Laromaine Sagué

2023

Departament de Química, Facultat de Ciències
Universitat Autònoma de Barcelona
Institut de Ciència de Materials de Barcelona

La **Dra. Anna Laromaine Sagué**, científica titular del CSIC

CERTIFICA:

Que **Sumithra Yasaswini Srinivasan**, graduada en bioingeniería i amb un màster en Nanotecnologia mèdica per la Universitat SASTRA de la India, ha dut a terme aquesta tesi doctoral sota la seva direcció i que queda recollida en aquesta memòria que porta per títol *“Polypyrrole nanoparticles & composites: Cardiac arrhythmia treatment evaluated in cells & Caenorhabditis elegans”* per optar al títol de Doctora en Ciència de Materials per la Universitat Autònoma de Barcelona.

I perquè així consti, signen el present certificat:

Bellaterra, 31 de Maig de 2023

வெள்ளத் தனைய மலர்நீட்டம் மாந்தர்தம்
உள்ளத் தனையது உயர்வு

-Thiruvalluvar (Kural: 595)

A person can grow as high as their motivation; as
a lotus stalk grows as deep as the water

To my Parents, Santhanalakshmi and Srinivasan
& My beloved Raguraam

Glossary

α -MHC	Heavy chain cardiac myosin
σ	Conductivity
$(\text{NH}_4)_2\text{S}_2\text{O}_8$	Ammonium persulfate
AFM	Atomic Force Microscopy
ATR-FTIR	Attenuated Total Reflectance-Fourier Transform InfraRed
Au	Gold
AV node	Atrioventricular node
BC	Bacterial Cellulose
BC-Ppy/BP	Bacterial cellulose-Polypyrrole composites
BODIPY	4,4-difluoro-4-bora-3a,4a-diaza-s-indacene
BSA	Bovine Serum Albumin
C	Carbon
CA	Cardiac Arrhythmia
CCS	Cardiac Conduction System
<i>C. elegans</i>	<i>Caenorhabditis elegans</i>
CF	Cardiac fibroblast
CGC	Caenorhabditis Genetics Center
CM	Cardiomyocyte
CNF	Cellulose nanofiber
CNC	Cellulose nanocrystal
COP	Chemical Oxidative Polymerization
CP	Conjugated Polymer
CR	Center for Research in Agricultural Genomics
CTAB	CetylTrimethylAmmonium Bromide
CTE	Cardiac Tissue Engineering
cTnT	Cardiac Troponin T
Cu	Copper
CVD	Cardiovascular diseases
Cx	Connexin
DC	Direct Current
dECM	decellularized ECM
DLS	Dynamic Light Scattering
DMEM	Dulbecco's Modified Eagle Medium
DM	Differentiation medium
DTAB	DodecylTrimethylAmmonium Bromide
ECG	Electrocardiogram
ECM	Extracellular Matrix
<i>E. Coli</i>	<i>Escherichia Coli</i>
FeCl_3	Ferric chloride
FeO	Iron Oxide
FGM	Fibroblast Growth Medium
FTIR	Fourier Transform InfraRed
GM	Growth Medium
H	Hydrogen

hCF	Adult human Cardiac Fibroblast
HS	Human-Induced Pluripotent Stem Cells
hiPSC	Hestrin-Schramm
IBEC	Institute for Bioengineering of Catalonia
IBGM	Institute of Biomedicine and Molecular Genetics
IDIBELL	Institute of Biomedical Research of Bellvitge
LB	Luria-Bertani
LQT	Long QT syndrome
MC neurons	Cholinergic motor neurons
MI	Myocardial Infarction
MQ	Milli-Q water
N	Nitrogen
NaClO	Sodium Hypochlorite
NaOH	Sodium Hydroxide
NGM	Netamode Growth Media
NIR	Near InfraRed
NP	NanoParticle
OTAB	OctadecylTrimethylAmmonium Bromide
PL	Propranolol
PANI	Polyaniline
PEDOT	Poly (3,4-ethylene dioxythiophene)
PHEMA	Poly (2-hydroxyethyl methacrylate)
Ppy	Polypyrrole
PT	Polythiophene
PTFE	Polytetrafluoroethylene
PVA	Poly Vinyl Alcohol
Py	Pyrrole monomer
RA	Retinoic Acid
RE	Racepinephrine
RF	Radiofrequency
ROI	Regions of Interest
SAN	Sinoatrial node
SEM	Scanning Electron Microscopy
SERCA	Sarcoendoplasmic reticulum calcium ATPase
SPION	Super Paramagnetic Iron Oxide Nanoparticle
SR- μ FTIR	Synchrotron radiation-sourced FTIR microspectroscopy
TEM	Transmission Electron Microscopy
TGA	ThermoGravimetric Analysis
Ti	Titanium
UV	UltraViolet
VGCC	Voltage-gated calcium channels

Acknowledgments

I vividly remember getting spellbound as a kid upon learning how clay pots and cotton clothes work in water exchange and how humans have applied it in our daily lives. My curiosity and fascination with the science of materials and their applications in everyday life only grew over the years. I heard the term “nanotechnology” for the first time as a teenager in school, which led me to take up the Integrated Master’s course on “Bioengineering and Medical Nanotechnology” at SASTRA University in India. I want to thank my professors, Dr. Sridharan and Dr. Thiagarajan Raman, for being great role models and driving me toward a research career. I would also like to thank Dr. Virendra Gajbhiye, at Agharkar Research Institute, for providing me with one of my best learning opportunities and imparting hard work, teamwork, leadership, and writing skills. Thank you for introducing polypyrrole nanoparticles to me, that I have not stopped exploring their potential in nanomedicine.

I came across the group of Nanoparticles and Nanocomposites to choose for a Marie-Curie COFUND fellowship, DOCFAM 2020. Upon reading about their work, I felt an instant belonging to the group, as it had the perfect amalgamation of materials science and biomedicine, something that I always hoped for. Even though *C. elegans* was entirely new for me, using them in nanoparticle assessment was a pleasant surprise that instantly hooked me. I take immense pleasure in thanking my supervisor, Dr. Anna Laromaine, for guiding me throughout this journey. Thank you for introducing *C. elegans* and their tremendous potential. Thank you for teaching me that it is never wrong to ask questions and take inspirations from other fields. Especially thank you very much for identifying my strengths and weaknesses and guiding me in this Ph.D. accordingly.

I would also like to thank Dr. Anna Roig and Dr. Marti Gich, investigators in our group, for showing interest and providing advice and ideas at the right moments. Thanks to my group members for welcoming me and making me feel at home in a foreign country with no known people. Special thanks to Irene for being that friend I can always rely on and brainstorming with me for cell culture problems, Soledad for keeping the happiness quotient high and cheering me up on my crazy ideas, and Luo for your teachings in *C. elegans* and life. Thank you, Miquel, Jan, and Ma, for your endless jokes and for bringing the team together. Thank you, Amanda, for being a great ally to travel along in our *C. elegans* research. Thank you, Nerea, Thomas, Nanthilde, and Allan, for the beautiful company. Thank you, Maite, for taking care of our bureaucratic work, and to all the new

members of our group Nico, Pablo, Pol, Darla, Aurna, Anna, Xuesong, Li, Laura, and many others I might have forgotten who keep the group as dynamic and friendly as it is. I want to thank the lovely ICMABers for giving me some of the best memories to take back home. My first office mate, Artur, and my fellow Ph.D. traveler, Sohini, for the initial days of comfort and support; Jewel and Adara, for the conversations and companionship; and all the other old and new ICMABers for giving me some of the happiest days and keeping in touch.

I want to thank my collaborators who guided me with their expertise and contributed significantly to improving this thesis. Dr. Mariano, Dr. Bernhard, and Dr. Osnat, for teaching the four-probe technique and knowledge of the electrical conductivity of materials. Dr. Nuria from ALBA for teaching me all about the SR- μ FTIR sample preparation, data processing and analysis. Dr. Mayte, Dr. Javier, and Dr. Rosalba from IBGM for hosting me for a month and teaching me calcium imaging techniques; and Dr. Pilar for being a great colleague and sparing your time and complete focus for these experiments. Dr. Julian from IDIBELL, Barcelona, for the collaboration to perform CRISPR-Cas9 editing and always helping us with our *C. elegans* questions all these years, and Dr. Dmytro for patiently teaching me everything about genetics, your time and efforts for the CRISPR-Cas9 editing. Dr. Soledad and Marina from IBEC, for their expert knowledge and contribution to cardiac cell culture experiments, for being willing to solve problems and completing the work quickly. I want to thank Dr. Imma and Nerea from ICMAB for the collaboration and opportunity to explore *C. elegans* for *in-vivo* thermometry applications and Dr. Nuria and Anurag from CRAG for the chance to employ the FTIR technique for analyzing plant samples.

Last but not least, I am eternally grateful for my family. Thank you, Mom, for being my pillar of support and encouraging me in my choices. Thank you, Dad, for always trusting in me more than anyone, always doing your best, and putting us ahead of yourself. Thank you, Abhinav, for your unconditional love, being my bundle of joy, and reminding me about the kid in me that needed answers. Special thanks to my husband, Raguraam, for being my best cheerleader, hype person, and best friend.

Finally, I would like to thank the two fellowships that supported me financially during the years. The grant from DOC-FAM, European Union's Horizon 2020 research and innovation program under the Marie Skłodowska-Curie grant agreement No 754397, and the Ministry of Science and Innovation (MICINN) "Severo Ochoa" program for centers of excellence through the BEAT project (FUNFUTURE-FIP-2020).

Attributions

I would like to thank the people that contributed to the thesis:

- Dr. Zhongrui Luo taught me the experiments and handling of *C. elegans*.
- Dr. Soledad Roig Sánchez introduced and taught me Bacterial cellulose culturing.
- Amanda Muñoz shared brainstorming research ideas and solved experimental problems together.
- Dr. Nuria Benseny Cases taught me to use the synchrotron radiation sourced Fourier-transform infrared microspectroscopy (SR- μ FTIR) for the FTIR analysis of *C. elegans* at the ALBA synchrotron center.
- The ICMAB technical services: Dr. Judit Oro performed the TEM visualization, and Ana Esther Carrilo carried out SEM image acquisition of polypyrrole nanoparticles and cellulose nanofibers. Dr. Vega Lloveras trained me in Fourier-transform infrared spectroscopy and absorption spectroscopy for nanomaterial characterizations and the optical microscope for *C. elegans* imaging. Roberta Ceravola performed the thermal gravimetric analysis of bacterial cellulose and polypyrrole nanoparticles. José Amable Bernabé taught me to use dynamic light scattering particle size analyzer to measure nanoparticles' size. Andrés Gómez carried out the AFM measurements, and Marta Gerbolés performed and taught me to measure the surface contact angle of cellulose films.
- Dr. Laura Gonzalez Moragas, optimized the protocols for the growth and evaluation of *C. elegans*, and Dr. Muling Zheng established the protocols on bacterial cellulose.
- Dr. Estefanía Peña and Alejandro Aperici from University of Zaragoza, performed the uniaxial and biaxial tensile testing of cellulose and cellulose-polypyrrole films.
- Dr. Pilar Álvarez Illera, Dr. Mayte Montero, Dr. Javier Alvarez, and Dr. Rosalba Fonteriz, from the Aging and Calcium group of Institute of Molecular

Biology and Genetics (IBGM), taught me to perform calcium imaging studies on *C. elegans*.

- Dr. Dmytro Kukhtar and Dr. Julian Ceron from the disease models in *C. elegans* group of The Bellvitge Biomedical Research Institute (IDIBELL) introduced me to *C. elegans* genetics and taught me to perform genome editing using CRISPR-Cas9.
- The *NANOPTO* group from ICMAB provided the four-probe instrument for conductivity measurements, and Dr. Mariano Campoy, Dr. Bernhard Dörfling, and Dr. Osnat Zapata taught me and helped me to use the instrument.
- Dr. Soledad Perez and Marina Martinez from the group of Biomaterials for Regenerative Therapies of The Institute of Bioengineering of Catalonia collaborated for the cell culture experiments of cardiac cells on cellulose-polypyrrole scaffolds, which resulted in a publication entitled “Conductive Bacterial Nanocellulose-Polypyrrole patches promote cardiomyocyte differentiation”.
- Dr. Imma Ratera and Nerea Gonzalez from the Biomaterials and Molecular Electronics group of ICMAB collaborated for the *in-vivo* nano thermometry evaluation of radical organic nanoparticles in *C. elegans*, leading to the publication entitled “Ratiometric Nanothermometer Based on a Radical Excimer for In Vivo Sensing”.
- Dr. Anurag Kashyap, Dr. Nuria Sanchez Coll, and Dr. Montserrat Capellades from the bacterial plant diseases and plant cell death group from The Center for Research in Agricultural Genomics (CRAG) collaborated with us for the FTIR analysis of bacteria-infected tomato plant samples, leading to the publication entitled “Induced ligno-suberin vascular coating and tyramine-derived hydroxycinnamic acid amides restrict *Ralstonia solanacearum* colonization in resistant tomato roots”.

Table of Contents

Glossary	x
Acknowledgments	xiv
Attributions	xviii
Foreword & Scope of the thesis	1
CHAPTER 1: Introduction to cardiac arrhythmia, therapies and bioevaluation strategies	9
1.1. Cardiac Arrhythmia	13
1.1.1. Pathophysiology of cardiac arrhythmia.....	13
1.2. Treatments for Cardiac Arrhythmia	15
1.3. Nanotechnology in Arrhythmia treatments.....	19
1.3.1. Nano-Pharmacotherapy	20
1.3.2. Nano-ablation therapy	20
1.3.3. Nanomaterial scaffolds for tissue engineering	22
1.4. Conducting Nanomaterials.....	24
1.5. Properties and Applications of Polypyrrole	26
1.6. Bacterial Cellulose.....	30
1.7. Bacterial cellulose-Polypyrrole for cardiac tissue engineering.....	31
1.8. Bio-evaluation Methodologies	32
1.8.1. <i>In-vitro</i> Models	33
1.8.2. <i>In-vivo</i> Models	34
1.8.3. Alternative Small Animal Models.....	36
1.9. The Pharynx of <i>Caenorhabditis elegans</i>	39
1.10. The opportunity of <i>Caenorhabditis elegans</i> for arrhythmia evaluation	41
1.11. Thesis Rationale.....	43

CHAPTER 2: Synthesis and Characterization of Polypyrrole nanoparticles53

2.1. Synthesis of Polypyrrole Nanoparticles	56
2.1.1. Methods of Synthesis	56
2.1.2. Parameters affecting chemical oxidative Polymerization	58
2.1.3. Polypyrrole nanoparticles synthesis protocol.....	61
2.2. Characterization of Polypyrrole nanoparticles.....	62
2.2.1 Size and Surface charge of Polypyrrole Nanoparticles	62
2.2.2 Size and Morphology by electron microscopy	64
2.2.3 Chemical structure and composition.....	65
2.2.4 Thermal and optical properties	67
2.2.5 Electrical conductivity	68
2.2.6 Stability of Ppy NPs.....	69
2.3. Conclusions.....	70

CHAPTER 3: Evaluation of systemic effects of Polypyrrole Nanoparticles in *Caenorhabditis elegans*.....77

3.1. <i>Caenorhabditis elegans</i>.....	81
3.2. Maintenance of <i>C. elegans</i>.....	83
3.3. Preparation for Exposure	84
3.4. Exposure	85
3.5. Evaluation of pyrrole monomer toxicity.....	86
3.6. Gastrointestinal fate of Polypyrrole Nanoparticles	87
3.6.1. Stability of nanoparticles in recovery procedure.....	87
3.6.2. Recovery of ingested nanoparticles from <i>C. elegans</i>	88
3.7. Systemic toxicity.....	89
3.7.1. Survival rate	89
3.7.2. Growth & Development	90
3.8. Reproductive effect.....	90
3.8.1. Reproductive rate	91
3.8.2. Transgenerational toxicity	92
3.9. Lipid accumulation	92
3.10. Oxidative effect	93

3.10.1. Sample preparation and analysis	93
3.10.2. Quantification through relative absorbance ratios	94
3.11. Conclusions.....	97

CHAPTER 4: *Caenorhabditis elegans*' pharynx to evaluate cardiac rhythm 99

4.1. Commercial anti-arrhythmic substances	103
4.1.1. General Toxicity.....	103
4.1.2. Pharynx pumping rate	105
4.1.3. Lipid accumulation.....	105
4.1.4. Lipid oxidation and metabolism.....	106
4.2. Pharynx pumping impaired strains	108
4.2.1. Systemic effects of drugs and nanoparticles	108
4.3. Pharyngeal effects.....	109
4.3.1. Pharyngeal pumping rate of mutant strains	109
4.3.2. Exposure duration	111
4.3.3. Excretion duration.....	112
4.4. Molecular effects.....	114
4.4.1. Calcium signalling	114
4.4.2. Calcium imaging.....	115
4.5. Conclusions.....	119

CHAPTER 5: Development and in-vitro evaluation of Polypyrrole Bacterial Cellulose biomaterial scaffolds 125

5.1. Bacterial cellulose as scaffold materials	129
5.2. BC and BC-Ppy materials used for <i>in-vitro</i> evaluation.....	132
5.2.1 BC synthesis protocol.....	132
5.2.2 BC-Ppy Synthesis protocol.....	133
5.3. Characterization of BC and BC-Ppy films.....	134
5.3.1 Physicochemical characteristics	134
5.3.2 Microstructure, size, and morphology	135
5.3.3 Surface topography	136
5.3.4 Chemical Structure and Composition	137
5.3.5 Thermal and Optical properties.....	139

5.3.6 Electrical conductivity	140
5.3.7 Mechanical behavior	142
5.3.8 Surface wettability	145
5.3.9 Stability of BC-Ppy	146
5.4. Cardiac cell types used for in-vitro evaluation	147
5.4.1. Cardiac Fibroblasts	147
5.4.2. Immortalized cardiomyocyte models	148
5.5. Material selection and pre-conditioning	149
5.6. In-vitro cell culture assays	150
5.6.1. Cardiac Fibroblasts viability, attachment, and morphology	150
5.6.2. By-product toxicity of scaffolds in H9c2 cell media	151
5.6.3. H9c2 cell viability and attachment	151
5.6.4. H9c2 cell Morphology	152
5.6.5. H9c2 maturation	156
5.7. Conclusions.....	161
6. ANNEX: Arrhythmogenic mutations in <i>Caenorhabditis elegans</i> using CRISPR-Cas9 editing.....	167
6.1. Gene Mutations and Arrhythmias	171
6.2. CRISPR-Cas9.....	172
6.3. CRISPR-Cas9 in <i>C. elegans</i>	175
6.4. Arrhythmia specific mutations in <i>C. elegans</i>	177
6.5. CRISPR-Cas9 editing to produce mutant strains.....	179
6.6. Functional impact of the mutations	180
6.7. Conclusions.....	181
7. Conclusions & Future Prospects	185
7.1. Conclusions.....	187
7.2. Future Prospects	189
8. CV & Publications.....	192
8.1. Curriculum Vitae.....	193
8.2. Publications	196

Foreword & Scope of the Thesis

Conjugated polymers are versatile materials with a wide range of unique and valuable properties for biomedical applications. The application of conjugated polymers in biosensing and drug delivery is well-known. Recently, the application of these polymers in modern therapeutic strategies such as tissue engineering has also been gaining rapid and steady attention. Among these, polypyrrole is one of the most studied conjugated polymers. The inherent conductivity of polypyrrole nanoparticles (Ppy NPs) is especially exploited in tissue engineering applications of conducting organs, such as the nerve and skin. In this thesis, we leverage the inherent conductivity of cardiac tissues and focus our attention on the potential of Ppy NPs in cardiac therapies.

Cardiovascular diseases stand as the leading cause of death worldwide. Among the patients with underlying heart disease, 90% report some form of cardiac arrhythmia. However, existing treatments for cardiac arrhythmia are sub-par, lacking heavily in efficiency and safety. Current therapies and practices have been widely reported to cause severe side effects affecting the lungs, liver, and heart. Thus, the investigation of Ppy NPs for cardiac therapies contributes to the development of safe, efficient, and multifunctional nanomedicine for the effective treatment of cardiac arrhythmia. Although some preliminary studies on different composites of Ppy NPs for cardiac therapy application exist, substantial animal studies are lacking, which is crucial for the progress of novel candidates to clinical trials.

In this thesis, we first evaluated Ppy NPs' biocompatibility and effects on cardiac rhythm using a small animal model, the *Caenorhabditis elegans* (*C. elegans*). The continuous pumping of *C. elegans*' pharynx resembles the human heart at the molecular and genetic levels. After thoroughly evaluating the nanoparticles in worms, we produced a composite scaffold of polypyrrole nanoparticles with bacterial cellulose as a potential cardiac patch and performed *in-vitro* evaluations in cardiac cells.

1. We begin this thesis with an introductory chapter that provides the scientific background and state-of-the-art research on the relevant topics. Briefly, **Chapter 1** discusses the prevalence, pathology, and current treatment options for cardiac arrhythmia and the efforts of nanotechnology to improve existing treatments and bring novel therapies. The various *in-vitro*, *in-vivo*, and small animal platforms

available to assess the efficacy of innovative nanomedicines are also discussed, with a particular focus on the opportunity of *C. elegans* to evaluate the effect of nanomaterials on cardiac rhythm.

2. The synthesis and characterization of Ppy NPs are discussed in **Chapter 2**. In this chapter, we assessed and reported the size, surface charge, morphology, conductivity, chemical structure, thermal and optical properties, and stability in various conditions.
3. The systemic toxicity endpoints in *C. elegans* were meticulously studied for Ppy NPs ranging from survival to intracellular lipid levels to estimate the NPs' safety in the organism and elaborated in **Chapter 3**.
4. **Chapter 4** discusses the application of the *C. elegans* pharynx as a model organ to study cardiac rhythms. We first established the animal model for such evaluations using two substances with known arrhythmic effects as control drugs and achieved the expected impact of those drugs. Following this, we evaluated the pharyngeal effects of Ppy NPs in wild-type and specific mutant strains. Finally, the influence of Ppy NP treatment in the intracellular Ca^{2+} signaling in the pharynx was also investigated to elucidate a possible mechanistic action of Ppy NPs.
5. The evaluation of cardiac-like effects of Ppy NPs in *C. elegans* led us to design a composite material with Ppy NPs and bacterial cellulose (BC-Ppy) with improved functionalities imparted by the BC. This material design will be closer to the practical application of cardiac patches for myocardial infarction and arrhythmias. Optimization of the scaffolds with varying Ppy content and *in-vitro* evaluation in cardiac cells are discussed in detail in **Chapter 5**.
6. The **Annex** opens the avenue for creating specific arrhythmic mutations in *C. elegans* through genome editing for future evaluation of anti-arrhythmic drugs and nanomaterials in custom-designed mutant strains.
7. Finally, the **Conclusions and Future perspectives** summarize the significant findings of this work, the main takeaways, and the future opportunities.
8. **CV and Publications**. The publications of the author during the time of the PhD.

Prólogo y alcance de la tesis

Los polímeros conjugados son materiales versátiles con una amplia gama de propiedades únicas y valiosas para aplicaciones biomédicas. La aplicación de polímeros conjugados en biosensores y administración de fármacos es bien conocida. Recientemente, la aplicación de estos polímeros en estrategias terapéuticas modernas, como la ingeniería de tejidos, también ha ido ganando atención de forma rápida y constante. Entre ellos, el polipirrol es uno de los polímeros conjugados más estudiados. La conductividad inherente de las nanopartículas de polipirrol (NPs de Ppy) se aprovecha especialmente en aplicaciones de ingeniería tisular de órganos conductores, como el nervio y la piel. En esta tesis, aprovechamos la conductividad inherente de los tejidos cardíacos y centramos nuestra atención en el potencial de las NPs de Ppy en terapias cardíacas.

Las enfermedades cardiovasculares son la principal causa de muerte en todo el mundo. Entre los pacientes con cardiopatías subyacentes, el 90% presenta algún tipo de arritmia cardíaca. Sin embargo, los tratamientos existentes para la arritmia cardíaca son deficientes, con grandes carencias en cuanto a eficacia y seguridad. Se ha informado ampliamente de que las terapias y prácticas actuales causan graves efectos secundarios que afectan a los pulmones, el hígado y el corazón. Así pues, la investigación de las NPs de Ppy para terapias cardíacas contribuye al desarrollo de una nanomedicina segura, eficiente y multifuncional para el tratamiento eficaz de la arritmia cardíaca. Aunque existen algunos estudios preliminares sobre diferentes compuestos de NPs de Ppy para su aplicación en terapias cardíacas, faltan estudios sustanciales en animales, lo cual es crucial para el progreso de nuevos candidatos a ensayos clínicos.

En esta tesis, evaluamos en primer lugar la biocompatibilidad de las NPs de Ppy y sus efectos sobre el ritmo cardíaco utilizando un pequeño modelo animal, el *Caenorhabditis elegans* (*C. elegans*). El bombeo continuo de la faringe de *C. elegans* se asemeja al corazón humano a nivel molecular y genético. Tras evaluar a fondo las nanopartículas en gusanos, produjimos un andamio compuesto de nanopartículas de polipirrol con celulosa bacteriana como posible parche cardíaco y realizamos evaluaciones *in vitro* en células cardíacas.

1. Comenzamos esta tesis con un capítulo introductorio que proporciona los antecedentes científicos y el estado del arte de la investigación sobre los temas relevantes. Brevemente, el **Capítulo 1** analiza la prevalencia, la patología y las opciones de tratamiento actuales de la arritmia cardíaca, así como los esfuerzos de la nanotecnología para mejorar los tratamientos existentes y aportar nuevas terapias. También se discuten las diversas plataformas *in vitro*, *in vivo* y de pequeños animales disponibles para evaluar la eficacia de las nanomedicinas innovadoras, con especial atención a la oportunidad de *C. elegans* para evaluar el efecto de los nanomateriales sobre el ritmo cardíaco.
2. La síntesis y caracterización de las NPs de Ppy se discuten en el **Capítulo 2**. En este capítulo, evaluamos y reportamos el tamaño, la carga superficial, la morfología, la conductividad, la estructura química, las propiedades térmicas y ópticas, y la estabilidad en diversas condiciones.

3. Los puntos finales de toxicidad sistémica en *C. elegans* se estudiaron meticulosamente para las NPs de Ppy, desde la supervivencia hasta los niveles de lípidos intracelulares, para estimar la seguridad de las NPs en el organismo, y se detallan en el **Capítulo 3**.
4. En el **Capítulo 4** se analiza la aplicación de la faringe de *C. elegans* como órgano modelo para estudiar los ritmos cardíacos. En primer lugar, establecimos el modelo animal para dichas evaluaciones utilizando dos sustancias con efectos arrítmicos conocidos como fármacos de control y logramos el impacto esperado de dichos fármacos. A continuación, evaluamos los efectos faríngeos de las NP de Ppy en cepas silvestres y mutantes específicas. Por último, también se investigó la influencia del tratamiento con NP de Ppy en la señalización intracelular de Ca^{2+} en la faringe para dilucidar una posible acción mecanicista de las NP de Ppy.
5. La evaluación de los efectos cardíacos de las NPs de Ppy en *C. elegans* nos llevó a diseñar un material compuesto con NPs de Ppy y celulosa bacteriana (BC-Ppy) con funcionalidades mejoradas impartidas por la BC. El diseño de este material estará más cerca de la aplicación práctica de parches cardíacos para el infarto de miocardio y las arritmias. La optimización de los andamios con contenido variable de Ppy y la evaluación *in vitro* en células cardíacas se discuten en detalle en el **Capítulo 5**.
6. El **anexo** abre la vía a la creación de mutaciones arrítmicas específicas en *C. elegans* mediante la edición del genoma para la futura evaluación de fármacos antiarrítmicos y nanomateriales en cepas mutantes diseñadas a medida.
7. Por último, las **Conclusiones y Perspectivas** de futuro resumen los hallazgos significativos de este trabajo, las principales conclusiones y las oportunidades futuras.
8. **CV y Publicaciones.** Todas las publicaciones del autor de su periodo doctoral.

Pròleg i abast de la tesi

Els polímers conjugats són materials versàtils amb una àmplia gamma de propietats úniques i valuoses per a aplicacions biomèdiques. L'aplicació de polímers conjugats en biodetecció i lliurament de fàrmacs és ben coneguda. Recentment, l'aplicació d'aquests polímers en estratègies terapèutiques modernes com l'enginyeria de teixits també ha guanyat una atenció ràpida i constant. Entre aquests, el polipirrol és un dels polímers conjugats més estudiats. La conductivitat inherent de les nanopartícules de polipirrol (Ppy NPs) s'aprofita especialment en aplicacions d'enginyeria de teixits d'òrgans conductors, com ara el nervi i la pell. En aquesta tesi, aprofitem la conductivitat inherent dels teixits cardíacs i centrem la nostra atenció en el potencial dels Ppy NPs en teràpies cardíques.

Les malalties cardiovasculars són la principal causa de mort a tot el món. Entre els pacients amb malaltia cardíaca subjacent, el 90% denuncien alguna forma d'arrítmia cardíaca. No obstant això, els tractaments existents per a l'arrítmia cardíaca són insuficients, mancants molt d'eficiència i seguretat. S'ha informat àmpliament que les teràpies i pràctiques actuals causen efectes secundaris greus que afecten els pulmons, el fetge i el cor. Així, la investigació de Ppy NP per a teràpies cardíques contribueix al desenvolupament d'una nanomedicina segura, eficient i multifuncional per al tractament eficaç de l'arrítmia cardíaca. Tot i que existeixen alguns estudis preliminars sobre diferents compostos de Ppy NP per a l'aplicació de teràpia cardíaca, falten estudis substancials en animals, la qual cosa és crucial per al progrés de nous candidats als assaigs clínics.

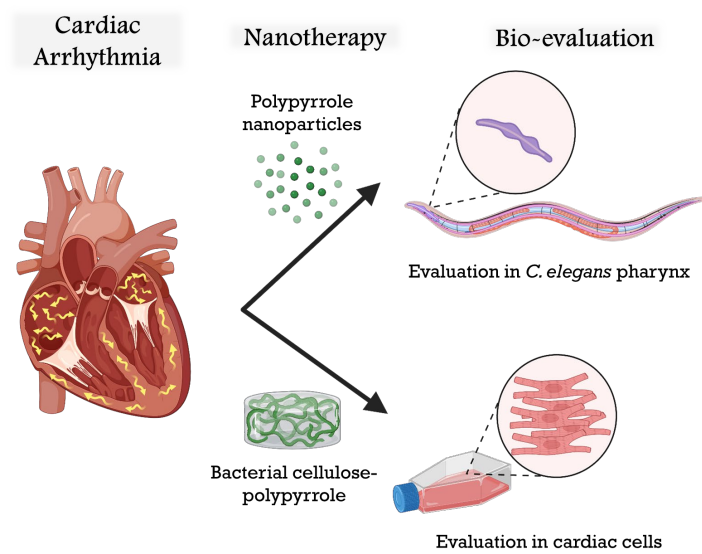
En aquesta tesi, primer hem avaluat la biocompatibilitat i els efectes dels Ppy NPs sobre el ritme cardíac mitjançant un model animal petit, el *Caenorhabditis elegans* (*C. elegans*). El bombeig continu de la faringe de *C. elegans* s'assembla al cor humà a nivell molecular i genètic. Després d'avaluar a fons les nanopartícules dels cucs, vam produir una bastida composta de nanopartícules de polipirrol amb cel·lulosa bacteriana com a potencial pegat cardíac i vam realitzar avaluacions in vitro en cèl·lules cardíques.

1. Comencem aquesta tesi amb un capítol introductori que ofereix el bagatge científic i la recerca d'última generació sobre els temes rellevants. Breument, el **capítol 1** analitza la prevalença, la patologia i les opcions de tractament actuals per a l'arítmia cardíaca i els esforços de la nanotecnologia per millorar els tractaments existents i aportar noves teràpies. També es discuteixen les diferents plataformes in vitro, in vivo i d'animals petits disponibles per avaluar l'eficàcia de nanomedicines innovadores, amb especial atenció a l'oportunitat de *C. elegans* d'avaluar l'efecte dels nanomaterials sobre el ritme cardíac.
2. La síntesi i la caracterització dels Ppy NP es discuteixen al **capítol 2**. En aquest capítol, hem avaluat i informat la mida, la càrrega superficial, la morfologia, la conductivitat, l'estructura química, les propietats tèrmiques i òptiques i l'estabilitat en diverses condicions.
3. Els punts finals de toxicitat sistèmica a *C. elegans* es van estudiar meticulosament per a les NP Ppy que van des de la supervivència fins als nivells de lípids intracel·lulars per estimar la seguretat de les NP a l'organisme i es detallen al **capítol 3**.

4. El **capítol 4** tracta l'aplicació de la faringe de *C. elegans* com a òrgan model per estudiar els ritmes cardíacs. Primer vam establir el model animal per a aquestes avaluacions utilitzant dues substàncies amb efectes arrítmics coneguts com a fàrmacs de control i vam aconseguir l'impacte esperat d'aquests fàrmacs. Després d'això, es van avaluar els efectes faringis dels Ppy NPs en soques mutants de tipus salvatge i específiques. Finalment, també es va investigar la influència del tractament amb Ppy NP en la senyalització intracel·lular de Ca^{2+} a la faringe per dilucidar una possible acció mecanicista dels Ppy NP.
5. L'avaluació dels efectes cardíacs dels Ppy NPs a *C. elegans* ens va portar a dissenyar un material compost amb Ppy NPs i cel·lulosa bacteriana (BC-Ppy) amb funcionalitats millorades impartides pel BC. Aquest disseny de material s'acostarà més a l'aplicació pràctica dels pegats cardíacs per a l'infart de miocardi i les arrítmies. L'optimització de les bastides amb contingut variable de Ppy i l'avaluació in vitro en cèl·lules cardíques es discuteixen amb detall al **capítol 5**.
6. L'**annex** obre la via per crear mutacions arrítmiques específiques en *C. elegans* mitjançant l'edició del genoma per a l'avaluació futura de fàrmacs i nanomaterials antiarrítmics en soques mutants dissenyades a mida.
7. Finalment, les **Conclusions i les perspectives** de futur resumeixen les conclusions significatives d'aquest treball, les principals conclusions i les oportunitats de futur.
8. El **currículum i les publicacions**. Totes les publicacions del autor del seu període doctoral.

Chapter 1

Introduction to cardiac arrhythmia, therapies and bioevaluation strategies



PREFACE

This chapter lays out the background and rationale of this thesis. Here, we discuss the prevalence and pathophysiology of cardiac arrhythmia, the available treatment options in practice, and those currently under research with the help of nanotechnology. The most recent research trend for arrhythmia treatment is the use of conducting polymeric nanoparticles. We focus on polypyrrole nanoparticles and their properties, applications, and composites for cardiac therapies. Lastly, among other cell culture and animal models, we present *Caenorhabditis elegans* (*C. elegans*) as a small animal platform for evaluating anti-arrhythmic drugs and nanomaterials.

Index

1.1. Cardiac Arrhythmia.....	13
1.1.1. Pathophysiology of Cardiac Arrhythmia	13
1.2. Treatments for Cardiac Arrhythmia.....	15
1.3. Nanotechnology in Arrhythmia treatments	19
1.3.1. Nano-Pharmacotherapy	20
1.3.2. Nano-ablation therapy	20
1.3.3. Nanomaterial scaffolds for tissue engineering	22
1.4. Conducting Nanomaterials	24
1.5. Properties and Applications of Polypyrrole.....	26
1.6. Bacterial Cellulose	30
1.7. Bacterial cellulose-Polypyrrole for cardiac tissue engineering	31
1.8. Bio-evaluation Methodologies	32
1.8.1. <i>In-vitro</i> Models	33
1.8.2. In-vivo Models.....	34
1.8.3. Alternative Small Animal Models	36
1.9. The Pharynx of <i>Caenorhabditis elegans</i>.....	39
1.10. The opportunity of <i>Caenorhabditis elegans</i> for arrhythmia evaluation	41
1.11. Thesis Rationale.....	43

1.1. Cardiac Arrhythmias

The disorders affecting the heart and the circulatory system are collectively referred to as cardiovascular diseases (CVDs). CVDs are the leading cause of mortality, representing 32% of deaths worldwide and 45% of all deaths in Europe^{1,2}. The major types of CVDs include coronary artery disease, valve abnormalities, aneurysms, cardiac arrhythmias, cardiomyopathies, pericarditis, and heart failure. Among all types of CVDs, cardiac arrhythmias (CA) is a highly prevalent disorder, with 90% of heart patients reported to show signs of arrhythmia which amounts to 18% of cardiac deaths^{3,4}.

CA is characterized by irregular beating of the heart due to an improper propagation of the electrical impulse across the cardiac cells⁵. The abnormal heart rhythm can be either faster than normal, above 100 beats/min, known as tachycardia, or slower than normal, below 60 beats/min, known as bradycardia. The tachyarrhythmia can be further classified according to its origin in the conduction pathway as supraventricular arrhythmias, arising in the atria or atrioventricular node (AVN), and ventricular arrhythmias, originating in the ventricles⁶.

CA arises as a result of two primary conditions: myocardial infarction (MI) and dysregulation in the ion channel subunits. MI occurs when a region of the cardiac muscle is dead due to a lack of blood and oxygen supply obstructing the flow of electrical signals across the healthy regions, resulting in arrhythmia⁷. On the other hand, ion channels connecting the cardiomyocytes maintain the cardiac conduction system regulating the cardiac beating. Therefore, dysfunctions in the ion channels also lead to CA⁸.

1.1.1. Pathophysiology of cardiac arrhythmia

The heart is made of conducting myocardial tissues that generate and propagate electrical impulses through a specialized cardiac conduction system (CCS) (Figure 1). The CCS coordinates the muscle contractions leading to a regulated rhythmic cardiac beating of the atria and ventricles to pump blood across the body^{9,10}.

The conducting pathway begins at the sinoatrial node (SAN) (Figure 1, I), which initiates an electrical signal that propagates to the left and right atria (Figure 1, II), then through the AVN (Figure 1, III). The AVN is responsible for delaying impulse propagation, ensuring prolonged contraction of the atria for complete blood transport before ventricular contraction can begin. The impulse travels through AVN and reaches the atrioventricular bundle (His bundles) (Figure 1, IV). The atrial and ventricular cardiomyocytes are separated by a layer of connective tissue consisting of His bundles and Purkinje fibers that

carry the electrical impulse to ventricles, causing ventricular depolarization (Figure 1, V)^{10,11}.

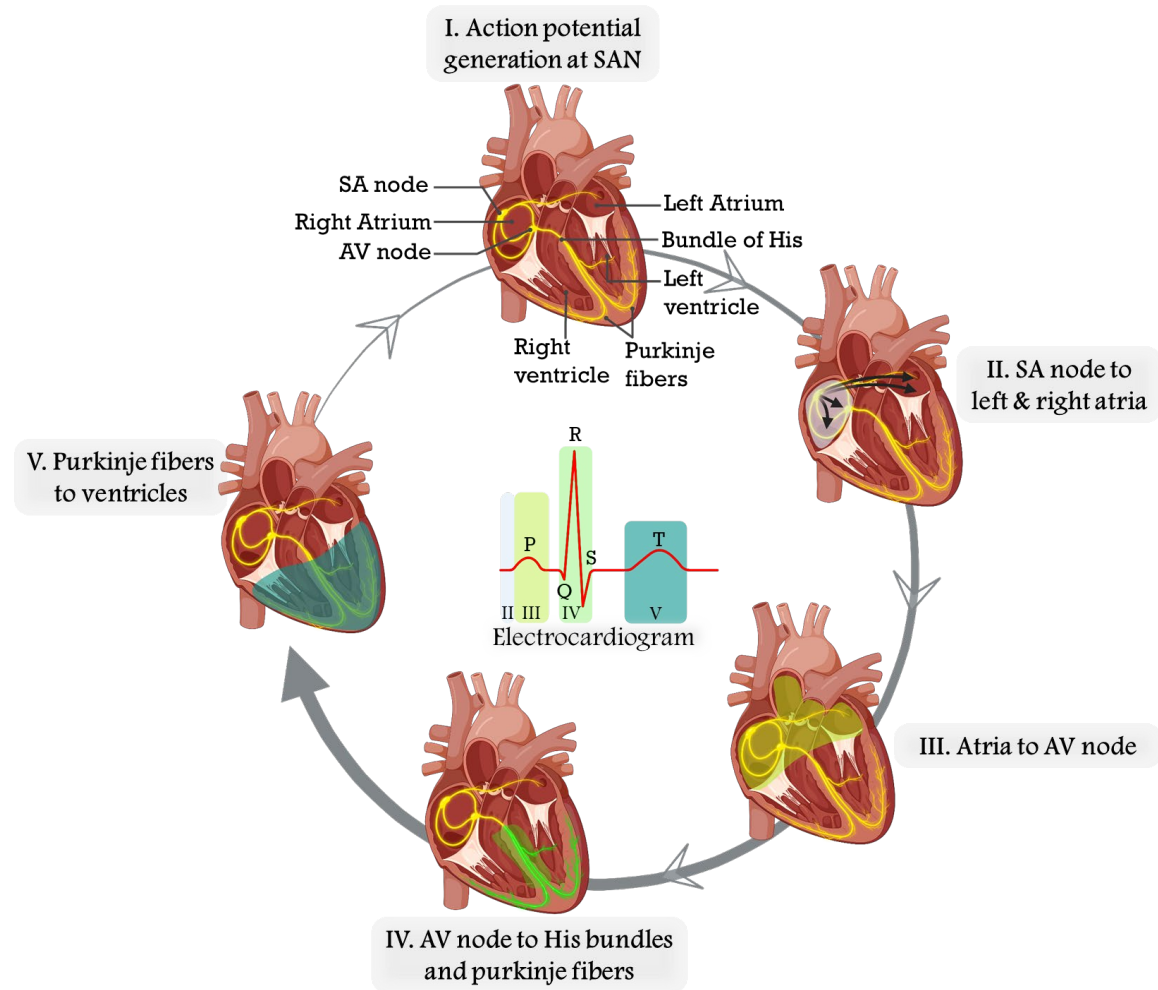


Figure 1. The cardiac conduction system of the heart: the stages of action potential propagation from the sinoatrial node (SAN) to the ventricles with the corresponding regions in the heart highlighted -sinoatrial node (grey), atria (light green), His bundles (dark green), and ventricles (teal green). The electrocardiogram at the center shows the different stages of cardiac conduction as P wave, QRS complex, and T wave with the equivalent color code.

The events of cardiac conduction and impulse propagation leading to pumping can be understood by the electrocardiogram (ECG) (Figure 1). When propagated to the atrial muscles, the action potential causes depolarization of the atrial cardiomyocytes, which is perceived as the P wave. Likewise, when the impulse travels to the ventricles, ventricular depolarization forms the QRS complex. Finally, the repolarization of ventricular myocytes induces the formation of T waves and completes the cycle of action potential and muscle contractions¹².

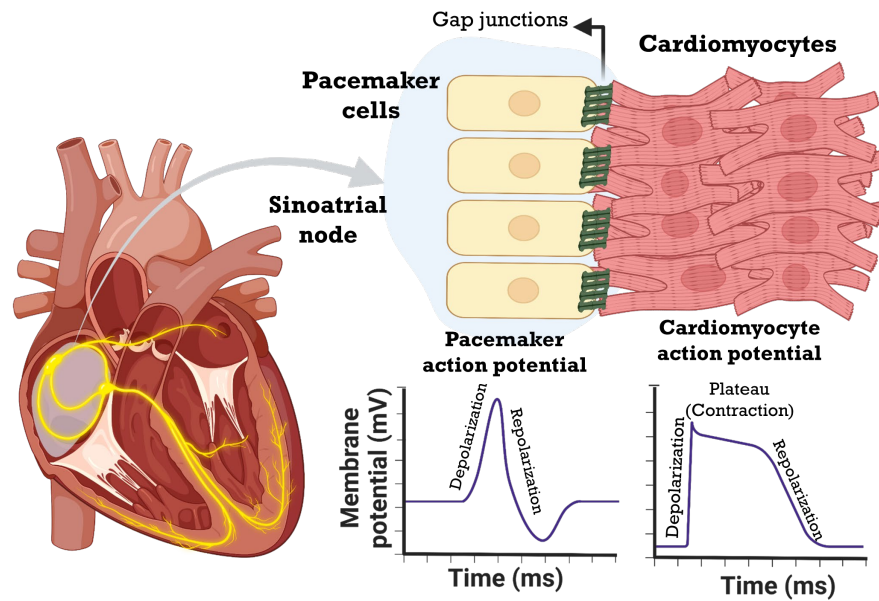


Figure 2. The interaction between the pacemaker cells and cardiomyocytes at the sinoatrial node via gap junctions propagates the electrical impulse and causes depolarization and repolarization with their respective action potentials.

The generation and conduction of electrical signals in the CCS are mediated via specific intercellular interactions¹⁰. The sinoatrial node consists of a specialized myocardial cell called pacemaker cells, and the atrial and ventricular muscles are composed of cardiac-specific contractile muscle cells called cardiomyocytes. The cardiomyocytes are connected to each other and to the pacemaker cell via gap junctions (Figure 2), consisting of ion channels for transporting cations such as Na^+ , Ca^{2+} , and K^+ . Voltage-gated calcium channels sense the electrical impulse generated by SAN, resulting in Ca^{2+} ion influx, leading to a series of influx and efflux of cations. The transport of cations in and out of cells changes membrane potential, leading to a regulated cycle of depolarization and repolarization. Therefore, these ion channels are responsible for the electrical coupling of cells and action potential propagation, which is crucial for a synchronous contraction of the heart¹⁰. Consequently, any dysregulation of the cardiac conduction system due to congenital abnormalities, myocardial infarction, impaired development, or dysfunction results in cardiac arrhythmias.

1.2. Treatments for Cardiac arrhythmia

Existing treatments and management of cardiac arrhythmia are categorized as pharmacological therapy and external/surgical interventions. Pharmacological therapies use anti-arrhythmic drugs to target molecular pathways affecting the cardiac rhythm, and

external therapies include pacemaker implants, direct current (DC) cardioversion, or RF ablation¹³.

Pharmacological therapy

The ion channels are over-activated in tachyarrhythmias, making them the most common targets for anti-arrhythmic drugs¹⁴. The anti-arrhythmic drug therapies are grouped according to the Vaughan Williams classification, depending on the specific ion channels and the stage of action potential that the drugs act upon (Figure 3)⁶.

The different types of anti-arrhythmic drugs are sodium channel blockers (class I), beta-blockers (class II), potassium channel blockers (class III), and calcium channel blockers (class IV). Drugs with primary targets other than the ion channels and those with unknown mechanisms do not fall into the Vaughan Williams classification and are grouped as class V drugs. Existing drugs for arrhythmia treatment have been widely reported to cause serious complications such as heart failure, stroke, obstructive lung disease, and headaches and cause undesirable pro-arrhythmic effects leading to bradycardia^{14–16}.

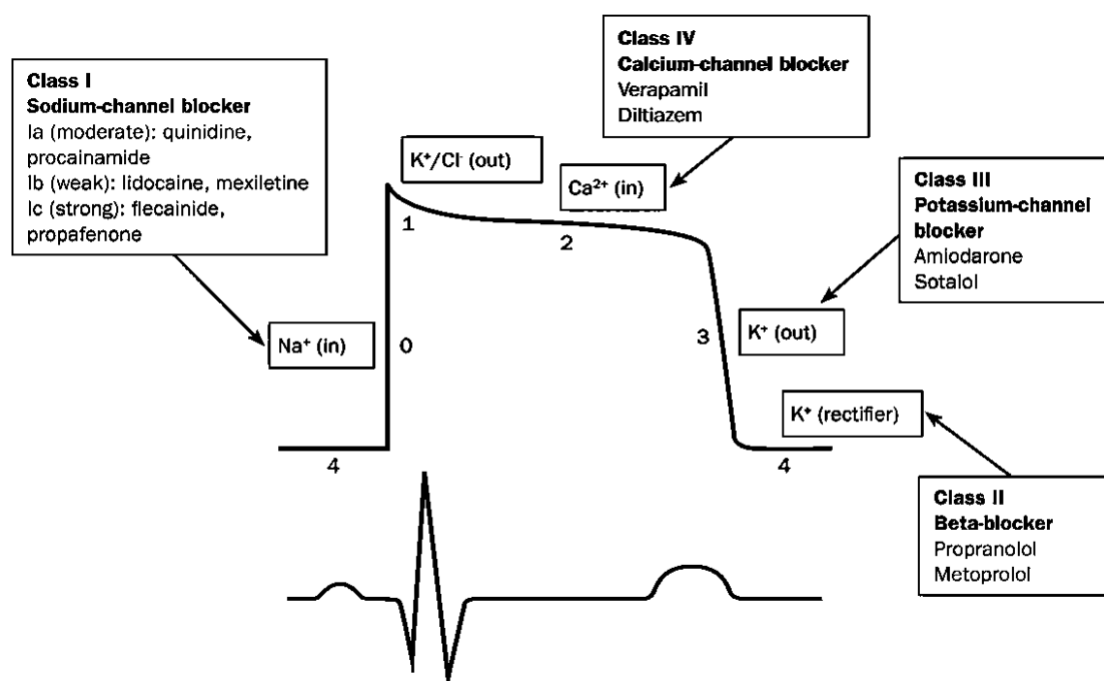


Figure 3. Types of anti-arrhythmic drugs, according to the Vaughan Williams classification, and their mechanism of action at the different stages of the action potential (top) and ECG (bottom) of humans. Reprinted from www.solutionpharmacy.in.

Pacemaker implants

Another leading therapeutic strategy is using pacemakers for managing bradycardias, certain types of tachycardias, syncope, and heart failure¹⁷. A pacemaker is an implantable electrical device that sends small electrical signals initiating depolarization and contraction through leads that connect the device with the heart¹⁸. The pacemakers are prescribed for patients with sinus bradycardia, SAN dysfunction, and AV block¹⁹. The devices are usually implanted on the left side under the collar bone, with the leads inserted into the atria and ventricles (Figure 4a). The pacemakers are programmed to generate an action potential and stimulate contractions by delivering small electrical impulses. Sometimes, the devices are used to sense the intrinsic heart rate and rhythm and resynchronize when needed¹⁹. Even though pacemaker implantations are a common procedure and account for 900,000 implants worldwide each year, they are invasive and require continuous follow-up and monitoring. They also cause serious complications such as hematoma, pneumothorax (air in the pleural space), myocardial perforation, immune rejection, thrombosis, etc^{20,21}.

Direct current cardioversion

In the case of direct current (DC) cardioversion, an external electric shock is applied to the heart through electrode patches to reset the disordered conduction and facilitate the SAN to regulate the heart rate (Figure 4b). A long-term co-administration of anti-arrhythmic drugs is necessary to maintain the restored functions, and patients are more susceptible to reverting to atrial flutter or atrial fibrillation. DC cardioversion therapy also poses the risk of embolus and thrombus formations and increases the risk of stroke¹³.

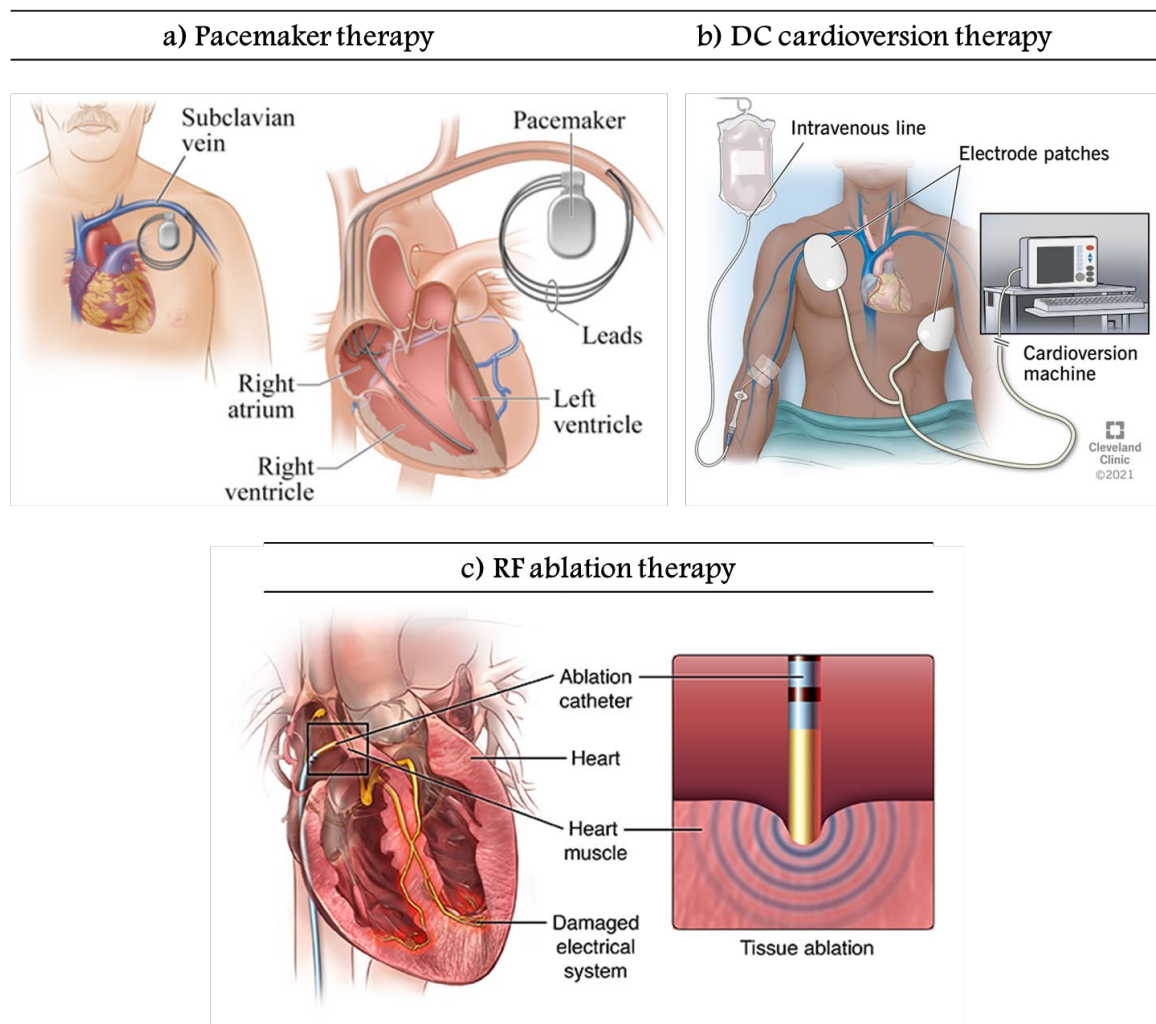


Figure 4. Therapeutic modalities for the treatment of cardiac arrhythmia a) Pacemaker therapy showing the implanted pacemaker device (Adapted from ©Healthwise, Incorporated), b) DC cardioversion therapy with the electrode patches to deliver the electric shock current and stimulate the heart (Adapted from ©Cleveland Clinic), c) RF ablation therapy displaying the catheter inserted into the atria (Adapted from www.divinehearthospital.com).

Radiofrequency ablation

Radiofrequency (RF) ablation is a recent advance in treating and managing arrhythmias. An electrode is inserted into the heart through a catheter, and the electrical activity within the heart is precisely mapped through electrophysiology to identify the region causing arrhythmia. Then, an incident RF energy is applied to ablate the affected tissue and disrupt the improper conduction (Figure 4c). Since the affected tissue is destroyed, pro-arrhythmic effects in the future or the supportive use of anti-arrhythmic drugs are avoided. Although RF ablation exhibits lesser side effects than the previously

discussed treatment options, it could still cause complications such as bruising or bleeding at the catheter insertion site, arrhythmias, infection, and blood clots²².

1.3. Nanotechnology in arrhythmia treatments

Nanotechnology refers to the science of designing, producing, and applying materials at the nanoscale, i.e., materials having at least one dimension measuring between 1-100 nm (nanomaterials). The advent of nanotechnology revolutionized biomedical science and biotechnological research tremendously. Since the 2000s, the application of nanomaterials in the diagnosis, treatment, and management of cardiovascular diseases has been steadily increasing and rapid growth is seen especially in the last decade²³ (Figure 5).

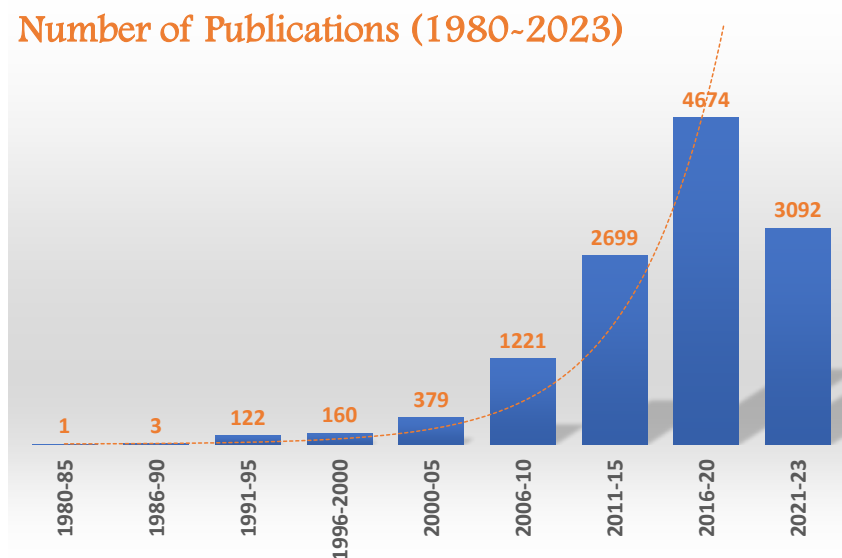


Figure 5. a) Annual publications and citations growth of literature regarding nanotechnology for cardiovascular disease applications. Histogram prepared with data obtained from the Web of Science database, excluding review articles and book chapters. Search Criteria: (TS (topic search) = (nanoparticle* or nano* or nanotechnology* or nanomedicine* or nanosheet* or nanofiber* nanorod* or nanotube* or nanowire* or nanovesicle*)) AND TS = (cardiovascular disease* or arrhythmia* or infarction* or heart failure* or heart* or valve disease* or coronary artery disease* or valve aneurysm* or atherosclerosis* or cardiomyopathy* or pericarditis*) (day of access: May 31, 2023)

Particularly for arrhythmia treatments, using nanomaterials as drug delivery vehicles, bioimaging agents, and tissue engineering scaffolds enables early diagnosis and prevention of heart failure, minimizes off-target toxicity, and facilitates cardiac regeneration and healing^{24,25}. Nanotechnology is also combined with conventional strategies like pharmaceutical therapy and RF ablation, improving the efficacy and specificity of these

arrhythmia treatments. Especially in the last five years, research interest in these areas have been showing a rapid and consistent rise in the trend.

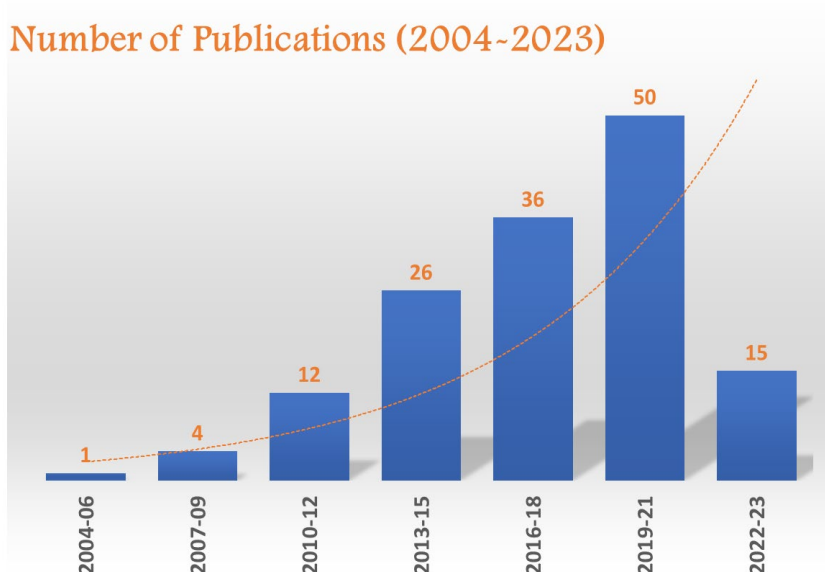


Figure 6. The number of publications in nano- and biomaterials for cardiac arrhythmia and myocardial infarction applications between 2004-2023. Histogram prepared with data obtained from the Web of Science database with combinations of the keywords: “arrhythmia”, “myocardial infarction”, “nanoparticles”, “nanomedicine”, “cardiac tissue engineering”, and “biomaterials” (day of access: May, 26, 2023).

1.3.1. Nano-pharmacotherapy

Nanoparticles (NPs) are beneficial as drug carriers since they can precisely reach and penetrate intricate locations within the heart due to their small size²⁵. Additionally, at the nanoscale, the surface area of NPs increases tremendously, providing an opportunity for tailored surface modifications that enhances cell-nanoparticle interactions enhancing cell uptake²⁴. Various types of nanoparticles, such as polymeric, micellar, mesoporous, lipid NPs, and nanotubes, are reported as effective carrier materials for cardiac drugs²⁶ (Figure 6). The surface of these NPs is modified or conjugated with targeting moieties such as cardiac targeting peptides, proteins, and receptors which can facilitate targeted delivery, enhancing their efficiency and preventing off-target side effects. NPs with unique properties such as optical absorption, magnetism, electrical conductivity, pH sensitivity, etc., can be used to design drug delivery carriers with stimuli-responsive properties. Upon application of the appropriate external stimuli, the carrier releases the drug at the target site, improving target specificity. The unique properties of materials at the nanoscale have been

scrutinized by different researchers for the delivery of anti-arrhythmic drugs, cardiomyocytes or stem cells for regeneration, and miRNA for gene therapy²⁶.

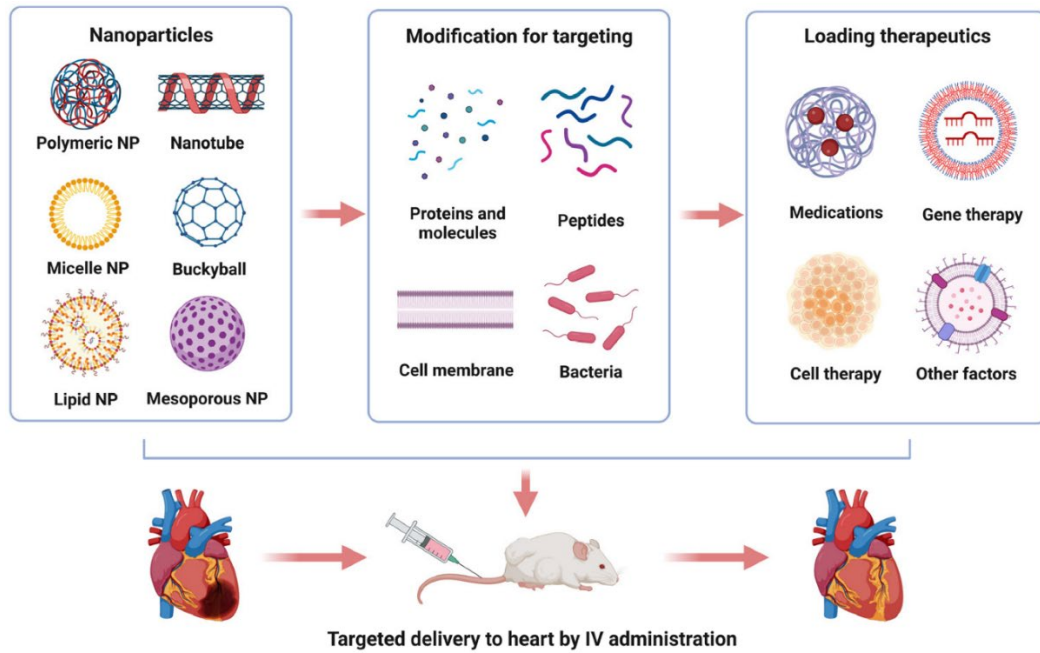


Figure 6. Illustration of nanoparticle-based drug delivery for treating myocardial injuries²⁶, depicting some common NPs employed, their surface modification strategies, and the different cargo materials that can be delivered intracardially through the NP carriers.

The widely used class III anti-arrhythmic drug amiodarone was loaded in cyclodextrin NPs and targeted to cardiac tissue-resident macrophages through an L-lysine surface modification. The accumulation of amiodarone, specifically in cardiac macrophages, can improve the drug's effectiveness since the macrophages play an essential role in cardiac conduction and contractions. Bare amiodarone has a prolonged circulation time and significant off-target accumulation in the thyroid, liver, and lungs. Thus, encapsulation of the drug in cyclodextrin nanocarriers led to a 250% increased uptake by the heart over the lungs compared to bare amiodarone.²⁷

In another recent research²⁸, the authors produced collagen hydrogel loaded with polyethylene imine (PEI)-coated gold NPs, to impart a positive charge to the NP's surface that can effectively conjugate with negatively charged anti-arrhythmic drugs. Phenylephrine, known for terminating supraventricular tachycardias and preventing ventricular arrhythmias, was loaded into the NPs through electrostatic forces. They reported that $\approx 78\%$ of the drug could be effectively released from the NPs within 96h, and *in-vitro* analysis with rat ventricular cardiomyocytes revealed that the drug-nanocarrier

complex promoted the earlier onset of synchronous contractions among the cardiomyocytes. In the absence of Au NPs, collagen-phenylephrine showed signs of the arrhythmic beating of cardiomyocytes; a shorter contraction duration and relaxation time combined with higher contraction amplitude were observed for the PEI-Au NPs-collagen-phenylephrine complex compared with drug-loaded onto only collagen hydrogels without PEI-Au NPs, emphasizing the role of NPs in efficient drug release and reduced side effects.

1.3.2. Nano-ablation therapy

A recent nanotechnology approach in arrhythmia treatment research uses NPs to facilitate focused RF ablation at the regions of interest. In the conventional RF ablation strategy, when the RF energy is applied to cardiomyocytes, the surrounding cells are also affected, causing cell damage. To circumvent this, photodynamic therapy (PDT) uses NPs as photosensitizers (PS) to achieve myocyte-specific ablation.

The study conducted by Avula et al.²⁹ is a clear example of such an approach; the chlorophyll-based PS chlorin e6 (Ce6) is attached to polyethylene glycol (PEG), which was conjugated with cardiac targeting peptide (CTP) molecules. The CTP on the surface enabled myocyte-specific targeting of the PS-NP complex. In-vivo evaluation in rat and sheep hearts resulted in a complete electrical blockage at the ablated region, terminating the abnormal electrical activity and restoring the cardiac rhythm. Conventional RF ablation methods do not leave the surrounding tissues completely unharmed. Nevertheless, with the help of nanotechnology, the authors achieved cell-specific ablation of cardiomyocytes while providing complete protection to the bystander cells.

Another class of NPs that are useful in nano-ablation therapies is metallic NPs such as Copper (Cu), Iron oxide (FeO), and Titanium (Ti). These NPs have been reported to improve the size of ablation lesions in ex-vivo bovine myocardium³⁰. The RF energy applied by the catheter tip is received by the metallic NPs, known to possess electrical and thermal conductivity. Thus, the NPs propagated the incoming RF energy enabling a deeper penetration and causing a more intense thermal injury than ablation treatment without NPs.

1.3.3. Nanomaterial scaffolds for tissue engineering

A significant bottleneck in MI is the poor regenerative capacity of cardiomyocytes. Cardiac tissue is among the least regenerative tissue in the human body, making it nearly impossible to recover to new functional tissue. Nano-biomaterials with structural and

mechanical properties mimicking the extracellular matrix (ECM) are prevalent in cardiac tissue engineering (CTE) to treat MI. Features such as a porous surface, nanofibril mesh-like structures, reactive groups, and functional motifs promote interaction with the biomolecules within the tissues eliciting tissue regeneration.

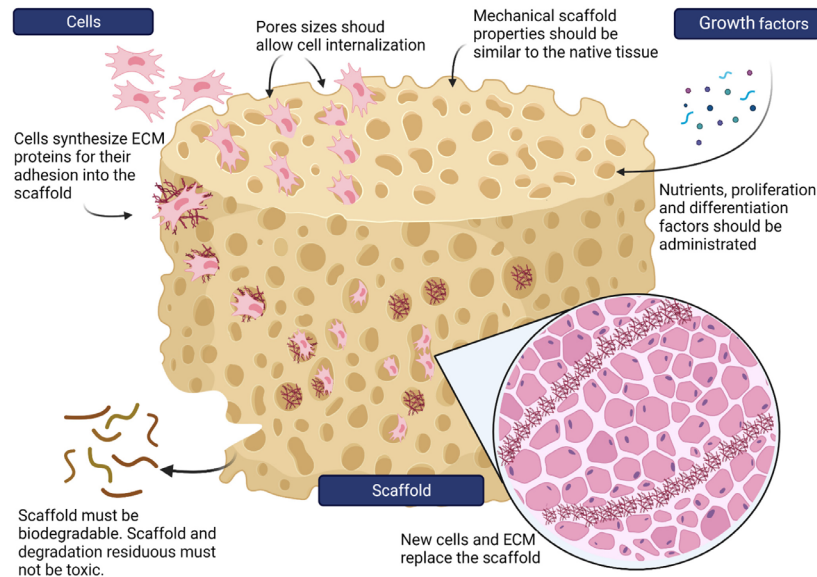


Figure 7. Scheme of the principal properties of scaffolds necessary for cardiac tissue engineering³¹.

The physicochemical properties of nanomaterial matrices like surface energy, surface area to volume ratio, surface roughness, wettability, and reactivity are favorable to promote cell adhesion, migration, differentiation, etc^{32,33}. An ideal scaffold material for CTE should be biocompatible with all cell types of cardiac tissue like fibroblasts, cardiomyocytes, endothelial cells, etc., possess 50-90% porosity to support nutrient and oxygen diffusion, mechanically strong and flexible to withstand the shear force caused by blood flow and the repetitive contractile motions³¹ (Figure 7).

Polymers are the most extensively studied materials as tissue engineering matrices, either synthetic polymers such as Poly (lactic-co-glycolic acid) (PLGA), poly (caprolactone) (PCL), poly (glycerol sebacate), poly (urethane), etc. or natural biopolymers like cellulose, chitosan, alginate, albumin, hyaluronic acid and collagen^{34,35}. Synthetic polymers possess enhanced mechanical properties, can be manufactured with reproducible physical properties and mechanical strength, and are biodegradable. On the other hand, biopolymers have some advantages: they are highly biocompatible and do not induce immune rejection. The natural environment provided by biopolymers also facilitates better attachment, proliferation, differentiation by the cells, and overall behavior of the cells³².

The polymer matrices are often impregnated with therapeutic molecules, targeting components, stem cells, and multifunctional NPs to promote healing and regeneration of the injured area. Electrically conducting NPs are particularly interesting as additives in CTE scaffolds, as they can impart electrical conductivity necessary for cardiac electrical impulse propagation by the scaffolds.

1.4. Conducting Nanomaterials

The inherent electrical propagation within the heart makes cardiac muscles electrically conducting, while the infarcted region in MI becomes non-conducting (Figure 8a). Using conducting nanomaterials around the affected tissue could improve the conduction flow of cardiac impulses and thus improve the cardiac function of an infarcted heart³⁶.

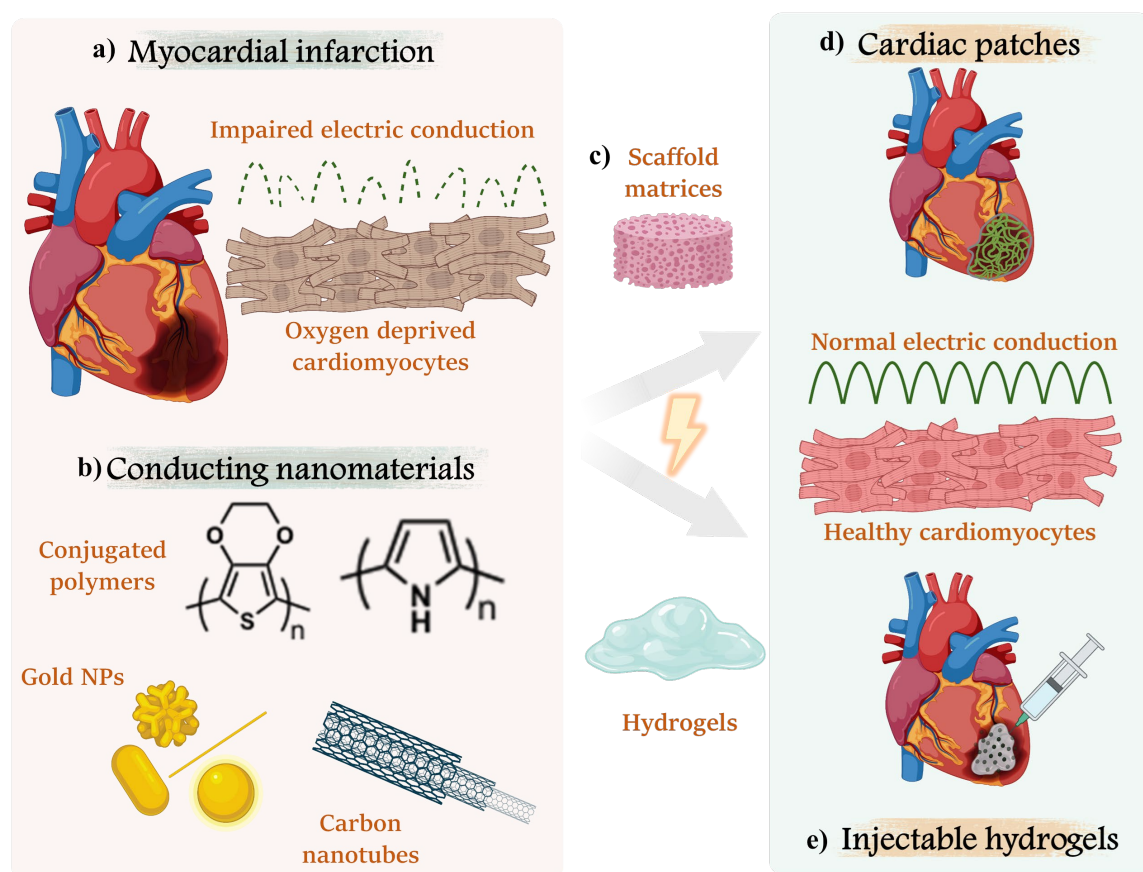


Figure 8. a) The impaired electric conduction among oxygen deprived cardiomyocytes in myocardial infarction, b) Examples of some conducting nanomaterials and the TE strategies for cardiac tissue regeneration and improved cardiac function, c) Polymeric materials – as reinforcements in the form of scaffold matrices and hydrogels, d) Suturable cardiac patches or e) injectable hydrogels, that can repair the injured area and restore the electric conduction.

Nanomaterials with electrical conductivity, such as conjugated polymers, gold NPs, and carbon nanotubes, are commonly researched to impart conductivity to the scaffolds used in CTE (Figure 8b)³⁷. Conjugated polymers (CPs) are especially popular because, in addition to electrical conductivity, they also possess the advantages of polymeric materials, such as the chemical reactivity to functionalize with other materials, stability, and biocompatibility.

The materials are usually combined with other reinforcements (Figure 8c), such as polymeric matrices or hydrogels, to produce cardiac patches (Figure 8d) or injectable conducting hydrogels (Figure 8e), respectively. The composites are also loaded with cardiomyocytes or stem cells to facilitate cardiac regeneration and healing of the infarct. Exploring this direction is a relatively new subject, with studies emerging worldwide during the last few years³⁶.

Conjugated Polymers

CPs are intrinsically conducting polymers with characteristic conjugated aromatic or alkyl chain bonds. The alternating single and double bonds result in delocalized π -electrons, which imparts these polymers with electrical conductivity. CP NPs possess other properties particularly beneficial for biomedical applications, such as ease of synthesis, surface functionality, aqueous stability, etc³⁸. Furthermore, the unique structure of the materials also renders them with NIR-absorption capacity³⁹. This distinctive combination of properties has been utilized by several scientists across the world, especially in the last decade, to produce functional nanomaterials for biomedical applications such as smart stimuli-responsive drug delivery, photothermal therapy, photodynamic therapy, biosensors, tissue engineering, bioimaging, etc³⁸.

NPs of polypyrrole (Ppy), Polyaniline (PANI), Polythiophene (PT), Poly (3,4-ethylene dioxythiophene) (PEDOT), Poly (acetylene) are some examples of CPs used for biological applications^{38,40}. Figure 9 shows a list of common CPs with their chemical structure, all possessing conjugated bonds in their polymeric backbone. Among all the different CPs, Polypyrrole (Ppy) is the most common CP (Figure 9, green) for biomedical applications owing to its ease of synthesis and processing, dispersibility in water, and biocompatibility^{41,42}.

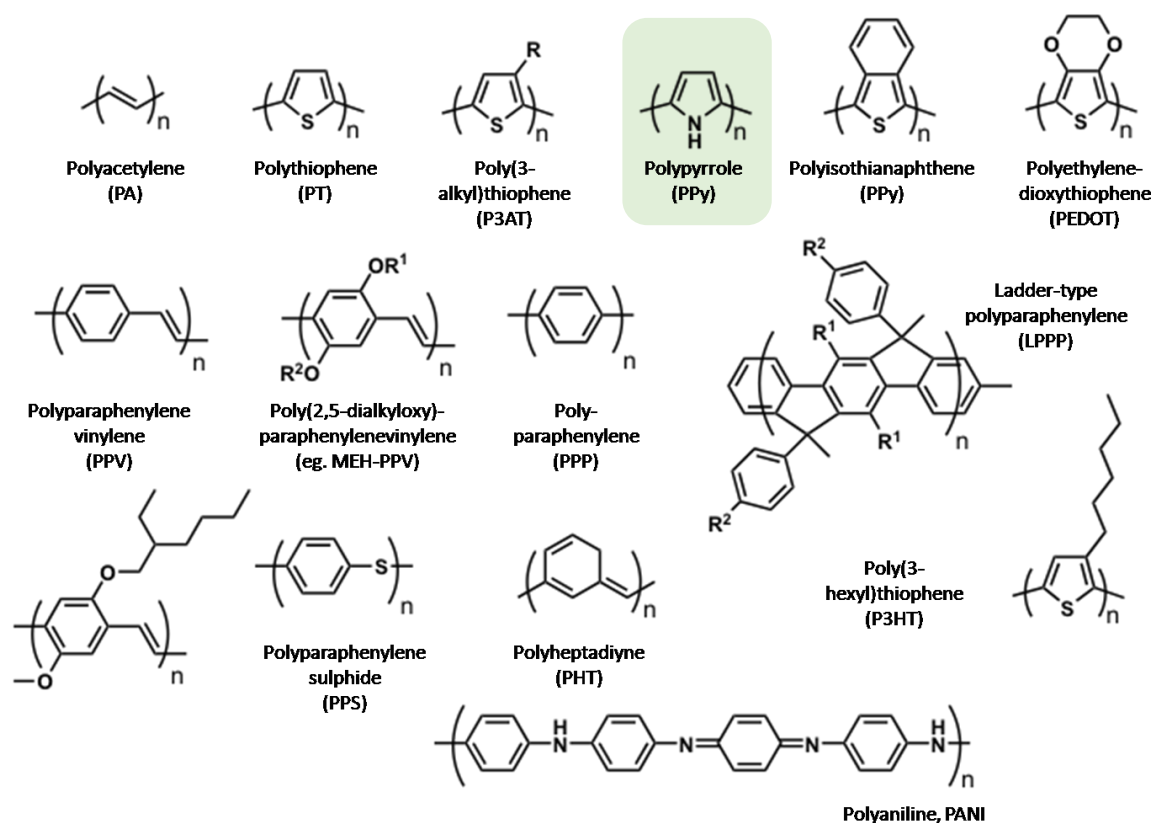


Figure 9. Some commonly used conjugated polymers with their chemical structures⁴⁰. As shown, we can observe the aromatic pentose ring with a secondary amine in the Ppy (green) structure.

1.5. Properties & Applications of Polypyrrole

Ppy is the polymer of pyrrole, which upon oxidation and doping with an anion, gains electrical conducting capability. Pyrrole is a heterocyclic, aromatic pentose ring with a secondary amine functional group. Interestingly, polypyrrole is an insulator but can become conducting upon oxidation by dopants. Ppy NPs are not soluble but dispersible and stable in water. The conjugated structure renders conductivity and strong and broad absorption in the entire NIR region⁴³. The electrical conductivity can be fine-tuned in a wide range by modifying the doping and oxidation levels of Ppy NPs. The NPs are yellow, becoming progressively darker to black upon oxidation, with intermediate colors depending on the dopant type.

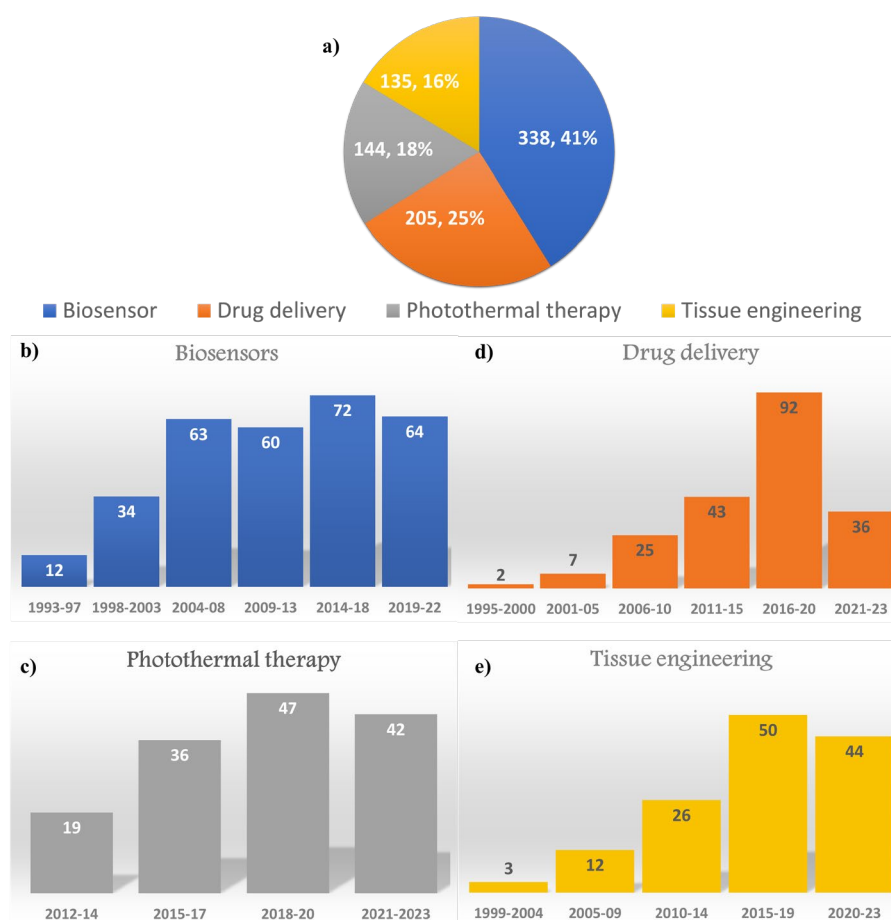


Figure 10: a) The distribution of research articles focusing on Ppy NPs in biomedical applications such as biosensors, drug delivery, photothermal therapy, and tissue engineering in the past 30 years, number of research articles published in b) 30 years on biosensors, c) 10 years on photothermal therapy, d) 30 years on drug delivery, and e) 25 years on tissue engineering applications of Ppy NPs. Data were obtained from the web of science database, using keywords: “polypyrrole”, “nanoparticles”, “biosensors”, “drug delivery”, “photothermal therapy”, and “tissue engineering”.

The oxidation state and conductivity of Ppy NPs can be reverted through reversible electrochemical redox switching⁴⁴. Ppy NPs are also environmentally and thermally stable up to 350 °C⁴⁵, in addition to maintaining physicochemical properties such as size and morphology in aqueous conditions, rendering ideal properties for biosensors. The remarkable stability also facilitates robust storage and transport conditions for Ppy materials, an influencing aspect for commercial nanomedicine. Thus, Ppy NPs possess a plethora of favorable properties rendering them a leading position in several biomedical applications, including drug delivery, biosensing, photothermal therapy, and tissue engineering (Figure 10a). The most popular and earlier utility of Ppy NPs has been in fabricating biosensors (Figure 10a, b), followed by their use as drug delivery carriers

(Figure 10d); however, lately, other applications such as in photothermal therapy and tissue engineering are also rising in popularity since the last 10 years (Figure 10c, e).

Drug delivery systems

Ppy NPs are explored as stimuli-responsive drug delivery systems⁴⁶ since they possess electrically controlled drug release behaviour⁴⁷ and photo-responsive and photothermal behaviors⁴⁸. Good biocompatibility, thermal and aqueous stability of Ppy have also been advantageous for intra-venous drug delivery applications. Likewise, several reports show surface modifications with specific antibodies or targeting agents to provide targeted delivery⁴⁹, and nanocomposites with other materials such as polymers, magnetic NPs, and metallic NPs can impart interesting properties to the drug delivery system achieving an innovative stimuli-responsive therapeutic platform^{46,47,50}.

Photothermal cancer therapy (PTT)

Photothermal therapy (PTT) is a therapeutic strategy for cancer treatment that uses a photo-absorbent in the Near infra-red (NIR) region to convert light into heat leading to heat-induced killing of cancer cells. It is crucial to have a strong NIR absorbance since this radiation can penetrate deep tissues within the human body, which renders Ppy NPs as a promising PTT agent^{39,51}. Frequently, Ppy NPs are used as a delivery platform for anti-cancer drugs to offer chemotherapy and also stimulated using a NIR source to promote the PTT effect, thus enabling a combinatorial effect⁴⁸. Studies showing a further complex design, including a magnetic NP for magnetic resonance imaging (MRI) guided delivery⁵², magnetic hyperthermia⁵³, or a photosensitizer to impart photodynamic therapy in addition to chemotherapy and PTT have also been reported⁵⁴, showing the infinite possibilities of using Ppy for PTT along with other therapeutic modalities to eliminate cancer cells.

Biosensors

PPy NPs have also been applied in electrochemical biosensors^{55,56} because their conductivity is tunable in a wide range from insulating to metallic conductivities by modifying the doping levels and the ability of redox switching of electrical conductivity by doping/de-doping⁴⁴. The NPs can be easily synthesized through chemical polymerization. The low electropolymerization potential also makes them a promising material for biosensing, in addition to their stability under environmental conditions such as varying pHs and temperature. Immobilization of enzymes (oxidases, peroxidases, and

dehydrogenases) on the Ppy electrode surface for sensing analytes like glucose⁵⁷, cholesterol, and bilirubin⁵⁸, are examples of using Ppy in electrochemical biosensing.

Polypyrrole composites for cardiac therapies

Ppy is mechanically rigid with poor flexibility and ductility; therefore, it is often combined with hydrogel polymers to make an injectable formulation for intra-cardiac administration^{59,60} or with polymeric scaffold membranes for CTE^{41,61–63} (Figure 10). The polymeric support can be synthetic polymers such as polylactic-co-glycolic acid, polycaprolactone, polyurethane, polycarbonate, etc. Recently, Aziz *et al.*⁶⁴ produced electrospun scaffolds made of Polycarbonate-Polyurethane fibers (PCNU) and incorporated Ppy NPs on the scaffolds. The conductive Ppy-PCNU scaffolds promoted cell alignment in isolated neonatal rat cardiomyocytes, synchronized the contractions of physically separated cardiomyocytes, and resolved atrial fibrillation in rat hearts. However, the long-term toxicity of such synthetic polymers is a concern since the slow degradation of PCNU results in the release of CO₂ and other toxins, such as glycols and diamines.

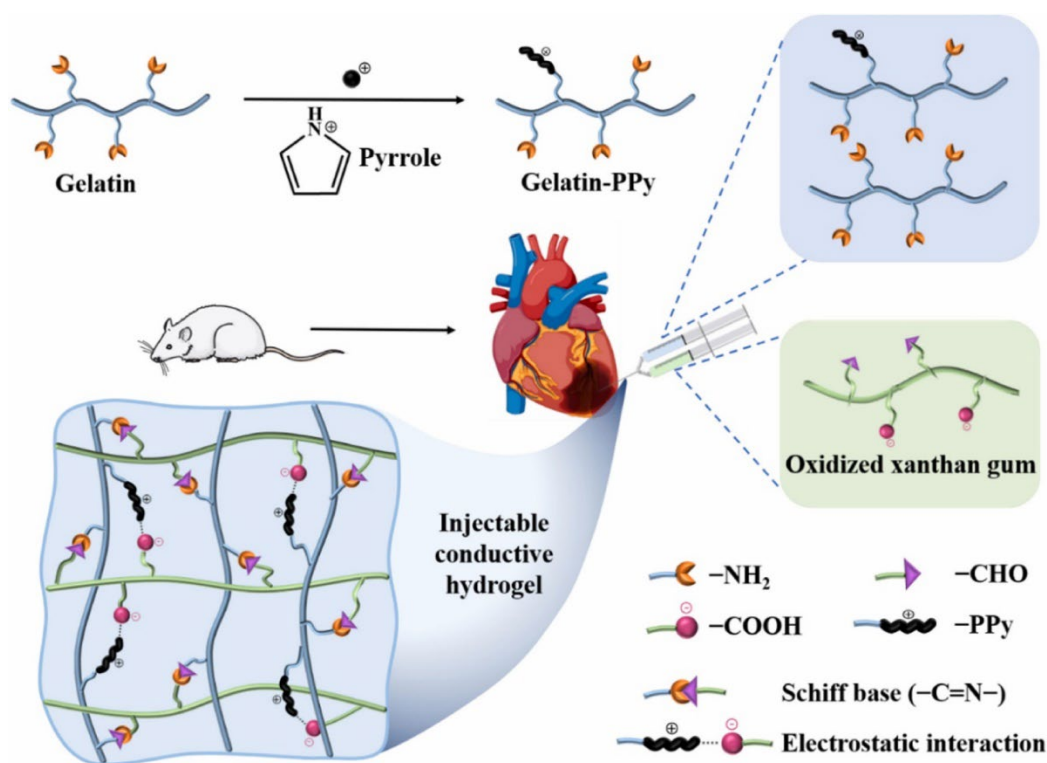


Figure 11: Schematic representation of an injectable gelatin-xanthan gum hydrogel grafted with Ppy NPs. The hydrogel is injected intracardially into rat hearts in the infarcted myocardium to restore cardiac function. Reprinted from Zhang *et al.*⁶⁵.

On the other hand, combining Ppy with biopolymeric matrices from natural sources is a recent research attraction for cardiac therapies since they are highly biocompatible, and the composites can provide excellent electrical, mechanical, and structural properties. Examples of such materials reported in combination with CPs, especially Ppy, include alginate⁶⁶, decellularized ECM (dECM)^{61,67}, cellulose^{68,69}, collagen^{70,71}, etc. Recent work on this aspect conducted by Zhang *et al.*⁶⁵ reported Ppy NPs grafted gelatin-xanthan gum hydrogels that were injectable and conducive for myocardial repair (Figure 11), preventing the induction of arrhythmias in rat hearts. The conduction velocity of impulse across the heart also increased with a concomitant reduction in scar size, increased vessel density, and a reduced inflammatory response surrounding the infarcted region. Although the hydrogels possessed porous morphologies, the microstructure did not resemble the interconnected mesh-like fibrous structure of native ECM. Thus, biopolymers that can exhibit such microstructures in their naturally produced forms, like bacterial cellulose (BC), can be beneficial in promoting better cell behavior, such as adhesion, migration, and maturation.

1.6. Bacterial cellulose

Among the polymers investigated for tissue engineering, cellulose is the most abundant biopolymer on earth, possessing excellent biocompatibility. They are naturally produced by plants from sources like wood and cotton, marine animals such as tunicate, and bacteria⁷². Besides natural sources, cellulose can be produced chemically using cellulose acetate as a precursor. However, cellulose from natural sources is primarily preferred for biomedical applications owing to its outstanding biocompatibility over synthetic cellulose. In addition to biocompatibility, cellulose also displays other notable properties such as high mechanical strength, hydrophilicity, surface functionality, etc., that are highly significant for biomedical applications such as substrates for structural support, drug delivery patches, hydrogels, and transdermal patches for wound healing^{73,74}. Two major forms of nanocellulose are nanofibers (CNFs) and nanocrystals (CNCs). While both share chemical structures and properties, their physical and mechanical properties can be varied vastly. CNCs possess needle-like morphologies of less than 50 nm width, length in the range of 100 nm, and crystalline nature. CNFs exhibit flexible continuous and interconnected fibrous morphology with a wide range of diameter and length running up to several μm s, which can be controlled by modifying the growth conditions. CNFs are generally reported to have much higher flexibility and mechanical strength and are

amorphous. The thinner and longer fibrous structures provide better structural integrity and reinforcement capability to CNFs, making them preferred scaffold materials over CNCs⁷⁵.

Among the different natural sources to produce nanocellulose, bacterial cellulose (BC) is particularly interesting since BC possesses remarkably higher purity than plant cellulose, which shows traces of hemicellulose, lignin, pectin, or even ash⁷⁶. BC also displays no immunogenicity because of this inherent purity and is highly crystalline (84-89%) compared to plant cellulose (40-60%). BC is produced by acetic-acid Gram-negative bacterial cultures of *Aerobacter*, *Agrobacterium*, *Komagataeibacter*, *Pseudomonas*, *Achromobacter*, *Azobacter*, *Rhizobium*, *Salmonella*, and *Alcaligenes* and Gram-positive bacterium *Sarcina ventriculi*. BC has a much higher porosity than plant cellulose, which is valuable for transporting biomolecules and their signals and results in higher water retention capacity. The naturally produced BC possesses a random interconnected network of nanofibers, mimicking the cardiac ECM in terms of morphology, fiber diameter, and pore sizes⁷⁷. To summarize, BC holds a strong position in biomedical applications because of the higher flexibility, porosity, hydrophilicity, purity, and malleability of BC over plant cellulose⁷⁶.

1.7. Bacterial Cellulose-Polypyrrole composites for cardiac tissue engineering

BC has properties that are favorable for the cardiac tissue. Adding Ppy NPs can provide the electrical conductivity essential for cardiac tissue scaffolds to promote cell-cell impulse propagation and regeneration.

He *et al.*⁶⁹ obtained cellulose hydrogels from the tunicate sea squirts and functionalized them with Ppy NPs (Figure 12) through in-situ polymerization resulting in a conductivity of ≈ 0.2 S/m. Evaluation of cardiac-specific protein expressions, synchronous contractions, and calcium transients in primary cardiomyocytes showed that the composite tunicate cellulose-Ppy scaffolds rendered ≈ 2 -fold higher cardiac protein expressions, beating frequency, and amplitude. Further evaluation in MI-induced rat models showed that the scaffolds could reduce the infarct size and volume by almost 50% compared to untreated groups, along with enhanced cardiac protein expression and myocardial tissues.

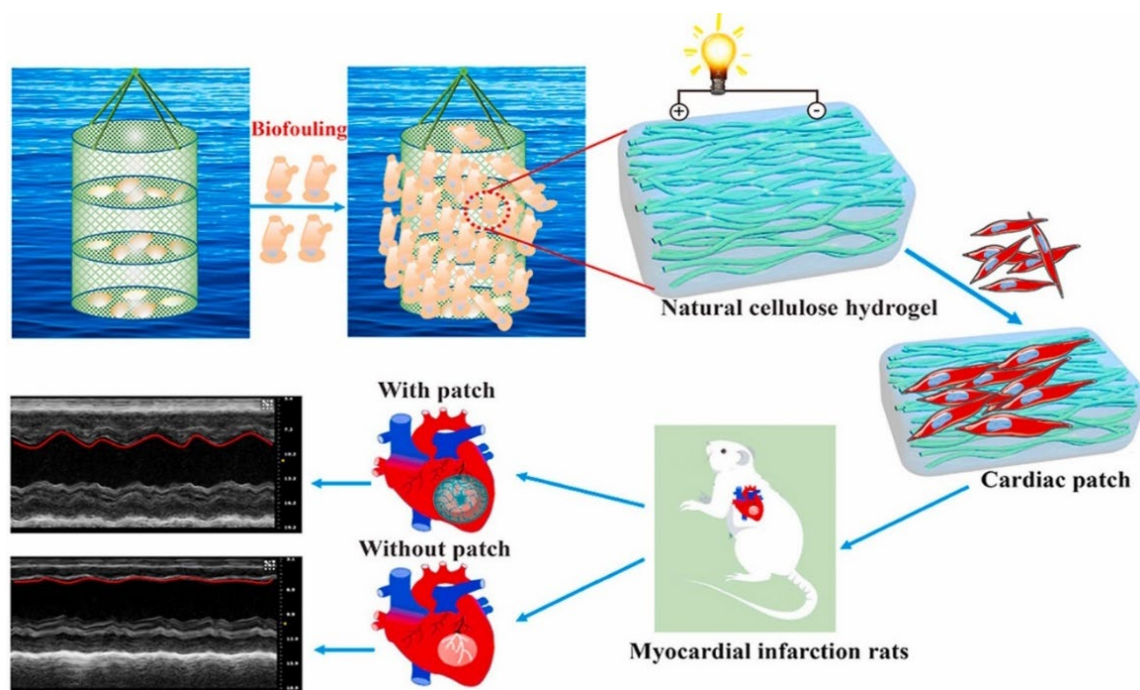


Figure 12. The sea squirts-derived cellulose patch functionalized with Ppy NPs for myocardial infarction from the waste of marine culture⁶⁹.

Owing to the remarkable purity, biocompatibility, flexibility, porosity, hydrophilicity, and mechanical strength of bacterial cellulose over cellulose derived from other sources, we chose BC as our scaffold material. We investigated various concentrations of Ppy NPs resulting in BC: Ppy materials with different material properties to fine-tune and select the ideal candidate for CTE. The design of BC: Ppy composites, optimization of Ppy concentration to achieve desirable scaffold properties, and their evaluation in cardiac cell types are elaborated in Chapter 5.

Any nano-biomaterial must be carefully designed considering the suitable material properties for the application, in this case, to be used for arrhythmia treatments. A thorough investigation of its biocompatibility, therapeutic efficiency, biodegradation or elimination, and pharmacokinetics/pharmacodynamics, must be carried out with the help of bio-evaluation platforms.

1.8. Bio-evaluation Methodologies

Novel nanotherapeutic strategies for treating cardiac arrhythmia and myocardial infarction must be rigorously evaluated *in-vitro* and *in-vivo* to establish their safety and efficacy. A crucial setback in applying nanomaterials for cardiac therapy is the difficulty of producing cardiac disease-specific animal models⁷⁸. Unlike cancer or other disorders, developing animal models of cardiovascular diseases is more complicated and expensive.

3D cell cultures and stem cells are more prevalent in cardiac evaluations but have resulted in multiple proof-of-concept studies using nanomaterials for cardiac therapeutic applications until the in-vitro testing stage; only a handful have proceeded until animal studies.

1.8.1. *in-vitro* models

Traditional 2D cell culture models are always the go-to platforms for initial toxicity evaluation and the efficiency of novel therapies. Nanomaterials for cardiac applications are often evaluated in isolated rat primary cardiomyocytes, embryonic rat cardiomyocytes H9c2⁷⁹, immortalized mouse cardiomyocyte cell lines HL-1^{80,81} and AC16⁸², and human induced pluripotent stem cell-derived cardiomyocytes (hiPSC-CM). The heart has a complex tissue organization consisting of various cell types and microstructures. Consequently, evaluating the materials in the different cell types in a more realistic environment is important. While 2D cell cultures using such cell lines are helpful for the primary evaluation of the materials, they do not provide a platform for co-culturing multiple cell types nor reflect the complex tissue structure and microenvironment.

3D cell culture models

Recent advances in *in-vitro* evaluation focus on using 3D cell culture organoids and organ-on-a-chip platforms. The 3D cell culture model systems are mainly categorized into two⁸³ (Figure 13): 1. Those containing a scaffold matrix, typically a hydrogel loaded with cardiac cells forming a contractile engineered heart tissue (EHT), and 2. Free-standing spheroids formed by self-assembly without scaffold matrices. Recently, the use of scaffold-free spheroids with a mixed population of cell types, such as cardiomyocytes, fibroblasts, stem cells, and endothelial cells, is on the rise⁸⁴. The 3D system is also often designed with micropatterns, microfluidics, pumps, perfusions, and sensors for a system as realistic as possible⁸³.

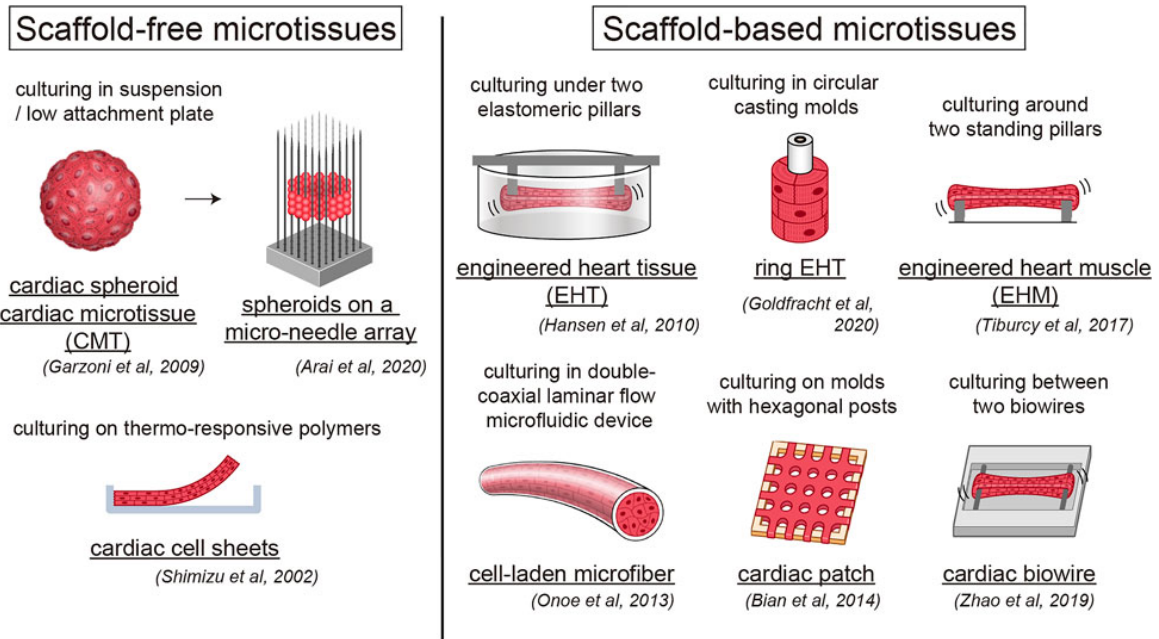


Figure 13. Overview of the design of scaffold-free options like spheroids and sheets and scaffold-based human-engineered heart tissue (EHT) models such as rings, microfibers, patches, and wires⁸⁵.

The heart-on-a-chip is a microfluidic device that can resemble the mechanisms of the heart, reproducing contractility, conduction velocity, and vasculature^{86,87}. Specific mechanisms of an organ can be precisely designed and studied through this system, especially to understand cardiopathology and cardiotoxicity. However, the main drawback with such a platform is that only certain aspects of an organ can be built, and the entire functions of an organ cannot be replicated in a single device. Nevertheless, a vascularized organ with chambers, a pumping function, and a conduction system are not yet achievable in 3D cell cultures.

1.8.2. *in-vivo* models

Almost all of the traditional animal models starting from mice and rats⁸⁸ to larger animals like rabbits, pigs, and dogs, are currently explored animal models for studying cardiac arrhythmia^{88,89}. However, the choice of animal depends mainly on the cause and type of arrhythmia being investigated. An ideal animal model should possess cardiac structural, genetic, and functional resemblance to the human heart, the practical feasibility of housing and breeding at reasonable costs, and the possibility to induce precise genetic modifications to generate tailored animal models⁹⁰. Unfortunately, a perfect animal model meeting all the above needs for arrhythmia research does not exist. Nevertheless, different animals can be employed based on various aspects/mechanisms of the cardiac rhythm

under scrutiny, among other factors such as cost and ethical committee approvals. For instance, the most popular animals, mice and rats, vastly differ in their cardiac electrophysiology from humans. They are not the most preferred models, but they are suitable for genetic studies⁹⁰.

Arrhythmias induced by myocardial ischemia, such as ventricular and atrial fibrillation and ventricular tachycardia, can be studied on mice and rats^{91,92}. Even though a rabbit model MI was developed, no arrhythmias have been reported to date⁹³. Previously, dogs have been used as a common ischemia model, but not in recent years because a pacemaker must be used to induce pacing along with ischemia to observe a significant phenotype in dogs. On the other hand, changes in ventricular ion channel functions induced by myocardial ischemia can be studied using pig models since the phenotypical changes observed were similar to those observed in humans. Pigs are a primary choice of evaluation for arrhythmias caused by ischemia owing to the similarity in anatomy and the ability to induce reproducible infarct sizes⁹⁴.

Exciting findings about atrial fibrillation were achieved using goats as the animal model: artificial induction of atrial tachycardia (tachypacing) causes electrical changes resulting in persistent atrial fibrillation, which induces morphological changes in cardiomyocytes and leads to myocardial dedifferentiation⁹⁵. Other animals such as dogs, sheep, rabbits, and pigs are also suitable animal models for studying atrial fibrillation induced by atrial tachypacing⁹⁰ among which pigs and dogs share a closer electrophysiology with humans than goats, and pigs being the cheapest option of all. Thus, even though goats have been more widely studied to date, pigs might become a viable option soon. Heart failure caused by ventricular tachycardia is studied in dogs, pigs, and rats. Pigs have been reported to be a reliable model for studying alcohol-induced atrial fibrillation and rats for pulmonary hypertension-induced arrhythmias^{96,97}.

Genetically modified mutant strains of animals, like mice, rabbits, and pigs, are used to study the electrophysiology and molecular pathways involved in arrhythmias. Especially, potassium channel mutations (KCNQ1 and KCNH2) of rabbits are an ideal model to study repolarization, TGF- β 1 mutated goats for atrial fibrillation, and SCN-5A mutated pigs as Brugada syndrome models^{98–101}.

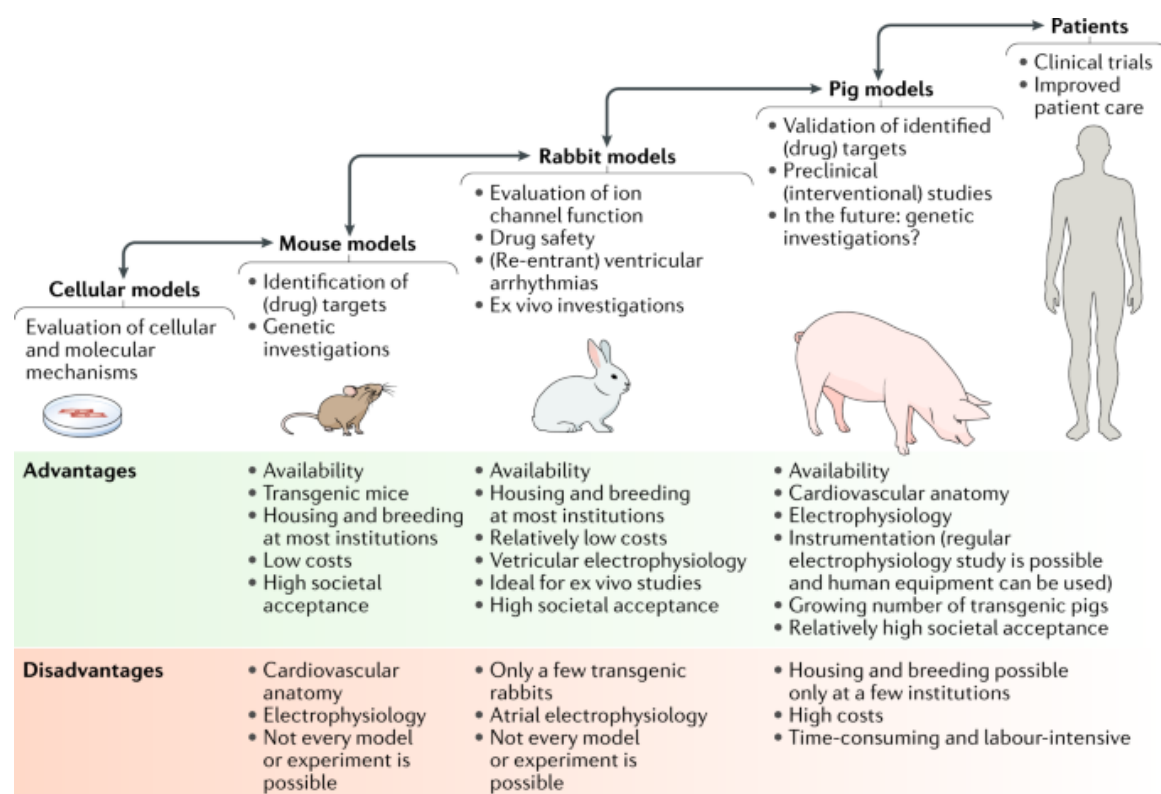


Figure 14. Advantages and disadvantages of different animal species for research. Mice, rabbits, and pigs are the most appropriate models for most studies on arrhythmias⁹⁰.

Although rats and mice provide far more reliability and information for other diseases such as cancer and organ systems like the digestive and nervous systems, they are not the best models for cardiovascular studies owing to their differences compared with the human heart, necessitating an amplified use of higher animals like dogs, rabbits, pigs, and goats (Figure 14). However, each type of arrhythmia requires a different animal model, and creating transgenic mutations in large animals are complicated, expensive, and not encouraged until later developmental stages. They also have a lesser reproduction rate and longer gestational periods than smaller animals, resulting in a low yield of mutant strains.

1.8.3. Alternative small animal models

The use of small animals like zebrafish, *drosophila melanogaster*, and *Caenorhabditis elegans* has seen a surge as model animals for toxicity and efficacy evaluation of drugs at early developmental stages, especially in the assessment of nanomaterials. These models provide the opportunity to implement the 3Rs (reduce, reuse, and recycle), offer valuable information on large scales, and accelerate the animal testing of novel candidates.

Zebrafish

Zebrafish (*Danio rerio*) is an optically transparent freshwater fish with a high reproductive rate. The zebrafish heart comprises only one atrium and one ventricle. Nevertheless, similarities between the human CCS and zebrafish conduction system have been identified. Zebrafish also possess pacemaker cells in the junction sinus venosus and atrium (the equivalent of SAN), and slow-conducting atrioventricular cardiomyocytes in the AVN region are also present, drawing similarities to human heart^{102,103} (Figure 15a). The average heart rate of zebrafish is 120-180 beats per minute (bpm), one of the few animals with a heart rate closest to the human heart (60-90 bpm). The components of ECG and the corresponding phases of the action potential are also similar to humans, with a P wave, QRS complex, and a T wave (Figure 15b, c). Genes encoding some cardiac ion channels are orthologous between zebrafish and humans. Several zebrafish strains with mutated ion channels have been produced and studied as arrhythmia models^{104,105}. However, due to a lower ryanodine receptor expression and a lack of T-tubules, the sarcoplasmic reticulum does not contribute to the Ca^{2+} transients in zebrafish as much as humans. Thus, intracellular Ca^{2+} signaling, an important mechanism influencing arrhythmias, is not shared by zebrafish and humans and therefore cannot be used for studying the Ca^{2+} transient levels¹⁰⁵.

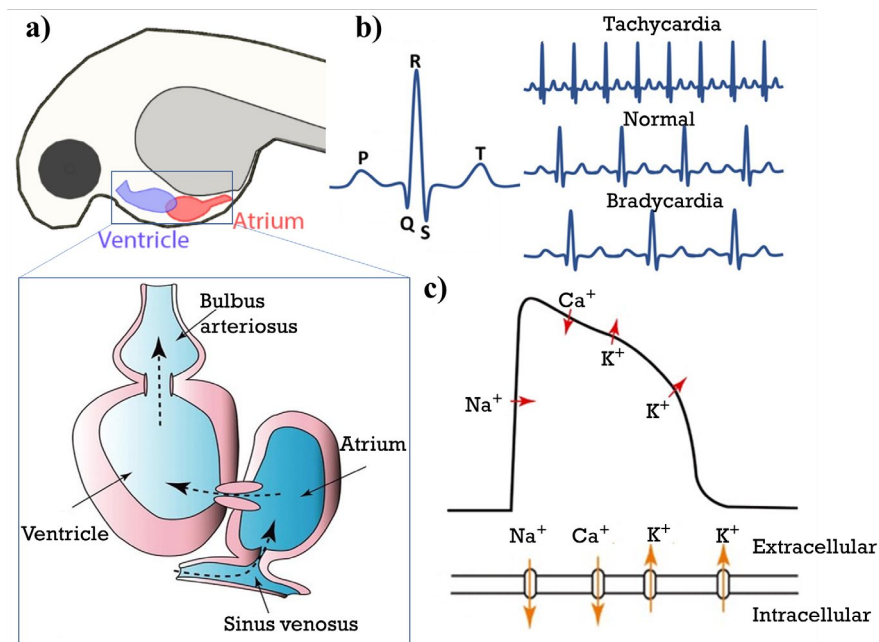


Figure 15. A) Anatomy of zebrafish adult heart showing the atrium and ventricle, B) ECG patterns in zebrafish heart under normal, bradycardia, and tachycardia conditions, C) Action potential pattern with the corresponding ion transfer events.

In this context, zebrafish larvae have been used as an effective small animal model for studying cardiac effects^{102,106}. Cornet *et al.* evaluated the effect of 25 compounds on the heart rate frequencies in zebrafish larvae. They found that the drugs cause similar impacts in zebrafish larvae as in humans and obtained 68% true positive rate (cardiotoxic drugs affecting the heart rate) and 89% true negative rate (non-toxic drugs not affecting the heart rate), higher than hiPSC-CMs and rodents¹⁰⁷. Further, to scale up this process, the same group has developed Zecardio, a combined hardware and software screening system that facilitated high-resolution imaging and high throughput analysis¹⁰⁸. Using this platform, 92 compounds with known clinical cardiotoxicity profiles were analyzed and compared with the data obtained from tests using human induced pluripotent stem cells (hiPSC-CMs). They found that zebrafish show higher sensitivity and an overall 30% higher true positives than hiPSC-CMs. They cite that the complexity of metabolism influencing the ADME, adrenergic signaling, and ion-channel mechanisms of the zebrafish model show a closer resemblance with humans over hiPSC-CMs. However, although not a major risk for initial stage testing, a severe disadvantage of zebrafish models is the lower specificity leading to unwanted rejection of safe drugs, necessitating the research on other small animal models^{107,108}.

Drosophila melanogaster

Drosophila melanogaster (or the common fruit fly) is an invertebrate model exhibiting functional and developmental homology, especially the components and structure of the sarcomere to the human heart^{109–111}. The analysis of ECG patterns has also benefited the use of *Drosophila* for studying cardiac dysfunctions such as channelopathies and cardio-myopathies. Specifically, a key player in influencing cardiac pumping and muscle contractions, calcium signaling, is tightly regulated by several proteins such as voltage-gated Ca^{2+} channels (VGCC), ryanodine receptors (RyR), and sarcoendoplasmic reticulum calcium ATPase (SERCA) pump. Interestingly, mutations in RyR and SERCA channels have also induced arrhythmic effects in *Drosophila* models^{111,112}. The voltage-gated K^{+} channels of *Drosophila* (e.g. KCNQ) have been identified to show orthology to human channels, facilitating the development of channelopathy disease models through genetic mutations of potassium channels¹¹³. Therefore, *Drosophila* is a promising candidate for studying the arrhythmic effects of drugs with potassium channels as their targets. Celecoxib, a non-steroidal anti-inflammatory drug with cyclooxygenase-2 as its primary

target, showed inhibition of voltage-gated K^+ channels inducing arrhythmia when studied on *Drosophila* larval heart and isolated rat ventricular myocytes¹¹⁴.

Caenorhabditis elegans

Among the small animal models, *Caenorhabditis elegans* (*C. elegans*) is a recent alternative for cardiac arrhythmia studies. *C. elegans* are free-living nematode worms, commonly found in the soil, with bacteria as their primary food source. The anatomy of *C. elegans* comprises mainly five organ systems: the skin, digestive, nervous, muscular, and reproduction systems (Figure 16). The genome of *C. elegans* contains $\approx 20,000$ genes, and it was the first animal model to have its entire genome sequenced in 1998. They also have a finite number of neurons (302) and were the first model to have a completed connectome in 2019¹¹⁵.

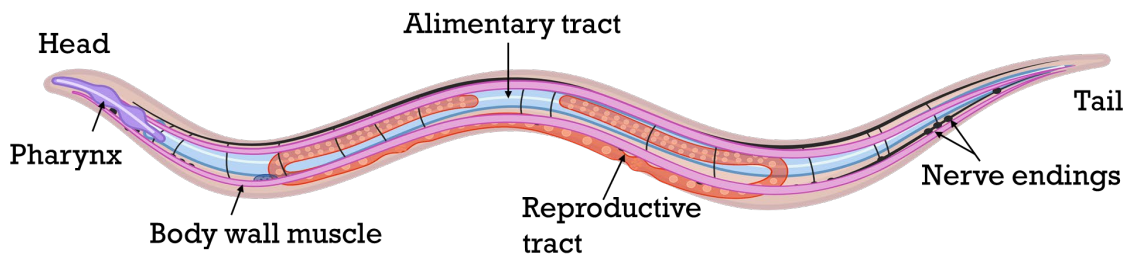


Figure 16. *C. elegans* and its major anatomical features: pharynx, body wall muscle, reproductive tract, alimentary tract, and nerve endings shown in a hermaphrodite worm.

Owing to these physiological, behavioral, and experimental advantages, *C. elegans* are a popular small animal model for research in developmental biology, aging-related studies, and the nervous system. In the past decade, the use of *C. elegans* for testing nanomaterials has been gaining attention, concurrent with the rise of novel nanomaterials for biomedical applications and the inevitable need for small animal models for their rigorous evaluation^{116,117}. *C. elegans* are a promising tool to study toxicology on a large scale, to identify their molecular targets, the pharmacokinetics of nanomaterials such as their dissolution or accumulation, biodistribution, and pharmacodynamics such as absorption, distribution, metabolism, and excretion (ADME).

1.8. The pharynx of *Caenorhabditis elegans*

The worms possess pharynx, a continuously pumping filter-feeder responsible for grinding the ingested substances and their progression toward the intestine¹¹⁸. The pharynx comprises a buccal cavity, procorpus, metacorpus (anterior bulb), isthmus, terminal bulb,

and pharyngeal-intestinal valve¹¹⁹ (Figure 17). The pharyngeal muscle cells in the isthmus undergo repetitive contractions resulting in isthmus peristalsis, facilitating the food movement¹²⁰. The pharynx grinder comprises three pair of muscle cells which contracts and rotates upon contraction, enabling the grinding of the ingested substance and movement to the intestine through the pharyngeal-intestinal valve^{119,121}.

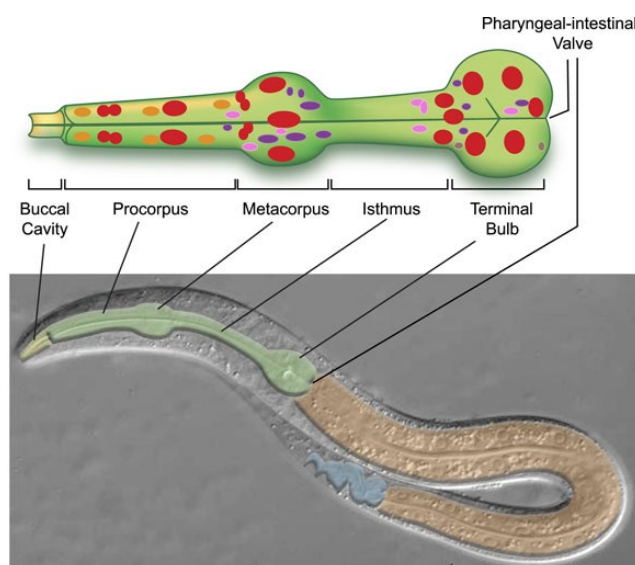


Figure 17. The *C. elegans*' pharynx – the filter-feeding organ. Anatomical features and structural organization of the pharynx, red - muscles, purple - neurons, orange - epithelia, pink - marginal cells, and brown - glands¹²².

Pharynx pumping

The corpus, isthmus, and terminal bulb are made of muscle cells that are electrically coupled to each other, contracting and relaxing throughout the life of the worms, similar to the human heart^{119,123}. The contractions are initiated at the corpus by excitation of the cholinergic motor (MC) neurons (Figure 18a), progressing through the isthmus and reaching the terminal bulb. The coupling between the muscle cells is mediated through gap junctions that propagate the action potential from one cell to the next via voltage-gated cation channels, resulting in muscle contractions. Thus, the corpus, anterior isthmus, and terminal bulb undergo an almost simultaneous contraction (Figure 18b). Whereas the posterior isthmus exhibits a delayed contraction resulting in a traveling wave of contraction called peristalsis (Figure 18d).

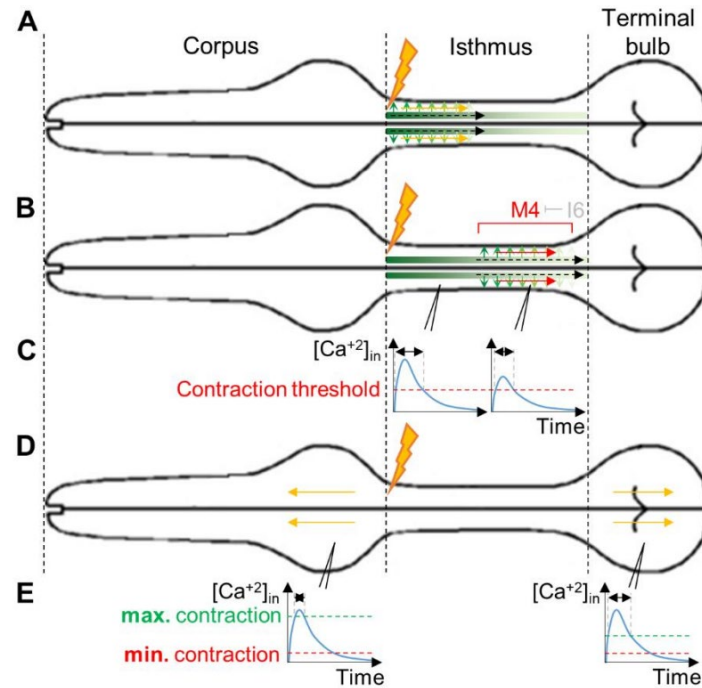


Figure 18. Suggested mechanisms for the contraction dynamics of the various pharyngeal areas. A) excitation of cholinergic motor (MC) neurons (lightning) at the corpus-isthmus border and pharyngeal muscle depolarization, B-C) Ca^{2+} influx and a near-simultaneous contraction of the corpus, anterior isthmus, and terminal bulb (C) Schematic Ca^{2+} dynamics at the anterior and posterior isthmus muscles during a pump. $[\text{Ca}^{2+}]_{\text{in}}$ reach lower maximal values at the posterior than at the anterior isthmus resulting in shorter contractions at the posterior than anterior isthmus, causing peristalsis at the posterior and pumping at the anterior isthmus. (D-E) The suggested mechanism for corpus and TB dynamics and different $[\text{Ca}^{2+}]$ thresholds of contraction. (E) Schematic Ca^{2+} dynamics at the corpus (left) and terminal bulb (right) muscles during a pump. ¹²³

1.9. The opportunity of *Caenorhabditis elegans* for arrhythmia evaluation

The action potential follows a series of Calcium (Ca^{2+}) mediated membrane depolarization and contraction, followed by repolarization before returning to its resting state, analogous to the human cardiac action potential¹²² (Figure 19). The depolarization-repolarization cycle is controlled by a tightly regulated transport of Potassium (K^{+}) and Ca^{2+} ions through the potassium channels and L-type and T-type voltage-gated calcium channels. Mutations in the ion channels can thus lead to a dysregulation in the muscle contraction perceived as altered pharyngeal pumping, the same way ion channelopathies in the heart lead to cardiac arrhythmia^{124,125}. Notably, the sodium, potassium, and calcium channels of *C. elegans*, such as *nca-1*, *nca-2* (sodium), *exp-2* (potassium), *egl-19*, *cca-1*

(calcium), *unc-68*, etc., are genetically homologous to *NALCN* (sodium), *KCNQ1* (potassium) and *CACN1* (calcium), and *RyR2* of humans, respectively¹²⁶ (Table 1).

a) Cardiac Action Potential b) Pharyngeal Action Potential

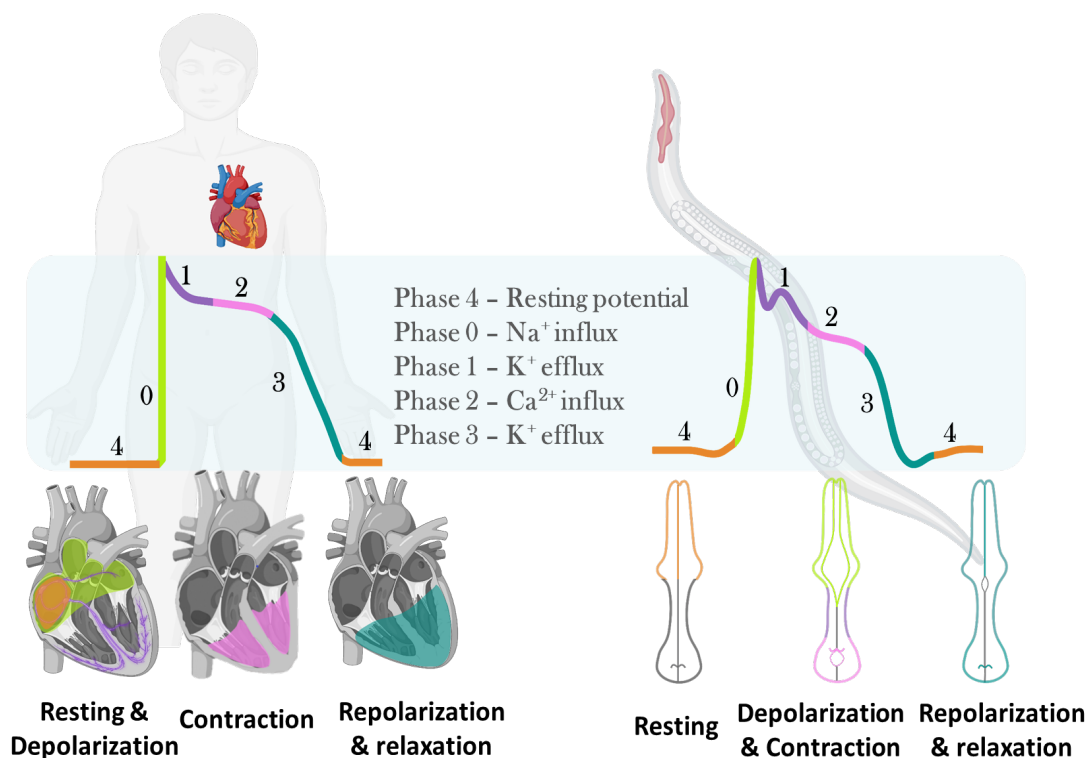


Figure 19. Similarities between the action potential propagation in a) humans and b) *C. elegans* generated by the cation transfers across cardiomyocytes and pharyngeal muscle cells, respectively.

Owing to the genetic and structural similarities between the *C. elegans* pharynx and the human heart, genetic modifications are carried out in *C. elegans* to produce disease models with arrhythmia-specific phenotypes. The Cav1.2 channel is an L-type voltage-gated calcium channel encoded by *CACNA1A* genes homologous to *egl-19* genes in the pharynx. Mutations in Cav1.2 channels result in long QT syndrome in humans. Homologous mutations in *egl-19* of *C. elegans* also induced long QT-like phenotypes such as a prolonged pump duration and impaired ability to pump at high frequency¹²⁷. Similarly, the same group also created mutations, *csq1* and *unc-68*, which are orthologous to the human Ca^{2+} channels. These mutations resulted in altered pharyngeal pumping, such as missed pumps, pumping at half frequency, or no pumping. Interestingly, when the worms were treated with an anti-arrhythmic agent, benzothiazepine, the impaired pumping caused by the mutations reverted to regular pharyngeal pumping in the worms¹²⁸. The characteristic

arrhythmia causing mutations of the heart resulting in a corresponding arrhythmia-like phenotype in *C. elegans* is solid evidence that encourages the application of *C. elegans* as an animal model for cardiotoxicity and anti-arrhythmic efficacy assessment of nanomaterials.

Table 1. Orthologous cation channels such as sodium, potassium, and calcium channels in *C. elegans* and humans¹²⁶.

Ion Channels	<i>C. elegans</i> genes	Human orthologs
Sodium channels	<i>nca-1, nca-2</i>	<i>NALCN</i>
Potassium channels	<i>exp-2</i>	<i>KCN genes (B1-2, F1, G1, S1-3, V1-2)</i>
	<i>egl-19</i>	<i>CACNA1 genes (A-F, S)</i>
Calcium channels	<i>cca-1</i>	<i>CACNA1 (G-I)</i>
	<i>unc-68</i>	<i>RyR (1-3)</i>

1.10. Thesis Rationale

Cardiovascular diseases (CVDs) are still the number one cause of death worldwide, and the existing treatments in practice only focus on managing the arrhythmias without treating the underlying cause and pose serious contraindications, poor efficiency, and specificity. Therefore, to effectively treat and manage arrhythmias, a multifunctional therapy with high efficiency, biocompatibility, and minimal side effects is crucial in today's healthcare landscape.

After carefully exploring the current research trends through existing literature on novel treatment options for cardiac arrhythmia, we embarked on the applications of Ppy NPs in cardiac therapies. Although intrinsically conducting polymers, especially Ppy NPs, are a trend in cardiovascular therapeutic research, there is an evident lack of animal studies. The more commonly studied form is Ppy composite scaffolds as potential cardiac patches. However, a thorough investigation of the cardiac effects of bare Ppy NPs and their possible molecular mechanism must be understood before developing more complex composite materials with practical applications.

The lack of *in-vivo* studies of Ppy NPs for arrhythmia could be because of the difficulty in producing animal models with specific mutations of interest. Since arrhythmia models are often higher animals like dogs and pigs, lack of expertise, housing facilities, funding, and

ethical approval hinders the progress of novel treatment options like nanomedicines, in this case, the Ppy NPs.

Small animals such as zebrafish and fruit flies provide valuable information when used for arrhythmia research, concomitantly enabling facile, rapid, and large-scale evaluation. However, zebrafish is not ideal for Ca^{2+} signaling, a key mechanism of action for anti-arrhythmic treatments. Also, the assessment of the arrhythmic effects of drugs on zebrafish models showed that the zebrafish displayed a low specificity for these drugs. *Drosophila* is a suitable animal model for assessing specific aspects of arrhythmia, such as the Ca^{2+} activity and channelopathies of K^{+} ion channels, but not other types and characteristics of arrhythmias. Thus, a need for a versatile, extensive, and robust small animal model gave rise to the potential use of *C. elegans* for anti-arrhythmic NPs and drug screenings at the initial stage.

C. elegans enable fast, facile, and high throughput toxicity evaluation of NPs. Additionally, the analogy drawn between the worms' pharynx and a human heart and their structural and genetic homology shows tremendous promise to exploit these models to evaluate the arrhythmic effects of NPs. *C. elegans* also boasts a set of distinctive advantages: the creation of mutant strains is straightforward through feeding of the worms to mutagens or the use of genome editing tools for site-specific mutations, the mutant strains can be maintained frozen for several years, and each worm can produce up to 300 offspring in 72 hours, giving rise to a massive population of mutant strains in a short period. Consequently, we chose *C. elegans* as a novel testing platform for assessing the toxicity and pharyngeal effects of Ppy NPs.

The feasibility of extensively evaluating Ppy NPs in *C. elegans* encouraged us to design a composite material of Ppy NPs and bacterial cellulose (BC-Ppy) with improved functionalities imparted by the BC, which will be much closer to a practical application, such as the use of cardiac patches for MI and arrhythmias. *In-vitro* evaluation of the scaffolds in cardiac fibroblasts and the cardiomyocyte cell line H9c2 were performed individually. The behavior of cardiac cells in the presence of scaffolds sheds light on the role of Ppy NPs and the benefits of BC in influencing these cell behaviors. It opens up avenues for further investigation of BC-Ppy composites as cardiac patches.

References

1. Wilkins E, Wilson L, Wickramasinghe K, Bhatnagar P, Leal J, Luengo-Fernandez R, Burns R, Rayner M, T. N., Nichols, M., Townsend, N., Scarborough, P. & Rayner, M. Cardiovascular disease in Europe: Epidemiological update 2017. in *European Cardiovascular Disease Statistics 2017*, **32**, 1–192 (European Heart Network, Brussels., 2017).
2. Townsend, N. *et al.* Cardiovascular disease in Europe: Epidemiological update 2016. *Eur Heart J* **37**, 3232–3245 (2016).
3. Artucio, H., Pereira, M. & Artucio, H., & Pereira, M. Cardiac arrhythmias in critically ill patients: an epidemiologic study. *Crit Care Med* **18**, 1383–1388 (1990).
4. Srinivasan, N. T. & Schilling, R. J. Sudden cardiac death and arrhythmias. *Arrhythm Electrophysiol Rev* **7**, 111–117 (2018).
5. Xiao, Y. F. Cardiac arrhythmia and heart failure: From bench to bedside. *J Geriatr Cardiol* **8**, 131–132 (2011).
6. Barton, A. K., McGowan, M., Smyth, A., Wright, G. A. & Gardner, R. S. Classification and choice of anti-arrhythmic therapies. *Prescriber* **31**, 11–17 (2020).
7. Frampton, J., Ortengren, A. R. & Zeitler, E. P. Arrhythmias After Acute Myocardial Infarction. *Yale J Biol Med* **96**, 83–94 (2023).
8. Borchard, U. & Hafner, D. ion channels and arrhythmias. *Z Kardiol* **89**, III/6-III/12 (2000).
9. van Weerd, J. H. & Christoffels, V. M. The formation and function of the cardiac conduction system. *Development* **143**, 197–210 (2016).
10. Laske, T. G. & Iatzo, P. A. The Cardiac Conduction System. in *Handbook of Cardiac Anatomy, Physiology, and Devices*. (ed. Iatzo, P. A.) 123–136 (Humana Press., 2005).
11. Padala, S. K., Cabrera, J. A. & Ellenbogen, K. A. Anatomy of the cardiac conduction system. *Pacing Clin Electrophysiol*, **44**, 15–25 (2021).
12. Christoffels, V. M. & Moorman, A. F. M. Development of the cardiac conduction system: why are some regions of the heart more arrhythmogenic than others? *Circ Arrhythm Electrophysiol* **2**, 195–207 (2009).
13. Helen Williams. Arrhythmias options for treatment. *Pharm J* 1–13 (2005).
14. Hanayneh, S., Panna, M. E., Miles, W. M. & Goel, R. Anti-arrhythmic Drugs—a Review and Comment on Relevance in the Current Era: Part 1. *Curr Treat Options Cardiovasc Med*, **23** (2021).
15. Hanayneh, S., Panna, M. E., Miles, W. M. & Goel, R. Anti-arrhythmic Agents: a Review and Comment on Relevance in the Current Era—Part 2. *Curr Treat Options Cardiovasc Med*, **23** (2021).
16. Kowey, P. R. Pharmacological Effects of Anti-arrhythmic Drugs Review and Update. *Arch Intern Med* **158**, 325–332 (1998).
17. Gregoratos, G. Indications and Recommendations for Pacemaker Therapy. *Am Fam Physician* **71**, 1563–1570 (2005).

18. Coombes D. Pacemaker therapy 1: clinical indications, placement and complications. *Nursing Times [online]* **117**, 22–24 (2021).
19. Reynolds, C. & Saile, K. Pacemaker Therapy. in *Section IV: Cardiovascular System, In Small Animal Surgical Emergencies* 365–376 (2015).
20. Townsend, T. Five common permanent cardiac pacemaker complications. *Nurs Crit Care (Ambler)* **13**, 46–48 (2018).
21. George, G. & Aujayeb, A. Cardiac-Device Implantation and Pneumothorax—A Symptom-Based Approach: Experience from a District General Hospital. *Reports* **5**, 39 (2022).
22. Joseph, J. P. & Rajappan, K. Radiofrequency ablation of cardiac arrhythmias: Past, present and future. *Q J Med* **105**, 303–314 (2012).
23. Zheng, Z., Zhu, S., Lv, M., Gu, Z. & Hu, H. Harnessing nanotechnology for cardiovascular disease applications - a comprehensive review based on bibliometric analysis. *Nano Today*, **44** (2022).
24. Jiang, W., Rutherford, D., Vuong, T. & Liu, H. Nanomaterials for treating cardiovascular diseases: A review. *Bioact. Mater.* **2**, 2, 185–198 (2017).
25. Chopra, H. *et al.* Nanomaterials: A Promising Therapeutic Approach for Cardiovascular Diseases. *J. Nanomater.*, **2022** (2022).
26. Li, D., Son, Y., Jang, M., Wang, S. & Zhu, W. Nanoparticle Based Cardiac Specific Drug Delivery. *Biology*, **12** (2023).
27. Ahmed, M. S. *et al.* A Supramolecular Nanocarrier for Delivery of Amiodarone Anti-Arrhythmic Therapy to the Heart. *Bioconjug Chem* **30**, 733–740 (2019).
28. Roshanbinfar, K. *et al.* Collagen Hydrogel Containing Polyethylenimine-Gold Nanoparticles for Drug Release and Enhanced Beating Properties of Engineered Cardiac Tissues. *Adv Healthc Mater* 1–20 (2023).
29. Mahesh Avula, U. R. *et al.* Cell-selective arrhythmia ablation for photomodulation of heart rhythm. *Sci Transl Med* **7**, 172–182 (2015).
30. Nguyen, D. T. *et al.* Enhanced Radiofrequency Ablation With Magnetically Directed Metallic Nanoparticles. *Circ Arrhythm Electrophysiol* **9**, (2016).
31. Roacho-Pérez, J. A. *et al.* Artificial Scaffolds in Cardiac Tissue Engineering. *Life* **12**, 1117. (2022).
32. Chen, Q. Z., Harding, S. E., Ali, N. N., Lyon, A. R. & Boccaccini, A. R. Biomaterials in cardiac tissue engineering: Ten years of research survey. *Mater. Sci. Eng. R Rep.*, **59**, 1–37 (2008).
33. R Amin, D. *et al.* Nanomaterials for Cardiac Tissue Engineering. *Molecules*, **25**, 1–21 (2020).
34. Dhandayuthapani, B., Yoshida, Y., Maekawa, T. & Kumar, D. S. Polymeric scaffolds in tissue engineering application: A review. *Int J Polym Sci* **2011**, (2011).
35. Tang, X. *et al.* Polymeric Biomaterials in Tissue Engineering and Regenerative Medicine. in *Natural and Synthetic Biomedical Polymers* 351–371 (Elsevier Inc., 2014).

36. Liu, W., Zhao, L., Wang, C. & Zhou, J. Conductive nanomaterials for cardiac tissues engineering. *Engineered Regeneration*, **1**, 88–94 (2020).
37. Mousavi, A. *et al.* Multifunctional Conductive Biomaterials as Promising Platforms for Cardiac Tissue Engineering. *ACS Biomater Sci Eng*, **7**, 55–82 (2021).
38. Lin, H. *et al.* Conjugated polymers for biomedical applications. *Chem. Comm.*, **58**, 7232–7244 (2022).
39. He, Y., Cao, Y. & Wang, Y. Progress on Photothermal Conversion in the Second NIR Window Based on Conjugated Polymers. *Asian J. Org. Chem.*, **7**, 2201–2212 (2018).
40. Rasmussen, S. C. On the Origin of “Synthetic Metals”: Herbert McCoy, Alfred Ubbelohde, and the Development of Metals from Nonmetallic Elements. *Bull Hist Chem*, **41**, (2016).
41. Huang, Z. B., Yin, G. F., Liao, X. M. & Gu, J. W. Conducting polypyrrole in tissue engineering applications. *Front. Mater. Sci.*, **8**, 39–45 (2014).
42. Liang, Y. & Goh, J. C. H. Polypyrrole-Incorporated Conducting Constructs for Tissue Engineering Applications: A Review. *Bioelectricity*, **2**, 101–119 (2020).
43. Vernitskaya, T. V & Efimov, O. N. Polypyrrole: a conducting polymer; its synthesis, properties and applications. *Russ. Chem. Rev.*, **66**, 443–457 (1997).
44. Zhang, Q. *et al.* Redox switch of ionic transport in conductive polypyrrole-engineered unipolar nanofluidic diodes. *Nano Res*, **10**, 3715–3725 (2017).
45. Jakab, E., Mészáros, E. & Omastová, M. Thermal decomposition of polypyrroles. *J Therm Anal Calorim*, **88**, 515–521 (2007).
46. Kiran Raj, G. *et al.* Conductive polymers and composites-based systems: An incipient stride in drug delivery and therapeutics realm. *J Control Release*, **355**, 709–729 (2023).
47. Miar, S., Ong, J. L., Bizios, R. & Guda, T. Electrically Stimulated Tunable Drug Delivery From Polypyrrole-Coated Polyvinylidene Fluoride. *Front Chem*, **9**, (2021).
48. Ma, X. *et al.* Host–Guest Polypyrrole Nanocomplex for Three-Stimuli-Responsive Drug Delivery and Imaging-Guided Chemo-Photothermal Synergetic Therapy of Refractory Thyroid Cancer. *Adv Healthc Mater*, **8**, (2019).
49. Chen, J. *et al.* Synthesis of Size-Tunable Hollow Polypyrrole Nanostructures and Their Assembly into Folate-Targeting and pH-Responsive Anti-cancer Drug-Delivery Agents. *Chem. Eur. J.* **23**, 17279–17289 (2017).
50. Saheeda, P. *et al.* Multi-walled carbon nanotubes/polypyrrole nanocomposite, synthesized through an eco-friendly route, as a prospective drug delivery system. *Polymer Bulletin* (2022).
51. Zeng, W. *et al.* Renal-Clearable Ultrasmall Polypyrrole Nanoparticles with Size-Regulated Property for Second Near-Infrared Light-Mediated Photothermal Therapy. *Adv Funct Mater* **31**, (2021).
52. Zhou, B. *et al.* Polypyrrole-based nanotheranostic agent for MRI guided photothermal-chemodynamic synergistic cancer therapy. *Nanoscale* **13**, 19085–19097 (2021).

53. Bao, J. *et al.* Polypyrrole-Coated Magnetite Vortex Nanoring for Hyperthermia-Boosted Photothermal/Magnetothermal Tumor Ablation Under Photoacoustic/Magnetic Resonance Guidance. *Front Bioeng Biotechnol* **9**, (2021).
54. Tran, T. H. *et al.* Combined photothermal and photodynamic therapy by hyaluronic acid-decorated polypyrrole nanoparticles. *Nanomedicine* **12**, 1511–1523 (2017).
55. Geetha, S., Rao, C. R. K., Vijayan, M. & Trivedi, D. C. Biosensing and drug delivery by polypyrrole. *Anal. Chim. Acta*, **568** 119–125 (2006).
56. Kavitha, N. *et al.* Polymer nanohybrid composites as conductive platform for the electrochemical sensing of pathogens. *Curr. Res. Green Sustain. Chem.*, **5** (2022).
57. Shrestha, B. K., Ahmad, R., Shrestha, S., Park, C. H. & Kim, C. S. Globular Shaped Polypyrrole Doped Well-Dispersed Functionalized Multiwall Carbon Nanotubes/Nafion Composite for Enzymatic Glucose Biosensor Application. *Sci Rep* **7**, (2017).
58. Kumar, A. *et al.* Ultrahigh sensitive graphene oxide/conducting polymer composite based biosensor for cholesterol and bilirubin detection. *Biosens Bioelectron* **X 13**, (2023).
59. Tohidi, H. *et al.* An Electroconductive, Thermosensitive, and Injectable Chitosan/Pluronic/Gold-Decorated Cellulose Nanofiber Hydrogel as an Efficient Carrier for Regeneration of Cardiac Tissue. *Materials* **15**, 1–16 (2022).
60. Zhan, J. *et al.* An injectable and conductive TEMPOL/polypyrrole integrated peptide co-assembly hydrogel promotes functional maturation of cardiomyocytes for myocardial infarction repair. *Compos B Eng* **236**, 109794 (2022).
61. Parchehbaf-Kashani, M. *et al.* Heart Repair Induced by Cardiac Progenitor Cell Delivery within Polypyrrole-Loaded Cardiogel Post-ischemia. *ACS Appl Bio Mater* **4**, 4849–4861 (2021).
62. Cui, Z. *et al.* Polypyrrole-chitosan conductive biomaterial synchronizes cardiomyocyte contraction and improves myocardial electrical impulse propagation. *Theranostics* **8**, 2752–2764 (2018).
63. Liu, S. *et al.* Soft-Template Construction of 3D Macroporous Polypyrrole Scaffolds. *Small* **13**, (2017).
64. Fadle Aziz, M. R. *et al.* A Polypyrrole-Polycarbonate Polyurethane Elastomer Alleviates Cardiac Arrhythmias via Improving Bio-Conductivity. *Adv Healthc Mater* 2203168 (2023).
65. Zhang, L. *et al.* An injectable conductive hydrogel restores electrical transmission at myocardial infarct site to preserve cardiac function and enhance repair. *Bioact Mater* **20**, 339–354 (2023).
66. Yang, B. *et al.* A conductive PEDOT/alginate porous scaffold as a platform to modulate the biological behaviors of brown adipose-derived stem cells. *Biomater Sci* **8**, 3173–3185 (2020).
67. Parchehbaf-Kashani, M. *et al.* Design and characterization of an electroconductive scaffold for cardiomyocytes based biomedical assays. *Mat. Sci. Engg. C* **109**, (2020).

68. Ajdary, R. *et al.* Multifunctional 3D-Printed Patches for Long-Term Drug Release Therapies after Myocardial Infarction. *Adv Funct Mater* **30**, (2020).
69. He, Y. *et al.* From waste of marine culture to natural patch in cardiac tissue engineering. *Bioact Mater* **6**, 2000–2010 (2021).
70. Sirivisoot, S., Pareta, R. & Harrison, B. S. Protocol and cell responses in threedimensional conductive collagen gel scaffolds with conductive polymer nanofibres for tissue regeneration. *Interface Focus* **4**, (2014).
71. Zanzanizadeh Ezazi, N. *et al.* Fabrication and Characterization of Drug-Loaded Conductive Poly(glycerol sebacate)/Nanoparticle-Based Composite Patch for Myocardial Infarction Applications. *ACS Appl Mater Interfaces* **12**, 6899–6909 (2020).
72. Avila Delucis, R., Cademartori, P. H. G., Fajardo, A. R. & Amico, S. C. Cellulose and its Derivatives: Properties and Applications. in *Polysaccharides* 221–252 (2021).
73. Liang, L., Huang, C. & Ragauskas, A. J. Nanocellulose-based Materials for Biomedical Applications. *JSM Chem* **5**, 1048 (2017).
74. Kaur, P. *et al.* Nanocellulose: Resources, Physio-Chemical Properties, Current Uses and Future Applications. *Front. nanotechnol.*, **3** (2021).
75. Randhawa, A. *et al.* A Review of Properties of Nanocellulose, Its Synthesis, and Potential in Biomedical Applications. *Applied Sciences (Switzerland)*, **12** (2022).
76. Naomi, R., Idrus, R. B. H. & Fauzi, M. B. Plant-vs. Bacterial-derived cellulose for wound healing: A review. *Int. J. Environ. Res. Public Health*, **17**, 1–25, (2020).
77. Tsui, J. H. *et al.* Conductive silk–polypyrrole composite scaffolds with bioinspired nanotopographic cues for cardiac tissue engineering. *J Mater Chem B* **6**, 7185–7196 (2018).
78. Silva, K. A. S. & Emter, C. A. Large Animal Models of Heart Failure: A Translational Bridge to Clinical Success. *JACC: Basic Transl. Sci*, **5** 840–856 (2020).
79. Kimes, B. W. & Brandt, B. L. Properties of a clonal muscle cell line from rat heart. *Exp Cell Res* **98**, 367–381 (1976).
80. Claycomb, W. C. *et al.* HL-1 cells: A cardiac muscle cell line that contracts and retains phenotypic characteristics of the adult cardiomyocyte (simian virus 40 T oncogenepotassium channelsdofetilide). *Cell Biology*, **95** (1998).
81. White, S. M., Constantin, P. E. & Claycomb, W. C. Cardiac physiology at the cellular level: use of cultured HL-1 cardiomyocytes for studies of cardiac muscle cell structure and function *Am J Physiol Heart Circ Physiol*. **286**, H823-9 (2004).
82. Davidson, M. M. *et al.* Novel cell lines derived from adult human ventricular cardiomyocytes. *J Mol Cell Cardiol* **39**, 133–147 (2005).
83. Zuppinger, C. 3D Cardiac Cell Culture: A Critical Review of Current Technologies and Applications. *Front Cardiovasc Med*, **6** (2019).
84. Zuppinger, C. 3D culture for cardiac cells. *Biochim Biophys Acta Mol Cell Res*, **1863**, 1873–1881 (2016).

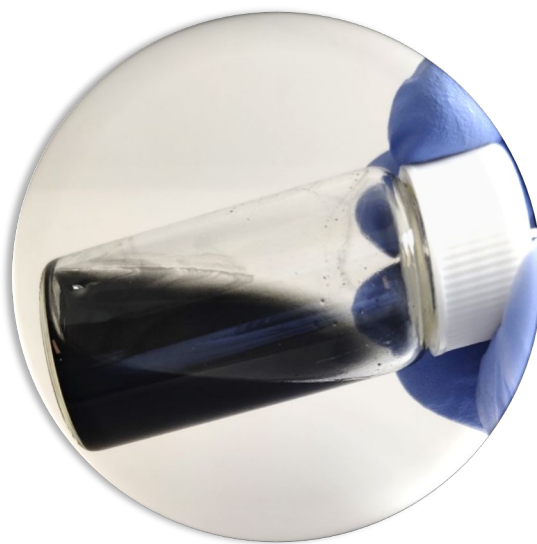
85. Tani, H. & Tohyama, S. Human Engineered Heart Tissue Models for Disease Modeling and Drug Discovery. *Front. Cell Dev. Biol.*, **10** (2022).
86. Ahn, S. *et al.* Mussel-inspired 3D fiber scaffolds for heart-on-a-chip toxicity studies of engineered nanomaterials. *Anal Bioanal Chem* **410**, 6141–6154 (2018).
87. Dutta, S. *et al.* Optimization of an in silico cardiac cell model for proarrhythmia risk assessment. *Front Physiol* **8**, (2017).
88. Patten, R. D. & Hall-Porter, M. R. Small animal models of heart failure development of novel therapies, past and present. *Circulation: Heart Failure*, **2**, 138–144 (2009).
89. Blackwell, D. J., Schmeckpeper, J. & Knollmann, B. C. Animal Models to Study Cardiac Arrhythmias. *Circ Res* **130**, 1926–1964 (2022).
90. Clauss, S. *et al.* Animal models of arrhythmia: classic electrophysiology to genetically modified large animals. *Nat. Rev. Cardiol.*, **16** 457–475 (2019).
91. Curtis, M. J., Macleod, B. A. & Walker, M. J. Models for the Study of Arrhythmias in Myocardial Ischaemia and Infarction: the use of the Rat. *J Mol Cell Cardiol* **19**, 399–419 (1987).
92. Gehrman, J. *et al.* Electrophysiological characterization of murine myocardial ischemia and infarction. *Basic Res Cardiol* **96**, 237–250 (2001).
93. Tan, M. Y. *et al.* Development of a new model for acute myocardial infarction in rabbits. *J. Vet. Med. Sci.* **79**, 467–473 (2017).
94. Baehr, A., Klymiuk, N. & Kupatt, C. Evaluating novel targets of ischemia reperfusion injury in pig models. *Int. J. Mol. Sci.* **20** (2019).
95. Lu, Z. *et al.* Atrial fibrillation begets atrial fibrillation: autonomic mechanism for atrial electrical remodeling induced by short-term rapid atrial pacing. *Circ Arrhythm Electrophysiol* **1**, 184–192 (2008).
96. Anadon, M. J. *et al.* Alcohol concentration determines the type of atrial arrhythmia induced in a porcine model of acute alcoholic intoxication. *Pacing Clin. Electrophysiol.* **19**, 1962–1967 (1996).
97. Benoist, D. *et al.* Cardiac arrhythmia mechanisms in rats with heart failure induced by pulmonary hypertension. *Am J Physiol Heart Circ Physiol* **302**, 2381–2395 (2012).
98. Lang, C. N., Koren, G. & Odening, K. E. Transgenic rabbit models to investigate the cardiac ion channel disease long QT syndrome. *Prog. Biophys. Mol. Biol.* **121** 142–156 (2016).
99. Polejaeva, I. A. *et al.* Increased Susceptibility to Atrial Fibrillation Secondary to Atrial Fibrosis in Transgenic Goats Expressing Transforming Growth Factor- β 1. *J Cardiovasc Electrophysiol* **27**, 1220–1229 (2016).
100. Park, D. S. *et al.* Genetically engineered SCN5A mutant pig hearts exhibit conduction defects and arrhythmias. *J. Clin. Investig.* **125**, 403–412 (2015).
101. Baczkó, I., Hornyik, T., Brunner, M., Koren, G. & Odening, K. E. Transgenic Rabbit Models in Proarrhythmia Research. *Front. Pharmacol.* **11** (2020).

102. Tessadori, F. *et al.* Identification and Functional Characterization of Cardiac Pacemaker Cells in Zebrafish. *PLoS One* **7**, (2012).
103. Echeazarra, L., Hortigón-Vinagre, M. P., Casis, O. & Gallego, M. Adult and Developing Zebrafish as Suitable Models for Cardiac Electrophysiology and Pathology in Research and Industry. *Front. Physiol.* **11** (2021).
104. MacRae, C. A. Cardiac arrhythmia: In vivo screening in the zebrafish to overcome complexity in drug discovery. *Expert Opin Drug Dis* **5** 619–632 (2010).
105. Gauvrit, S., Bossaer, J., Lee, J. & Collins, M. M. Modeling Human Cardiac Arrhythmias: Insights from Zebrafish. *J. cardiovasc. dev. dis.* **9** (2022).
106. Milan, D. J., Peterson, T. A., Ruskin, J. N., Peterson, R. T. & MacRae, C. A. Drugs that induce repolarization abnormalities cause bradycardia in zebrafish. *Circulation* **107**, 1355–1358 (2003).
107. Cornet, C. *et al.* ZeGlobalTox: An innovative approach to address organ drug toxicity using zebrafish. *Int J Mol Sci* **18**, (2017).
108. Dyballa, S. *et al.* Comparison of Zebrafish Larvae and hiPSC Cardiomyocytes for Predicting Drug-Induced Cardiotoxicity in Humans. *Toxicol. Sci.* **171**, 283–295 (2019).
109. Piazza, N. & Wessells, R. J. Drosophila models of cardiac disease. in *Prog Mol Biol Transl Sci* . **100** 155–210 (Elsevier BV, 2011).
110. Cammarato, A. *et al.* A mighty small heart: The cardiac proteome of adult Drosophila melanogaster. *PLoS One* **6**, (2011).
111. Taghli-Lamalle, O., Plantié, E. & Jagla, K. Drosophila in the heart of understanding cardiac diseases: Modeling channelopathies and cardiomyopathies in the fruitfly. *J. Cardiovasc. Dev. Dis.* **3** (2016).
112. Abraham, D. M. & Wolf, M. J. Disruption of Sarcoendoplasmic Reticulum Calcium ATPase Function in Drosophila Leads to Cardiac Dysfunction. *PLoS One* **8**, (2013).
113. Ocorr, K. *et al.* KCNQ potassium channel mutations cause cardiac arrhythmias in Drosophila that mimic the effects of aging. *Proc. Natl. Acad. Sci. U.S.A.* **104**, 3943–3948 (2007).
114. Frolov, R. V., Berim, I. G. & Singh, S. Inhibition of delayed rectifier potassium channels and induction of arrhythmia: A novel effect of celecoxib and the mechanism underlying it. *J. Biol. Chem.* **283**, 1518–1524 (2008).
115. Meneely, P. M., Dahlberg, C. L. & Rose, J. K. Working with Worms: Caenorhabditis elegans as a Model Organism. *Curr. Protoc. Essent. Lab. Tech.* **19**, (2019).
116. Moragas, L. G. Evaluating inorganic nanoparticles in the living organism Caenorhabditis elegans. (Universitat de Autonomia de Barcelona, 2016).
117. Wu, T., Xu, H., Liang, X. & Tang, M. Caenorhabditis elegans as a complete model organism for biosafety assessments of nanoparticles. *Chemosphere* **221** 708–726 (2019).
118. Avery, L. & Shtonda, B. B. Food transport in the C. elegans pharynx. *J. Exp. Biol.* **206**, 2441–2457 (2003).

119. Altun, Z. F. & Hall, D. H. Alimentary System, Pharynx. in *WormAtlas* (2009).
120. Avery, L. & You, Y. J. C. elegans feeding. in *Wormbook* (2012).
121. Song, B. & Avery, L. The pharynx of the nematode *C. elegans*. *Worm* **2**, e21833 (2013).
122. Mango, S. E. The *C. elegans* pharynx: a model for organogenesis. in *WormBook: the online review of C. elegans biology* 1–26 (2007).
123. Sherman, D. & Harel, D. Deciphering the underlying mechanisms of the pharyngeal motions in *Caenorhabditis elegans*. *Neurons and Cognition* (2019).
124. Davis, M. W., Fleischhauer, R., Dent, J. A., Joho, R. H. & Avery, L. A mutation in the *C. elegans* EXP-2 potassium channel that alters feeding behavior. *Science* (1979) **286**, 2501–2504 (1999).
125. Lagoy, R., Kim, H., Mello, C. & Albrecht, D. A *C. elegans* model for the rare human channelopathy, Timothy syndrome type 1. *MicroPubl Biol* 18–20 (2018).
126. Shaye, D. D. & Greenwald, I. Ortholist: A compendium of *C. elegans* genes with human orthologs. *PLoS One* **6**, (2011).
127. Schöler, C., Fischer, E., Shaltiel, L., Steuer Costa, W. & Gottschalk, A. Arrhythmogenic effects of mutated L-Type Ca²⁺-channels on an optogenetically paced muscular pump in *Caenorhabditis elegans*. *Sci Rep* **5**, 1–16 (2015).
128. Fischer, E., Gottschalk, A. & Schöler, C. An optogenetic arrhythmia model to study catecholaminergic polymorphic ventricular tachycardia mutations. *Sci Rep* **7**, 1–12 (2017).

Chapter 2

Synthesis and Characterization of Polypyrrole nanoparticles



PREFACE

Chapter 2 elucidates the production of Polypyrrole nanoparticles (Ppy NPs) in solution, and provides a detailed characterization of the NPs. Size, morphology, chemical structure and composition, thermal degradation, optical absorption, and electrical conductivity of the NPs were characterized. Lastly, the stability of the NPs was thoroughly scrutinized in different aqueous conditions and pH.

Index

2.1. Synthesis of Polypyrrole Nanoparticles	57
2.1.1. Methods of Synthesis	57
2.1.2. Parameters affecting chemical oxidative Polymerization	59
2.1.3. Polypyrrole nanoparticles synthesis protocol.....	62
2.2. Characterization of Polypyrrole nanoparticles.....	63
2.2.1 Size and Surface charge of Polypyrrole Nanoparticles	63
2.2.2 Size and Morphology by Electron Microscopy	65
2.2.3 Chemical structure and composition	66
2.2.4 Thermal and optical properties	68
2.2.5 Electrical conductivity	69
2.2.6 Stability of Ppy NPs	70
2.3. Conclusions.....	71

2.1. Synthesis of Polypyrrole Nanoparticles

2.1.1. Methods of Synthesis

Ppy possesses electrical conductivity and infrared absorption only in its oxidized and doped form. Therefore, most Ppy synthesis involves doping with anions; the dopant ions are introduced during or after oxidation within the polymeric backbone (Figure 1). The combination of a conjugated chemical structure and the doping imparts unique properties to Ppy, such as its tunable electrical conductivity, NIR absorption, and reversible doping/de-doping redox ability. Although several synthesis techniques, such as photochemical¹, emulsion², and plasma polymerization³, are explored, electrochemical and chemical oxidative polymerization are the most common.

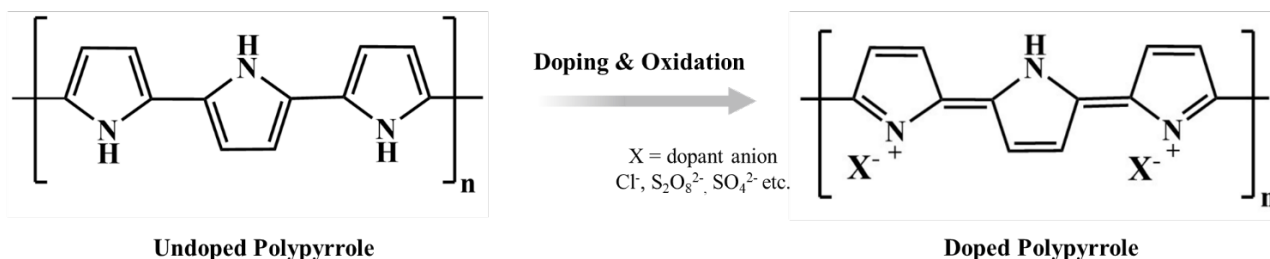


Figure 1. Structure of Ppy and the doping and oxidation resulting in doped Ppy.

Electrochemical synthesis

In the electrochemical synthesis of Ppy, the electrolyte solution comprises the monomer (pyrrole), a solvent, and an acid which acts as the source of the dopant ion (Figure 2a). Electrochemical synthesis has three major types: galvanostatic, potentiostatic, and potentiodynamic methods⁴, where a current or potential is applied to initiate the oxidation reaction eliminating the need for an additional oxidant. The monomer oxidation leads to the formation of cation radicals. The monomer molecules with cation radicals react with each other, forming dimers, followed by further polymer growth⁴⁻⁶. The resulting polymer films are deposited on the anode surface, which is lifted off at the end of the reaction⁴. Several parameters play a role in the properties of the resulting polymer, such as the electrode material^{4,7}, dopant ion, electrolyte concentration, pH⁸⁻¹⁰, temperature, electrodeposition method, duration, and the number of cycles¹¹.

Moreover, the polymerization rate depends on the surface charge, the hydrophilicity of the electrode surface, etc. One of the main limitations of the electrochemical synthesis of Ppy is the requirement of high potential for monomer oxidation. The electrolyte must be stable at

such high potentials, capable of dissolving the monomer, and devoid of impurities. Also, the electrode material must not dissolve at high oxidation potentials^{4,6}. Even during the synthesis process, the solvent can affect the solubility of the polymer. The reaction temperature also influences the polymerization rate, induces undesired reactions, and affects the reaction efficiency. Synthesis of Ppy through electrochemical methods is also limited by the complexity of removing Ppy from the substrate, the cost of production, the time-consuming process, the inability to produce Ppy in varied forms other than films, and the low production yield^{4,6,12}. For further information and an in-depth review of the electrochemical synthesis of Ppy, readers are directed to previously published articles on the same topic^{4,5,8,11–13}.

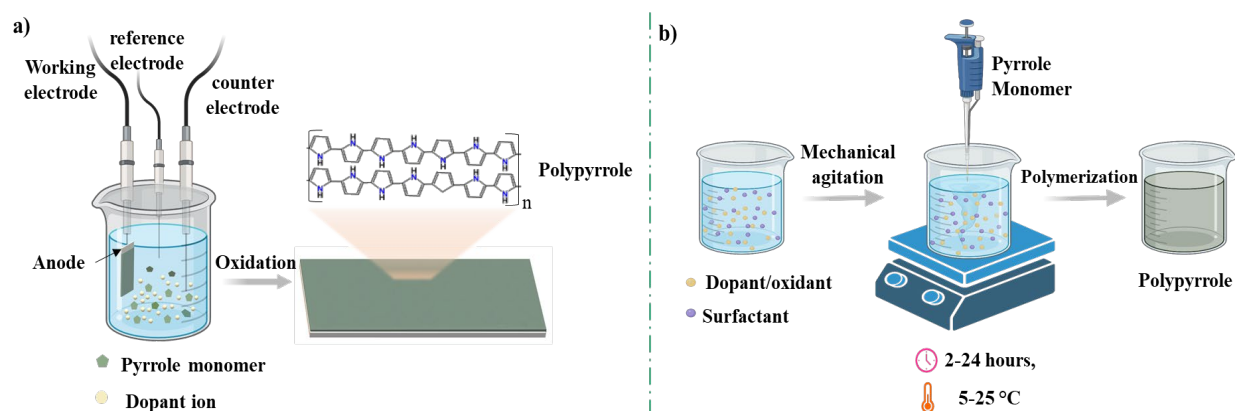


Figure 2. Schematic representation of the two most common synthesis methods of Ppy NPs: a) electrochemical polymerization and b) Chemical oxidative polymerization.

Chemical Oxidative polymerization

Ppy Nps utilized in this work were produced by chemical oxidative polymerization (COP). In this polymerization method, the monomer is mixed with an oxidant and surfactant in the solution^{14,15} (Figure 2b). The oxidant often acts as the donor of the dopant ion as well as the initiator of the polymerization reaction¹⁶. The most commonly used oxidant initiators include FeCl_3 , $(\text{NH}_4)_2\text{S}_2\text{O}_8$, $\text{K}_2\text{Cr}_2\text{O}_7$, $\text{K}_2\text{S}_2\text{O}_8$, H_2O_2 , H_2SO_4 , $\text{Fe}[(\text{CN})_6]_3$ ^{17–22}. A surfactant is also added along with the oxidant and monomer to improve the stability of the resulting polymer. The properties of the polymer depend primarily on the monomer concentration, oxidant: monomer ratio, surfactant: monomer ratio, reaction temperature, duration, and frequency of agitation. Therefore, the COP method exerts better control over defining the properties of the polymer as needed by precisely modifying the reaction parameters. Chemical

oxidation provides several advantages over other methods, such as ease-of-synthesis, high yields, ability to co-polymerize with other polymers, produce composites with different nanomaterials, and versatility to produce different morphologies such as nanoparticles, fibers, wires, sheets, and tubes^{6,12}. Diverse morphologies of the polymer can be obtained through a soft or hard template-mediated synthesis or surfactant-assisted polymerization^{15,23}.

Due to all the above advantages of COP over electrochemical polymerization, as well as our expertise and experimental simplicity, *we used COP to produce Ppy NPs from pyrrole monomer.*

2.1.2 Parameters influencing chemical oxidative polymerization

As mentioned in the previous section, the properties of Ppy can be precisely controlled by manipulating the different reaction parameters to obtain the required size, morphology, solubility, and conductivity. In this section, we will present an overview of all the parameters that need to be taken under consideration to produce Ppy NPs through COP with defined properties.

Oxidizing agent and dopant

Generally, in COP, the oxidizing agent used to oxidize pyrrole monomer acts as the dopant and initiator of the polymerization reaction. The type of oxidant used and the subsequent dopant anion are among the most influencing parameters in deciding the properties of Ppy NPs. Although Ferric chloride (FeCl_3) and ammonium persulfate ($(\text{NH}_4)_2\text{S}_2\text{O}_8$) are the two most commonly used oxidants with chloride and sulfide as the dopant anion^{17,18,36}, respectively, other oxidants such as H_2O_2 , $\text{K}_3[\text{Fe}(\text{CN})_6]$, H_2SO_4 , HCl are also studied^{20–22}. The oxidation potential of the oxidants determines the extent of oxidation and rate of reaction. A potent oxidizing agent with high oxidation potential (H_2O_2 , $\text{FeCl}_3 \approx 0.7 \text{ V}$) results in a fast polymerization reaction, leading to larger particle sizes. At the same time, oxidants such as $\text{K}_3[\text{Fe}(\text{CN})_6]$ have a relatively lower oxidation potential ($\approx 0.4 \text{ V}$), facilitating a slower reaction and more controlled NP sizes²¹. Therefore, the major rate-limiting factor in Ppy synthesis is the type of oxidant and its molar ratio with the monomer. The molar ratio of oxidant: monomer also affects the size, distribution, and conductivity of Ppy NPs since it is directly correlated with the anion doping levels. Several studies have reported that if the oxidant concentration

and the oxidant: monomer ratio is higher, the reaction rate is faster, promoting the growth of NPs rather than the seeding of new particles^{37–39}. Exploring the literature showed us that 2.4 times the molar concentration of monomer would be the best ratio to produce controlled NPs with uniform size distribution and good conductivity^{17,18,40,41}.

Consequently, *we used 0.24 M FeCl₃.6H₂O as the oxidant-dopant for 0.1 M pyrrole monomer to balance the conductivity, size, and distribution.*

Monomer concentration

The initial concentration of pyrrole monomer in the chemical oxidation reaction affects the size of Ppy NPs. An increase in monomer concentration increases Ppy NPs size since a higher number of monomer molecules in the reaction solution causes the growing polymer chain to interact with more molecules, enhancing the polymerization rate. A higher rate of reaction naturally promotes the growth of NPs rather than the seeding of new NPs. A previous study has established that using 0.1M pyrrole monomer results in Ppy NPs of \approx 80-120 nm diameter.

Therefore, we chose 0.1 M pyrrole for the preparation of the NPs.

Surfactants and Templates

Template-mediated COP facilitates the synthesis of Ppy in tightly controlled nanoscale sizes. Templates used during the synthesis process can be classified into hard physical templates and soft micellar templates^{23,24}. Hard templates include the most famous MCM-41 porous aluminosilicate²⁵, electrospun scaffolds, polymeric membranes²⁶, and carbon nanotubes^{27,28}. However, hard-template-assisted polymerization is a complex two-step process; involving the preparation of the template beforehand and the removal of polymer from the templates, resulting in a loss of yield^{23,29}.

Whereas in soft-template synthesis, surfactants or polymers are added to the reaction solution resulting in the formation of micellar mesophase structures. These micellar structures act as templates that allow the polymerization of Py monomers within the self-assembled channels in defined shapes and sizes, resulting in uniform nanoscale particles^{24,30–32}. The type of surfactant used regulates the shape and size of the Ppy. For instance, *Zhang et al.* reported

that using cetyltrimethylammonium bromide (CTAB) as the surfactant in neutral aqueous conditions promotes the formation of Ppy in nanowire/ribbon-like structures²³. Similarly, Aimei *et al.* also reported the addition of 1.0 M HCl along with CTAB and pyrrole monomer, resulting in a non-woven, mesh-like nano fibrillar morphology of Ppy¹⁵. The chain length of the template molecule plays a vital role in determining the size and shape of Ppy nanostructures^{23,33}. For example, using a long-chain cationic surfactant such as CTAB/DTAB (Dodecyltrimethylammonium Bromide) produces fibrillar, wire-like, or ribbon structures of Ppy. In contrast, short-chain cationic surfactants such as Octadecyldimethylammonium bromide (OTAB) or non-ionic surfactants such as PEG promote spherical Ppy nanoparticles.

Among other surfactants that act as soft templates, PVA is a popular choice for Ppy synthesis as it is a water-soluble, biocompatible polymeric surfactant. Hong *et al.* investigated the formation of Ppy NPs with uniform size and stability using PVA as the surfactant and FeCl₃ as the oxidant to oxidize the pyrrole monomer. The iron cations and lone electron pairs of PVA form a chelate complex; this PVA-iron cation complex acts as a self-assembled precursor for Ppy NPs formation³⁴. Molecular weight and concentration of the surfactant also play an essential role in the properties of Ppy because higher molecular weight PVA leads to more stable complexes, and increasing concentration of PVA results in a change in the complex structure from rods to globules^{34,35}. Different molecular weights of PVA (9k, 13k, 31k) and concentrations ranging from 1.25 to 7.5 wt% of monomer were studied. They found that with higher molecular weight and concentration of PVA, the diameter of Ppy NPs reduces.

Therefore, in this work, ***we used PVA (30,000-70,000) at 7.5 wt% of monomer to yield spherical and stable Ppy NPs of uniform size distribution.***

Reaction conditions

The rate of polymerization, the extent of polymer chain growth, and subsequently size and structure of Ppy are also governed by the reaction conditions such as temperature, duration, and mode of agitation. At high reaction temperatures, the reaction enthalpy increases, leading to increased mobility of pyrrole molecules and dimers within the reaction solution, causing more collisions and faster polymerization⁴¹. Therefore, low temperatures (5-15 °C) are preferred for a controlled reaction rate and uniform size distribution. Likewise, with long

reaction durations, precursors are consumed, resulting in individual polymer chains interacting and forming large polymeric aggregates^{39,40}. Therefore, it is crucial to precisely control the duration so that the polymerization reaction is complete, but further aggregation is also prevented. Next, the mode and speed of agitation of the reaction solution should be selected to promote more individual particles and avoid aggregation. While high-speed stirring has been reported to help produce individual NPs, ultrasonication is comparatively more effective in forming a stable dispersion of Ppy NPs^{40,42}.

Considering the role of duration, temperature, and mode of agitation, we decided to employ *ice-bath ultrasonication at 5 °C for 4 hours of polymerization to form stable, well-dispersed Ppy NPs*.

2.1.3. Polypyrrole nanoparticle synthesis protocol

Based on the literature study and previous experience, we designed all the parameters that govern the properties of Ppy carefully to suit our study requirement⁴⁰. The critical material properties are that the Ppy NPs should be stable in water, exhibit uniform size distribution, and conductivity in the semi-conducting range suitable for biomedical applications. The oxidant used for initiating polymerization of the pyrrole monomer, doping Cl⁻ ions, and Ppy oxidation was FeCl₃.6H₂O, along with PVA as the surfactant to stabilize and mediate Ppy NPs formation. First, 0.24 M FeCl₃.6H₂O and 7.5% PVA (w/w of monomer) were added to Milli-Q water and heated to 60 °C to ensure complete dissolution of PVA (Figure 3a). Following this, the solution is cooled down to 5 °C in an ice-bath sonicator. Fresh ice was added to the sonicator bath every 30 minutes to maintain a constant temperature. Next, 0.1 M pyrrole monomer is added slowly to the reaction solution using a pipette under constant sonication to ensure better incorporation and mixing (Figure 3b). The polymerization is allowed to continue for 4 hours under sonication. The solution turns black when the polymerization is complete (Figure 3c).

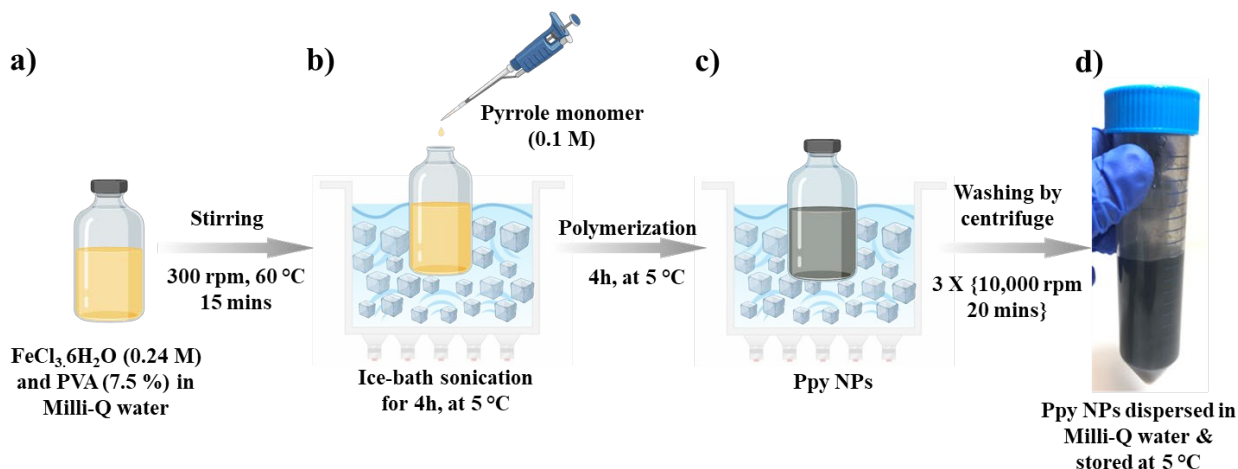


Figure 3. Synthesis of Ppy NPs carried out in our laboratory and the resulting final product.

After 4 hours, the resulting NPs solution is washed by centrifugation at 12,000 rpm for 20 mins, and the supernatant is discarded. The washing is repeated until all the precursors are removed and a clear supernatant is obtained. The final NPs pellet is redispersed in Milli-Q water and stored in the refrigerator at 4-5 °C (Figure 3d).

2.2. Characterization of Ppy NPs

We characterized the synthesized Ppy NPs using several techniques, such as dynamic light scattering (DLS), scanning electron microscopy (SEM), and transmission electron microscopy (TEM), to understand their size, distribution, morphology, and microstructure. Fourier transform infrared (FTIR) spectroscopy and elemental analysis were utilized to elucidate the chemical composition and interactions. Further, four-probe measurements, thermogravimetry analysis, and UV-Vis-NIR absorption were employed to investigate the electrical, thermal, and optical properties, respectively. We also assessed the stability of Ppy NPs in different solutions and conditions for the further assays with *C. elegans*.

2.2.1. Size and surface charge of Ppy NPs

The hydrodynamic diameter is measured by a dynamic light scattering (DLS) technique. The NPs are colloiddally suspended in the chosen solvent. Briefly, an incoming light is passed through a transparent cuvette, which gets scattered upon hitting the surface of particles. The diffusion movement of the particles within the solvent influences the scattered

light intensity and causes fluctuations. The particle size is then computed by comparing the diffusion coefficient of NP with a sphere of known size that diffuses at the same rate. Larger particles have a slower diffusion giving rise to slower fluctuations in light intensity than smaller particles⁴³. In a nutshell, the particle size is calculated by measuring the diffusion speed through the intensity of the scattered light. However, the hydrodynamic diameter does not depend only on the particle size. The particle surface's structure, polarity, and the solvent's ionic strength influence hydrodynamic diameter^{44,45}. The hydrodynamic diameter of Ppy would be much higher than the exact diameter that can be measured from electron microscopy, where the particles are not suspended in liquid but are dried on a platform.

Zetasizer Nano ZS (Malvern) with a He/Ne 633 nm laser at 25 °C was used for DLS size and zeta potential measurements. Ppy NPs were dispersed at 100 µg/mL concentration in 1 mL Milli-Q water and sonicated for 30 minutes before measurement. Three measurements were made for each sample consisting of 10 runs per measurement. Ppy samples from three batches were measured, and the average was computed. The size was plotted using the Zetasizer® software as a function of particle number, volume, and intensity distributions and found identical size in all three particle size distributions. The intensity-weighted mean hydrodynamic size (Z-average) was found to be 196 ± 62 nm with a polydispersity index of 0.17 (Figure 4a).

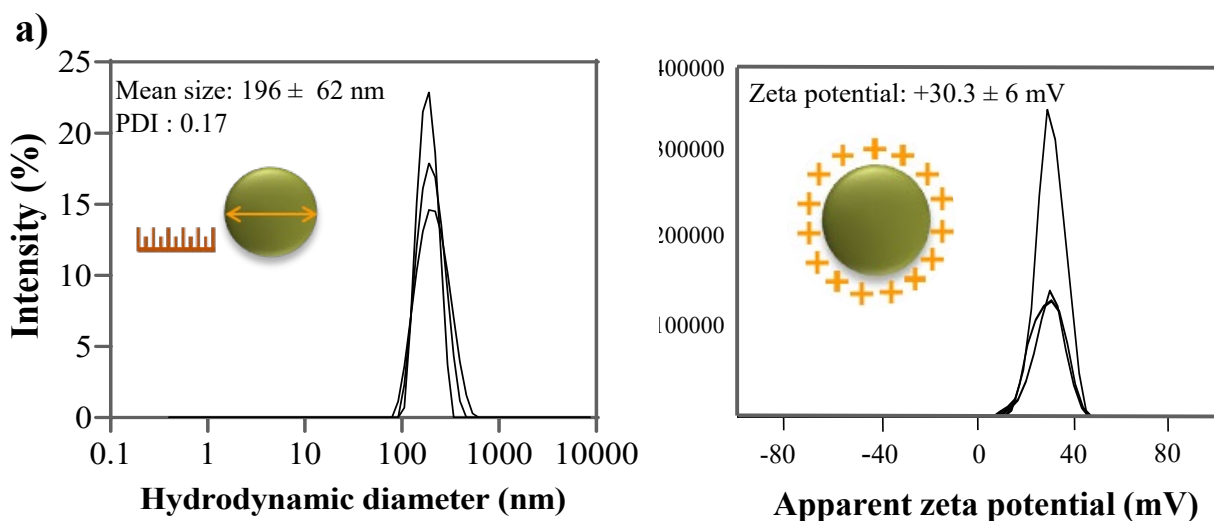


Figure 4. Hydrodynamic size and surface charge of Ppy NPs dispersed in Milli-Q water, as measured by Zetasizer Nano ZS.

The surface charge of the NPs in a solution can also be determined by zeta potential measurements using the same instrument. The surface charge of a particle in an aqueous condition elucidates inter-particle electrostatic interactions. The higher the magnitude of the surface charge, the higher the inter-particle electrostatic repulsion, preventing aggregation. Generally, a zeta potential value outside the range of -25 mV to +25 mV results in stable nanoparticles in the solution. For zeta potential measurements, 12 runs were performed at 25 °C with a particle count rate of 163 kcps. The zeta potential of Ppy NPs dispersed in Milli-Q water was $+30.3 \pm 6$ mV (Figure 4b), owing to the positively charged nitrogen atoms of the amine groups in the polymeric chain. The zeta potential is in accordance with the polydispersity index, indicating good colloidal stability of Ppy NPs in Milli-Q water.

2.2.2. Size & Morphology by Electron Microscopy

We employed SEM and TEM to analyze the size, morphology, and microstructure of Ppy NPs. Unlike DLS, SEM provides information on the size of the nanostructures in the dry state, therefore, not strongly dependent on the type of solvent, viscosity, and the particle's surface charge. On the other hand, the NPs can be visualized at a much higher resolution using TEM; therefore, TEM offers a better understanding of the morphology, microstructures, and size distribution. We used ImageJ software to measure the particle diameter and plotted the frequency distribution using GraphPad Prism.

Images of Ppy NPs from 10 $\mu\text{g/mL}$ and 1 $\mu\text{g/mL}$ concentrations revealed similar information on the size, morphology, and distribution. Therefore, we did not observe an effect of the concentration on the degree of aggregation and hence, the size distribution of the population. We found the particles were of spherical morphology and uniform size, with a mean diameter of 132 ± 31 nm as measured from a population of 131 NPs (Figure 5). The size of NPs produced is found to be in agreement with the previously published reports using this protocol⁴⁶.

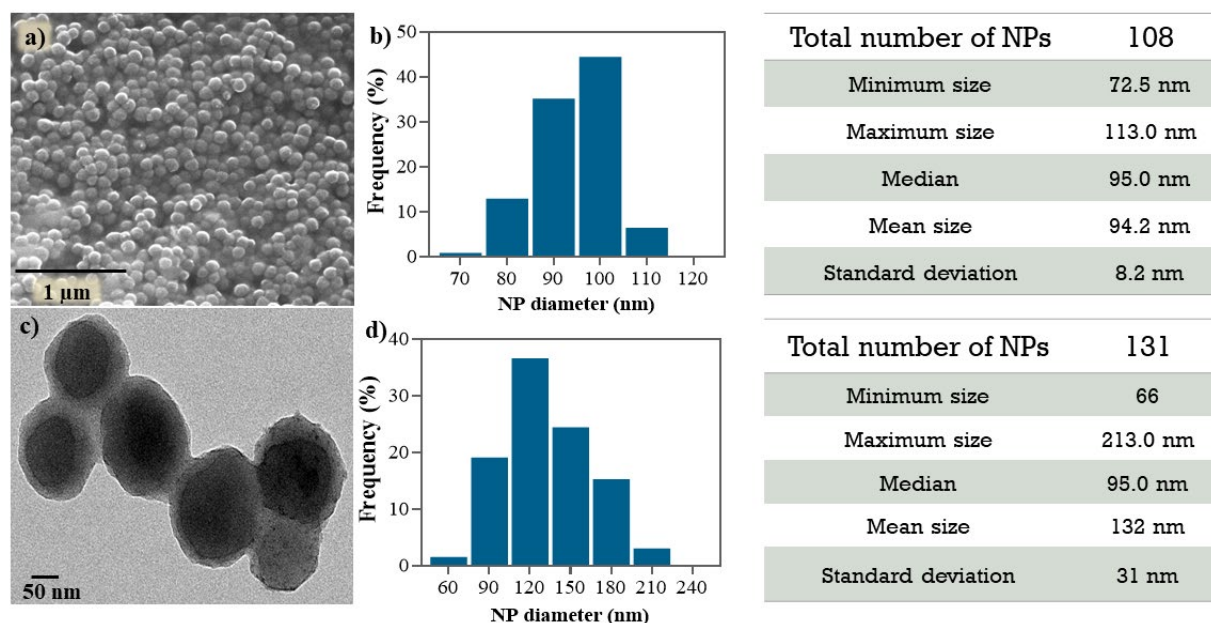


Figure 5. a,b) SEM images and size distribution c,d) TEM images and size distribution of Ppy NPs.

2.2.3. Chemical Structure and Composition

Ppy is composed of a long conjugated polymeric backbone made of pyrrole (C_4H_5N) as the repeating units - a heterocyclic aromatic organic compound with secondary amines. Pyrrole monomer undergoes oxidation in the presence of $FeCl_3 \cdot 6H_2O$ to form doped Ppy chains. Therefore, the basic elemental composition of Ppy comprises carbon, hydrogen, and Nitrogen, along with the dopant ion, Cl^- . The chemical structure of Ppy (Figure 6a, c) and the elemental composition and distribution (Figure 6b) are studied through FTIR spectroscopy and elemental analysis, respectively.

For the elemental analysis, ≈ 2 mg dried powder of Ppy NPs composites was used from three different synthesis batches. The percentage of distribution of three elements, namely: Carbon (C), Hydrogen (H), and Nitrogen (N), was computed, and the mean was plotted (Figure 6b). The empirical formula of Ppy is $H(C_4H_2NH)_n H$; therefore, the relative proportion of each element should be such that for every N atom, 4 C and 5 H atoms should be present. We found reproducible distribution from the three batches, amounting to $\approx 56\%$ Carbon, $\approx 15\%$ Nitrogen, and $\approx 5\%$ Hydrogen, with the remaining attributed to Cl^- ions and Oxygen, confirming the key elemental composition of Ppy NPs. The atomic ratios of the elements with respect to Nitrogen atoms agree with the theoretical value, giving rise to the molecular formula $C_{4.51}N_{1.05}H_{4.64}$.

$$\text{Molecular formula} = \frac{\text{Percentage of elemental distribution}}{\text{Atomic mass of each element}}$$

The FTIR spectra help to elucidate the materials' molecular structure and chemical interactions. Each chemical bond absorbs radiation at different wavelengths, causing characteristic modes of vibration and vibrational energy. Consequently, each compound constitutes unique spectra with peaks at distinct positions, intensities, and shapes⁴⁷. Therefore, FTIR is highly useful in studying chemical modifications, interactions between components in a composite material, functionalization, etc. Ppy NPs were analyzed in dry powder form, and the scan was performed in Attenuated Total Reflectance-Fourier Transform Infrared (ATR-FTIR) mode in a Spectrophotometer Jasco 4700 instrument at a spectral range of 400-4000 cm^{-1} with 32 scans and a resolution of 4 cm^{-1} .

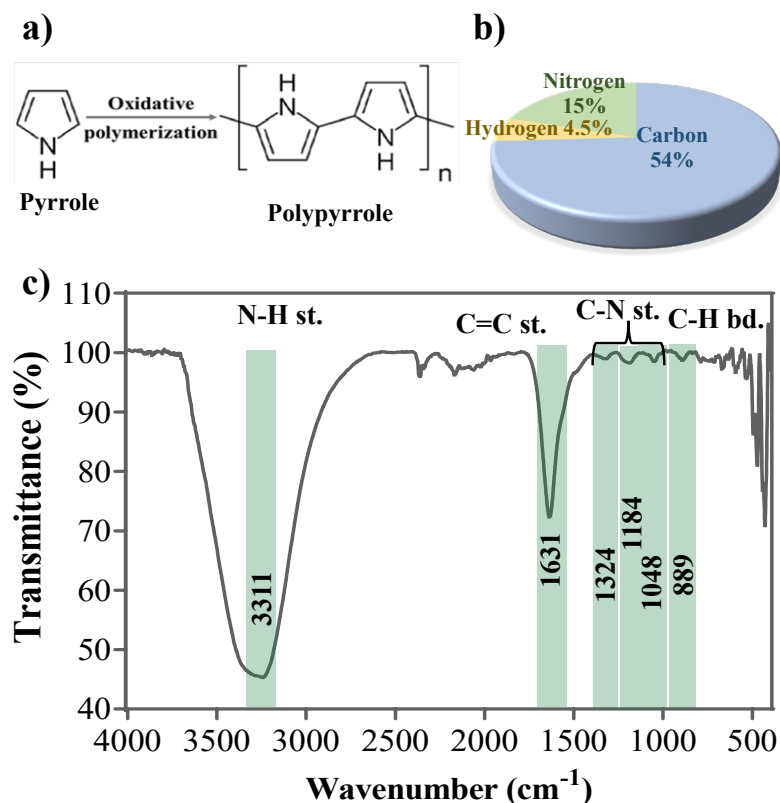


Figure 6. a) Formation of Ppy from pyrrole monomer, b) Carbon (C), Hydrogen (H), and Nitrogen (N) elemental composition, and c) FT-IR spectra of Ppy NPs with specific functional groups.

The most significant characteristic peaks are highlighted in green (Figure 6c). The broad, intense peak at $\approx 3311\text{ cm}^{-1}$ for Ppy is due to the N-H stretching of secondary aromatic amines. The peak at 1631 cm^{-1} occurs from the C=C stretching of conjugated alkenes. The small peaks at 1324 , 1184 , and 1048 cm^{-1} correspond to C-N stretching from aromatic amines, and 889 cm^{-1} is due to C H bending of the alkane chains. These peaks together confirm the formation of Ppy NPs with their characteristic functional groups^{18,48}.

2.2.4. Thermal and Optical properties

Thermogravimetric analysis (TGA) helps in understanding the behavior of materials in a wide range of temperatures. Thermal behavior is fundamental in bio-applications to investigate a biomaterial's stability and behavior at physiological temperatures, storage, and sterilization. For this, $\approx 1\text{ mg}$ of dried powder was heated at a temperature range of $25\text{--}800\text{ }^{\circ}\text{C}$ at a rate of $10\text{ }^{\circ}\text{C}/\text{min}$ in a liquid Nitrogen atmosphere. The thermal degradation occurs in three stages (Figure 7a): the first 50% of weight loss occurs between $150\text{--}400\text{ }^{\circ}\text{C}$, the second phase of weight loss of about 35% occurs around $400\text{--}500\text{ }^{\circ}\text{C}$, followed by the residual polymer chain degradation (15%) around $650\text{--}750\text{ }^{\circ}\text{C}$ ⁴⁹. The maximum degradation occurs between $200\text{--}400\text{ }^{\circ}\text{C}$ with 50% weight loss occurring at $410\text{ }^{\circ}\text{C}$; the decomposition rate is rather gradual, as we can observe the broad peak in the DSC curve. The residual polymer chain degradation (final 15%) happens at around $650\text{--}750\text{ }^{\circ}\text{C}$. Overall, TGA spectra showed that Ppy has good thermal stability up to temperatures as high as $400\text{ }^{\circ}\text{C}$.

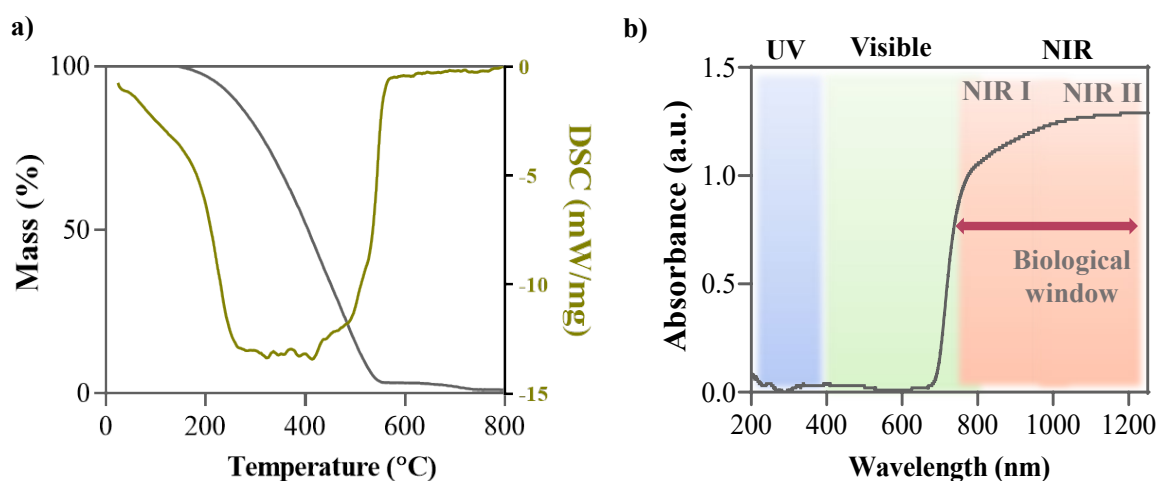


Figure 7. a) Thermal degradation of Ppy NPs between 200 and $800\text{ }^{\circ}\text{C}$, b) UV-Vis-NIR absorbance spectra of Ppy NPs.

Ppy NPs also possess absorption in the entire near-infrared (NIR) region. The NIR has a higher diffusion compared to UV and visible rays owing to its longer wavelength than the other two rays, allowing deep penetration into the tissues within the body that are difficult to reach otherwise. NIR absorption imparts photothermal conversion property to Ppy NPs. Several scientists have used the NIR absorption of Ppy NPs for applications such as theranostics, bioimaging, and photothermal therapy⁵⁰. We examined this property of Ppy NPs using a Cary 5000 UV-Vis-NIR spectrophotometer in the 200-1200 nm wavelength range. Ppy NPs were dispersed in water by sonication and analyzed in a quartz cuvette. The Ppy NPs solution exhibited a strong and broad absorption in the NIR region between 700-1200 nm (Figure 7b), implying a photothermal property⁵¹.

2.2.5. Electrical conductivity

Another material property imparted in Ppy due to its conjugated structure is its electrical conductivity. We measured the resistivity of Ppy NPs using a four-probe instrument and calculated the electrical conductivity using the van der Pauw method⁵². Films of Ppy NPs were prepared by pressing the NP powder in a pelletizer, and thickness was measured using a micrometer. The film was placed on a glass slide, and contacts were made using silver paint. Then, the glass slide was placed on an in-house built Keithley instrument, and probes were secured at the four ends of the film, forming a square. An incoming current (200 nA) was passed, and the voltage was recorded to plot the I-V, from which resistance was estimated. The sheet resistance (i.e., the resistance without taking the thickness into account) was measured in 6 directions; namely: the four sides of the square and the two diagonals, and averaged (R_{sheet}). From this, conductivity (σ) is calculated using the formula,

$$\sigma \text{ (S/cm)} = \frac{1}{R_{sheet} \text{ (ohm)} \times \text{Thickness (cm)}}$$

Here, the thickness of the film = 140 μm (0.014 cm) and $R_{sheet} = 90.472 \text{ } \Omega$; therefore, the conductivity of Ppy NPs was calculated to be 0.8 S/cm.

2.2.6. Stability of Ppy NPs

In order to evaluate Ppy NPs using *C. elegans* as the *in-vivo* small animal model for cardiac arrhythmia, it is indispensable to test the stability and behavior of Ppy NPs in the solutions and conditions used in the *C. elegans* experiments. Ppy NPs remained colloiddally stable for at least 6 months without any visible precipitation or aggregation, which we further confirmed through DLS analysis. Upon DLS analysis of NPs prepared and stored in Milli-Q water 12 months before, we found the particles maintained their size (164 nm) and remained dispersed in Milli-Q water (Figure 8a). Further, we tested the stability of Ppy NPs in M9 buffer, which contains salts such as disodium phosphate, potassium monophosphate, magnesium sulfate, and sodium chloride, used for maintenance and aqueous treatment of *C. elegans* with nanoparticles and drugs, before exposing the worms to Ppy NPs. The M9 buffer promotes slight aggregation of Ppy NPs with an increase in the size ≈ 311 nm and PDI of 1 (Figure 8a); however, not to the extent that could hinder the ingestion of NPs by the worms, as *C. elegans* can ingest NPs at sizes as large as $1\ \mu\text{m}^{53-55}$.

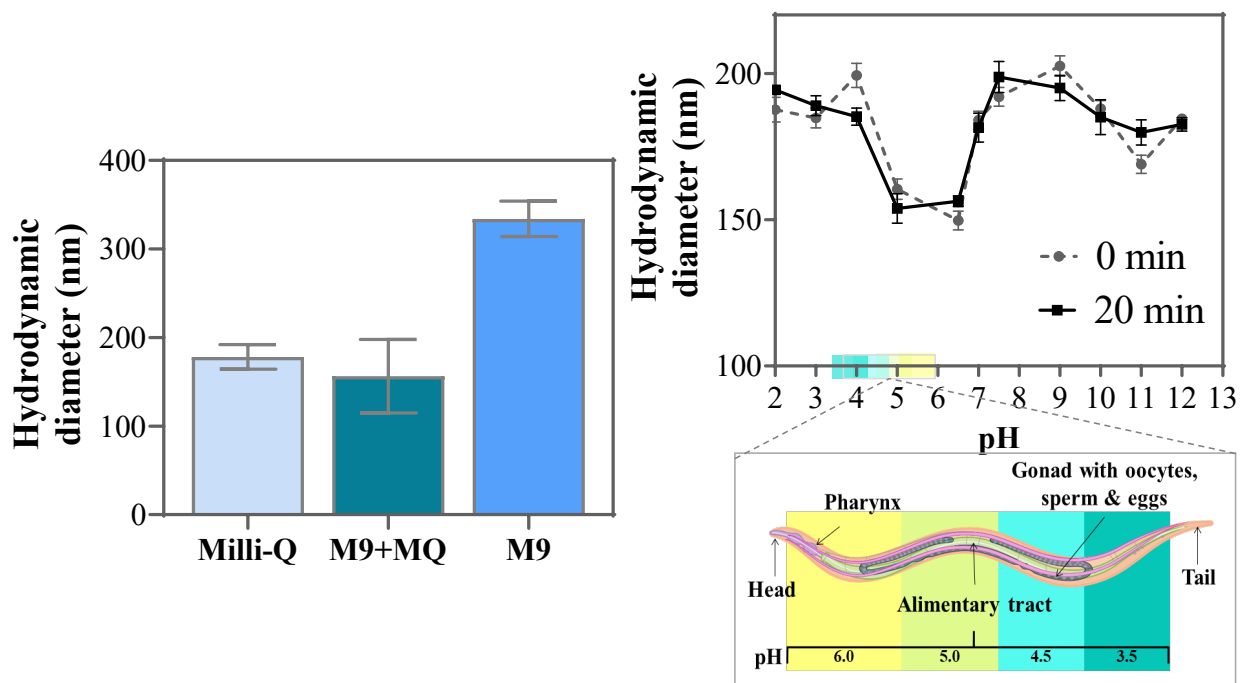


Figure 8. Stability of Ppy NPs a) after storage in Milli-Q water (MQ) for 6 months, M9 buffer, and equal volume M9:MQ solution, b) in pH range between 2 and 13 at 0 and 20 minutes.

Nonetheless, in a solution of equal volume M9 buffer and MilliQ water (M9:MQ), the particle size did not increase and was maintained (220 nm) (Figure 8a). Therefore, we performed aqueous exposure of worms to Ppy NPs in a solution of M9:MQ (1:1) to provide an optimum condition for *C. elegans*' growth and the dispersion of NPs. Much like humans, the intestine of *C. elegans* also exhibits a wide range of pH from 6 to 3 (anterior to posterior end). Since *C. elegans* would ingest the NPs and process them at the intestine, we tested the behavior of the NPs in the intestinal pHs. Notably, *C. elegans* feeding and excretion rate are very fast compared to humans leading to short resident times of ingested food within the intestine (less than 2 minutes)^{56–58}. Hence, we tested the stability of Ppy NPs in the pH range of 2–13 using HCl (acidic pH), Milli-Q (neutral pH), and NaOH (basic pH) solutions by measuring the size in DLS at 0 minutes and after 20 minutes. The size measurements at both time points correlated well with no aggregation or dissolution, indicating Ppy NPs were stable in all the pHs (Figure 8b). In conclusion, exposing the worms to Ppy NPs in an aqueous 50% M9 environment is feasible without affecting the NPs stability or dispersion.

2.3. Conclusions

In this thesis, we have chosen Ppy as the CP of interest for two reasons: first, because Ppy possesses outstanding biocompatibility and physicochemical stability exceeding other CPs, and second, based on my previous experience in the synthesis of Ppy NPs and Ppy nanocomposites. The synthesis method of Ppy NPs is straightforward and designed carefully with extensive bibliographic study, considering all the influencing parameters and our planned application. Properties such as size, stability, morphology, thickness, etc., were reproducible among different synthesis batches, as each characterization was performed with samples from at least three separate batches. The Ppy NPs solution utilized for *in-vivo* evaluation in *C. elegans* was appropriately evaluated for stability in the worms' physiologic conditions. They exhibit favorable properties in size, morphology, conductivity, and behavior, making the NPs suitable for evaluation in *C. elegans*.

References

1. Zhang, S. *et al.* Effects of UV radiation on the preparation of polypyrrole in the presence of hydrogen peroxide. *Radiation Effects and Defects in Solids* **170**, 821–831 (2015).
2. Jang, H. J. *et al.* Polypyrrole film synthesis via solution plasma polymerization of liquid pyrrole. *Applied Surface Science* **608**, 155129 (2023).
3. Hoshina, Y., Zaragoza-Contreras, E. A., Farnood, R. & Kobayashi, T. Nanosized polypyrrole affected by surfactant agitation for emulsion polymerization. *Polymer Bulletin* **68**, 1689–1705 (2012).
4. Gvozdenović, M. M., Jugović, B. Z., Stevanović, J. S. & Grgur, B. N. Electrochemical synthesis of electroconducting polymers. *Hemijska Industrija* **68**, 673–684 (2014).
5. Chikouche, I. & Dehchar, C. Potentiostatic electrosynthesis of polypyrrole film onto silicon support. 50–56 (2022).
6. Pang, A. L., Arsad, A. & Ahmadipour, M. Synthesis and factor affecting on the conductivity of polypyrrole: a short review. *Polymers for Advanced Technologies* **32**, 1428–1454 (2021).
7. Ishaq, S. *et al.* One step strategy for reduced graphene oxide/cobalt-iron oxide/polypyrrole nanocomposite preparation for high performance supercapacitor electrodes. *Electrochimica Acta* **427**, 140883 (2022).
8. Demoustier-Champagne, S., Ferain, E., Jérôme, C., Jérôme, R. & Legras, R. Electrochemically synthesized polypyrrole nanotubes: Effects of different experimental conditions. *European Polymer Journal* **34**, 1767–1774 (1998).
9. Shukla, A., Sen, K. & Das, D. Studies on electrolytic and doping behavior of different compounds and their combination on the electrical resistance of polypyrrole film via electrochemical polymerization. *Journal of Applied Polymer Science* **139**, (2022).
10. Hryniewicz, B. M., Lima, R. V., Wolfart, F. & Vidotti, M. Influence of the pH on the electrochemical synthesis of polypyrrole nanotubes and the supercapacitive performance evaluation. *Electrochimica Acta* **293**, 447–457 (2019).
11. Pruna, A. I., Rosas-Laverde, N. M. & Mataix, D. B. Effect of deposition parameters on electrochemical properties of polypyrrole-graphene oxide films. *Materials* **13**, 1–12 (2020).
12. Jadoun, S. & Riaz, U. A review on the chemical and electrochemical copolymerization of conducting monomers: recent advancements and future prospects. *Polymer-Plastics Technology and Materials* **59**, 484–504 (2020).
13. Moloney, E. Electrochemical synthesis and characterisation of polypyrrole / chitosan films doped with molecular anions. *PhD Thesis* (2014).
14. Kang, H. C. & Geckeler, K. E. Enhanced electrical conductivity of polypyrrole prepared by chemical oxidative polymerization: Effect of the preparation technique and polymer additive. *Polymer* **41**, 6931–6934 (2000).

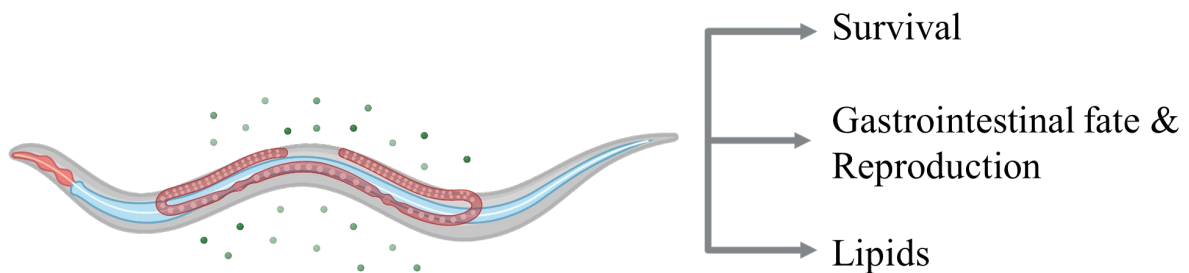
15. Wu, A., Kolla, H. & Manohar, S. K. Chemical synthesis of highly conducting polypyrrole nanofiber film. *Macromolecules* **38**, 7873–7875 (2005).
16. Myers, R. E. Chemical oxidative polymerization as a synthetic route to electrically conducting polypyrroles. *Journal of Electronic Materials* **15**, 61–69 (1986).
17. Chitte, H. K., Shinde, G. N., Bhat, N. V. & Walunj, V. E. Synthesis of Polypyrrole Using Ferric Chloride (FeCl_3) as Oxidant Together with Some Dopants for Use in Gas Sensors. *Journal of Sensor Technology* **01**, 47–56 (2011).
18. Šeděnková, I., Taboubi, O., Paúrová, M., Hromádková, J. & Babič, M. Influence of the type and concentration of oxidant on the photoacoustic response of polypyrrole nanoparticles for potential bioimaging applications. *Synthetic Metals* **292**, (2023).
19. Ovando-Medina, V. M. *et al.* A semi-conducting polypyrrole/coffee grounds waste composite for rhodamine B dye adsorption. *Iranian Polymer Journal (English Edition)* **27**, 171–181 (2018).
20. Ramanavičius, A. *et al.* Chemical oxidative synthesis of polypyrrole particles and functionalization by proteins. *Biologija* 43–46 (2006).
21. Andriukonis, E., Ramanaviciene, A. & Ramanavicius, A. Synthesis of polypyrrole induced by $[\text{Fe}(\text{CN})_6]^{3-}$ and redox cycling of $[\text{Fe}(\text{CN})_6]^{4-}/[\text{Fe}(\text{CN})_6]^{3-}$. *Polymers* **10**, 12–16 (2018).
22. Almontaser, F. M. A., Majumder, S., Baviskar, P. K., Sali, J. V. & Sankapal, B. R. Synthesis and characterization of polypyrrole and its application for solar cell. *Applied Physics A: Materials Science and Processing* **123**, (2017).
23. Zhang, X., Zhang, J., Song, W. & Lu, Z. Controllable synthesis of conducting polypyrrole nanostructures. *Journal of Physical Chemistry B* **110**, 1158–1165 (2006).
24. Hao, L., Dong, C., Zhang, L., Zhu, K. & Yu, D. Polypyrrole Nanomaterials : Structure , Preparation and Application. (2022).
25. Wysocka-Żołopa, M., Zabłocka, I., Grądzka, E., Goclon, J. & Winkler, K. Synthesis and characterization of polypyrrole@MCM-41 nanocomposites. *Microporous and Mesoporous Materials* **317**, (2021).
26. Dong, H., Prasad, S., Nyame, V. & Jones, W. E. Sub-micrometer Conducting Polyaniline Tubes Prepared from Polymer Fiber Templates. *Chemistry of Materials* **16**, 371–373 (2004).
27. Chang, B. H. *et al.* Conductivity and Magnetic Susceptibility of Nanotube/Polypyrrole Nanocomposites. *Journal of Low Temperature Physics* **119**, 41–48 (2000).
28. Tao, Z. *et al.* Polypyrrole coated carbon nanotube aerogel composite phase change materials with enhanced thermal conductivity, high solar-/electro- thermal energy conversion and storage. *Journal of Colloid and Interface Science* **629**, 632–643 (2023).
29. Ikegame, M., Tajima, K. & Aida, T. Template synthesis of polypyrrole nanofibers insulated within one-dimensional silicate channels: Hexagonal versus lamellar for recombination of polarons into bipolarons. *Angewandte Chemie - International Edition* **42**, 2154–2157 (2003).

30. Schulz, B., Orgzall, I., Díez, I., Dietzel, B. & Tauer, K. Template mediated formation of shaped polypyrrole particles. *Colloids and Surfaces A: Physicochemical and Engineering Aspects* **354**, 368–376 (2010).
31. Liu, S. *et al.* Soft-Template Construction of 3D Macroporous Polypyrrole Scaffolds. *Small* **13**, (2017).
32. Wang, B. *et al.* Soft-templated synthesis of core–shell heterostructured Ni₃S₂@polypyrrole nanotube aerogels as anode materials for high-performance lithium ion batteries. *New Journal of Chemistry* **45**, 13127–13136 (2021).
33. Zhou, Z., Shao, Y., Gao, X., Liu, Z. & Zhang, Q. Structural regulation of polypyrrole nanospheres guided by hydrophobic chain length of surfactants. *Journal of Materials Science* **54**, 14309–14319 (2019).
34. Hong, J. Y., Yoon, H. & Jang, J. Kinetic study of the formation of polypyrrole nanoparticles in water-soluble polymer/metal cation systems: A light-scattering analysis. *Small* **6**, 679–686 (2010).
35. Mezhuev, Y. O., Plyushchii, I. V., Korshak, Y. V., Shtil'man, M. I. & Gritskova, I. A. Dispersion Oxidative Polymerization of Pyrrole in Aqueous Solutions of Polyvinyl Alcohol. *Russian Journal of General Chemistry* **89**, 1477–1484 (2019).
36. Castro-Carranza, A. *et al.* Effects of FeCl₃ as oxidizing agent on the conduction mechanisms in polypyrrole (PPy)/pc-ZnO hybrid heterojunctions grown by oxidative chemical vapor deposition. *Journal of Polymer Science, Part B: Polymer Physics* **54**, 1537–1544 (2016).
37. Poddar, A. K., Patel, S. S. & Patel, H. D. Synthesis, characterization and applications of conductive polymers: A brief review. *Polymers for Advanced Technologies* **32**, 4616–4641 (2021).
38. Dey, S. & Kar, A. K. Morphological and optical properties of polypyrrole nanoparticles synthesized by variation of monomer to oxidant ratio. *Materials Today: Proceedings* **18**, 1072–1076 (2019).
39. Yussuf, A., Al-Saleh, M., Al-Enezi, S. & Abraham, G. Synthesis and Characterization of Conductive Polypyrrole: The Influence of the Oxidants and Monomer on the Electrical, Thermal, and Morphological Properties. *International Journal of Polymer Science* **2018**, (2018).
40. Srinivasan, S. Y., Gajbhiye, V. & Bodas, D. Development of nano-immunosensor with magnetic separation and electrical detection of Escherichia coli using antibody conjugated Fe₃O₄@Ppy. *Nanotechnology* **32**, (2020).
41. Brusamarello, C. Z. *et al.* Polypyrrole production through chemical polymerization using anionic and cationic dopants: The influence of synthesis conditions and reaction kinetics. *Materials Today Communications* **26**, 101740 (2021).
42. Pang, A. L., Arsad, A. & Ahmadipour, M. Synthesis and factor affecting on the conductivity of polypyrrole: a short review. *Polymers for Advanced Technologies* **32**, 1428–1454 (2021).

43. Abe, M. Measurement Techniques and Practices of Colloid and Interface Phenomena. in *Measurement Techniques and Practices of Colloid and Interface Phenomena* (2019).
44. Fischer, K. & Schmidt, M. Pitfalls and novel applications of particle sizing by dynamic light scattering. *Biomaterials* **98**, 79–91 (2016).
45. Pieniażek, M. Hydrodynamic Radius of Hydrophobic and Hydrophilic Polystyrene Latex Particles. *Journal of Colloid and Interface Science* **145**, (1991).
46. Srinivasan, S. Y., Gajbhiye, V. & Bodas, D. Development of nano-immunosensor with magnetic separation and electrical detection of Escherichia coli using antibody conjugated Fe₃O₄@Ppy. *Nanotechnology* **32**, (2020).
47. Torres-Rivero, K., Bastos-Arrieta, J., Fiol, N. & Florido, A. *Metal and metal oxide nanoparticles: An integrated perspective of the green synthesis methods by natural products and waste valorization: applications and challenges. Comprehensive Analytical Chemistry* **94** (Elsevier B.V., 2021).
48. Tikish, T. A., Kumar, A. & Kim, J. Y. Electrical and Optical Properties of Polypyrrole and Polyaniline Blends. *Polymer Science - Series A* **62**, 680–690 (2020).
49. Jakab, E., Mészáros, E. & Omastová, M. Thermal decomposition of polypyrroles. *Journal of Thermal Analysis and Calorimetry* **88**, 515–521 (2007).
50. Guo, B., Glavas, L. & Albertsson, A. C. Biodegradable and electrically conducting polymers for biomedical applications. *Progress in Polymer Science* **38**, 1263–1286 (2013).
51. Zeng, W. *et al.* Renal-Clearable Ultrasmall Polypyrrole Nanoparticles with Size-Regulated Property for Second Near-Infrared Light-Mediated Photothermal Therapy. *Advanced Functional Materials* **31**, (2021).
52. Pauw, Lj. A method of measuring specific resistivity and Hall effect of discs of arbitrary shape. *Philips Research Reports* **13**, 1–9 (1958).
53. Suzuki, Y., Kikuchi, K., Tsuruta-Numayama, K. & Ishikawa, T. Particle selectivity of filtering by *C. elegans*. *Theoretical and Applied Mechanics Letters* **9**, 61–65 (2019).
54. Schöpfer, L. *et al.* Microplastics Effects on Reproduction and Body Length of the Soil-Dwelling Nematode *Caenorhabditis elegans*. *Frontiers in Environmental Science* **8**, 1–9 (2020).
55. Fueser, H., Mueller, M. T. & Traunspurger, W. Rapid ingestion and egestion of spherical microplastics by bacteria-feeding nematodes. *Chemosphere* **261**, 128162 (2020).
56. Davis, M. W., Fleischhauer, R., Dent, J. A., Joho, R. H. & Avery, L. A mutation in the *C. elegans* EXP-2 potassium channel that alters feeding behavior. *Science* **286**, 2501–2504 (1999).
57. Ghafouri, S. & McGhee, J. D. Bacterial residence time in the intestine of *Caenorhabditis elegans*. *Nematology* **9**, 87–91 (2007).
58. Suzuki, Y., Kikuchi, K., Numayama-Tsuruta, K. & Ishikawa, T. Reciprocating intestinal flows enhance glucose uptake in *C. elegans*. *Scientific Reports* **12**, 1–11 (2022).

Chapter 3

Evaluation of systemic effects of Ppy NPs in *Caenorhabditis elegans*



Ppy NP treated *C. elegans*

PREFACE

The synthesized Ppy NPs are evaluated for their systemic effects in a small animal model, the *Caenorhabditis elegans* (*C. elegans*). Toxicity endpoints, such as survival, growth and development, gastrointestinal fate, reproductive rate, and effect of the treatment on the growth of the next generation, were measured in worms with and without Ppy treatment. The total lipid accumulation, lipid peroxidation, and metabolism to assess whether treatment with Ppy NPs induces any oxidative stress or metabolic impact.

Index

3.1. <i>Caenorhabditis elegans</i>	81
3.2. Maintenance of <i>C. elegans</i>	83
3.3. Preparation for Exposure.....	84
3.4. Exposure	85
3.5. Evaluation of pyrrole monomer toxicity	86
3.6. Gastrointestinal fate of Polypyrrole Nanoparticles	87
3.6.1. Stability of nanoparticles in recovery procedure	87
3.6.2. Recovery of ingested nanoparticles from <i>C. elegans</i>	88
3.7. Systemic toxicity	89
3.7.1. Survival rate.....	89
3.7.2. Growth & Development	90
3.8. Reproductive effect	90
3.8.1. Reproductive rate.....	91
3.8.2. Transgenerational toxicity	92
3.9. Lipid accumulation	92
3.10. Oxidative effect.....	93
3.10.1. Sample preparation and analysis	93
3.10.2. Quantification through relative absorbance ratios	94
3.11. Conclusions	96

3.1. *Caenorhabditis elegans*

The fully-grown adult wild-type *Caenorhabditis elegans* (*C. elegans*) are ≈ 1 mm in length, with a three-day growth cycle from hatching (250 μm) to egg-bearing adults (1 mm) (Figure 1). *C. elegans* are mainly self-fertilizing hermaphrodites with a rare occurrence ($<0.2\%$) of males in the population. The worms are transparent and exhibit a life span of ≈ 2 to 3 weeks. The transparency offers facile visualization of the worms' organs and internal structures through an optical microscope, and the short life-cycle enables the evaluation of materials at different developmental stages. Additionally, the worms display a prolific reproduction rate, producing around ≈ 300 offspring within 72 hours, facilitating large-scale evaluation¹⁻³.

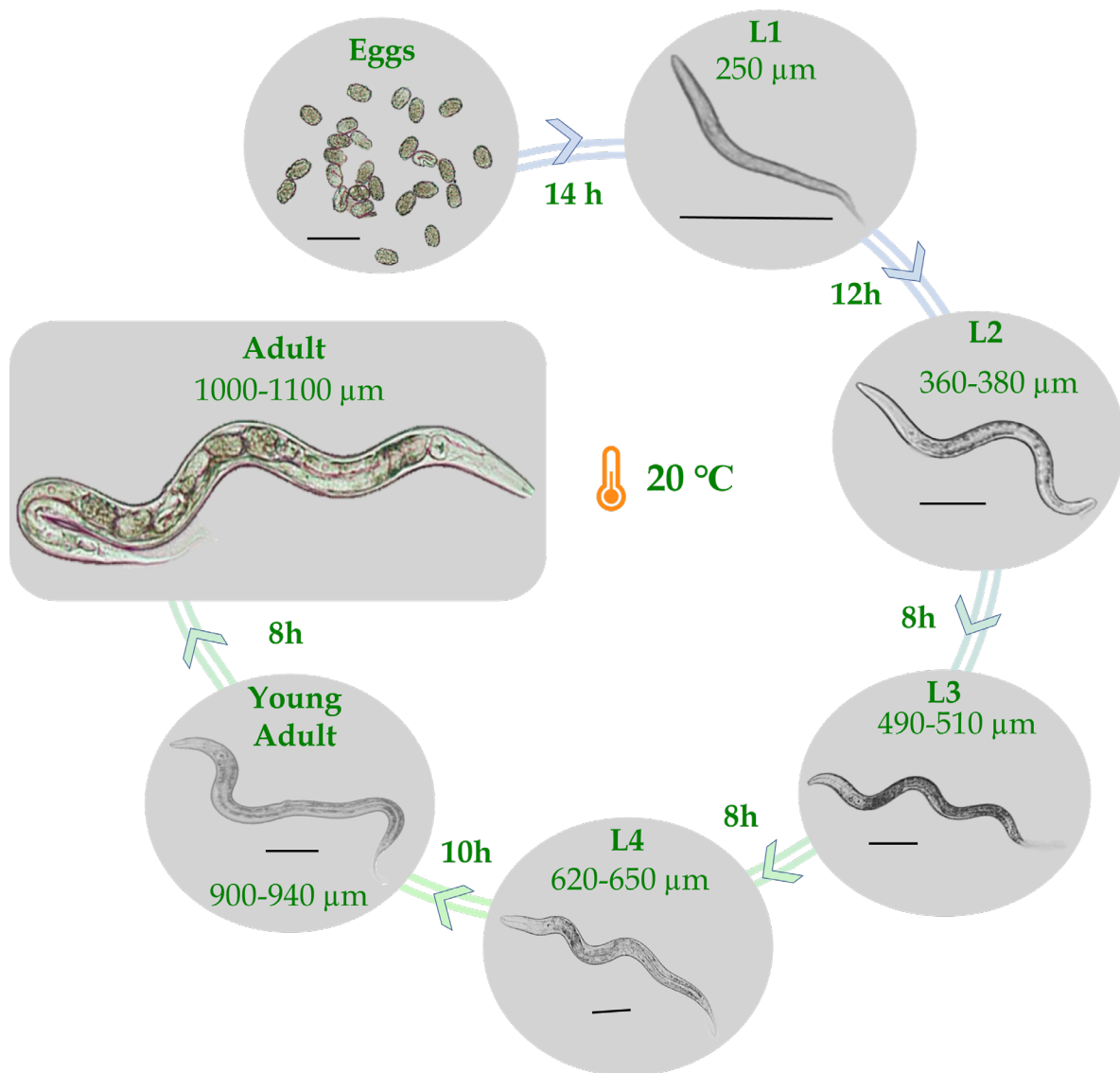


Figure 1. Developmental stages of the worms at 20 °C, detailing their body length and time taken for the growth from eggs to egg-bearing adults. Scale bar: 100 μm .

Our group has used *C. elegans* to test nanomaterials and evaluate several toxicity endpoints, like survival, growth and development, reprotoxicity, transgenerational toxicity, lifespan, and oxidative stress, to name some. The group has previously evaluated inorganic nanoparticles (NPs) such as gold (Au NPs), super-paramagnetic iron oxide NPs (SPIONs) coated with bovine serum albumin (BSA-SPIONs) and citrate (C-SPIONS) to understand the influence of size, surface coatings, and food availability on the toxicity in *C. elegans* during the Ph.D. thesis of Laura Gonzalez and Zhongrui Luo^{4,5}. They optimized protocols for *C. elegans* maintenance and exposure to NPs, and evaluation of different NPs in *C. elegans* through various assays. They found that the SPIONs were more compatible in *C. elegans* than Au NPs, and the BSA coating improved the biocompatibility of SPIONs over citrate coating. Upon evaluating food availability during nanoparticle treatment to *C. elegans*, they found that co-administration of NPs and food alleviates the toxic effects of NPs observed and improves the NPs uptake.

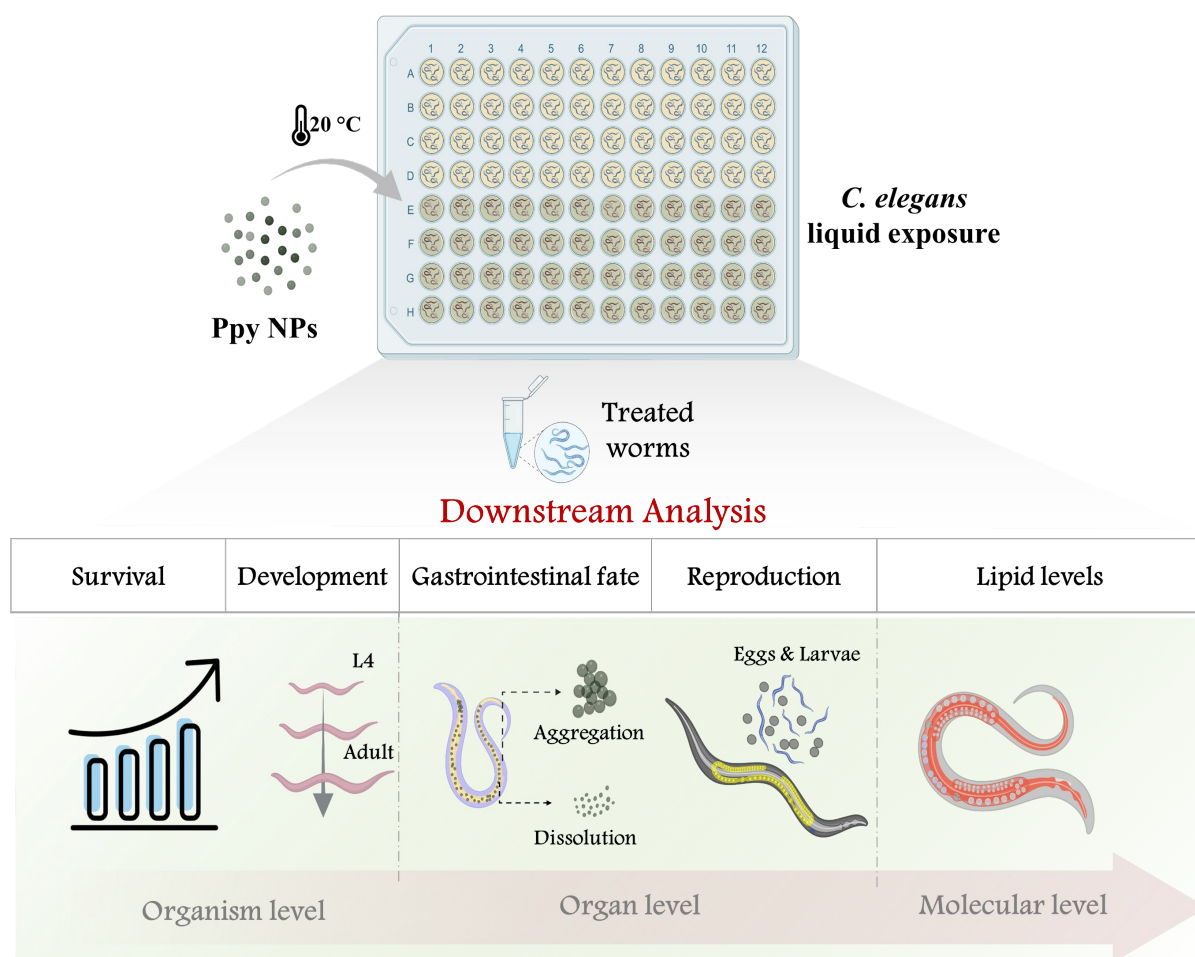


Figure 2. Experimental workflow of analysis of systemic effects upon Ppy NPs treatment.

Taking advantage of the group's expertise, we utilized *C. elegans* as a small animal model to evaluate the efficacy and safety of Ppy NPs, which were synthesized and the size, morphology,

surface charge, stability, and other properties were characterized (elaborated in Chapter 2). Then the toxicity profile of Ppy NPs was assessed in *C. elegans* through various assays, such as survival rate, development, gastrointestinal fate, reproduction, transgenerational effect, lipid accumulation, and oxidative impact (Figure 2).

3.2. Maintenance of *C. elegans*

The *C. elegans* and their food source *E. coli* bacterial strain (OP50), were obtained from Caenorhabditis genetics center (CGC), University of Minnesota, in nematode growth media (NGM) agar plates.

Nematode Growth Media agar plates

The NGM is the standard media for the culture and maintenance of *C. elegans*. The components of NGM media, agar, peptone, tryptone, and yeast are mixed in the required volume and autoclaved at 120 °C for 30 mins. The K₃PO₄, CaCl₂, and MgSO₄ salts were added as solutions in Milli-Q water to avoid salt deposits in the media. When the autoclaved mixture is cooled to ≈ 60 °C, a cholesterol solution is added since cholesterol could degrade at high temperatures. The complete media is mixed well and added to Petri-dishes (30 or 90 mm \varnothing) at 15-30 mL volume/plate inside the bio-hood. The plates were left to solidify, sealed with parafilm and stored at room temperature until use (Figure 3).

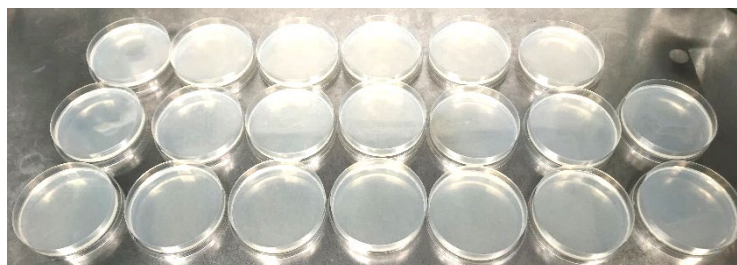


Figure 3. NGM agar plates for growth and maintenance of *C. elegans*.

Bacterial food source

The *Escherichia coli* (*E. coli*) bacterial strain OP50 was used as the food source for the worms⁶. The bacteria obtained from CGC are transferred to fresh Luria-Bertani (LB) broth agar plates by streaking (Figure 4a), incubated at 37 °C until confluency is achieved, and stored at 4 °C for further use. An isolated colony is picked using a sterile loop, transferred to liquid LB, grown at 37 °C for 24 hours, and used as the food source for the worms (Figure 4b). ≈ 600 μ L OP50 (O.D.₆₀₀ = 1.0) is added to NGM agar plates, spread using an L-shaped cell spreader, and allowed to dry at room temperature in the bio-hood. The OP50-seeded NGM plates (Figure 4c) are incubated at 37 °C a day before use. The liquid OP50 culture was heat killed at 80 °C for

30 minutes and re-dispersed in M9 buffer (Figure 4d) to be used as a food source for the exposure.

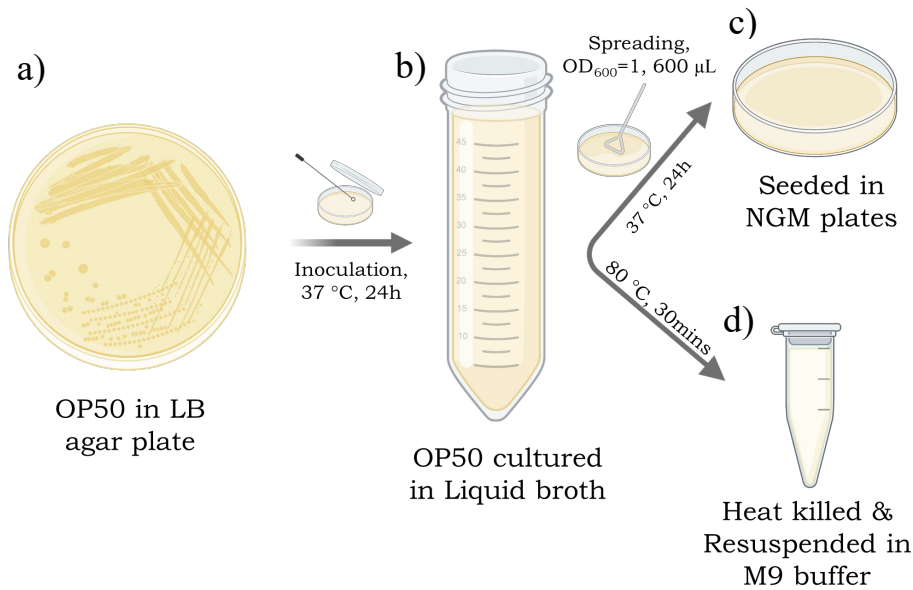


Figure 4. OP50 bacterial culture in solid media, growth in liquid broth media, and the two ways of using OP50 for *C. elegans*.

Storage and Temperature

The best-recommended temperature for maintenance of *C. elegans* is between 15 °C to 25 °C¹. In our laboratory, the worms are stored in an incubator maintained at 20 °C, and the experiments were performed inside a sterile laminar flow cabinet (bio-hood) at room temperature. The worms obtained from CGC are transferred to fresh NGM agar plates containing bacteria and stored in the incubator.

3.3. Preparation for exposure

We used synchronized young adult stage worms for treatments to ensure the reproducibility of the treatment effects. The synchronization is achieved by a bleaching protocol involving a series of steps from chunk to transfer.

Chunk

Chunking is the process of cutting a piece of agar from an old plate containing worms using sterile pipette tips and placing it upside down on a fresh plate. The chunk allows worms to consume more OP50 food and develop further so that most of the worm population in the plate reaches the gravid stage after 48 hours, with plenty of eggs.

Cleaning

The M9 buffer is added to plates containing gravid worms and washed well to detach worms from the agar. The worms are collected from the NGM plates using sterile Pasteur pipettes and transferred to sterile Eppendorf tubes. Then, the worms are washed at least thrice with M9 buffer by centrifugation to ensure the complete removal of bacteria.

Bleaching

After the washes using M9 buffer, the supernatant is discarded, and 100 μ L worm pellet is obtained. To this, 50 μ L of each, household bleach Sodium Hypochlorite (NaClO) and 5 M sodium hydroxide (NaOH), the remaining M9 buffer to bring the total volume to 1 mL are added and mixed well.

The mixture containing worms, bleach, NaOH, and M9 buffer, is vortexed for \approx 8-10 minutes until all the worms are digested, leaving the eggs intact. The eggs are washed immediately with M9 buffer thrice to remove the bleach and NaOH completely, which can hinder with egg hatching if left for a long time. Then, we incubate the eggs dispersed in M9 buffer at room temperature under shaking for 24 hours for the eggs to hatch and reach L1 stage. The worms are arrested at L1 stage until transfer to solid media with food. The L1 worms in M9 buffer can be stored up to a week at 20 °C or in the refrigerator.

Transfer

After all the worms are synchronized to L1 stage, the excess M9 buffer is removed using a sterile pipette, and the worms are transferred to OP50-seeded NGM plates. \approx 38-45 hours post transfer, all the worms are developed to a uniform L4-young adult stage and ready for exposure.

3.4. Exposure

The worms are collected from the NGM plates using a Pasteur pipette and washed with M9 buffer by centrifugation until excess OP50 and debris are removed. The volume is adjusted such that the count is \approx 10 worms/ μ L. The standard exposure duration was 24 hours, unless otherwise mentioned, at 20 °C. We treated the worms with three concentrations of Ppy NPs: 20, 100, and 500 μ g/mL to estimate the survival rate and development. The 500 μ g/mL was difficult for cleaning and visualizing the worms. Therefore, for the remaining assays, we worked with only 100 μ g/mL concentration. The exposures are carried out in sterile 96-well plates in a 50:50 (M9 buffer:MQ water) liquid exposure system, at 100 μ L/well volume (Figure 5). The colloidal stability of Ppy NPs in M9 buffer was estimated previously through DLS

(refer to Chapter 2), and we found some aggregation. Therefore, 50 μL of Ppy NPs dispersed in Milli-Q water was added to 50 μL M9 buffer with OP50 and *C. elegans* (Table 1).

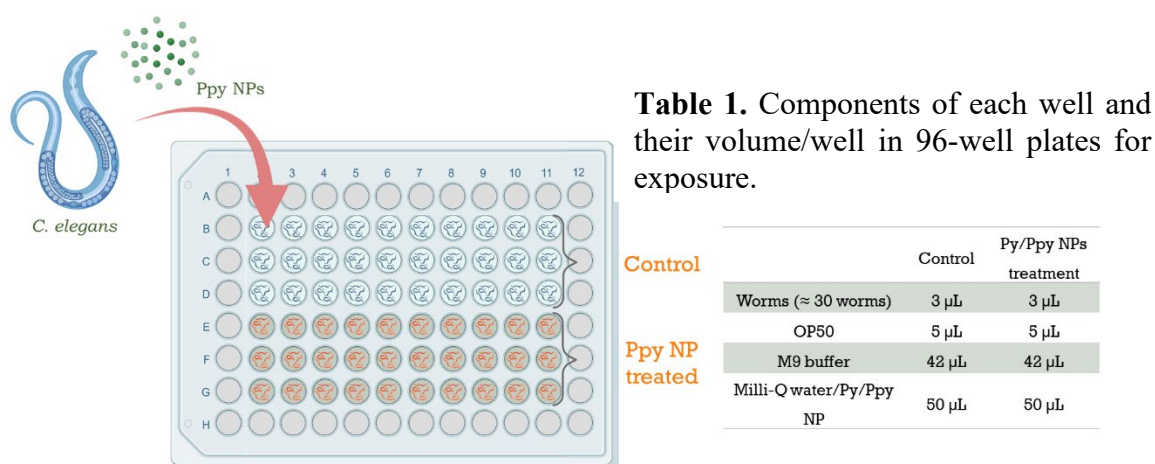


Figure 5: Common experimental setup used for *C. elegans* exposure in a 96-well plate.

After exposure, the worms are collected using sterile Pasteur pipettes and washed by centrifugation to remove excess NPs or drugs, bacteria, and other debris, until a clear suspension with worms is obtained.

3.5. Pyrrole toxicity

We treated the worms with pyrrole monomer to investigate whether the monomer exhibited any inherent toxicity to the worms due to its chemical composition (Figure 6a, b). The worms were exposed to 100 $\mu\text{g}/\text{mL}$ of pyrrole monomer for 24 hours, and the survival rate and body length of the treated worms were compared to the untreated worms. After exposure, the well plate is visualized under a stereomicroscope, where alive and dead worms in each well are counted, and the survival rate is estimated by the following formula,

$$\text{Survival rate (\%)} = \frac{\text{number of alive worms}}{\text{total number of worms}} \times 100$$

The body length was computed from the microscopic images using ImageJ software. We found that the pyrrole monomer (Py) treatment did not induce any adverse toxic response in the worms, as both the survival percentage, as well as the body length was unaffected after 24 hours of treatment (Figure 6c).



Figure 6. Optical microscopic images of *C. elegans* untreated (a) Pyrrole monomer (100 µg/mL) treated (b), and Survival rate and body length after Pyrrole treatment for 24 hours (c). Scale bar: 100 µm.

3.6. Gastrointestinal fate of Polypyrrole nanoparticles

The fate of nanoparticles within the gastrointestinal tract such as its dissolution kinetics, accumulation, or digestion within the organism are crucial factors to understand the safety and mechanistic action of nanoparticles^{7,8}. Only limited studies exist on how nanoparticles respond to the varying environment of gastrointestinal tract, and the fate of Ppy NPs within the intestine has not been reported before. *C. elegans* offer the possibility to recover and investigate the ingested NPs. Bleaching the treated worms has been employed previously^{4,5} to dissolve the worms, leaving the ingested NPs.

3.6.1. Stability of Ppy NPs in recovery procedure

We performed a preliminary test to ensure that the NPs do not dissolve during the process of bleaching. We visually observed the stability of Ppy NPs (200 µg/mL) in the household bleach solution without dilution, at 1 M concentration (Figure 7a). The NPs completely dissolved after 60 mins incubation as we can observe a clear colour change, resulting in a transparent bleach solution after 60 mins (Figure 7a). Therefore, diluted concentrations of bleach were examined to identify a stable working concentration. We measured the hydrodynamic diameter of Ppy NPs dispersed in bleach (0.1 – 1.0 M) for 5 and 20 minutes and found that the size can be maintained up to 0.4 M bleach concentration for 5 minutes (Figure 7b, highlighted). Hence, we used only using bleach concentration under 0.4 M and duration of less than 5 minutes. The NPs were added to a mixture containing 0.3 M bleach and 5 M NaOH and vortexed for 4 minutes. Upon visualization of the NPs in TEM, we found the diameter of the NPs to be 128 ± 10 nm similar to the TEM sizes of as-synthesized Ppy NPs (132 ± 31 nm) confirming that the bleaching procedure does not dissolve the NPs (Figure 7c).

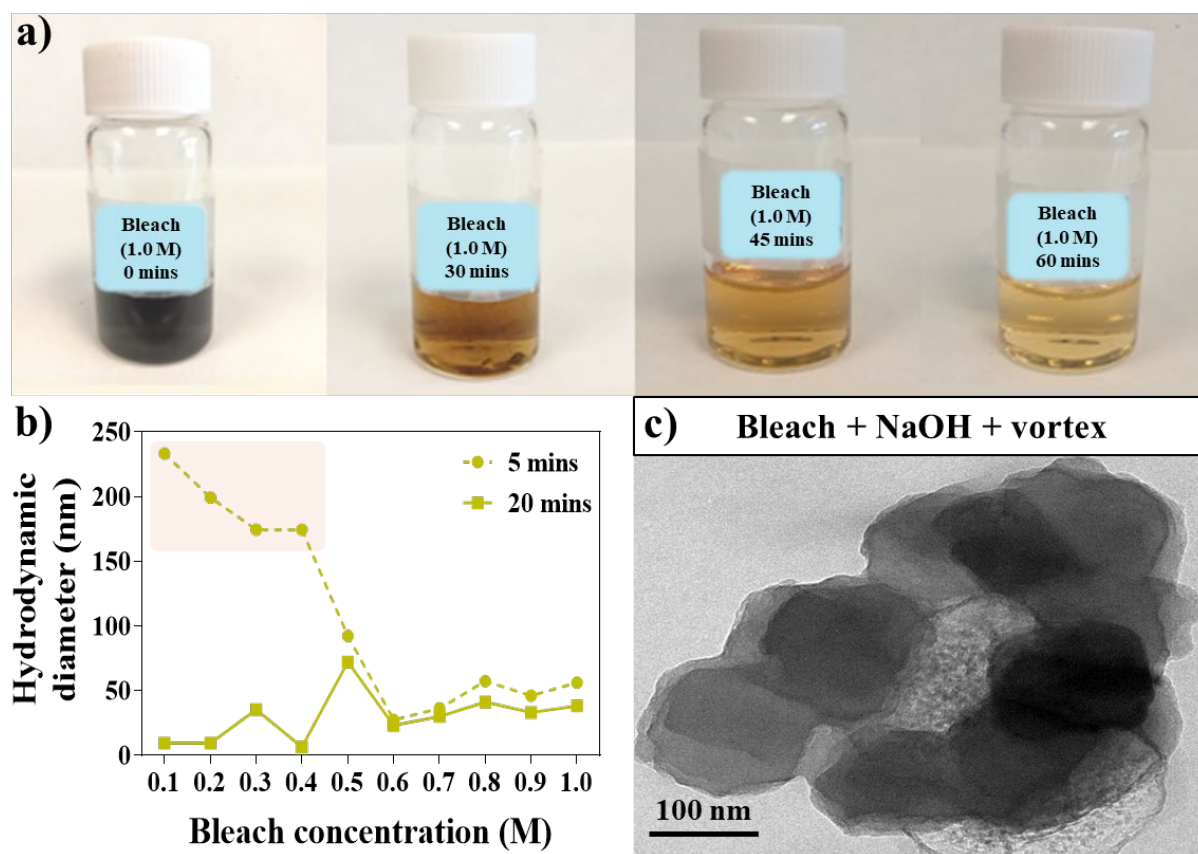


Figure 7. a) Aqueous stability of Ppy NPs in undiluted bleach solution (1.0 M), by visual observation, b) Hydrodynamic diameter of Ppy NPs in Bleach solutions (0.1-1.0 M) after 5- and 20-minutes incubation, c) TEM image of Ppy NPs vortexed (4 minutes) with NaOH (5 M) and bleach (0.3 M).

3.6.2. Recovery of ingested NPs from *C. elegans*

The worms were exposed to 100 $\mu\text{g/mL}$ Ppy NPs in 96-well plates, as explained earlier. After 24 hours, the worms are cleaned thoroughly and imaged. The bacterial food is colourless; therefore, we did not visualize anything within the intestine of the untreated worms (control) (Figure 8a). Whereas we could clearly observe accumulation of Ppy NPs in the intestinal tract of Ppy NP treated worms, owing to their black colour (Figure 8b).

Following the stability evaluation of Ppy NPs in bleach+NaOH mixture, we used the same process (0.3 M bleach + 5 M NaOH + 4 minutes vortexing) to dissolve the treated worms (Figure 8b) and recover the ingested NPs. The solution was immediately visualized in optical microscopy to ensure the worms were completely digested, whereas the ingested NPs were still present (Figure 8c). Following this, the recovered NPs were also visualized by TEM and DLS. TEM images revealed that the intestinal environment and the digestion process resulted in the aggregation of Ppy NPs as well as dissolution to some extent since the aggregates were made of smaller particles of 12 ± 3 nm diameter with clear circular boundaries (Figure 8d). Similarly,

the hydrodynamic diameter of the NPs was 311 ± 75 nm with a PDI of 0.3, corroborating the aggregation (Figure 8e).

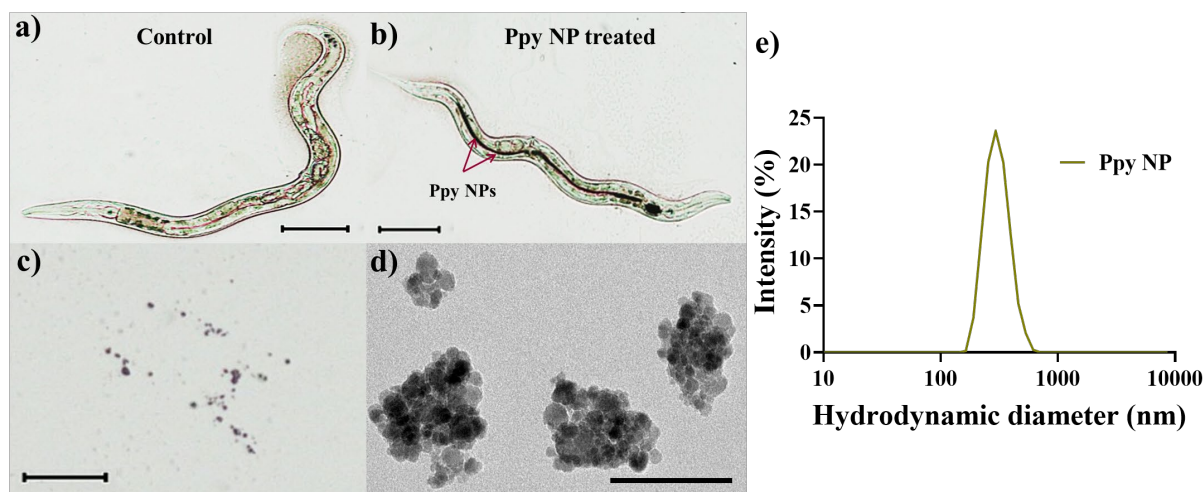


Figure 8. a) Untreated control worms, b) Ppy NP treated worms with NPs observed in the intestine, c) Optical microscopic image and d) TEM image of recovered ingested NPs, e) Hydrodynamic diameter of recovered ingested NPs. Scale bar: 100 μ m.

3.7. Systemic toxicity

3.7.1. Survival rate

The overall toxic effects of Ppy NPs were scrutinized by computing the survival rate of *C. elegans* after 24 hours exposure to three different concentrations of Ppy NPs: 20, 100, and 500 μ g/mL (Figure 9a-c). None of the concentrations showed any adverse toxicity to the survival of the worms. The worms exhibited a remarkable 99.6 % survival (Figure 9d) even at the highest NP concentration of 500 μ g/mL, establishing that the Ppy NPs do not induce any lethal effects in *C. elegans* at these concentrations.

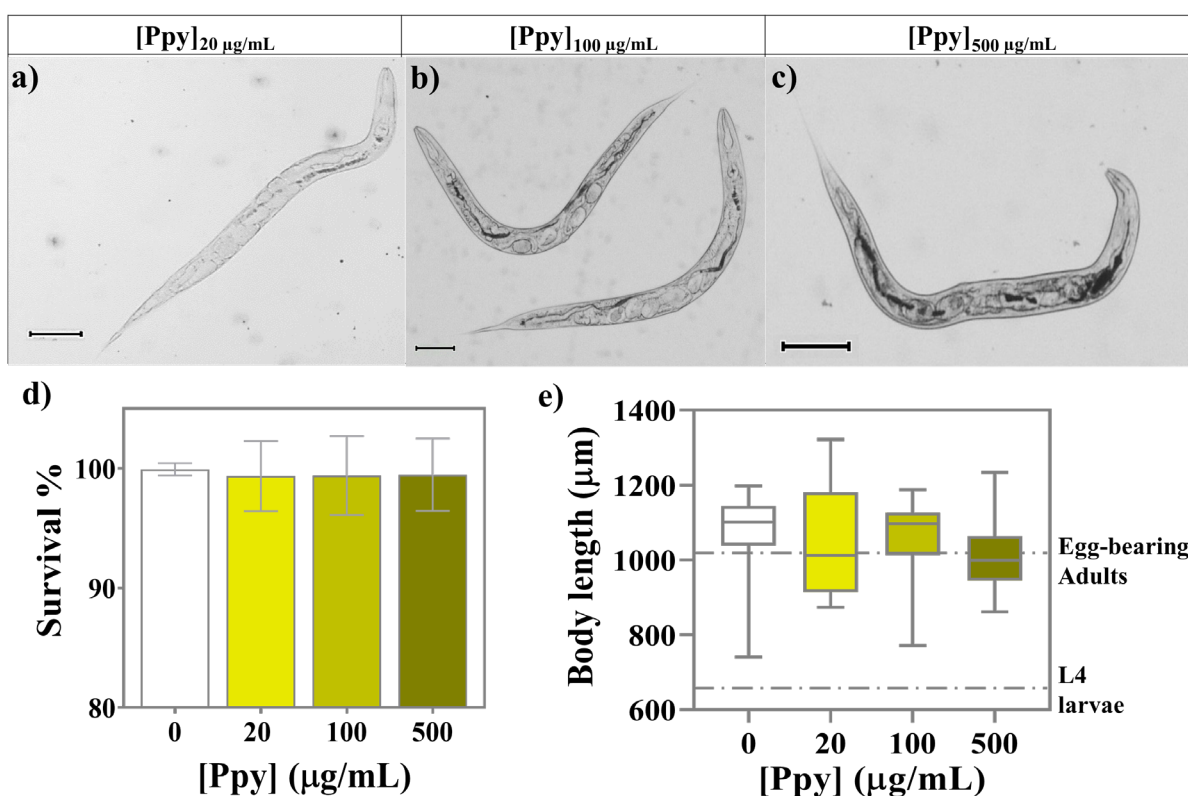


Figure 9. Optical microscopic images of *C. elegans* treated with Ppy NPs at concentrations a) 20 µg/mL, b) 100 µg/mL and c) 500 µg/mL, d) Survival rate and e) Body length of worms after NP treatment. Scale bar: 100 µm.

3.7.2. Growth and Development

The worms are exposed to Ppy NPs at L4-Young adult stage, when their body length is ≈ 800 µm. Therefore, at the end of exposure after 24 hours, according to the usual developmental rate, the worms should have reached the egg-bearing adult stage with a body length of ≈ 1000 - 1100 µm. Consequently, after exposure and cleaning, the body length of untreated and Ppy NP-treated worms was computed (Figure 9e). The worms from all the treatment groups showed similar body length at their fully developed, egg-bearing adult stage (≈ 1050 µm), substantiating that Ppy NPs does not affect the growth and development of the worms at any concentration.

3.8. Reproductive effect

Two toxicity endpoints, namely: reproductive rate and transgenerational toxicity, were evaluated in Ppy NPs treated worms to investigate the impact of the NPs on the reproductive system of *C. elegans*. *C. elegans* can produce up to 300 progenies within a span of 72 hours, referred to as the reproductive rate of the worms. The impact of parental exposure to

nanoparticles on the development and health of unexposed offspring is called transgenerational effect^{9,10}.

3.8.1. Reproductive rate

Treating *C. elegans* with nanoparticles or drugs can sometimes affect the reproductive rate. In order to estimate this, we counted the number of progenies produced by the worms for 72 hours after treatment. The treated and cleaned worms are singled out and placed in 12-well plates containing NGM and OP50, and the number of eggs and larvae produced are counted (Figure 10a). The worm is moved to a fresh well every 24 hours to facilitate ease of counting, and the progenies are counted for 72 hours in total. Both the untreated and treated worms produced ≈ 390 eggs and larvae in 72 hours after exposure and cleaning, showing no significant difference in the reproductive rate (Figure 10b).

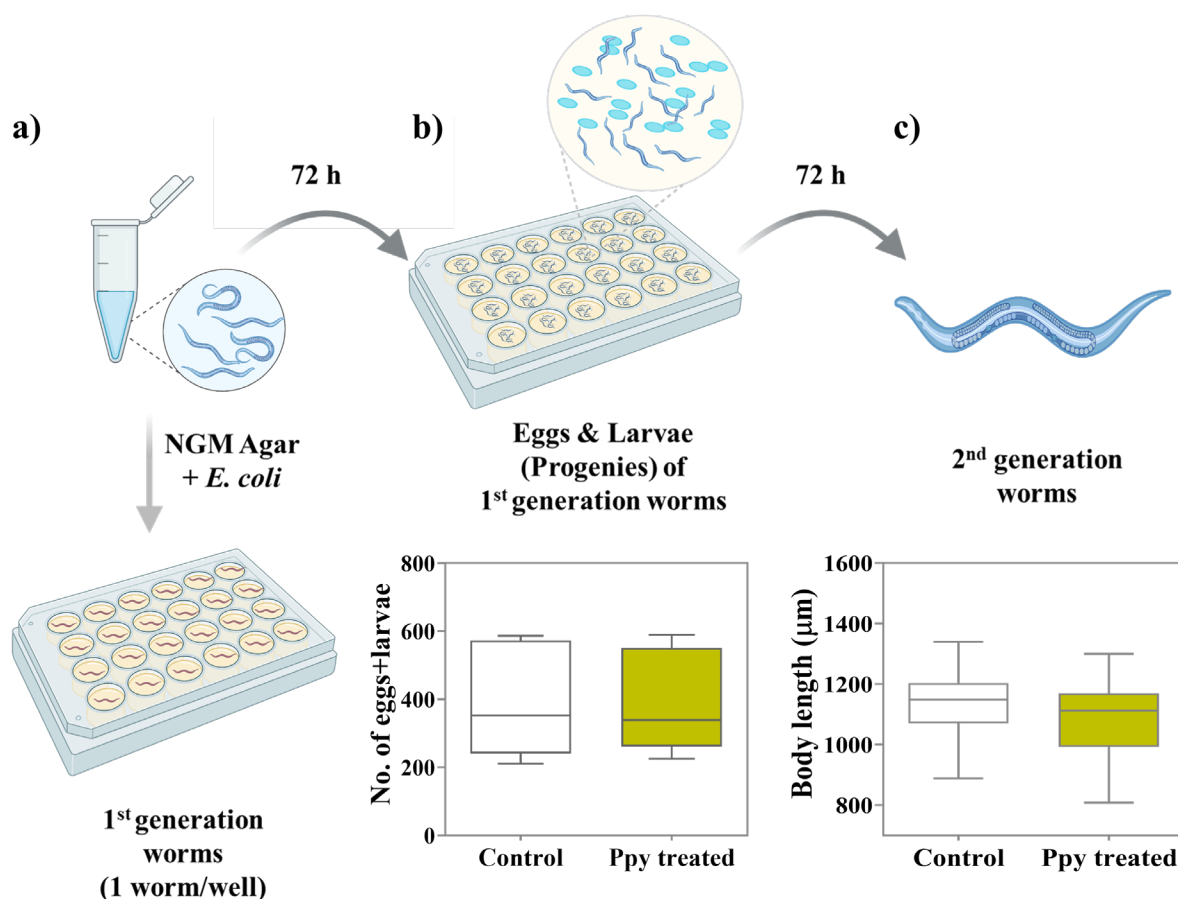


Figure 10. a) Reproductive toxicity assay of treated and cleaned worms in OP50-NGM well plates. b) Reproductive rate of untreated (control) and Ppy NP treated *C. elegans* after exposure, c) Body length of offspring (2nd generation worms).

3.8.2. Transgenerational toxicity

The eggs laid by the treated worms (1st generation worms) are allowed to grow in normal conditions (NGM with OP50 at 20 °C) for 72 hours, and we measured the body length of the 2nd generation worms. The offspring grew at the usual expected rate, reaching the fully-grown adult stage ($\approx 1200\ \mu\text{m}$) 72 hours after hatching (Figure 10c). Therefore, the NPs do not cause any negative impact on the reproductive system of *C. elegans*, nor on the development of unexposed progenies.

3.9. Lipid accumulation

Lipid accumulation and lipid metabolism represent the fat composition of an organism, which are known to be affected by several factors such as age, diet, environmental changes, genetic modifications, and manipulations with chemicals or drugs^{11–14}. Thus, the impact of a NP treatment on the lipid profiles is a key parameter to assess. *C. elegans* possess ≈ 400 genes (over 70%) associated with lipid storage; most of them are homologous to mammals. Several processes such as food intake, lipid biosynthesis, transport, and storage are conserved in *C. elegans*, making them an excellent animal model for studying lipid accumulation and quantitative profiling of lipid storage¹².

The lipids are stored as fat droplets within the intestinal cells of *C. elegans*, and can be clearly visualized when fluorescently stained, thanks to the optical transparency of the worms. BODIPY (4,4-difluoro-4-bora-3a,4a-diaza-s-indacene) is a widely used lipophilic fluorescent dye for visualization of lipid droplets within the worms. Compared to other lipid staining dyes like Nile Red, BODIPY has a high fluorescence quantum yield, narrow emission spectrum, and high extinction coefficient. BODIPY conjugates with fatty acid moieties, thus rendering higher specificity to stain lipid droplets without exhibiting cytoplasmic and nuclear fluorescence^{14,15}.

The worms were stained with BODIPY dye after exposure and cleaning to estimate whether Ppy NPs could affect lipid levels in worms. To a small volume ($\approx 100\ \mu\text{L}$) of worm pellet, 1 mL BODIPY (35 μM) is added and incubated under shaking for 30 min. The incubation allows ingestion of the dye by the worms. The stained worms are washed thoroughly with M9 buffer to remove the excess dye and paralyzed by adding 3 μL 10 mM tetramisole to an equal volume of worms in M9 buffer. Fluorescent images of the stained worms were obtained using a GFP filter (Figure 11a, b), and the intensity was quantified to estimate the total lipid content

in worms. We found no difference in the fluorescent intensity between untreated and Ppy NP-treated groups, suggesting that the total lipid levels were not affected (Figure 11c).

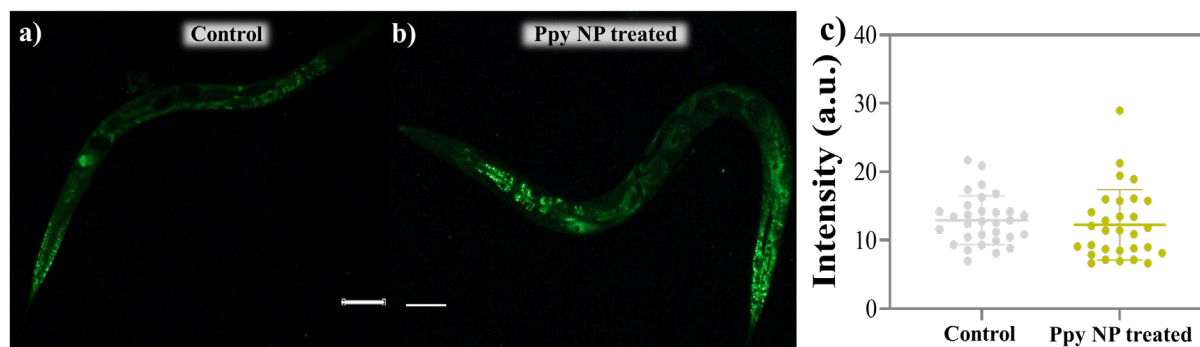


Figure 11. Fluorescent images of BODIPY stained a) control (untreated) worms, b) Ppy NP treated worms, c) Quantification of the total lipid content in control and treated worms.

3.10. Oxidative effect

Elevation or mitigation of oxidative stress experienced by cells is a common effect observed in NP treatments and are involved in wide range of disease pathologies. Oxidative stress increases lipid peroxidation due to free radical generation. We used synchrotron radiation sourced FTIR microspectroscopy (SR- μ FTIR) is used to obtain FTIR spectra of biological samples with characteristics peaks of biomolecules such as lipids and proteins, to extract information on protein aggregation, lipid peroxidation, etc¹⁶. SR- μ FTIR is non-destructible to samples, with an incident beam $<10\ \mu\text{m}$ in diameter (compared to conventional IR with 75-100 μm beam diameter), providing incident lights with 100-fold brightness compared to conventional FTIR instruments. Hence, for small and heterogenous biological samples such as the case of *C. elegans*, it is beneficial to use SR- μ FTIR in order to produce data with a 1000 times better signal-noise ratio over the conventional IR spectroscopy¹⁷.

3.10.1. Sample preparation and analysis

L3 worms were used for the SR- μ FTIR analysis since adult worms have thick cuticles making it hard for the incident rays to penetrate and produce signals with strong intensity. Briefly, L1 synchronized worms are transferred to NGM plates and allowed to grow for 8 hours. The worms are thoroughly cleaned to remove bacteria and exposed to Ppy NPs at 100 $\mu\text{g/mL}$ concentrations for 12 hours, where the worms have reached L3. After exposure, the worms must be cleaned thoroughly with Milli-Q water by centrifugation; debris, bacteria, or salt crystals must be removed completely since they can hamper worm visualization to select regions of interest (ROI). The cleaned worms are mounted on 10 or 25 mm CaF_2 windows,

with each drop containing ≈ 3 -5 worms and ≈ 9 drops /window. The windows are dried under vacuum and stored in an N_2 atmosphere until analysis. Briefly, we visualize the worms through the microscope at 36x magnification objective and choose several regions of interest (ROIs) within the alimentary tract of the worms. The scanning is performed in transmission mode through an MCT detector, producing FTIR spectra in the spectral range 900 - 400 cm^{-1} , and the spectra were extracted using OPUS 7.5 (Brucker). We also did post-processing of the spectral data like noise removal, baseline correction, and application of Savitsky–Golay second derivative using Unscrambler and Origin 2019b.

3.10.2. Quantification through relative absorbance ratios

The change in the biochemical composition of an organism with and without treatment can be assessed by comparing the FTIR spectral data between the two groups. The spectra exhibits distinctive peaks of biomolecules at specific regions. Peaks between 2800 - 3000 cm^{-1} represents the bonds and interactions among hydroxyl groups of lipid molecules. Whereas, the peaks in 1400 - 1800 cm^{-1} are characteristic of amide bonds from protein molecules, and the peaks between 1000 - 1200 cm^{-1} typical for the phosphate and carbonyl bonds from nucleic acids and carbohydrates. The FTIR spectra of untreated and Ppy NP treated worms are shown (Figure 12); no significant difference in peak positions and intensities were noted, showing that the NP treatment did not induce any drastic change in biochemical composition.

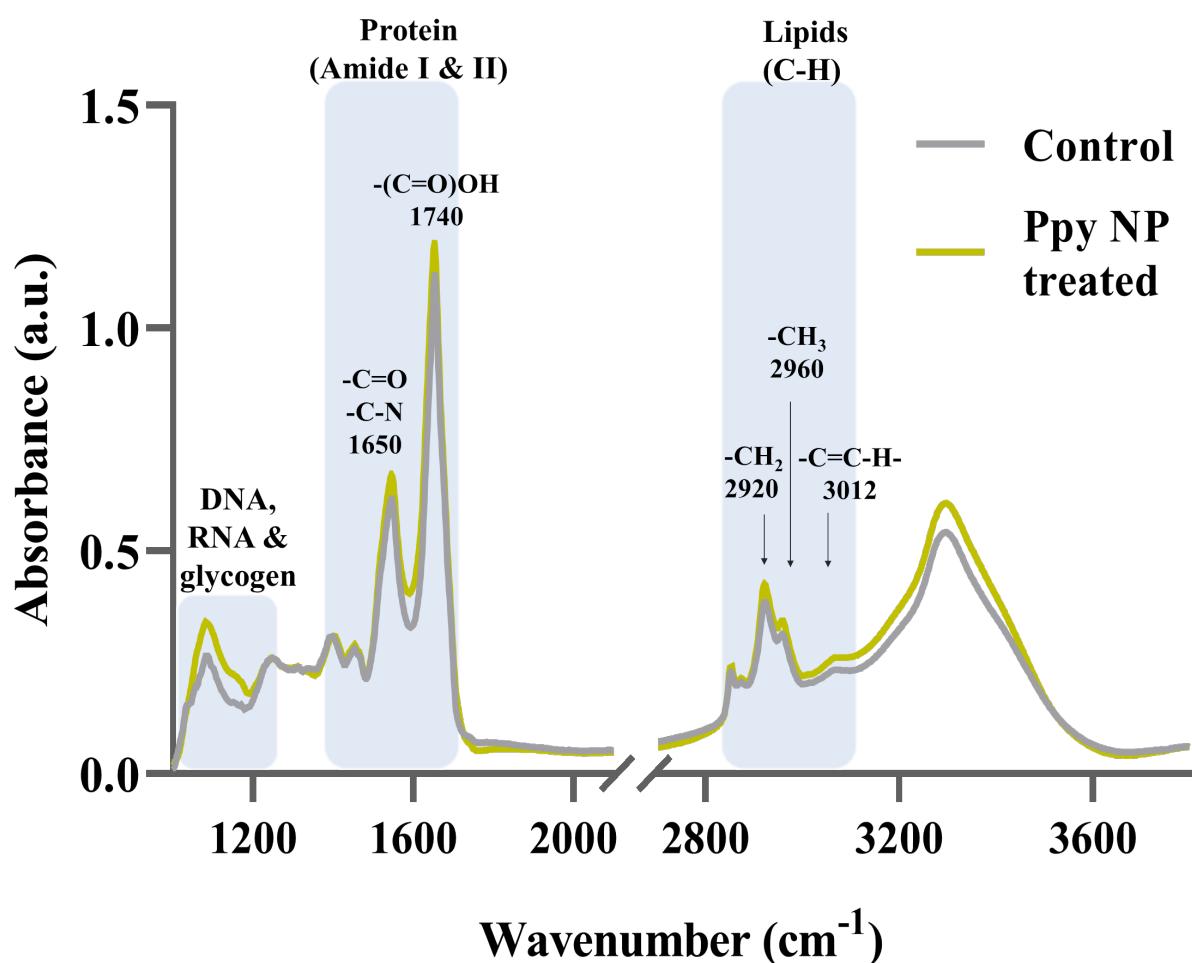


Figure 12. SR- μ FTIR spectra of control and Ppy NP treated worms showing the distinct spectral regions of the four biomolecules: Nucleic acids, carbohydrates (glycogen), Proteins, and lipids.

Relative absorbance ratios were calculated from the second derivatives obtained from the FTIR spectral data at specific regions corresponding to the biomolecules. Especially due to lipid oxidation, the amount of carbonyl groups increases, which can be calculated from the FTIR peak of carbonyl ester bonds at 1740 cm^{-1} . The ratio of lipid oxidation was computed as the ratio of absorbance at 1740 and at 2920 cm^{-1} (A_{1740}/A_{2920}). Another important parameter that could be affected due to NP treatment and plays an essential role in cellular mechanisms is the protein-to-lipid ratio. Interestingly, an increase in the absorbance ratio A_{2920}/A_{2960} could either correspond to increased lipid saturation or an enhanced protein-to-lipid ratio. Consequently, we also evaluated the protein-to-lipid content by measuring another absorbance ratio: A_{1650}/A_{1740} .

The treatment of worms with NPs can influence lipid metabolism because of a change in energy consumption or energy depletion. Lipid metabolism can be studied through two parameters:

the amount of saturated fatty acids and unsaturated fatty acids. The unsaturated lipids contribute more to the presence of double bonds ($C=C-H$), which can be quantified from the absorbance at 3012 cm^{-1} . Similarly, the absorbance at 2920 cm^{-1} ($C-CH_2$) represents the number of single bonds ($C-H$), that is, the saturated lipids. The lipid unsaturation and saturation were normalized with the peaks at 2920 cm^{-1} (A_{3012}/A_{2920}) and 2960 cm^{-1} (A_{2920}/A_{2960}), respectively¹⁸.

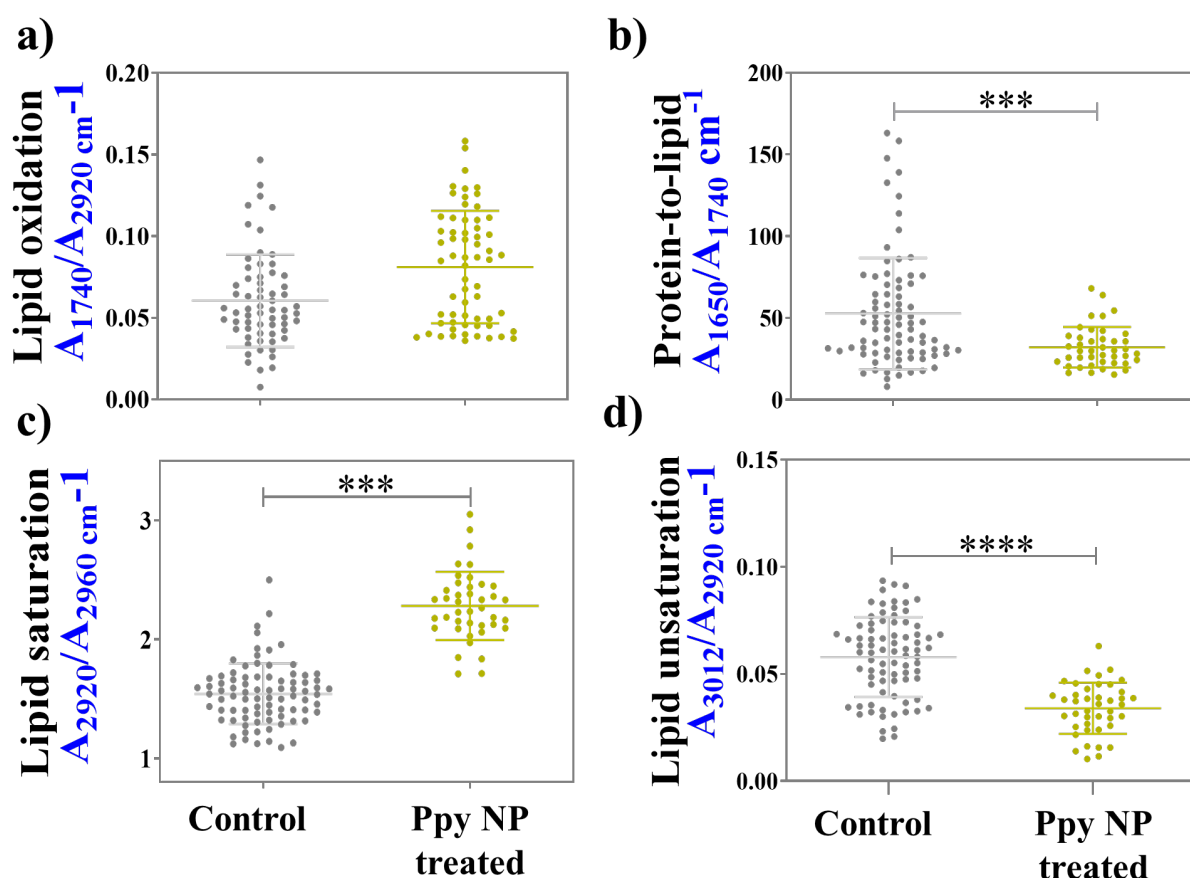


Figure 13. a) Lipid oxidation ratio (A_{1740}/A_{2920}), b) Amide oxidation ratio (A_{1650}/A_{1740}) c) Lipid saturation ratio (A_{2920}/A_{2960}) and d) lipid unsaturation ratio (A_{3012}/A_{2920}) of untreated (control) and treated worms (Ppy NP treated).

Notably, Ppy NPs treatment did not show a significant effect on the lipid oxidation levels (A_{1740}/A_{2920}) (Figure 13a). On the other hand, the A_{1650}/A_{1740} ratio is lower for the treated groups compared with the untreated control worms indicating possible reduced protein-to-lipid content in the worms (Figure 13c). The reduced protein content could be attributed to the co-administration of Ppy and OP50, leading to an overall reduced consumption of the protein-rich bacterial food. When lipid metabolism is enhanced, the lipid saturation increases with a concomitant decrease in unsaturation levels¹³. The SR- μ FTIR results showed that Ppy

increases the saturated lipid content (Figure 13d), indicating a rise in lipid metabolism, probably because Ppy increases the energy and fuel required for lipid metabolism. As expected, the amount of unsaturated fatty acids shows a contrasting effect (Figure 13e) as opposed to the saturated fatty acid content. In a nutshell, Ppy NPs do not seem to cause oxidative stress, further substantiating their safety. However, Ppy treatment indeed reduces the protein content and increases lipid metabolism, possibly caused by increased energy consumption.

3.11. Conclusions

We employed *C. elegans* as a powerful tool to rigorously evaluate various systemic effects of Ppy NPs. Firstly, we assessed the general toxic effects of pyrrole by measuring the survival rate and body length to eliminate the possibility of monomer toxicity. Following this, we exposed *C. elegans* to Ppy NPs and measured its impact at different levels of biological organization,

- (i) Organism level - through survival rate, growth, and development (body length).
- (ii) Organ level - impact on the reproductive system (reproductive rate and transgenerational development), gastrointestinal fate.
- (iii) Molecular-level - lipid accumulation, oxidation, lipid metabolism, and protein content.

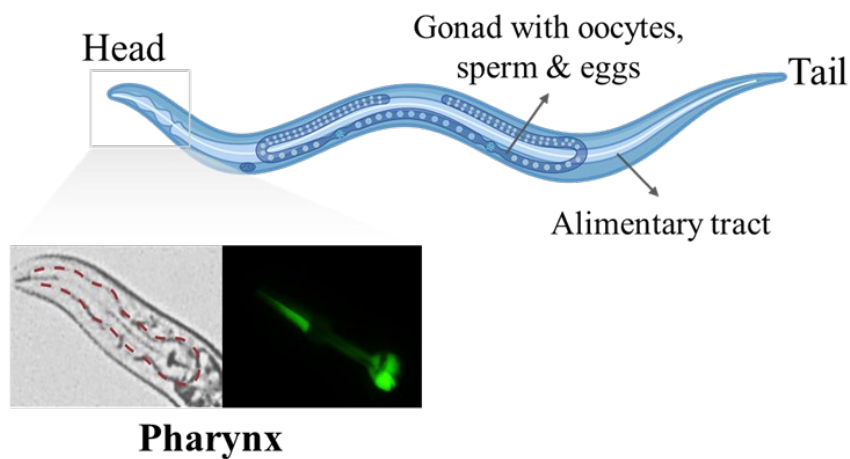
Remarkably, *C. elegans* did not show any undesirable toxic response to treatment with Ppy NPs in any of the assays tested, showing the exceptional biocompatibility of Ppy NPs and their promising potential as well as open up opportunities of Ppy nanocomposites for biomedical applications. Following the encouraging compatibility of Ppy NPs in *C. elegans*, we proceeded to evaluate the specific effects of the NPs on the pharyngeal behavior of the worms.

References

1. Corsi, A. K., Wightman, B. & Chalfie, M. A Transparent window into biology: A primer on *Caenorhabditis elegans*. in *WormBook: the online review of C. elegans biology* 1-31 (2015).
2. Riddle, D. L. *C. elegans II, 2nd edition*. **33** (Cold Spring Harbor Laboratory Press, 1997).
3. Hall, D. H. & Altun, Z. F. *C. elegans atlas*. (Cold Spring Harbor Laboratory Press, 2008).
4. Moragas, L. G. Evaluating inorganic nanoparticles in the living organism *Caenorhabditis elegans*. *Universitat de Autònoma de Barcelona*, 2016.
5. Luo, Z. *In vivo interactions between food availability and nanoparticles in Caenorhabditis elegans*. *Universitat de Autònoma de Barcelona*, 2016.
6. Meneely, P. M., Dahlberg, C. L. & Rose, J. K. Working with Worms: *Caenorhabditis elegans* as a Model Organism. *Curr. Protoc. Essent. Lab. Tech.* **19**, (2019).
7. Zhou, H. & McClements, D. J. Recent Advances in the Gastrointestinal Fate of Organic and Inorganic Nanoparticles in Foods. *Nanomaterials* **12** (2022).
8. Sohal, I. S. *et al.* Dissolution behavior and biodegradability of ingested engineered nanomaterials in the gastrointestinal environment. *ACS Nano* **12**, 8115–8128 (2018).
9. Lu, Q., Bu, Y., Ma, L. & Liu, R. Transgenerational reproductive and developmental toxicity of tebuconazole in *Caenorhabditis elegans*. *J Appl Toxicol.* **40**, 578–591 (2020).
10. Zhao, Y., Chen, J., Wang, R., Pu, X. & Wang, D. A review of transgenerational and multigenerational toxicology in the in vivo model animal *Caenorhabditis elegans*. *J Appl Toxicol.* **43** 122–145
11. Mantel-Teeuwisse, A. K. *et al.* Drug-Induced Lipid Changes A Review of the Unintended Effects of Some Commonly Used Drugs on Serum Lipid Levels. *Drug society* **24**, 443–456 (2001).
12. An, L., Fu, X., Chen, J. & Ma, J. Application of *Caenorhabditis elegans* in Lipid Metabolism Research. *Int J Mol Sci* **24**, 1173 (2023).
13. Oliveros, L. B., Videla, A. M., Giménez, M. S. & Gimenez, A. M. S. *Effect of dietary fat saturation on lipid metabolism, arachidonic acid turnover and peritoneal macrophage oxidative stress in mice*. *Braz. J. Med. Biol.* **37** (2004).
14. Klapper, M. *et al.* Fluorescence-based fixative and vital staining of lipid droplets in *Caenorhabditis elegans* reveal fat stores using microscopy and flow cytometry approaches. *J Lipid Res* **52**, 1281–1293 (2011).
15. Govender, T., Ramanna, L., Rawat, I. & Bux, F. BODIPY staining, an alternative to the Nile Red fluorescence method for the evaluation of intracellular lipids in microalgae. *Bioresour Technol* **114**, 507–511 (2012).
16. Kreuzer, M., Dučić, T., Hawlina, M. & Andjelic, S. Synchrotron-based FTIR microspectroscopy of protein aggregation and lipids peroxidation changes in human cataractous lens epithelial cells. *Sci Rep* **10**, (2020).
17. Holman, H.-Y. N., Martin, M. C. & McKinney, W. R. *Synchrotron-Based FTIR Spectromicroscopy: Cytotoxicity and Heating Considerations*. *J. Biol. Phys.* **29** (2003).
18. Benseny-Cases, N., Klementieva, O., Cotte, M., Ferrer, I. & Cladera, J. Microspectroscopy (μ FTIR) reveals co-localization of lipid oxidation and amyloid plaques in human Alzheimer disease brains. *Anal Chem* **86**, 12047–12054 (2014).

Chapter 4

Caenorhabditis elegans' pharynx to evaluate cardiac rhythm



PREFACE

Exploiting the structural and molecular similarity of *C. elegans*' pharynx with the human heart, we used the pharynx as a platform to evaluate arrhythmic effects. We first assessed two commercial drugs: Propranolol and racepinephrine, in wild-type worms to test whether they produce similar impact in pharyngeal pumping rate as observed in human cardiac pumping rate. Then, we employed two pharynx specific mutant strains, JD21 and DA464, to investigate the pharyngeal effects of the two drugs, and the strain specific impact of Ppy NPs. The strain with maximum impact, JD21 was chosen to scrutinize the specific molecular effects, by studying the intracellular calcium signalling in the pharynx through calcium imaging technique.

Index

4.1. Commercial anti-arrhythmic substances	103
4.1.1. General Toxicity.....	103
4.1.2. Pharynx pumping rate	105
4.1.3. Lipid accumulation.....	105
4.1.4. Lipid oxidation and metabolism.....	106
4.2. Pharynx pumping impaired strains	108
4.2.1. Systemic effects of drugs and nanoparticles	108
4.3. Pharyngeal effects	109
4.3.1. Pharyngeal pumping rate of mutant strains	109
4.3.2. Exposure duration	111
4.3.3. Excretion duration.....	112
4.4. Molecular effects.....	114
4.4.1. Calcium signalling	114
4.4.2. Calcium imaging.....	115
4.5. Conclusions.....	119

4.1. Commercial anti-arrhythmic substances

We evaluated two commercially available substances with known effects on heart rate for their general and pharyngeal effects in *C. elegans*, to assess the potential of using the worms as a model to study cardiac rhythm.

Propranolol (PL) belongs to the class of beta-blockers, acting as a non-selective β -adrenergic receptor antagonist¹ (Figure 1). PL also has sodium channel blocking effects² and acts as a weak antagonist with 5-HT_{1A}, 5-HT_{1B}, and 5-HT_{2B} serotonin receptors as its secondary targets^{3,4}. PL relaxes cardiac muscle cells, reducing the contractility, thereby decreasing the heart rate⁵. On the other hand, Racepinephrine (RE) is a racemic mixture of d-epinephrine and l-epinephrine, an over-the-counter α - and β -adrenergic receptor agonist (Figure 1), which is reported to induce tachycardia, i.e., increased heart rate^{6,7}.

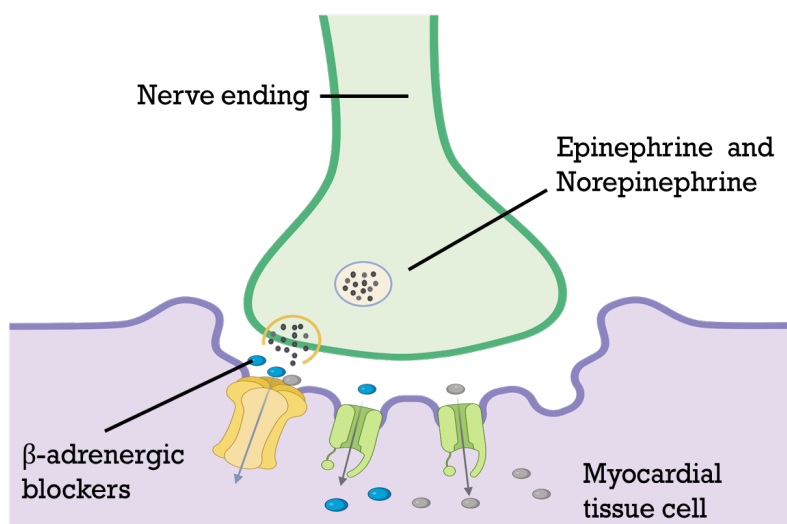


Figure1: Mechanistic action of β -adrenergic receptor agonist (Epinephrine) and antagonists (β -blockers) at the neuro-muscular junction, acting through the β -adrenergic receptors.

The mechanism of action of PL and RE in *C. elegans* could be mediated through the 5-HT serotonin receptors. It is well known that serotonin stimulates pharyngeal pumping in *C. elegans*; naturally, the serotonin receptor agonist RE could also produce a similar effect, resulting in an increase in pumping rate. In contrary, the serotonin receptor antagonist PL, could reduce the pharyngeal pumping rate.

4.1.1. General toxicity

Both PL and RE were assessed for their general toxicity in *C. elegans*, to ensure the safety of using these drugs in *C. elegans*. The worms were exposed to PL and RE for 24 hours at 20 °C, in 96-well plates, in the same manner as Ppy NPs exposure (Chapter 3). The worms

displayed 99.6% survival after 24 hours treatment with both PL and RE (Figure 2b). Likewise, they also exhibited similar growth rate to untreated worms, reaching $\approx 1100 \mu\text{m}$ length after 24 hours exposure (Figure 2c) and reproductive rate, producing ≈ 390 -400 progenies in 72 hours (Figure 2d). The second-generation worms also grew at a uniform expected rate, implying PL and RE treatment did not induce any transgenerational toxicity (Figure 2e). The survival, growth, and reproduction together prove that PL and RE are safe to be assessed in *C. elegans* for their pharyngeal effects.

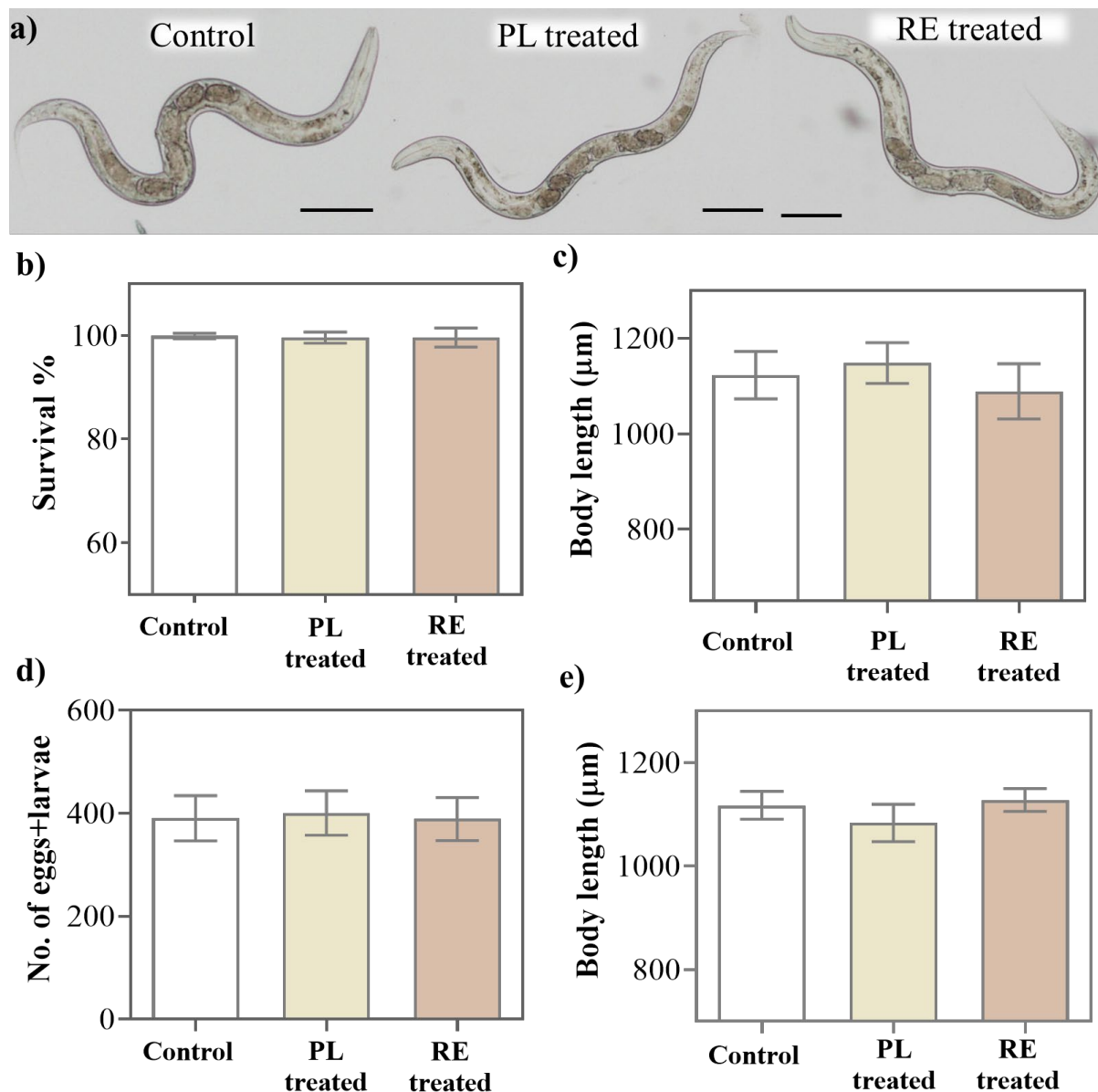


Figure 2. a) Representative images from optical microscope of untreated (control), PL and RE treated worms after exposure and cleaning, Systemic effects of PL and RE compared with untreated worms, b) Percentage of Survival (N=60), c) Development of the worms (body length) (N=40), d) Reproduction rate (progenies = eggs+larvae) (N=12), e) Progeny body length (N=30). Scale bars: 100 μm .

4.1.2. Pharynx pumping rate

The worms were treated with PL/RE (100 μ M) or Ppy NPs (100 μ g/mL) for 24 hours unless stated otherwise. After exposure and cleaning, \approx 15 worms were placed on 2% agarose pads with OP50, on a glass slide and secured with a cover glass on top to restrict movement. The worms were visualized through optical microscopy and the pharynx pumping videos were recorded using 48 MP mobile camera. We counted the pharynx pumping rate manually for 30 seconds for each worm to calculate the pumps/minute.

Exposure to PL has been shown to reduce cardiac pumping in humans and the worms treated with PL for 24 hours also exhibited a reduced pharynx pumping rate (Figure 3). Likewise, RE, treatment to worms increased the pharynx pumping rate of *C. elegans* (Figure 3). The effect of both the drugs on *C. elegans*'s pharynx pumping rate correlated well with the cardiac pumping effects observed in humans^{5–7,10}.

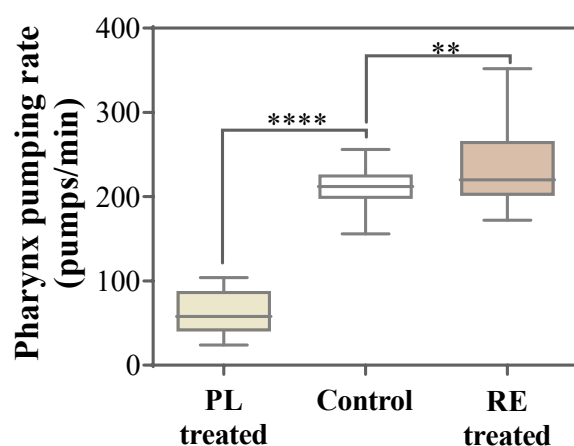


Figure 3. Pharynx pumping rate of PL and RE treated *C. elegans* in comparison with untreated (control) *C. elegans*.

4.1.3. Lipid Accumulation

The pharynx is a filter-feeder for the worms that controls the food movement towards the intestine⁸; any change in the pharynx pumping rate might affect the food ingestion by the worms. Thus, RE or PL that affect the pharynx pumping rate could also modulate the food ingestion, thereby the total lipid accumulation. The total lipid droplets were quantified by BODIPY staining assay (Figure 4a-c). The untreated (control) and PL/RE treated worms were cleaned after exposure and the staining is carried out through the same protocol used for Ppy NP treated worms (Chapter 3).

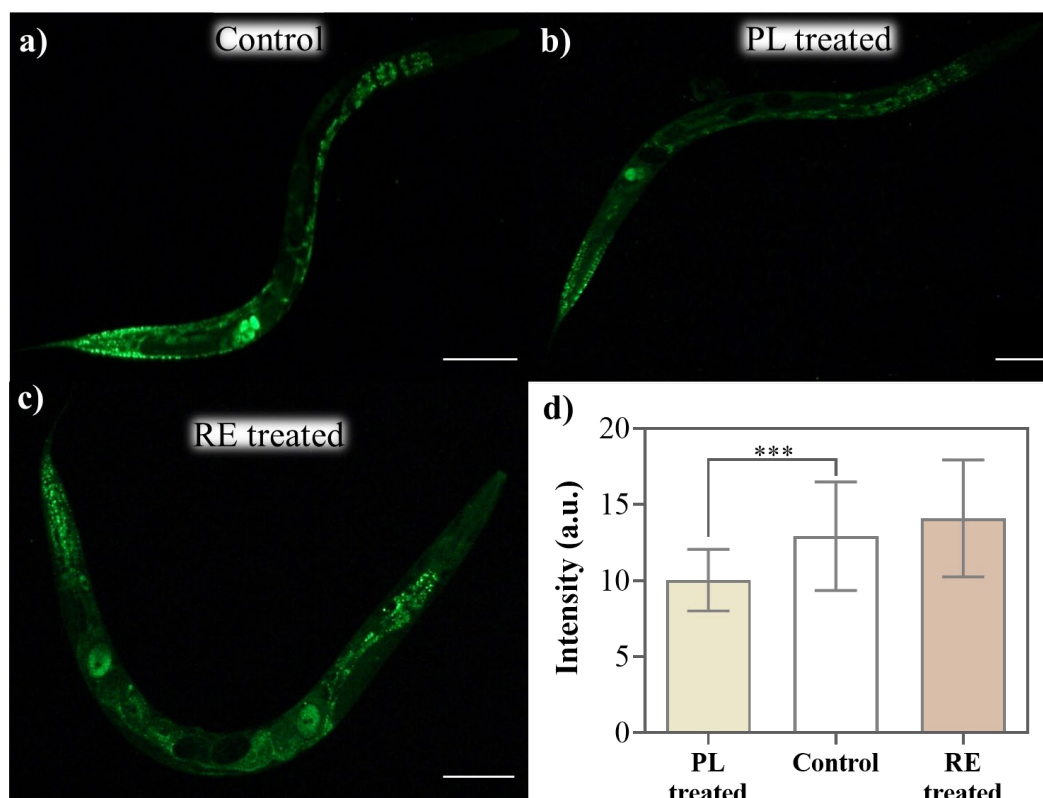


Figure 4. Fluorescent microscopic images of BODIPY stained worms under GFP filter (5X magnification): a) untreated (control), b) PL treated, c) RE treated worms, d) Quantification of total lipids by fluorescence intensity (N=30). Scale bars: 100 μ m.

Interestingly, we found that PL treatment reduced the amount of lipid droplets in worms (Figure 3d), which is a contrasting behaviour from that observed in humans⁹. This is probably because in humans PL does not affect the food ingestion in the alimentary tract, however in *C. elegans*, they exert effects in the pharynx that directly influences food ingestion and digestion, influencing the lipid accumulation in *C. elegans*. On the other hand, RE treatment did not show any impact on lipid accumulation, similar to Ppy treatment.

4.1.4. Lipid oxidation and metabolism

We employed the SR- μ FTIR technique to PL and RE treated worms in the same way as Ppy NP treated worms (Chapter 3) to evaluate the oxidative impact of PL and RE in *C. elegans* by measuring the lipid oxidation and lipid metabolism through the relative absorbance ratios. The lipid oxidation level in the worms increased with RE treatment, indicating that RE ingestion could potentially cause an oxidative stress (Figure 5a). Our results also corroborate with previous reports on role of RE in increasing oxidative stress^{11–13}. However, like Ppy NPs (Chapter 3), PL did not show a significant change in lipid oxidation (Figure 5a).

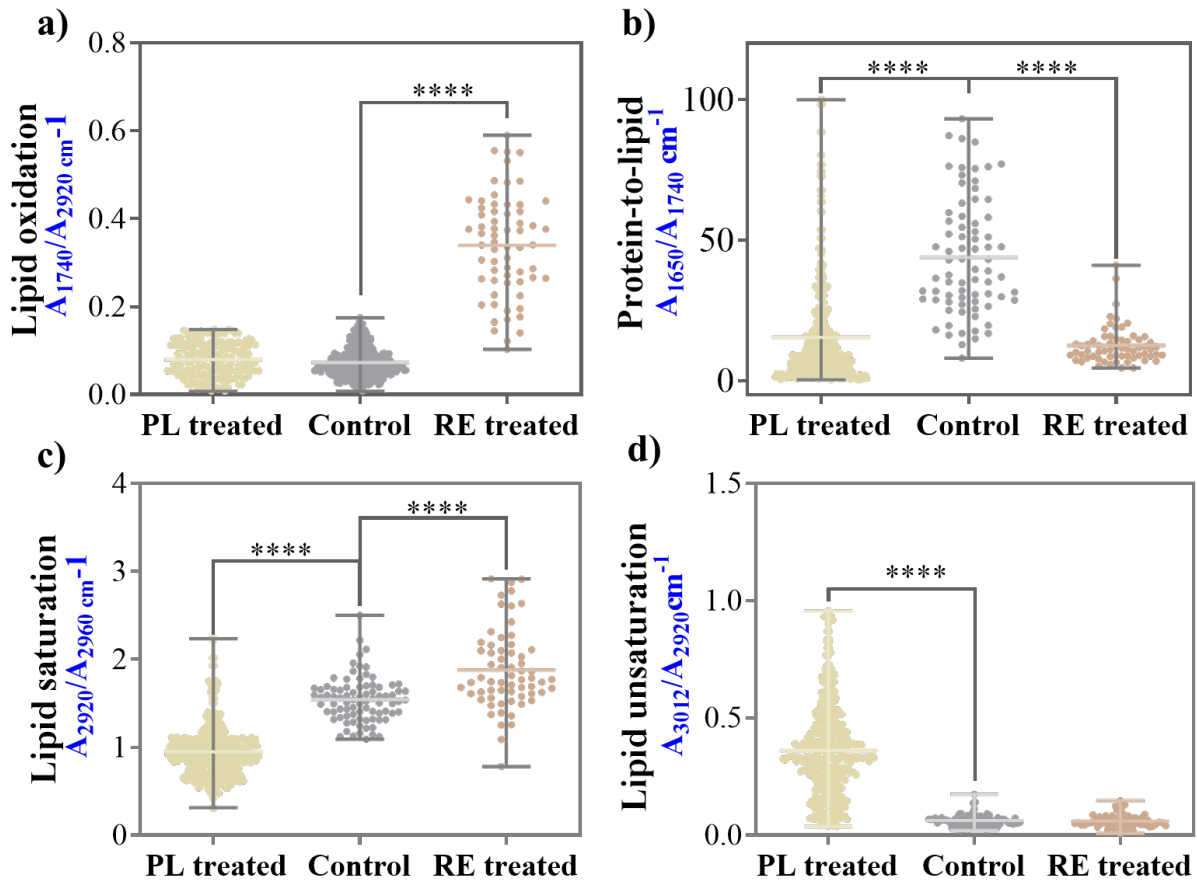


Figure 5. Relative absorbance ratios of a) Lipid oxidation (A_{1740}/A_{2920}), c) Protein to lipid (A_{1650}/A_{1740}) d) Lipid saturation (A_{2920}/A_{2960}) and e) lipid unsaturation (A_{3012}/A_{2920}) of untreated (control), PL and RE treated worms.

The ratio of protein to lipids is reduced in the PL and RE treated groups, akin to the effect caused by Ppy NPs (Figure 5b). A low protein content is also related to low lipid metabolism^{14–16}. The lipid metabolism can be understood by assessing the lipid saturation and unsaturation levels, since an enhance metabolism results in high saturated lipids and low unsaturated lipids¹⁷. The SR- μ FTIR results showed that PL treatment decreases lipid saturation in worms, whereas RE increases the saturated lipid content indicating an increase in lipid metabolism (Figure 5c). The RE's impact on lipid saturation also concurs with the Ppy NP's effect, further confirming the role of high pumping rate in increasing the amount of ingested food, rising energy and fuel consumption. The increase in saturated lipids content is substantiated by a corresponding increase in lipid oxidation (Figure 5a), together indicating an increase in oxidative stress upon RE treatment. In contrary, PL treatment decreases lipid saturation in worms and not a significant effect in lipid oxidation suggesting an alleviation of oxidative stress in the worms. Several researchers have reported the anti-oxidant role of PL in iron overloaded rats¹⁸, cirrhotic patients¹⁹, and resistive hypertension patients²⁰. The PL's decrease

in lipid metabolism, could also be attributed to the fact that the worms pump slowly after PL treatment, leading to reduced food intake, causing a decrease in lipid levels. This effect of PL treatment in lipid levels also agrees with the reduced lipid levels observed from BODIPY staining (Figure 4d). As expected, the amount of unsaturated fatty acids shows a contrasting effect as opposed to the saturated fatty acid content for both PL and RE treated worms (Figure 5d).

To summarize, we observed that RE appears to cause some oxidative stress. While PL do not seem to cause a significant oxidative stress, it indeed reduces the protein content and the lipid metabolism. In terms of protein content and lipid metabolism, RE follows a similar pattern to Ppy, possibly due to both the substance increasing the pharynx pumping rate of worms leading to an increased food intake, that affects metabolism.

4.2. Pharynx pumping impaired strains

Following the encouraging results of PL and RE in affecting the pharyngeal pumping rate, we employed two specific strains with mutations in the pharynx in addition to the wild-type N2 strain, to evaluate the effects of Ppy, PL, and RE. The two mutant strains were chosen based on the orthology of the mutations causing cardiac arrhythmia in humans. The JD21 strain has a deletion mutation in *cca-1*, a voltage-gated calcium channel homologous to human low-voltage T-type calcium channels *CACNA1G*, *CACNA1H*, and *CACNA1I* (Cav3 genes)²¹, with mutations implicated in long QT syndrome (LQT9)^{22,23}. On the other hand, the additional strain used, DA464, has a mutation in the *eat-5* innexin gap junction, which shares structural and functional similarities with human connexin gap junctions, mutations of which are associated with atrial fibrillation²⁴.

4.2.1. Systemic effects of drugs and nanoparticles

Prior to the evaluation of pharyngeal effects, we assessed the general toxicity of the three substances (Ppy, PL, and RE) in the JD21 and DA464 worms to measure survival rate, body length, and reproductive toxicity. Similar to the wild-type worms, the commercial drugs as well as the Ppy NPs did not show any adverse toxicity to the mutant strains, displaying survival rates of $\approx 98.5\%$ in JD21 worms and $\approx 96\%$ in DA464 worms (Figure 6a), growth rate resulting in the worms reaching $\approx 1100\ \mu\text{m}$ body length (Figure 6b), and healthy reproduction with ≈ 400 eggs laid by the worms from both the strains in all treatment groups (Figure 6c), exhibiting comparable behaviour with untreated worms.

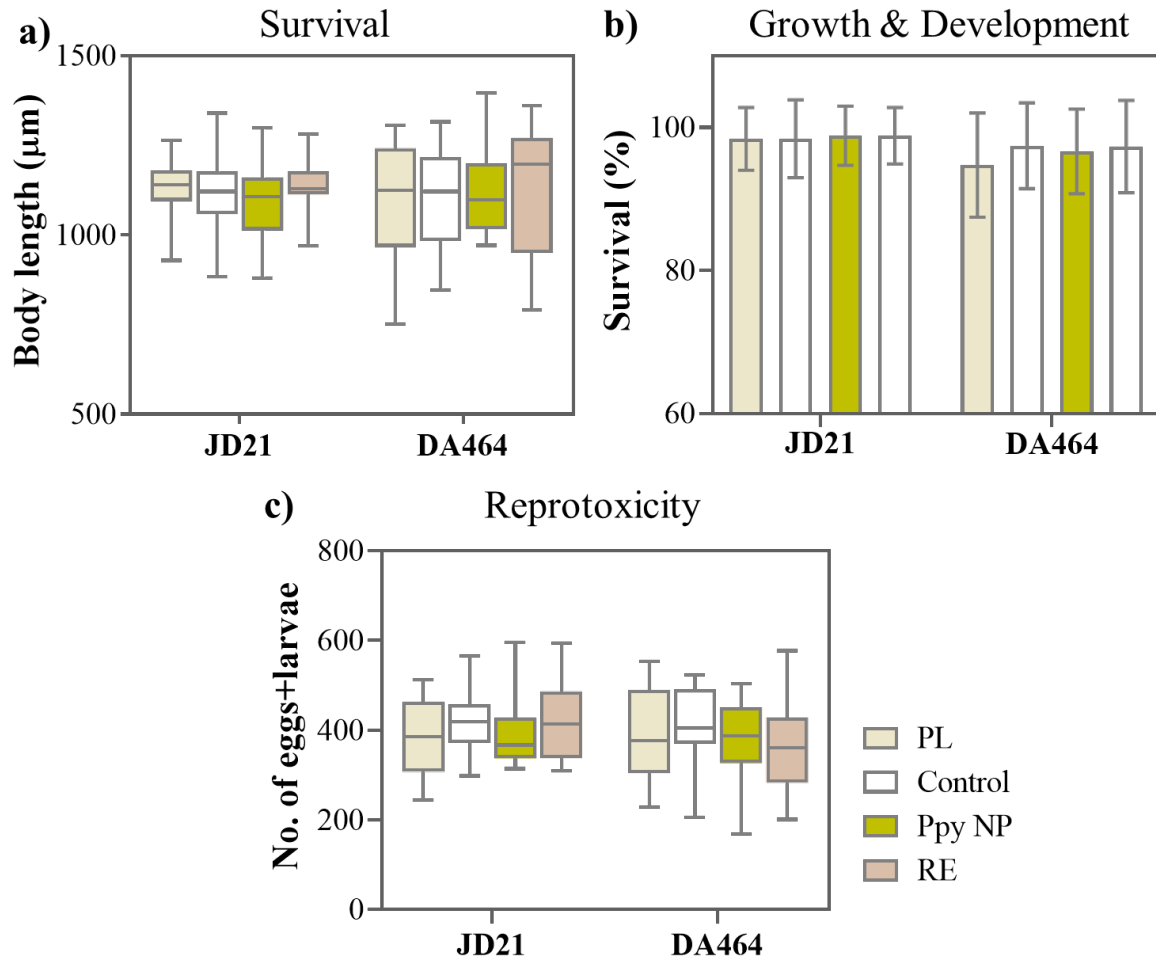


Figure 6. Systemic effects of PL, RE, and Ppy NP treatments in JD21 and DA464 worms, a) Survival rate (N=60), b) Growth rate (N=30), c) Reproductive rate (N=12). No statistical significance observed.

4.3. Pharyngeal effects

4.3.1. Pharyngeal pumping rate of mutant strains

We measured the pharynx pumping rate of the two mutant strains JD21 and DA464 worms, after 24 hours treatment with PL, Ppy NPs, and RE. PL reduced the pharynx pumping rate \approx 3-fold (65 pumps/min) in all the three strains (Figure 7a), showing that the effect of PL might not be dependent on the mutant genes of either JD21 or DA464, and causes reduction of pumping rate in healthy worms (N2) as well. On the other hand, RE did not significantly increase the pumping rate in wild-type but induced the maximum increase in DA464 strain (1.5 times compared to untreated worms) and an intermediate effect (1.2 times) in JD21 worms (Figure 7b).

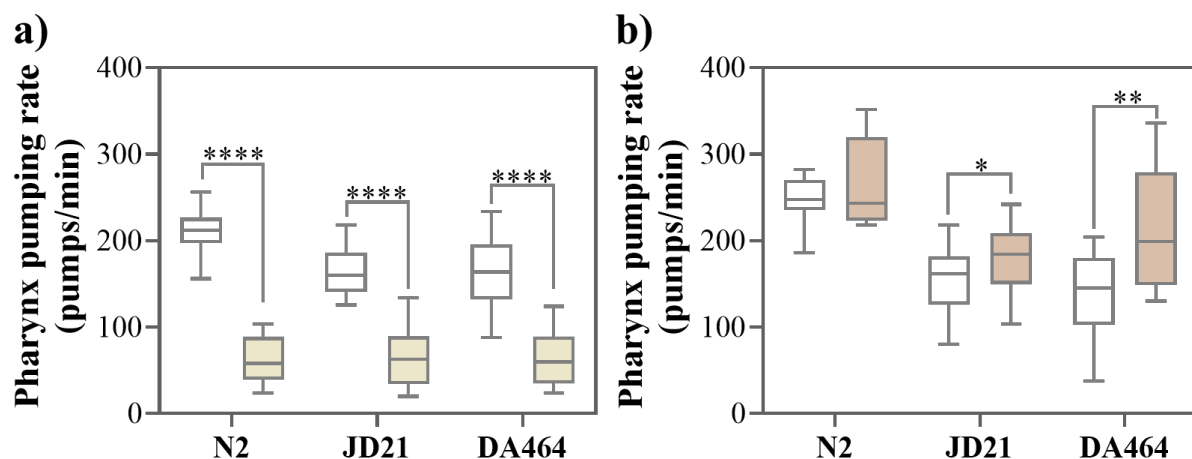


Figure 7. a) Pharynx pumping rate of PL treated and b) RE treated N2, JD21, and DA464 worms (N \approx 30), compared with the respective untreated worms.

Ppy NPs treatment increased the mean pharynx pumping rate of JD21 to \approx 243 pumps/min compared to \approx 190 pumps/min for the untreated worms, and DA464 worms to \approx 200 pumps/min over \approx 170 pumps/min for the control group. The NPs caused a more significant impact on the mutant strains than N2 worms (Figure 8), with the maximum change seen in JD21 worms (\approx 1.3 times), which has a deletion mutation in *cca-1* T-type voltage-gated calcium channel. Studies on the role of Ppy NPs in regulating intracellular calcium signalling in cardiac cells has been reported before^{25,26}. The higher impact in JD21 strain also suggests that Ppy NPs might possibly reverse the impaired calcium transport in JD21 strain, increasing the pumping rate comparable to untreated N2 worms.

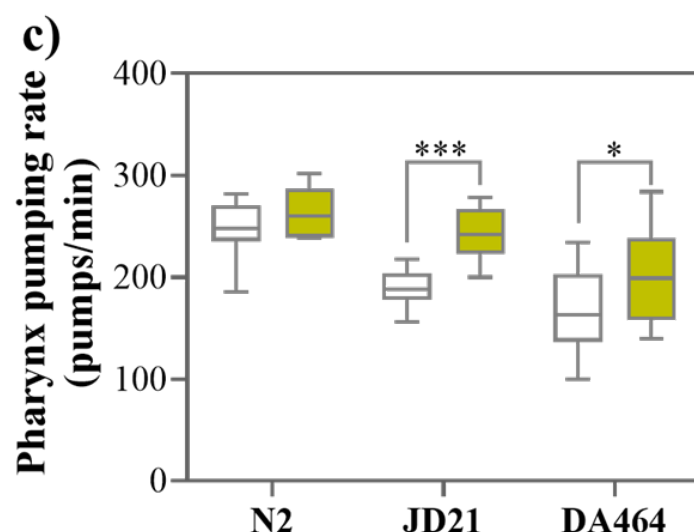


Figure 8. Pharynx pumping rate upon treatment with Ppy NPs compared with untreated N2, JD21, and DA464 worms (N \approx 30).

4.3.2. Exposure Duration

We treated the N2 worms with PL or RE and measured the pharynx pumping rate for four different durations: 4, 6, 8, and 24 hours of exposure. The pumping rate as a function of exposure duration were also computed for JD21 and DA464 strains, to understand effect on different mutant strains (Figure 9, Table1). The change in pumping rate in treated worms compared to untreated worms is computed by normalising each value to the mean pumping rate of untreated worms. In the case of PL treatment, the change in pharynx pumping rate occurred earlier at 4 hours for N2 and DA464 worms, whereas for the JD21 strain, the change was rather gradual. The maximum decrease for all the strains was observed after 24 hours of treatment.

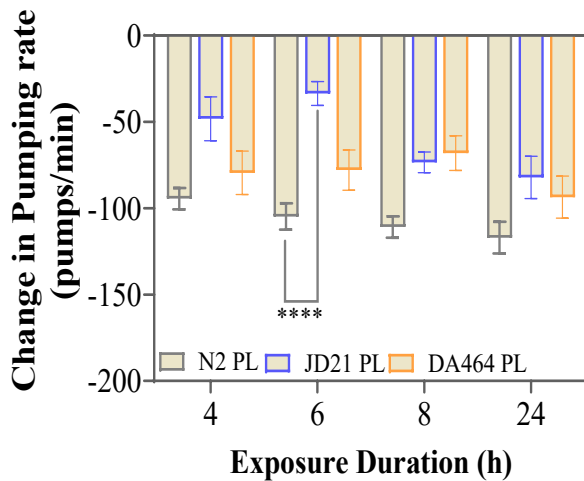


Table 1. Mean pumping rate of PL treated N2, JD21, and DA464 worms at different exposure durations.

PL	4h	6h	8h	24h
N2	93±34	87±40	75±36	63±24
JD21	100±46	109±22	74±19	64±30
DA464	68±40	57±37	62±30	64±30

Figure 9. The effect of treatment duration of PL in all the three strains: N2, JD21, and DA464, measured at 4, 6, 8, and 24 hours of exposure (N≈30).

The overall change in pumping rate after RE treatment was more for DA464 strain than the N2 and JD21 worms. The impact of RE was time-dependent in DA464 with the maximum increase between 4 hours and 6 hours, which was maintained nearly constant upto 24 hours. On the other hand, the wild-type worms also showed a time-dependent behaviour similar to DA464, but the maximum was attained at 24 hours unlike the 6 hours in DA464. For the JD21 strain, the increase occurred earlier at 4 hours of treatment and was maintained throughout at all the four exposure durations (Figure 10, Table 2).

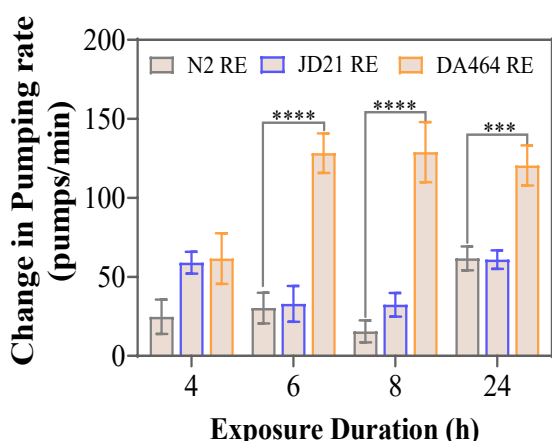


Table 2. Mean pumping rate of RE treated N2, JD21, and DA464 worms at different exposure durations.

RE	4h	6h	8h	24h
N2	225±45	233±34	229±24	269±51
JD21	199±31	162±54	186±38	205±32
DA464	209±62	263±50	259±60	278±40

Figure 10. The effect of treatment duration of RE in all the three strains: N2, JD21, and DA464, measured at 4, 6, 8, and 24 hours of exposure (N≈30).

The differential effect of Ppy NPs in pharynx pumping rate of JD21 and DA464 worms was more evident when we computed the pumping rate at different durations. The increase happened earlier for JD21 worms, at 4 hours, as well as much higher than the DA464 and N2 worms. The change in pumping rate was gradual and duration-dependent for JD21 strain, whereas for DA464, the change was maintained nearly the same between 6 and 24 hours (Figure 11, Table 3). The faster and higher increase of pumping rate in JD21 worms further suggests the possible role of Ppy NPs action could be mediated through calcium signalling.

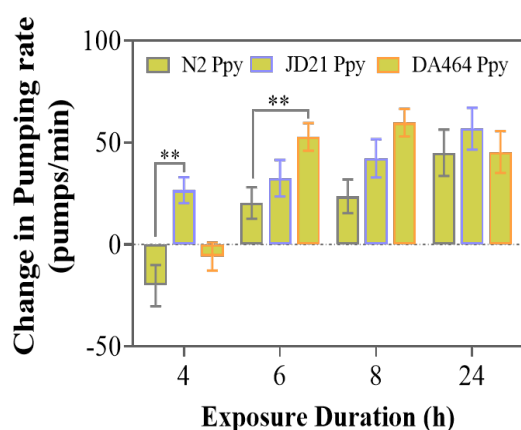


Table 3. Mean pumping rate of Ppy NP treated N2, JD21, and DA464 worms at different exposure durations.

Ppy NP	4h	6h	8h	24h
N2	199±38	223±29	238±31	255±48
JD21	174±26	175±31	190±30	203±29
DA464	142±21	187±21	190±21	203±29

Figure 11. The effect of treatment duration of Ppy NPs in all the three strains: N2, JD21, and DA464, measured at 4, 6, 8, and 24 hours of exposure (N≈30).

4.3.3. Excretion Duration

The optical transparency of *C. elegans* not only allows facile visualisation of the intestines and the ingested substances within, but also provides opportunity to follow the excretion of the ingested substances. The worms are beneficial for rapid and large-scale assessment of post-excretion effect since the resident time of ingested substances within the

worms is <10 minutes, accompanied with a fast metabolism. *C. elegans*, when fed with exclusive bacterial diet after stopping the exposure would excrete the ingested substance upon feeding. We exploited this tendency of the worms to study the effect of the drugs after terminating the exposure to understand the sustaining capacity of the drugs. While a small reduction in pharynx pumping rate could be still observed after excretion of PL for upto 24 hours, the worms returned to the basal rate at 72 hours (Figure 12a, Table 4).

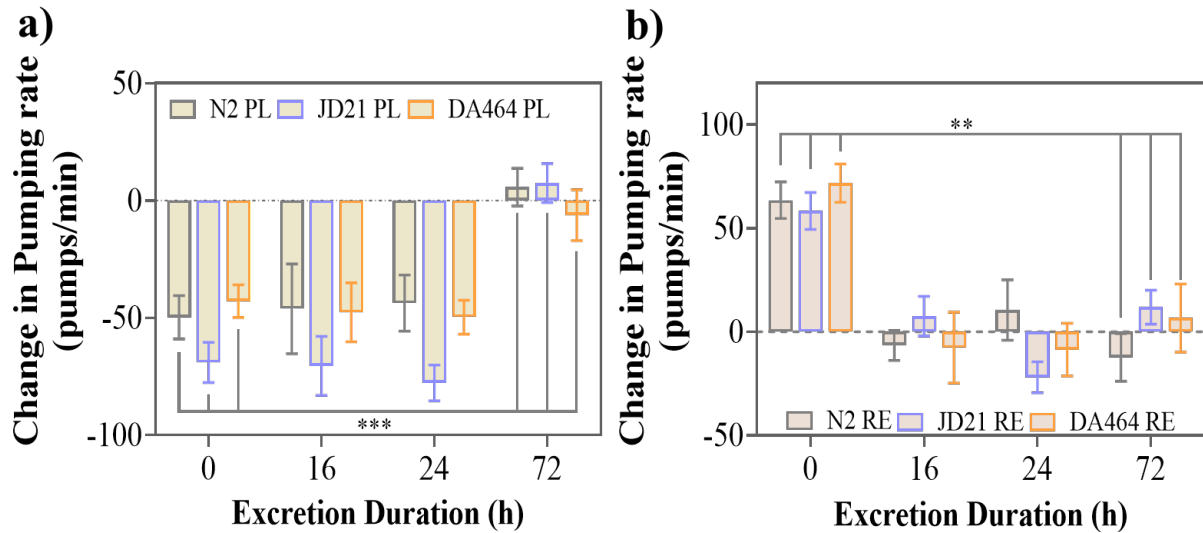


Figure 12. Change in pharynx pumping rate after excretion of ingested a) PL and b) RE, measured at 16, 24, and 72 hours of excretion in all the three strains (N \approx 30).

Table 4. Mean pumping rate of PL and RE treated N2, JD21, and DA464 worms at different exposure durations.

PL	0h	16h	24h	72h
N2	88 \pm 33	105 \pm 57	127 \pm 27	160 \pm 30
JD21	76 \pm 23	78 \pm 31	71 \pm 19	156 \pm 18
DA464	103 \pm 26	117 \pm 33	128 \pm 18	163 \pm 21

RE	0h	16h	24h	72h
N2	202 \pm 42	145 \pm 18	169 \pm 45	147 \pm 35
JD21	191 \pm 25	156 \pm 21	120 \pm 44	155 \pm 21
DA464	217 \pm 50	157 \pm 54	153 \pm 59	187 \pm 52

In the case of RE treatment, the pumping reached the basal rate at 16 hours post-excretion for both JD21 and DA464 worms, similar to the wild-type worms, suggesting the effect of RE on pharynx pumping rate might not be as strong as the effect of PL (Figure 12b, Table 4). The difference in the extent of impact between PL and RE also corroborates with the change in pumping rate at 24 hours of exposure, where we can observe that PL induces a more significant decrease than the increase caused by RE (Figure 7).

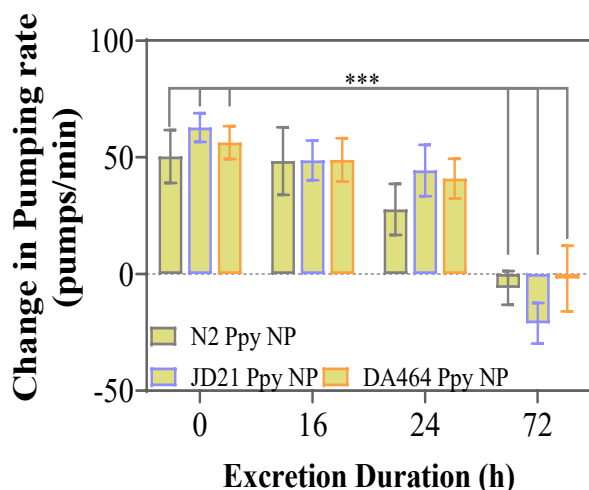


Table 5. Mean pumping rate of Ppy NP treated N2, JD21, and DA464 worms at different exposure durations.

Ppy NP	0h	16h	24h	72h
N2	189±42	200±46	198±38	157±30
JD21	209±41	197±23	195±27	127±21
DA464	216±39	213±28	219±27	179±31

Figure 13. Change in pharynx pumping rate after excretion of ingested Ppy NPs measured at 16, 24, and 72 hours of excretion in all the three strains (N≈30).

Ppy NPs increased the pharynx pumping rate of worms upon exposure and maintained this increase up to 24 hours post-excretion in JD21 and DA464 worms (Figure 13, Table 5). The effect caused by Ppy NPs, similar to PL, showed recovery 72 hours post-excretion. We did not observe any differential behaviour between the two strains in terms of post-excretion pharynx pumping rate. However, we found that the effects lasted longer in the mutant strains compared to wild-type, where the pumping rate started to decrease at 24 hours. The post-excretion results suggest a moderate lasting impact of Ppy NPs, indicating there could be some molecular interplay due to Ppy NPs treatment, that sustains the effect to some extent even after excretion.

4.4. Molecular effects

4.4.1. Calcium Signalling

The pharynx consists of corpus, isthmus, and terminal bulb, comprising muscle cells that are electrically coupled to each other, contracting and relaxing throughout the life of the worms²⁷. The contractions are initiated by excitation of the MC neurons which activates the acetylcholine receptors at the corpus, progressing through the isthmus and reaching the terminal bulb²⁸. Calcium (Ca^{2+}) plays a crucial role in the signal transductions between the contractile muscle cells regulating the pharyngeal pumping. The cells at resting state has a low cytosolic $[\text{Ca}^{2+}]$ and mitochondrial $[\text{Ca}^{2+}]$. The muscle cell depolarization causes activation of two types of voltage-gated calcium channels, the L-type and T-type Ca^{2+} channels which results in an influx of Ca^{2+} into the cytosol. The elevated cytosolic $[\text{Ca}^{2+}]$ further activates the ryanodine receptors (*unc-68*) at the sarcoplasmic reticulum within the posterior isthmus and terminal bulb through a calcium-induced calcium release mechanism, which prolongs the Ca^{2+}

rising phase. Upon repolarization, the voltage-gate potassium channels are activated, inducing closing of Ca^{2+} channels, returning the $[\text{Ca}^{2+}]$ levels to the resting state²⁷. Interestingly, several studies have reported that Ppy does influence the calcium transients within cardiac cells, imparting their effect on cardiac pumping^{25,26}. Bearing this in mind, we measured the Ca^{2+} transient levels in the pharynx, upon treatment with PL, Ppy and RE, to investigate whether these treatments affects pharyngeal pumping by influencing the calcium signalling.

4.4.2. Calcium Imaging

We employed fluorescent calcium imaging technique to quantify the calcium transients. Wild-type worms expressing the fluorescent Ca^{2+} sensor yellow cameleon protein YC2.1 in the pharynx, called as the AQ2038 strain are used for this experiment^{29–31}. The YC2.1 cDNA is integrated under the *myo-2* promoter expressed in the pharyngeal cytosol, with the sequence *pmyo-2::YC2.1*. The protein exhibits spectral changes upon calcium binding allowing monitoring of cytosolic $[\text{Ca}^{2+}]$ dynamics during pharyngeal pumping in the worms. We also crossed the JD21 strain with AQ2038 to produce JD21 expressing YC2.1 in pharyngeal cells (denoted as JD21- Ca^{2+}). Briefly, we crossed ten AQ2038 males with five JD21 hermaphrodites and maintained at 20°C for four to six days. The first cross, that is F1 generation adult worms (males) are picked from day 3 and crossed again with JD21 hermaphrodites, producing second cross. The process is repeated until fifth cross, and fluorescent hermaphrodites were genotyped to verify the JD21 mutation (*cca-1* deletion) and whether the fluorescent probe is incorporated.

The AQ2038 and the obtained JD21- Ca^{2+} worms were treated with PL and RE (100 μM), and Ppy NPs (100 $\mu\text{g/mL}$) concentrations at 20 °C, for 24 hours. After the exposure, the worms were cleaned with M9 and immobilized on 1% agar pads containing bacteria, using glue (Dermabond Topical Skin Adhesive, Johnson & Johnson, New Brunswick, NJ, USA). The agar pad is mounted in a chamber (Warner Instrument RC-25) (Figure 14a, sample chamber), 10 μL of PL or RE or Ppy NPs is added prior to measurement to stimulate pharynx pumping. The probes were excited at 430 nm and the emitted fluorescence images were obtained at two emission wavelengths, 480 and 535 nm (Figure 14b).

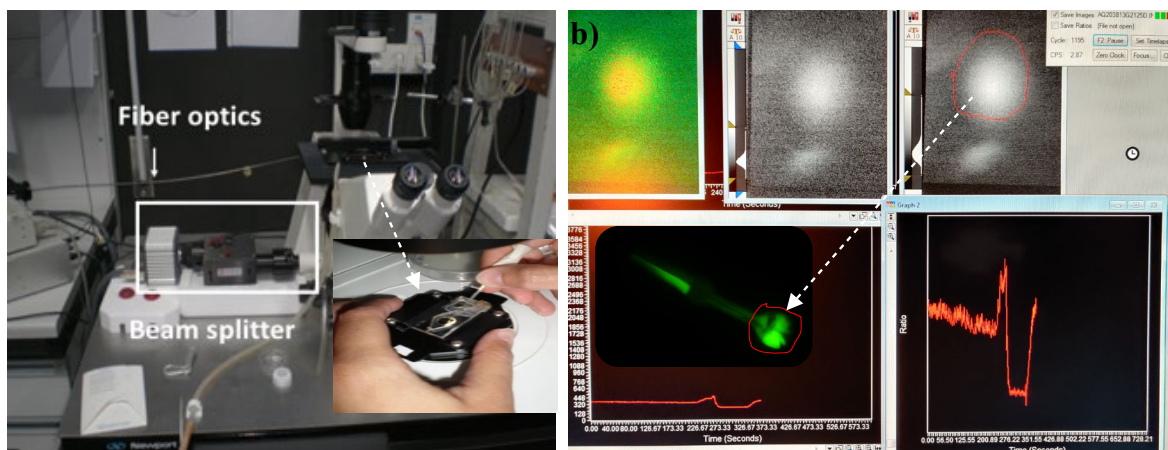


Figure 14. a) The sample chamber with *C. elegans* glued on agar pads, mounted on the fluorescence microscope sample stage, b) Snapshot of the pumping of the fluorescent pharynx and the calcium transient recordings.

The fluorescence emission patterns were recorded for 10 minutes for each worm and analyzed using the Metafluor program (Universal Imaging). The traces shown (Figure 14b, 15) were obtained as the ratio of the simultaneous images acquired at 535nm emission and 480nm emission (F535/F480). The emission spectra were then analyzed with a specific algorithm designed to calculate the width, intensity, and frequency of the Ca^{2+} peaks of each experiment³². The fluorescent peaks can be classified into two types: fast Ca^{2+} oscillations with sharp and narrow peaks called as “spikes” (Figure 15a, b, d), and prolonged peaks maintaining high Ca^{2+} for an extended period up to a few mins, resulting in “square-waves” (Figure 15c).

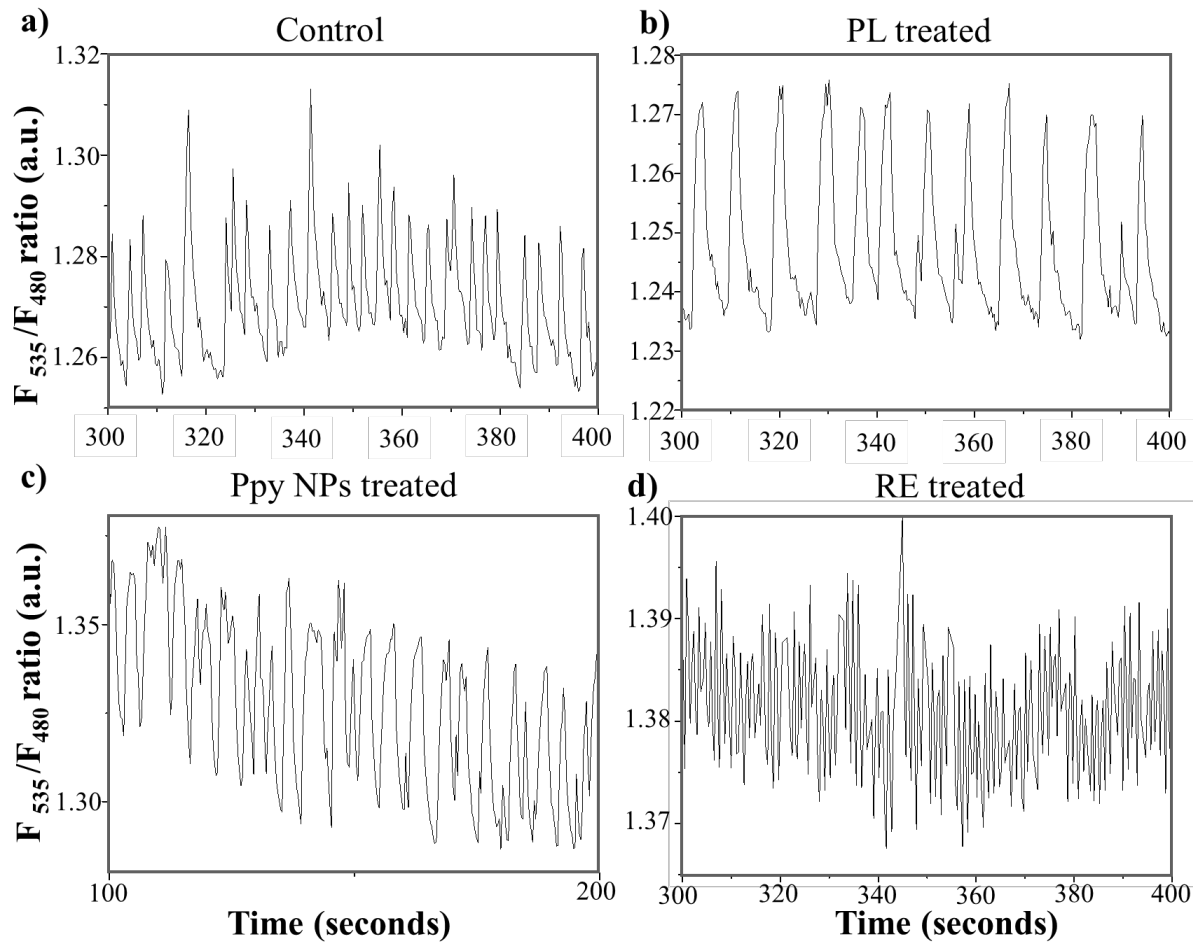


Figure 15. Calcium transient spikes recorded in a) untreated (control), b) PL treated, c) Ppy NPs treated, and d) RE treated worms.

Each peak represents an event of Ca^{2+} transport, therefore, higher frequency of spikes could signify a higher pumping rate. However, when the worms have been pumping at high rate for long time, they reach a fatigue state due to an energy depletion. During this state of energy depletion, a higher number of square waves are observed rather than sharp, narrow spikes, eventually resulting in lower frequency of spikes despite higher pumping rate. Four features of the calcium patterns were computed namely, the frequency of peaks, peak width at the baseline, peak width at half maximum, and peak height. Samples with more square peaks would exhibit a combination of lower frequency, equal or higher width at baseline and width at half maximum, and an equal or reduced peak height, compared to patterns with sharp and narrow spikes.

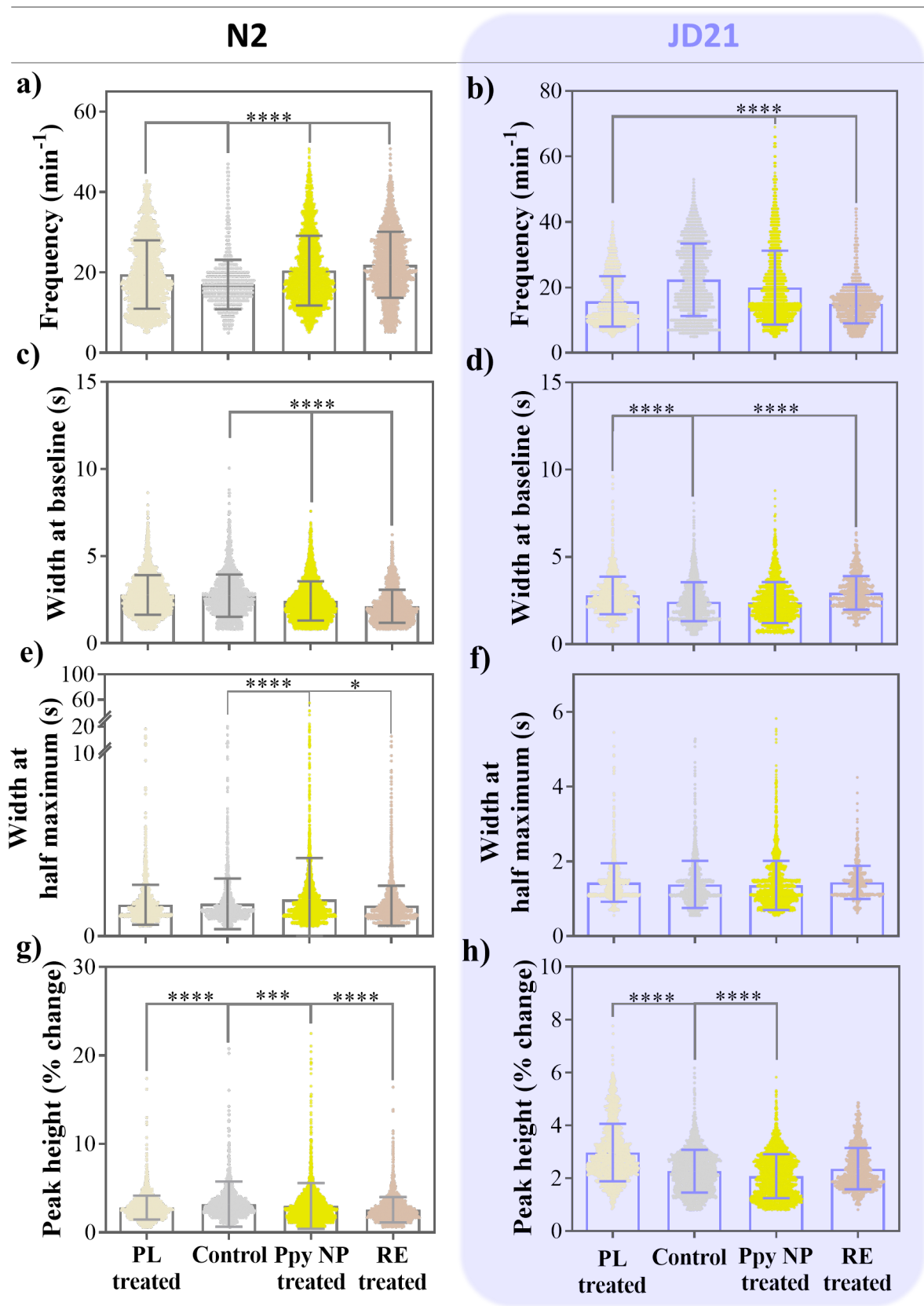


Figure 16. Quantification of the b) frequency of calcium transients, c) width at baseline, d) width at half maximum, and e) peak height of untreated (control), PL treated, RE treated, and Ppy NP treated worms in N2 and JD21 strains (N=20 worms).

The frequency of calcium transient peaks was higher for Ppy and RE treated worms and lower for PL treated worms when compared with untreated wild-type worms (Figure 16a), directly correlating with the increase or decrease in pharynx pumping rate observed. On the other hand, for the JD21 strain, the peak frequency decreased for Ppy and RE treated worms, suggesting a high number of square waves (Figure 16b). The peak width shows a corresponding increase in RE treated JD21 worms (Figure 16d), further confirming the presence of more square waves than untreated groups. Interestingly, the width at half maximum increased in Ppy treated wild-type worms (Figure 16e) also indicating the square waves, while it remained unchanged in the JD21 worms (Figure 16f). The peak height is not necessarily a direct indicator of square waves, but the square peaks could generally exhibit a lower height than sharp spikes, which when combined with the other parameters, could signify the presence of square waves. We observed a reduced peak height in Ppy and RE treated worms and increased peak height in PL treated worms of both the strains (Figure 16f, g), also pointing to the square waves.

To summarize, the peak parameters such as frequency, width, and height indicated that Ppy and RE treatments increase the calcium transients, whereas PL treatment reduces it, agreeing with the effect of the treatments on pharynx pumping rate. After Ppy treatment, the width at baseline and half maximum did not increase for the JD21 worms, which has a deletion mutation at the T-type Ca^{2+} channel *cca-1* (Figure 16d, f), as much as the wild-type worms (Figure 16c, e). The different response to Ppy NPs on wild-type and *cca-1* deleted strain suggests that the T-type Ca^{2+} channel *cca-1* plays a central role in the effect of Ppy NPs treatment.

4.5. Conclusions

PL and RE are commonly used drugs well known to induce a decrease and an increase in cardiac pumping rate in humans, respectively. We tested the effect of these two drugs in *C. elegans* to evaluate whether they could reproduce the same in effects in the pharynx pumping rate of the worms. Preliminary toxicity evaluations such as survival, development, and reproduction at 100 μM concentration proved that both the drugs are safe to be examined in *C. elegans*. We found that PL decreases while RE increases the pharynx pumping rate of the worms, validating that *C. elegans* can be utilised to measure the pumping rates of novel drugs and nanomaterials, to infer their possible anti-arrhythmic effects in humans. We also incorporated two mutant strains, JD21 and DA464, with orthologous mutations implicated in cardiac arrhythmia and exhibiting slow pharynx pumping rate. We found that PL, RE, and Ppy

NPs induces the expected effect in the pharynx pumping rate of mutant strains: PL decreases whereas RE and Ppy NPs increases the pumping rate. The change in pharynx pumping rate induced by Ppy NPs treatment in JD21 strain was fast as well as strong compared to N2 and DA464. Since JD21 possesses a deletion mutation in the L-Type voltage gated calcium channel *cca-1*, we postulated that the treatment of Ppy NPs could somehow normalize the impaired calcium signalling, thus regulating the pumping rate. To scrutinize this, we quantified the pharyngeal calcium transient levels of untreated and treated worms and found that the elevation in calcium transients were more obvious in wild-type compared to the JD21 strain, which has a loss-of-function mutation in *cca-1* channel. Therefore, we conclude that the molecular mechanistic action of Ppy NPs in affecting the pumping rate depends on intracellular calcium signalling, mediated through voltage-gated calcium channels.

References

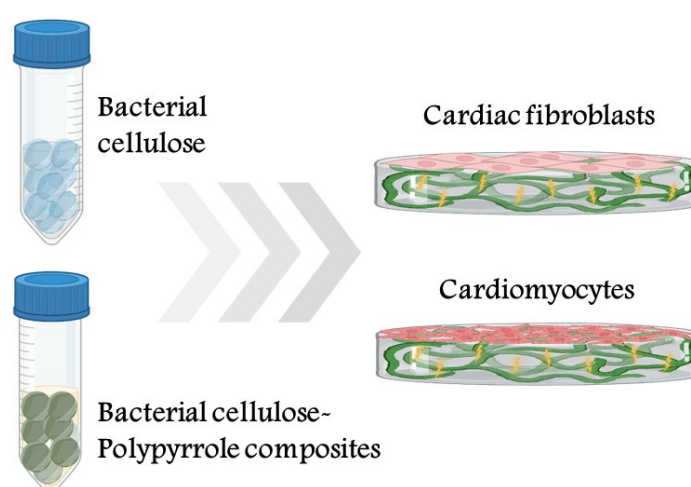
- (1) Martínez-Milla, J.; Raposeiras-Roubín, S.; Pascual-Figal, D. A.; Ibáñez, B. Role of Beta-Blockers in Cardiovascular Disease in 2019. *Revista Española de Cardiología (English Edition)* **2019**, 72 (10), 844–852.
- (2) Wang, D. W.; Mistry, A. M.; Kahlig, K. M.; Kearney, J. A.; Xiang, J.; George, A. L. Propranolol Blocks Cardiac and Neuronal Voltage-Gated Sodium Channels. *Front Pharmacol* **2010**, DEC.
- (3) Choppin, A.; O'Connor, S. E. Presence of Vasoconstrictor 5HT₁-like Receptors Revealed by Precontraction of Rabbit Isolated Mesenteric Artery. *Br J Pharmacol* **1995**, 114 (2), 309–314.
- (4) Bailey, S. R.; Elliott, J. Evidence for Different 5-HT(1B/1D) Receptors Mediating Vasoconstriction of Equine Digital Arteries and Veins. *Eur J Pharmacol* **1998**, 355 (2–3), 175–187.
- (5) Petersen, K. K.; Andersen, H. H.; Tsukamoto, M.; Tracy, L.; Koenig, J.; Arendt-Nielsen, L. The Effects of Propranolol on Heart Rate Variability and Quantitative, Mechanistic, Pain Profiling: A Randomized Placebo-Controlled Crossover Study. *Scand J Pain* **2018**, 18 (3), 479–489.
- (6) Lepeschkin, E.; Marchet, H.; Schroeder, G.; Wagner, R.; de Paula e Silva, P.; Raab, W. Effect of Epinephrine and Norepinephrine on the Electrocardiogram of 100 Normal Subjects*. *Am J Cardiol* **1960**, 5 (5), 594–603.
- (7) Leenen, F. H. H.; Chan, Y. K.; Smith, D. L.; Reeves, R. A. Epinephrine and Left Ventricular Function in Humans: Effects of Beta-1 vs Nonselective Beta-Blockade. *Clin Pharmacol Ther* **1988**, 43 (5), 519–528.
- (8) Avery, L.; Shtonda, B. B. Food Transport in the *C. Elegans* Pharynx. *Journal of Experimental Biology* **2003**, 206 (14), 2441–2457.
- (9) Velasco, M.; Hurt, E.; Urbina-quintana, A.; HERNANDEZ-PIEREITI, O.; Feldstein, E.; Camejo, G. *Effects of Prazosin and Propranolol on Blood Lipids and Lipoproteins in Hypertensive Patients*.
- (10) Nielsen, B. L.; Jørgensen, F. S. Propranolol (Inderal) in Cardiac Arrhythmias. *Acta Med Scand* **1966**, 180 (5), 631–638.
- (11) Thakur, A.; Alam, M. J.; Ajayakumar, M. R.; Ghaskadbi, S.; Sharma, M.; Goswami, S. K. Norepinephrine-Induced Apoptotic and Hypertrophic Responses in H9c2 Cardiac Myoblasts Are Characterized by Different Repertoire of Reactive Oxygen Species Generation. *Redox Biol* **2015**, 5, 243–252.
- (12) Manveen K. Gupta; T.V. Neelakantan; Mishra Sanghamitra; Rakesh K. Tyagi; Amit Dinda; Subir Maulik; Chinmay K. Mukhopadhyay; Shyamal K. Goswami. An assessment of the role of reactive oxygen species and redox signaling in norepinephrine-induced apoptosis and hypertrophy of h9c2 cardiac myoblasts. *Antioxid redox signal* **2006**, 8 (5 & 6), 1081–1093.

- (13) Álvarez-Diduk, R.; Galano, A. Adrenaline and Noradrenaline: Protectors against Oxidative Stress or Molecular Targets? *Journal of Physical Chemistry B* **2015**, *119* (8), 3479–3491.
- (14) Rietman, A.; Schwarz, J.; Blokker, B. A.; Siebelink, E.; Kok, F. J.; Afman, L. A.; Tomé, D.; Mensink, M. Increasing Protein Intake Modulates Lipid Metabolism in Healthy Young Men and Women Consuming a High-Fat Hypercaloric Diet. *Journal of Nutrition* **2014**, *144* (8), 1174–1180.
- (15) Wang, K.; Peng, X.; Yang, A.; Huang, Y.; Tan, Y.; Qian, Y.; Lv, F.; Si, H. Effects of Diets with Different Protein Levels on Lipid Metabolism and Gut Microbes in the Host of Different Genders. *Front Nutr* **2022**, *9* (June), 1–11.
- (16) El Khoury, D.; Anderson, G. H. Recent Advances in Dietary Proteins and Lipid Metabolism. *Curr Opin Lipidol* **2013**, *24* (3), 207–213.
- (17) Oliveros, L. B.; Videla, A. M.; Giménez, M. S.; Gimenez, A. M. S. *Effect of Dietary Fat Saturation on Lipid Metabolism, Arachidonic Acid Turnover and Peritoneal Macrophage Oxidative Stress in Mice*; 2004; Vol. 37.
- (18) Kramer, J. H.; Spurney, C. F.; Iantorno, M.; Tziros, C.; Chmielinska, J. J.; Mak, I. T.; Weglicki, W. B. D-Propranolol Protects Against Oxidative Stress and Progressive Cardiac Dysfunction in Iron Overloaded Rats. *Can J Physiol Pharmacol* **2012**, *90* (9), 1257–1268.
- (19) Taprantzi, D.; Zisimopoulos, D.; Thomopoulos, K. C.; Spiliopoulou, I.; Georgiou, C. D.; Tsiaoussis, G.; Triantos, C.; Gogos, C. A.; Labropoulou-Karatza, C.; Assimakopoulos, S. F. Propranolol Reduces Systemic Oxidative Stress and Endotoxemia in Cirrhotic Patients with Esophageal Varices. *Ann Gastroenterol* **2018**, *31* (2), 224–230.
- (20) Ranasinghe, H. N.; Fernando, N.; Handunnetti, S.; Weeratunga, P. N.; Katulanda, P.; Rajapakse, S.; Galappaththy, P.; Constantine, G. R. The Impact of Propranolol on Nitric Oxide and Total Antioxidant Capacity in Patients with Resistant Hypertension - Evidence from the APPROPRIATE Trial. *BMC Res Notes* **2020**, *13* (1), 10–14.
- (21) Shaye, D. D.; Greenwald, I. Ortholist: A Compendium of C. Elegans Genes with Human Orthologs. *PLoS One* **2011**, *6* (5).
- (22) Vaidyanathan, R.; Reilly, L.; Eckhardt, L. L. Caveolin-3 Microdomain: Arrhythmia Implications for Potassium Inward Rectifier and Cardiac Sodium Channel. *Frontiers in Physiology*. Frontiers Media S.A. November 9, 2018.
- (23) Balijepalli, R. C.; Kamp, T. J. Caveolae, Ion Channels and Cardiac Arrhythmias. *Progress in Biophysics and Molecular Biology*. October 2008, pp 149–160.
- (24) Guo, Y. H.; Yang, Y. Q. Atrial Fibrillation: Focus on Myocardial Connexins and Gap Junctions. *Biology*. MDPI April 1, 2022.
- (25) Cui, Z.; Ni, N. C.; Wu, J.; Du, G. Q.; He, S.; Yau, T. M.; Weisel, R. D.; Sung, H. W.; Li, R. K. Polypyrrole-Chitosan Conductive Biomaterial Synchronizes Cardiomyocyte

- Contraction and Improves Myocardial Electrical Impulse Propagation. *Theranostics* **2018**, 8 (10), 2752–2764.
- (26) Spearman, B. S.; Hodge, A. J.; Porter, J. L.; Hardy, J. G.; Davis, Z. D.; Xu, T.; Zhang, X.; Schmidt, C. E.; Hamilton, M. C.; Lipke, E. A. Conductive Interpenetrating Networks of Polypyrrole and Polycaprolactone Encourage Electrophysiological Development of Cardiac Cells. *Acta Biomater* **2015**, 28, 109–120.
 - (27) Shimozone, S.; Fukano, T.; Kimura, K. D.; Mori, I.; Kirino, Y.; Miyawaki, A. Slow Ca^{2+} Dynamics in Pharyngeal Muscles in *Caenorhabditis Elegans* during Fast Pumping. *EMBO Rep* **2004**, 5 (5), 521–526.
 - (28) Trojanowski, N. F.; Raizen, D. M.; Fang-Yen, C. Pharyngeal Pumping in *Caenorhabditis Elegans* Depends on Tonic and Phasic Signaling from the Nervous System. *Sci Rep* **2016**, 6.
 - (29) Nagai, T.; Yamada, S.; Tominaga, T.; Ichikawa, M.; Miyawaki, A.; Tsien, R. Y. Expanded Dynamic Range of Fluorescent Indicators for Ca^{2+} by Circularly Permuted Yellow Fluorescent Proteins. *Proceedings of the National Academy of Sciences of United States of America* **2004**, 101 (29), 10554–10559.
 - (30) Kerr, R.; Lev-Ram, V.; Baird, G.; Vincent, P.; Tsien, R. Y.; Schafer, W. R. Optical Imaging of Calcium Transients in Neurons and Pharyngeal Muscle of *C. Elegans*. *Neuron* **2000**, 26, 583–594.
 - (31) Alvarez-Illera, P.; Sanchez-Blanco, A.; Lopez-Burillo, S.; Fonteriz, R. I.; Alvarez, J.; Montero, M. Long-Term Monitoring of Ca^{2+} Dynamics in *C. Elegans* Pharynx: An in Vivo Energy Balance Sensor. *Oncotarget* **2016**, 7 (42), 67732–67747.
 - (32) Pilar Álvarez Illera. Calcium Dynamics in *Caenorhabditis Elegans* Pharynx, Instituto de Biomedicina y Genética Molecular (IBGM), 2018.

Chapter 5

Development and *in-vitro* evaluation of Polypyrrole-Bacterial Cellulose biomaterial scaffolds



PREFACE

The promising results of polypyrrole nanoparticles (Ppy NPs) tested in *C. elegans* inspired us to investigate the effect of Ppy NPs in cardiac cells by designing a composite with bacterial cellulose films (BC-Ppy). This chapter will discuss the synthesis, complete characterization, and evaluation of BC-Ppy films as potential cardiac tissue engineering scaffolds. BC-Ppy composites were characterized for size, morphology, surface roughness, chemical structure, and thermal and optical properties. Likewise, properties such as chemical composition, mechanical strength, and electrical conductivity of the films were evaluated as a function of Ppy concentration. Lastly, examination of BC-Ppy in human cardiac fibroblasts and mouse H9c2 cardiomyoblast cells for viability, attachment, and initiation of cell maturation provides further insight into their effective design and function for applications in human cardiac therapies.

Index

5.1. Bacterial cellulose as scaffold materials.....	129
5.2. BC and BC-Ppy materials used for <i>in-vitro</i> evaluation	132
5.2.1 BC synthesis protocol	132
5.2.2 BC-Ppy Synthesis protocol	133
5.3. Characterization of BC and BC-Ppy films	134
5.3.1 Physicochemical characteristics	134
5.3.2 Microstructure, size, and morphology	135
5.3.3 Surface topography	136
5.3.4 Chemical Structure and Composition	137
5.3.5 Thermal and Optical properties.....	139
5.3.6 Electrical conductivity	140
5.3.7 Mechanical behavior	142
5.3.8 Surface wettability	145
5.3.9 Stability of BC-Ppy	146
5.4. Cardiac cell types used for in-vitro evaluation.....	147
5.4.1. Cardiac Fibroblasts	147
5.4.2. Immortalized cardiomyocyte models	148
5.5. Material selection and pre-conditioning	149
5.6. In-vitro cell culture assays.....	150
5.6.1. Cardiac Fibroblasts viability, attachment, and morphology	150
5.6.2. By-product toxicity of scaffolds in H9c2 cell media	151
5.6.3. H9c2 cell viability and attachment.....	151
5.6.4. H9c2 cell Morphology	152
5.6.5. H9c2 maturation.....	156
5.7. Conclusions.....	161

5.1. Bacterial cellulose as scaffold materials

The design of cardiac tissue engineering scaffolds with Ppy NPs requires a reinforcing component. Bacterial cellulose (BC) is the most abundant naturally producing biopolymer on earth¹. BC is a highly biocompatible material with excellent flexibility, mechanical strength, surface wettability, and the ability to conjugate with various other biomaterials to yield multi-functional composites².

The most extensively studied biomedical application of BC is as a scaffold material for tissue engineering and regeneration^{74,75}, because in addition to biocompatibility, flexibility, and favourable mechanical properties, the fibrous morphology of thin and long fibers interconnecting with each other in random alignment mimics the native extracellular matrix (ECM)⁷⁶. Especially, the dimensions of BC fibers are closely similar to that of collagen fibrils present in the ECM. The high elastic modulus, ability to form any shape and size giving rise to 3-D scaffolds⁷⁷, functionality to produce innumerable composite structures with other nanomaterials that can yield specific properties such as fluorescence, conductivity, absorption, magnetism etc. has made BC as one of the most popular materials for tissue engineering on par with materials like alginate, collagen and decellularized ECM^{74,75}.

In addition to the properties listed above that are useful for TE, BC has shown inherent capability to favor adhesion and propagation of certain cell types. Additionally, BC functionalized with progenitor cells are investigated for its potential in promoting tissue regeneration and repair⁷⁸. BC membranes are employed as tissue engineering scaffolds for hard tissues like bones and cartilage as well as soft tissues including skin, lungs, heart, nerves to name some⁷⁴ (Figure 1).

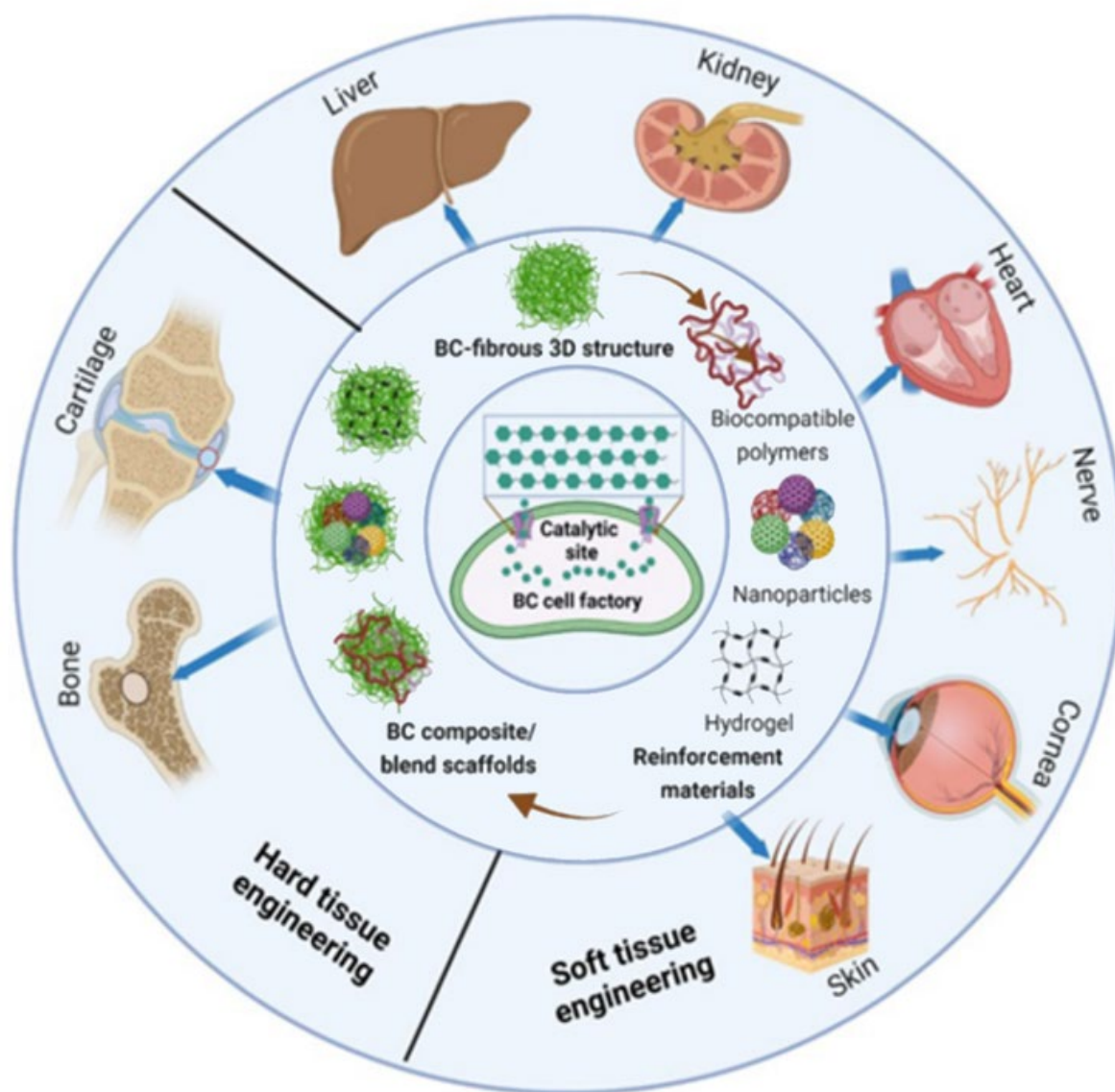


Figure 1. The application of BC and BC composites with NPs, hydrogels, and other polymers in hard tissue and soft tissue engineering⁷⁴.

Skin tissue engineering

The crucial properties of a scaffold material to be used for skin tissue engineering are flexibility, wound healing ability, moisturizing, anti-bacterial, and environmental protection^{73,74,79,80}. BC is intrinsically highly flexible imparting the ability to be used as effective dressing material for any region of the body. The water intake and water retention capacity of BC ensures that the skin is provided with enough moisture for wound healing. The porosity of BC surfaces and surface wettability is beneficial in extracting maximum efficacy of the additives and the high tensile strength (upto 260 MPa) and ductility ($\approx 32\%$ stretching strain) results in durability and stability of the material for wound dressings. Other properties like moisturizing, anti-microbial, anti-inflammatory, cell regeneration, etc. can be imparted by

functionalizing BC with drugs, chemicals or NPs. For example, BC functionalized with nanomaterials such as gold, silver NPs etc., imparts antimicrobial property to the material with prominent effect against popular pathogenic bacterial strains such as *Escherichia coli*, *Saccharomyces serviseae* and *Pseudomonas aeruginosa*^{81–83}, whereas crosslinking hyaluronic acid and BC matrix enhances its moisturizing and healing properties⁸⁴.

Bone tissue engineering

A biomaterial for bone tissue engineering must provide structural support for cell attachment, diffusion, migration, proliferation and differentiation⁸⁵. Therefore, biocompatibility, slow degradation, and high mechanical strength and stability of BC are seen as attractive properties that make them suitable for bone tissues⁸⁶. Additionally, three main properties are essential in a material: osteoinduction, osteoconduction, and osteointegration⁸⁷.

1. *Osteoconduction*: The material must be feasible for growth of new tissues on the surfaces and pores of the material and must be porous enough (pores > 100 µm) to allow transport of nutrients, gases and neovascularization to promote new bone formation (osteoconduction).
2. *Osteoinduction* refers to the ability of a material to recruit progenitor cells at the site of injury and promote new bone formation. The material must also be malleable to be applicable at sites of any sizes and shapes.
3. *Osteointegration* determines the implant stability, that is integration of the implant within the tissue, through a bone-to-implant surface contact and their interaction.

Addition of hydroxyapatite, bone marrow stem cells, proteins, and growth factors, has been reported to improve the efficacy of BC in bone repair by enhancing these osteo-specific properties^{88–90}.

Cardiac tissue engineering

A scaffold material for CTE should be biocompatible to all cell types of the cardiac tissue like fibroblasts, cardiomyocytes, endothelial cells, etc, porous to support cell adhesion and nutrient exchange, and possess suitable mechanical properties to withstand the shear force caused by blood flow and the repetitive contractile motions⁹¹. While BC exhibit all the above desirable properties, naked BC surfaces are not electrically conducting and does not provide a favourable environment for intercellular communication and electrical signal propagation. Consequently, composites of BC with other materials are employed as scaffolds for the treatment of MI.

Hydrogels consisting of decellularized ECM (dECM) and cellulose are biologically active, since they contain growth factors that can influence cell behaviors such as attachment, migration, proliferation and differentiation. The dECM hydrogel is injectable and polymerizes at physiological temperature conforming to the shape of the site of injury⁹². Furthermore, addition of progenitor cells is a promising approach to promote cardiomyocyte regeneration. In a recent preclinical study of BC patches for cell therapy of MI, BC co-cultured with bone marrow mesenchymal stem cells and skeletal muscle cells was implanted onto infarction induced wistar rats. The authors found that the cells adhered well onto the BC membrane, attain skeletal morphology, remarkable proliferation, and angiogenesis, suggesting an enhanced cardiac regeneration⁷⁸. Nevertheless, BC lacks inherent electrical conductivity necessary to coordinate intercellular communication among cardiomyocytes and regulate the cell beating. Incorporating Ppy NPs onto the BC films imparts conductivity to the scaffolds necessary for improved cardiomyocyte function.

5.2. BC and BC-Ppy materials used for *in-vitro* evaluation

We examined the possibility of producing Bacterial cellulose-Polypyrrole (BC-Ppy) composites with controllable material properties suitable for cardiac tissue engineering through in-situ polymerization of Ppy NPs in the presence of pre-synthesized BC films.

5.2.1. BC synthesis protocol

Our group has several years of expertise in producing BC under different experimental conditions with various structures and diverse properties³⁻⁵ and primarily utilizes them for biomedical applications, especially tissue engineering^{6,7}. In this thesis, we followed the production protocol previously optimized in the group by Soledad Roig⁴. *Komagataeibacter xylinus* strain (NCIMB 5346) purchased from CECT, Valencia, Spain, naturally produce BC films between media and air as a protective layer. The bacterial strain was cultured and maintained in Hestrin-Schramm (HS) agar plates at 4 °C in the refrigerator (Passage 2). Serial passages (Px) were made in liquid HS media culture until P4; BC was cultivated and harvested from P5. Briefly, 0.5 mL media containing P3 *K. xylinus* was inoculated in 4.5 mL fresh media and allowed to grow at 30 °C for 7 days (Figure 2a); this resulted in P4 bacteria (Figure 2b). Then, the bacterial solution was diluted with fresh media in a 1:14 ratio and cultured in a 24-well plate with 200 µL in each well and allowed to grow for 3 days or until an evident growth

of BC films on top of each well with nearly uniform thickness was observed after 3-5 days (Figure 2c).

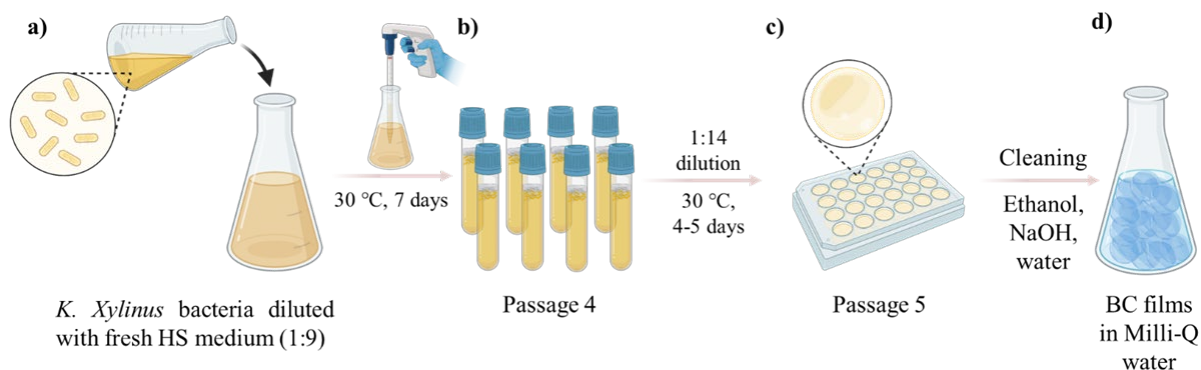


Figure 2. Schematic representation of the protocol for bacterial cellulose (BC) production from P3 to P5 and cleaning.

The resulting BC films undergo extensive cleaning to ensure the removal of all the bacteria and debris. The films were separated from bacteria using sterile tweezers and boiled in 1:1 water: ethanol mixture with continuous stirring for 40 mins. The films are rinsed, the solvent is changed, and the process is repeated until the supernatant becomes colorless (mostly 2 times). Next, BC films were washed twice in 0.1 M NaOH solution for 20 mins each, and in boiling water for 20 mins, twice with a change of water each time. If the pH is not neutral, the films are rinsed several times in surplus Milli-Q water at room temperature with continuous stirring and solvent change until a neutral pH is achieved (Figure 2d). The BC films are then redispersed in fresh Milli-Q water, autoclaved at 120 °C for 30 mins, and stored at room temperature for future use.

5.2.2. BC-Ppy Synthesis protocol

The as-synthesized BC films were utilized after complete washing and sterilization. The oxidant (Ferric chloride ($\text{FeCl}_3 \cdot 6\text{H}_2\text{O}$)) and surfactant (Polyvinyl alcohol (PVA)) concentrations, and the reaction conditions were same as described in Chapter 2 i.e., oxidant:monomer was 2.4:1, and 7.5 % (w/w of monomer) PVA was used, with a polymerization duration of 4 hours.

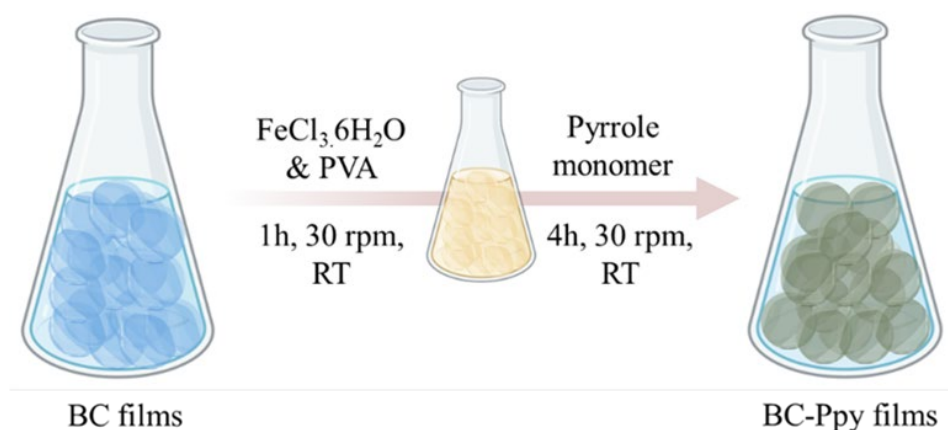


Figure 3. In-situ oxidative polymerization synthesis of Ppy NPs in presence of pre-synthesized BC films, to produce BC-Ppy films.

BC-Ppy films of varying amounts of Ppy were prepared by modifying the initial concentration of monomer added. Six concentrations of monomer: 1, 3, 5, 10, 50, and 100 mM, were used to produce BC-Ppy with a range of Ppy content and hereafter will be referred to as BP1, BP3, BP5, BP10, BP50, and BP100, respectively. For instance, for preparing BP100, 0.1 M pyrrole monomer should be employed. Therefore, in a 50 mL falcon tube, 0.24 M FeCl₃.6H₂O and 7.5% PVA were dissolved in 10 mL Milli-Q water. Five BC films were added and incubated for an hour in an orbital shaker at 50 rpm at room temperature to allow the precursors to penetrate the BC structures. Then, the pyrrole monomer was added slowly into the tubes under shaking to ensure uniform mixing of the monomer with the reaction solution. The oxidant and surfactant concentrations were adjusted according to the monomer concentration. The polymerization was continued for 4 hours, after which the films were washed 3-4 times by solvent exchange and shaking until a clear supernatant was obtained (Figure 3). After 4 hours, we obtained black coloured films (BP100), which indicated the effective incorporation of Ppy NPs on to the BC matrix. The in-situ oxidative polymerization of Ppy nanoparticles in the presence of pre-synthesized BC films was successful and reproducible. The BC-Ppy films are dried between Teflon plates with a 1 kg weight on top at room temperature for 1-2 days.

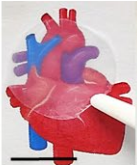

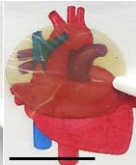
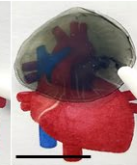






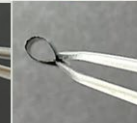

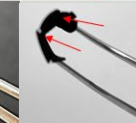

5.3. Characterization of BC and BC-Ppy films

5.3.1. Physicochemical characteristics

The synthesis method yielded BC-Ppy films with uniform distribution of Ppy NPs throughout the BC films. After washing and drying, the synthesized BC and BC-Ppy films

were circular with a diameter of ≈ 1.5 cm, varying thickness (10-160 μm), and an average weight of 1.46 mg (BC) and 1.62 mg (BP100). The films are transparent at lower Ppy content with shades of greenish brown. Even at the lowest concentration of 1 mM, Ppy NPs are uniformly distributed through the entire film without leaving blotches of Ppy accumulation (Table 1).

Table 1. Physicochemical properties: Thickness, transparency, and flexibility of BC and BC-Ppy composite films.

Sample	BC	BP1	BP3	BP5	BP10	BP50	BP100
[Py] (mM)	0	1	3	5	10	50	100
Thickness (μm)	11.0 ± 1.3	13 ± 2.6	17.9 ± 1.8	25.8 ± 5.1	44.9 ± 15.8	113.2 ± 25.7	139.8 ± 27.9
Conductivity (S/cm)	0	1.7×10^{-8}	3.2×10^{-5}	7.0×10^{-3}	0.02 ± 0.01	2 ± 1	3 ± 1
Colour & Transparency							
Flexibility							

The flexibility of the films was reduced while increasing the amount of Ppy NPs. In contrast, the thickness of films increases with increasing Ppy content, clearly due to more Ppy NPs attaching to the fibers and filling up the pores of BC. Therefore, merely with visual observation, we could infer that adding Ppy NPs changes the properties of the films, such as transparency, thickness, color, and flexibility (Table 1).

5.3.2. Microstructure, size, and morphology

The morphology of BC-Ppy composites, the diameter of BC fibers, and the Ppy NPs attached to the fibers was studied from the SEM and TEM images. The dried films are densely packed with fibers and particles, making it difficult for the incident electron beam to pass through and produce informative images. Therefore, the films were sonicated obtaining BC fibers, dried and redispersed them in water to improve the microstructure visualization. SEM images (Figure 4a, b) show that the Ppy NPs were spherical, decorating the BC and well attached to the fibers. For TEM imaging, the sonicated suspension was dropped on copper grids and air-dried for 10 minutes before imaging. Higher resolution and magnification of TEM images show better the attachment of particles to the fibers and confirm the shape and structure of BC fibers and Ppy NPs (Figure 4d, e). Notably, despite severe sample processing, the

attachment of Ppy NPs to fibers was still intact. The Ppy NPs do not seem aggregated in one region of the film but rather spread uniformly throughout the fiber length. Individual Ppy NPs possibly dissociated from the films could not be found in the entire SEM and TEM sample holders, nor in the solution, indicating that Ppy NPs anchor to BC fibers through a strong chemical interaction. The diameter of BC fibers and that of Ppy NPs were found to be 65 ± 11 nm (BC fibers) and 83 ± 8 nm (NPs) (Figure 4c, f). We infer that the presence of BC fiber meshes controls the growth of Ppy NPs, resulting in smaller particles than Ppy NPs prepared solely in water which displayed a mean size of ≈ 131 nm (Chapter 2).

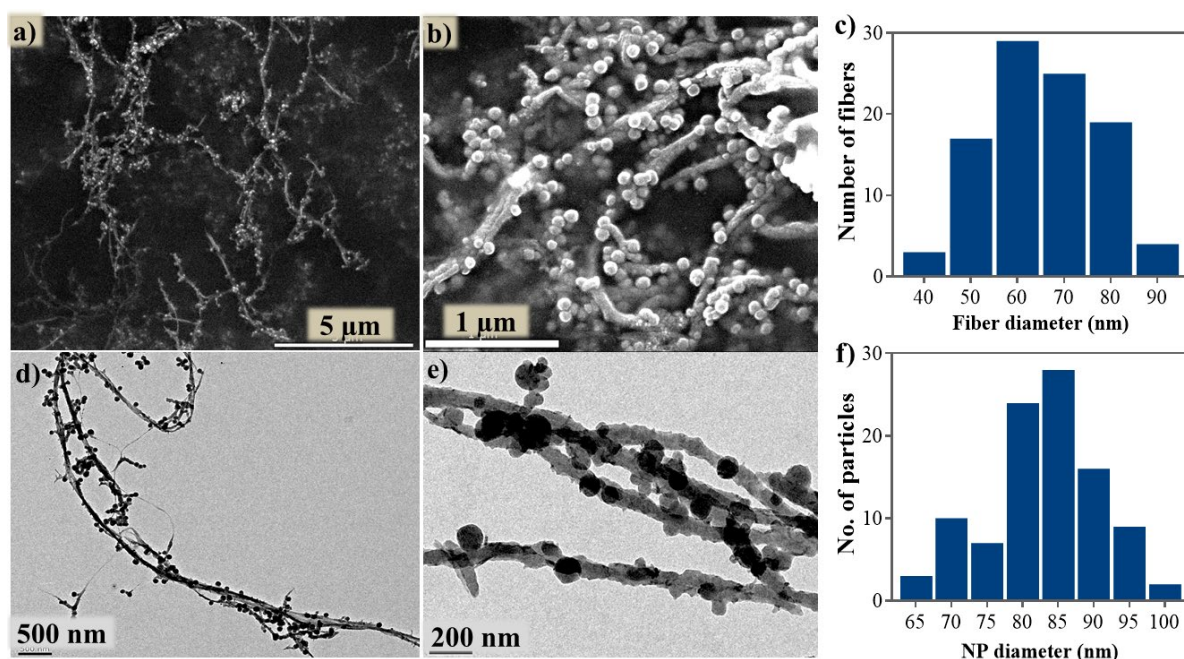


Figure 4. Size and morphology of Ppy decorated BC. a and b) SEM images at 20,000 X and 100,000 X, respectively; d and e) TEM images at 3000 X and 10000 X, respectively; and c and f) Size distribution of BC fibers (N=97) and Ppy NPs (N=99) plotted from TEM images.

5.3.3. Surface topography

The presence of nanoparticles on the surface of the films would influence the surface topography and, therefore, the roughness, an important material property that dictates cell attachment behavior⁷. As-synthesized BC and BC-Ppy composite films were left to dry on top of a glass slide at room temperature without any weight or teflon plates, ensuring that the films were well-adhered onto the glass slide and not detached or moved while the AFM probe scanned the samples. About 3 areas of 30x30 μm size from 3 different samples were scanned in tapping mode, and the mean surface roughness was calculated from the obtained images using Gwydion® software (Figure 5a, b). Indeed, the NP-containing BC-Ppy composites displayed higher roughness of ≈ 334 nm than BC films. Whereas the surface roughness of plain

BC films was only ≈ 130 nm (Figure 5c), validating that the NPs play a crucial role in the surface topography of the films. The spherical NPs bound onto the surface of the films were evident in the AFM image of the BC-Ppy composite (Figure 5b, grey arrows).

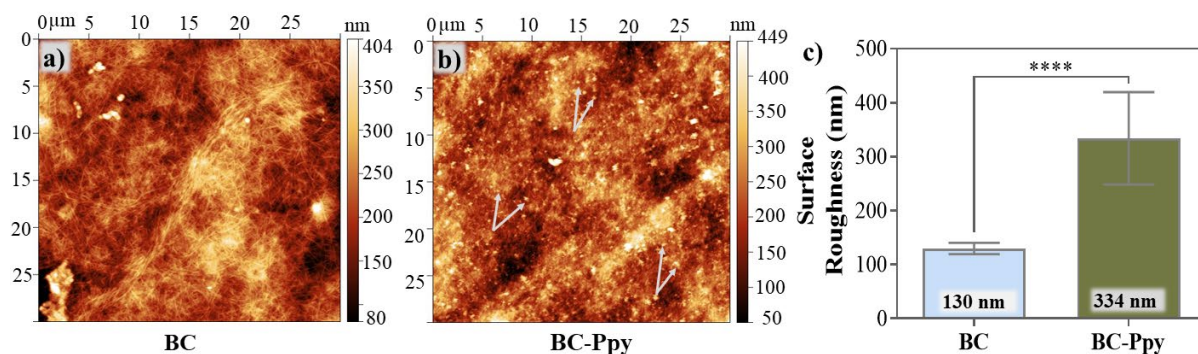


Figure 5. Topographical AFM images of a) BC and b) BC-Ppy surfaces, showing the decoration of Ppy NPs on BC surface (grey arrow) c) surface roughness of BC and BC-Ppy (N=9).

5.3.4. Chemical Structure and Composition

The chemical composition was assessed through CHN quantification, whereas the chemical structure and interaction between BC and Ppy were elucidated from FTIR spectroscopy. CHN analysis was performed with BC-Ppy films prepared from two different monomer concentrations, 10 mM and 100 mM, to investigate if changing the monomer concentration would impact the amount of Ppy yielded in the final material. Especially the estimation of nitrogen level directly indicates the amount of Ppy present since the BC component of the composite contains only trace Nitrogen. The films were blended and dried to obtain powders for the CHN analysis. We found a noticeable increase in the percentage of Nitrogen from $\approx 7\%$ at 10 mM to $\approx 12.7\%$ at 100 mM, similar to the bare Ppy NPs prepared with 100 mM pyrrole (Figure 6b).

Bacterial cellulose (BC) is present during the formation of Ppy, resulting in hydrogen bonding between the hydroxyl groups of BC and the amine groups of Ppy⁸ (Figure 6a). The plain BC and BC-Ppy composites were analyzed as dried stand-alone films. The scan was performed in Attenuated Total Reflectance-Fourier Transform Infrared (ATR-FTIR) mode in a Spectrophotometer Jasco 4700 instrument at a spectral range of $400\text{--}4000\text{ cm}^{-1}$ with 32 scans and a resolution of 4 cm^{-1} .

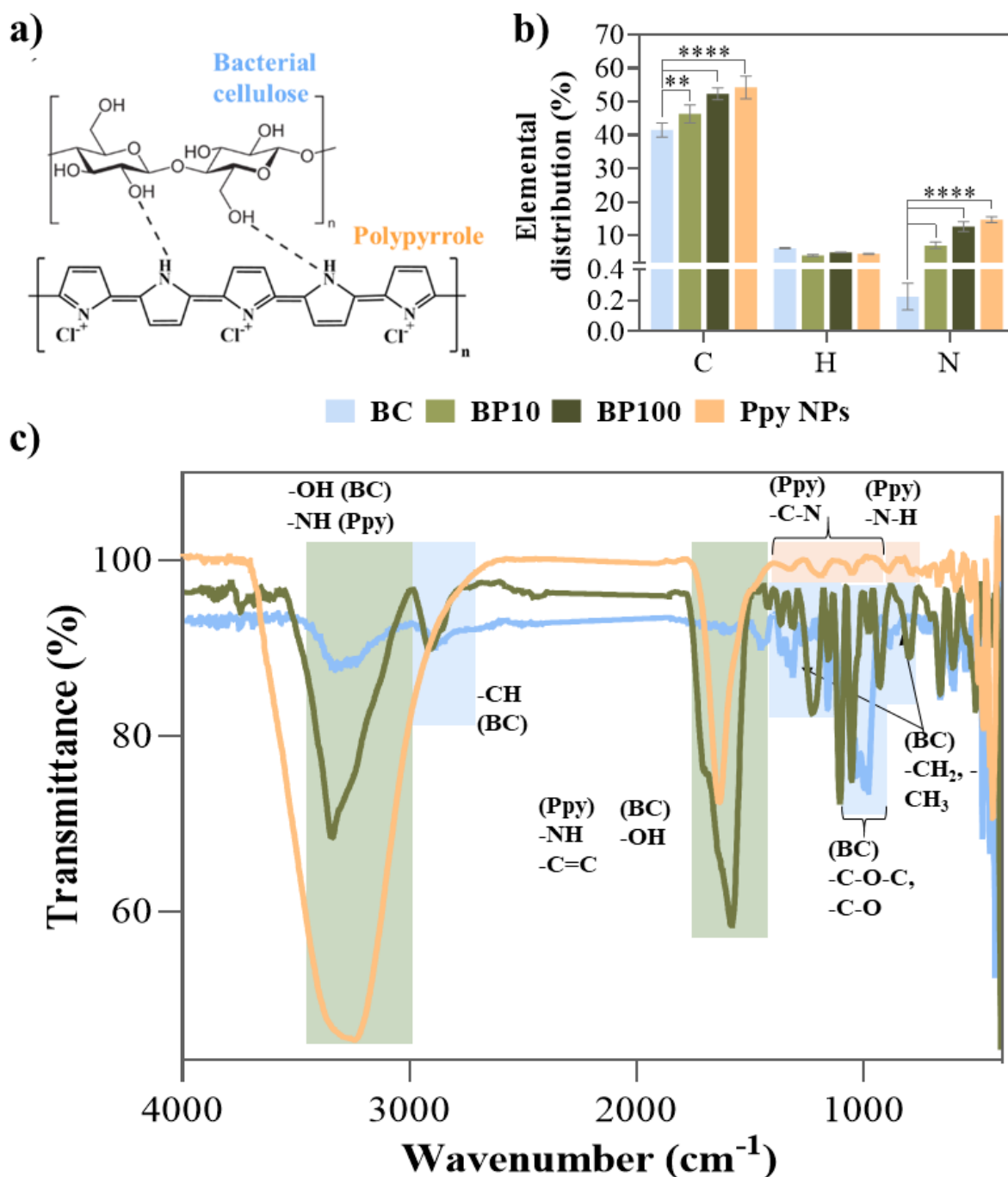


Figure 6. a) Formation of Ppy from pyrrole monomer, b) Carbon (C), Hydrogen (H), and Nitrogen (N) elemental composition, and c) FT-IR spectra of Ppy NPs with specific functional groups.

The most significant characteristic peaks are highlighted in blue (BC), orange (Ppy), and green (BC-Ppy) (Figure 6c). The -NH stretching from aromatic amines of Ppy (3311 cm^{-1}) and -OH stretching from hydroxyl groups of BC (3335 cm^{-1}) contribute to the intense and broad peaks in this region. The peak is shifted to 3393 cm^{-1} with a shoulder at 3245 cm^{-1} (marked with an arrow) for the BC-Ppy composites, pointing to hydrogen bonding between -OH of BC and -NH

of Ppy. The low-intensity peak at $\approx 2920\text{ cm}^{-1}$ in BC spectra occurs from the -CH stretching, also present in the BC-Ppy composites. The second prominent peak appears at $\approx 1635\text{ cm}^{-1}$ of Ppy spectra, owing to the -C=C alkene and -N-H bending. A weak band at $\approx 1611\text{ cm}^{-1}$ in the BC spectra can be noticed, attributed to -OH bending. Again, this peak is shifted to $\approx 1590\text{ cm}^{-1}$ in the BC-Ppy spectra due to hydrogen bonding. The series of small peaks in the region $\approx 1470 - 1200\text{ cm}^{-1}$ and $\approx 893\text{ cm}^{-1}$ is caused by C-H stretching of -CH₂ and -CH₃ groups in BC. These FT-IR spectra confirm the formation of Ppy NPs and BC films with specific functional groups as expected^{9,10}. The blue/red shift, change in peak shape, and appearance of shoulders in composites' -N-H and -OH region further validate the formation of hydrogen bond interaction between BC and Ppy and its chemical structure^{8,11-14}.

5.3.5. Thermal and Optical properties

The thermal stability of BC-Ppy was studied using thermogravimetric analysis (TGA) (Figure 7a). We found that Ppy NPs exhibit a more gradual thermal degradation than plain BC films. The degradation temperature at 50% weight loss (T50%) for BC was $330\text{ }^{\circ}\text{C}$ ¹⁶, whereas T50% for Ppy NPs was $410\text{ }^{\circ}\text{C}$ ¹⁵. In the case of BC-Ppy composites, adding Ppy NPs to the BC films increased the thermal stability resulting in an intermediate T50% of $360\text{ }^{\circ}\text{C}$. The thermal degradation of BC-Ppy occurs in two stages: the first significant weight loss around $360\text{ }^{\circ}\text{C}$ (T50%) due to the degradation of amorphous BC by depolymerization via glycosidic bond cleavage and the second degradation around $450\text{ }^{\circ}\text{C}$, attributed to the remnant polymeric chains⁸. To summarize, BC-Ppy materials showed good thermal stability up to temperatures as high as $250\text{ }^{\circ}\text{C}$, rendering suitability for sterilization by autoclave, storage at room temperature, and application in physiological temperatures.

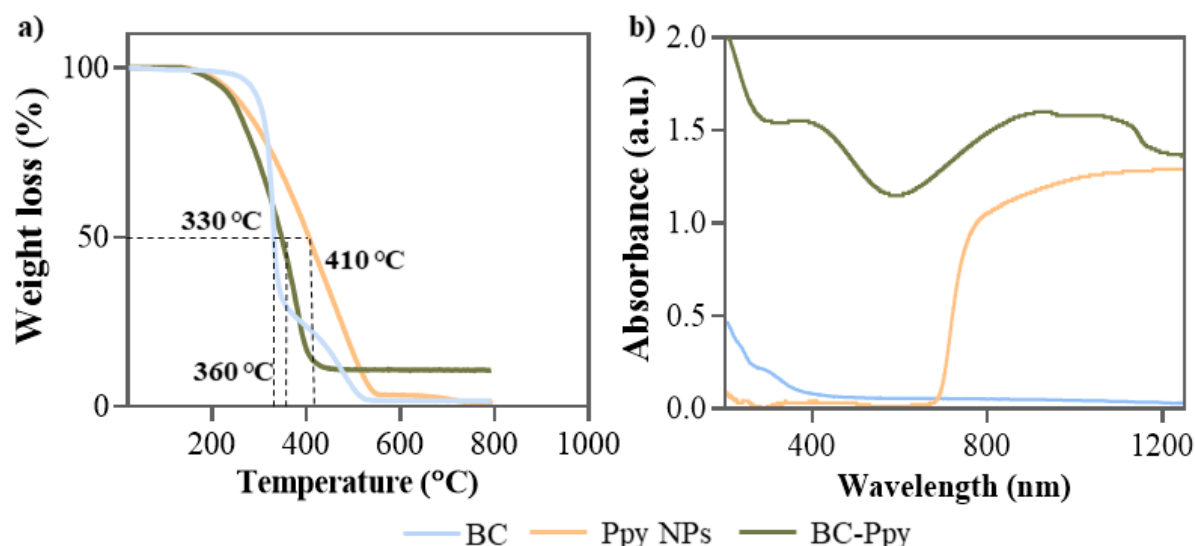


Figure 7. a) Thermal degradation of Ppy NPs between 200 and 800 °C, b) UV-Vis-NIR absorbance spectra of Ppy NPs.

We examined the absorption property of BC-Ppy using a Cary 5000 UV-Vis-NIR spectrophotometer in the wavelength range of 200-1200 nm (Figure 7b). The BC-Ppy films were analyzed as dried films. While the Ppy NPs solution exhibited a strong and broad absorption in the NIR region between 700-1200 nm, BC shows a typical absorption peak between 270 nm. Therefore, the composite material BC-Ppy shows collective absorption with peaks at 400 nm and the NIR region.

5.3.6. Electrical conductivity

A qualitative confirmation of the electrical conductance of BC-Ppy films was carried out using a simple LED setup. Two probes were connected to an external power supply, and the LED bulb was attached to one of the probes. While the BC-Ppy film was clamped to the other probe, the LED bulb was brought to contact with the film's surface. Upon contact, the LED lights up, confirming that the film can conduct electricity. The cell culture experiments are performed in an aqueous condition; therefore, we also did a test by placing the films in water. In both dry and wet conditions, the films conducted electricity to the LED bulbs (Figure 8a, b). Following this, quantitative analysis was performed by the four-probe instrument and computed using the van der Pauw method, as previously elaborated in chapter 2¹⁹.

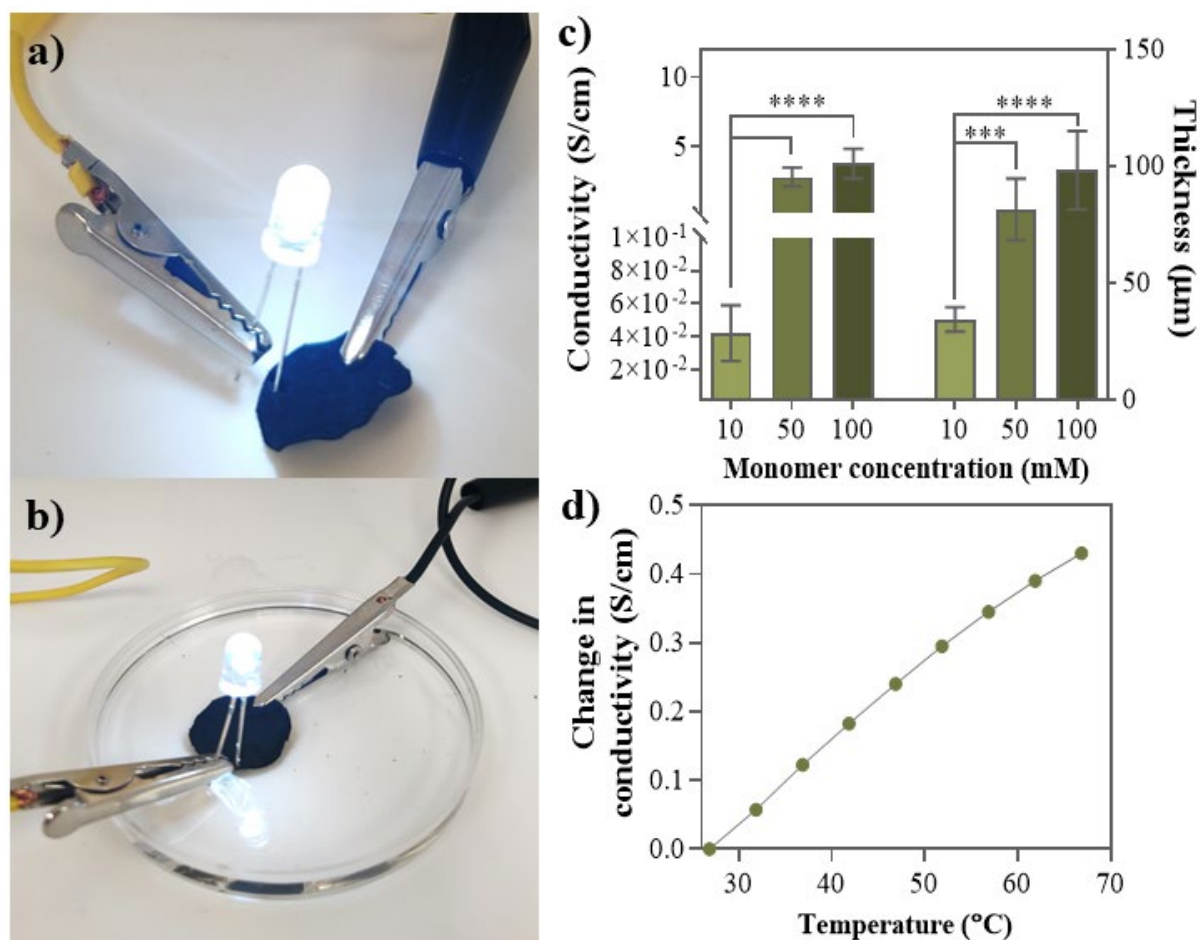


Figure 8. Conductivity of BC-Ppy demonstrated with an LED setup a) BC-Ppy in the dry state, b) dispersed in water, c) Conductivity and Thickness as a function of monomer concentration, d) Conductivity as a function of temperature.

Composites prepared from six different monomer concentrations (1,3,5,10,50,100 mM) were measured: BP1, BP3, BP5, BP10, BP50, and BP100. The composites with higher concentrations (from BP10) were measured directly as individual films. However, the conductivities of films BP1 to BP5 were lower than the measurable range of instruments. Therefore, we stacked five never-dried BC-Ppy films of each concentration and dried them together. The five films were well-adhered with each other and did not get separated easily, a feature previously investigated and reported⁵. This way, the overall conductivity and thickness of the stacked films are higher, making it feasible to measure them. The conductivity of the stacked film is then averaged to obtain individual conductivities.

Table 2: Thickness and electrical conductivity of BC-Ppy films at varying monomer concentrations

Py concentration [mM]	Sample name	Thickness (μm)	Conductivity (S/cm)
1	BP1	13	1.7×10^{-8}
3	BP3	18	3.2×10^{-5}
5	BP5	26	7.0×10^{-3}
10	BP10	45	0.02 ± 0.01
50	BP50	113	1.7 ± 1.3
100	BP100	140	2.4 ± 1.4

As expected, the conductivity varied as a function of monomer concentration (Table 2, Figure 8c). The thickness of the films also increased with increasing monomer concentrations, further substantiating the increase in Ppy content. The high Ppy content resulted in increased conductivity of the composite films, starting from $\approx 1.7 \times 10^{-8}$ S/cm for the composite with the lowest concentration (BP1) reaching as high as ≈ 4 S/cm for BP100 (Table 2) (Figure 8c). Therefore, the conductivity of BC-Ppy films can be precisely tuned by simply modifying the monomer concentration according to the application. For instance, for tissue engineering applications, biomaterials must possess conductivities concurrent with the targeted native tissue. We evaluated the dependence of the conductivity of BC-Ppy on temperature and found that temperature increases the electrical conductivity to ≈ 5 S/m for a change of 5°C (Figure 8d). This phenomenon can be attributed to the thermally activated transport of charge carriers across the domains²⁰.

5.3.7. Mechanical behavior

Another critical property to study in biomaterials for tissue engineering applications is the behavior of materials under mechanical wear and tear. To employ BC-Ppy composites as scaffolds for cardiac applications, they should be capable of withstanding repetitive cyclic force and exhibit good elasticity and tensile strength to endure the sheer blood flow and beating of the heart²¹. Tensile strength is the maximum stress a sample can withstand before failure. The strain at which fracture occurs is referred to as breaking strain, and the slope of the stress-strain curve represents Young's modulus of a material.

We employed Instron MicroTester 5548 with a 5 N and 10 N load cell for cyclic uniaxial and biaxial tensile testing at a 5 mm/min test speed. The experiments were performed in submerged conditions to simulate *in-vitro* and *in-vivo* conditions. The uniaxial test was conducted in the

standard dog-bone-shaped samples, and the biaxial test was performed in square-shaped samples. Growing BC in the required shape was necessary for two reasons: 1. Preparing a larger size and cutting it to the required dimensions and shapes can induce micro-cracks within the fibrous network, disrupting the actual mechanical strength, and 2. The scaffolds utilized for cell culture experiments are not cut to shape; instead, they are grown to the required shape and employed as such. Therefore, to measure the actual mechanical properties of the materials that the cells experience, BC was produced using 3-D printed molds (Figure 9). The samples were clamped and pulled from two edges with a 60 mm starting distance between the two holding clamps. For the biaxial tensile test, the material was pulled uniformly from four directions, with a distance of 9.5 mm between the clamps. Upon pulling, the sample stretches, and the increase in length is measured (Figure 9). Using the formula below, the instrument produces load vs. deformation data converted to stress vs. strain. Two load-deformation curves are obtained from the two axes for the biaxial tests.

$$\text{Stress (MPa)} = \frac{\text{Load (N)}}{\text{Cross-sectional area (mm}^2\text{)}}$$

$$\text{Strain (\%)} = \frac{\text{Deformed length (mm)}}{\text{Original length (mm)}} * 100$$

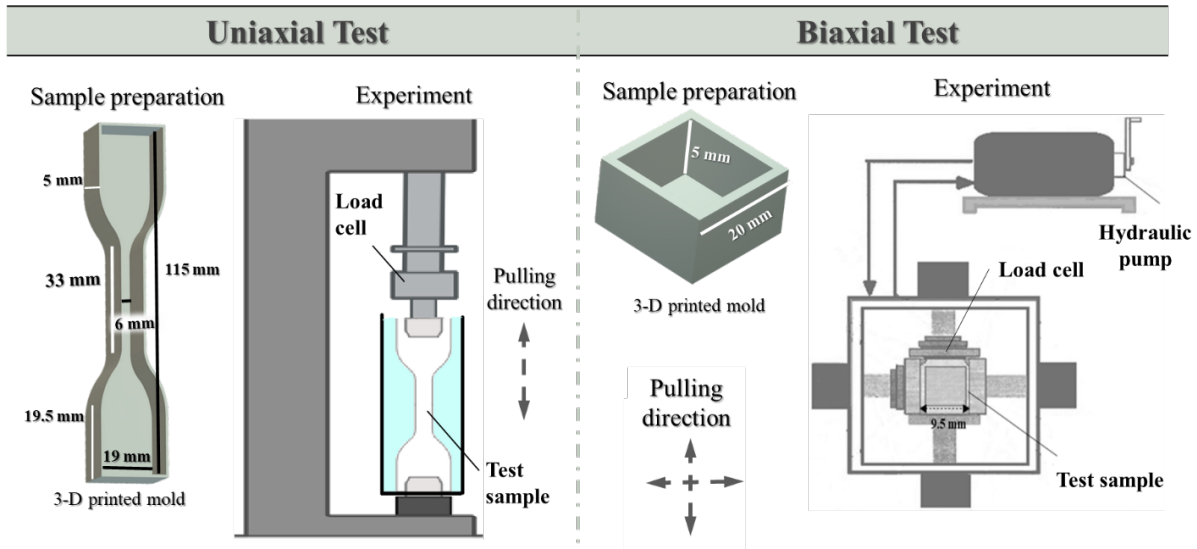


Figure 9. Dimensions of the 3-D printed mold used for growing BC and schematic representation of the uniaxial and biaxial tensile test experimental setup.

The tensile properties of BC and BC-Ppy films indicated that higher Ppy levels reduce the materials' tensile strength, Young's modulus, and breaking strain. Plain BC and four BC-Ppy films were measured: BP1, BP3, BP5, and BP10. While the average uniaxial tensile strength was ≈ 0.7 MPa for the remaining samples (BC to BP5), it reduced drastically to 0.3 MPa for

BP10 (Figure 10a, b). The breaking strain also showed a consistent pattern, an average of ≈ 11 % for the remaining samples and only 3.5 % for BP10 (Figure 10a, b). Similarly, the average young's modulus for the materials were around 10 MPa, except for the BP10 material which showed a decrease to ≈ 5 MPa. Although the initial samples up to BP5 do not show a drastic change in the strength and modulus from each other or in comparison with plain BC, the BP10 material showed a marked decrease of all the three parameters: Young's modulus, tensile strength and breaking strain in both the tensile tests (Figure 10). This was observed even while working with the samples, as the composites above BP10 were more brittle and delicate to handle.

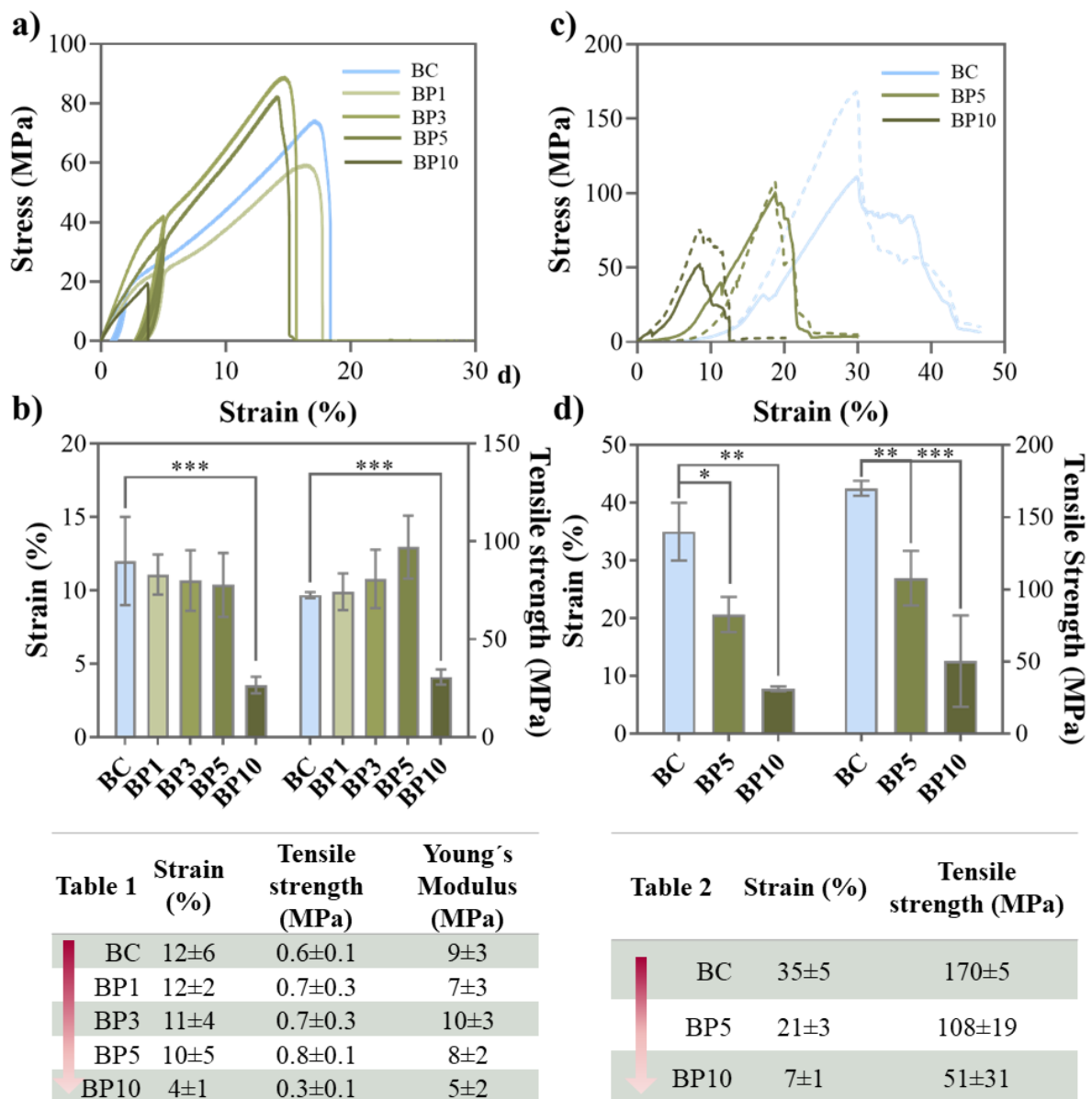
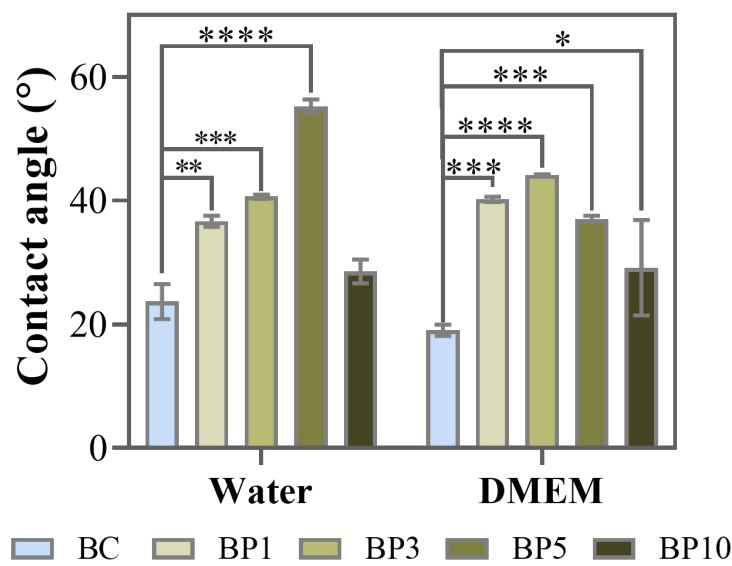


Figure 10. Uniaxial (top) and Biaxial (bottom) tensile properties of BC and BC-Ppy composites a,c) stress-strain curve, and b,d) tensile strength and breaking strain.

5.3.8. Surface wettability

The contact angle represents the wettability of scaffolds in specific solvents. We measured the contact angle in water and Dulbecco's Modified Eagle Medium (DMEM) - media used for cell culture, to comprehend the hydrophilicity of BC and BC-Ppy scaffolds, which in turn influences the cell behavior of these materials. The contact angle of nanocomposite scaffolds is highly dependent on the surface topography and the presence of nanoparticles on the surface. We measured the contact angle of BC, BP1, BP3, BP5, and BP10 composite materials (Figure 11).

a)



b)

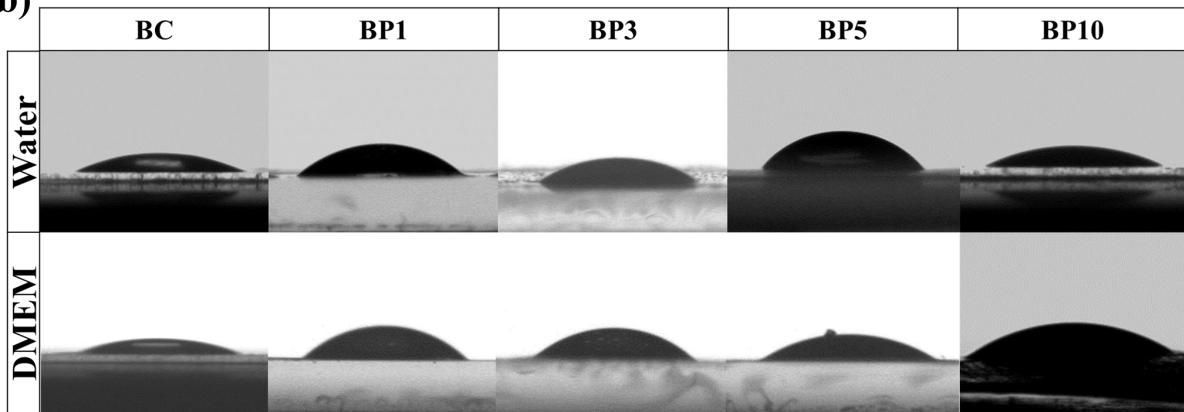


Figure 11. a) DMEM and water contact angle measurements of BC and BC-Ppy composites. b) Sample pictures of water and DMEM droplets on the scaffold surfaces.

We found that the contact angle increases with Ppy content, up to a particular concentration (BP5 in water, BP3 in DMEM). However, beyond this concentration, the contact angle starts to decrease. The differential behaviour of the scaffolds in the two solvents is probably due to

the differential ion content in the media compared to water. The aberrant behavior at higher concentrations could be due to the high doping amount, leading to high hydrophilic Cl^- ion levels. An increase in contact angle indicates a decrease in the hydrophilicity of the materials. Therefore, Ppy NPs on BC materials increase the hydrophobicity of the scaffolds, which is also substantiated by the increased surface roughness and amount of NPs in the materials.

5.3.9. Stability of BC-Ppy

We have assessed BC-Ppy films in solutions and sterilization conditions necessary for cell culture experiments. These studies ensure that the materials do not exhibit undesirable behaviors during *in-vitro* experiments or release any by-products that can hinder the overall effectiveness and application of the material. Two properties of the films were measured, i.e., the change in electrical conductivity and the possible leaching of Ppy NPs from the films into the solution upon storage, sterilization, and cell culture. Four critical conditions were tested: water storage, two sterilization modes (UV and autoclave), and incubation in the cell-culture media (DMEM) on 100 mM monomer concentration (BP100) samples. The films were suspended in Milli-Q water in falcon tubes and stored for a month to analyze their stability upon storage in water. Whereas for the cell-culture media, the films were placed in 24-well plates in 2mL complete DMEM medium for 24h at 37 °C. UV sterilization was performed in a laminar flow cabinet equipped with UV light for 30 minutes on each side, and autoclaving at 121 °C was carried out for 20 mins, with the films dispersed in Milli-Q water.

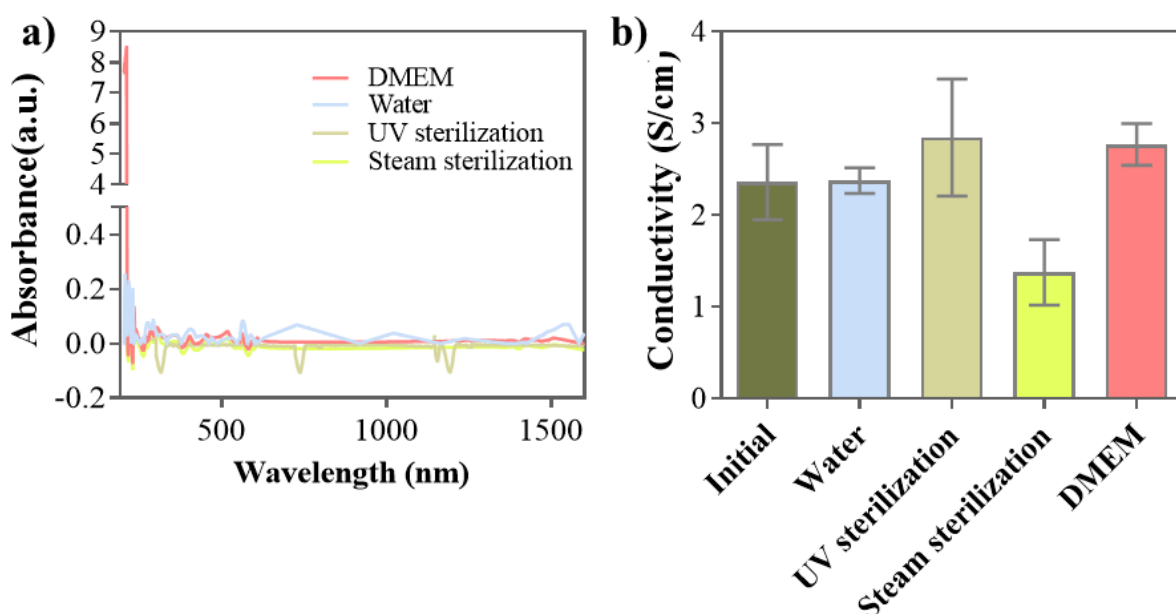


Figure 12. a) Leaching of Ppy NPs measured by UV-Vis-NIR absorption spectra of BC-Ppy composites b) Conductivity of BC-Ppy composites after treatment conditions

The UV-Vis-NIR scan revealed that the NPs do not leach from the films under these processing conditions, further confirming the strong interaction between BC fibers and Ppy NPs (Figure 12a). Even though storage in water, UV sterilization, and incubation in DMEM medium did not affect the electrical conductivity, sterilization by autoclave did show a reduction in the conductivity of the films (Figure 12b). Nonetheless, the decline was statistically non-significant and it has been reported that high temperatures can lead to over-oxidation of Ppy^{22–25}. Particularly in aqueous conditions, promote the diffusion of Cl⁻ ions into the solution, resulting in loss of electrical conductance²⁶. The stability of BC-Ppy composites during storage, sterilization by UV, and cell culture establish their suitability as scaffold materials for *in-vitro* evaluation.

5.4 Cardiac cell types used for *in-vitro* evaluation

All the cell culture experiments were carried out by Marina Martínez Hernández with the supervision of Soledad Pérez Amodio from the Biomaterials for Regenerative Therapies group in the Institute for Bioengineering of Catalonia (IBEC), Barcelona.

Preliminary investigation of biomaterial scaffolds for application as cardiac patches was performed using two major cardiac cell types, cardiac fibroblasts (CFs) and immortalized cardiomyocyte (CM) cell models or precursor cells.

5.4.1. Cardiac Fibroblasts

Cardiac fibroblasts (CFs) are spindle-shaped, elongated cells with a substantial endoplasmic reticulum responsible for constituting the extracellular matrix (ECM) and the fibrous tissue^{27,28} (Figure 13a). CFs play a vital role in maintaining the tissue's structural and mechanical integrity, regulating cell-cell signaling, communicating electrical signals, ECM deposition and maintenance, remodeling, and regeneration, etc^{28–30}. The interplay between CMs and CFs is still unclear due to the diverse and complex role of CFs in the cardiovascular system³¹. The number of cardiac fibroblasts increases, especially in diseased hearts, to repair and rebuild the tissue. When the heart is damaged due to myocardial infarction, the fibroblasts are activated and mature into their pathological phenotype, myofibroblasts³² (Figure 13b). Myofibroblasts exhibit a stellate morphology with increased expression of proteins such as collagen, and TGF- β , leading to higher cell proliferation, ECM production, cell adhesion and

migration, and resistance to cell death³⁰. Consequently, CFs are significant in a healthy heart and play an even more vital role in disease.

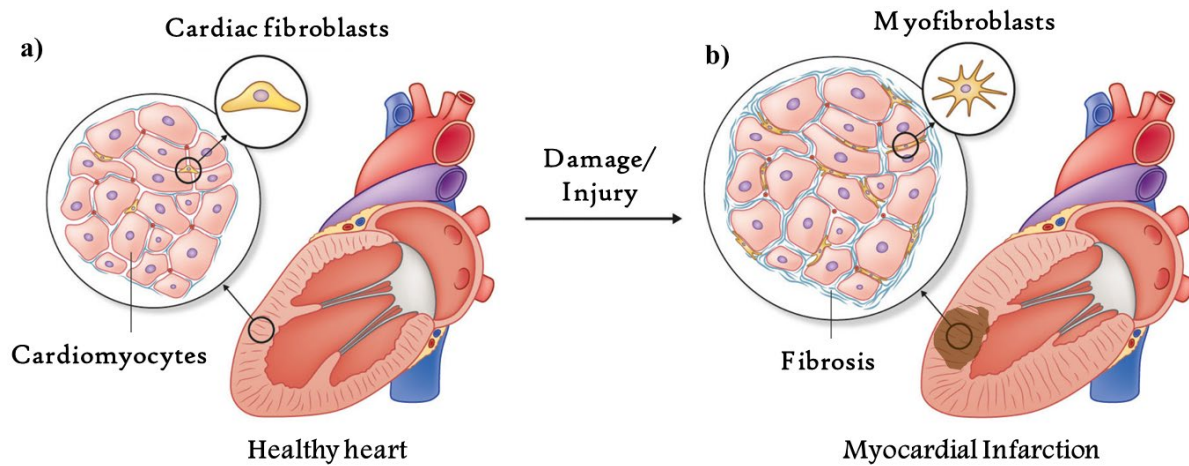


Figure 13. The organization of fibroblasts between cardiomyocytes, maintaining the fibrous tissue and ECM composition. Activation of fibroblasts upon injury, forming myofibroblasts and inducing fibrosis around the cardiomyocytes.

Since tissue engineering scaffolds provide the extracellular environment for cell-cell communication, evaluating scaffolds in the cell type closely involved with ECM is crucial. In addition to the changing phenotypes upon the damage, fibroblasts exhibit diverse phenotypes in various body tissues. Therefore, it is imperative to evaluate the behavior of fibroblasts in biomaterials for application in any tissue type. CFs are a less sensitive, more robust cell type to evaluate a biomaterial scaffold's initial toxicity and function before proceeding to more sensitive cell types like cardiomyocytes.

In this work, we employed Adult human Cardiac Fibroblasts (hCFs) (p5-p6, PromoCell®) to evaluate cell viability, attachment, proliferation, and morphology.

5.4.2 Immortalized cardiomyocyte models

Cardiomyocytes (CMs) are the largest cell types of the heart, covering $\approx 70\text{--}85\%$ of tissue volume. However, they account for only $\approx 30\%$ of cell number^{28,33}. Their cytoplasm consists of sarcomeres, the contractile unit of cardiomyocytes and extensive mitochondria, to take care of the high energy needs of the cells since they undergo continuous contractions^{34,35}. The cell wall contains intercalated discs with structures like desmosomes and gap junctions for inter-cellular and cell-cell electromechanical communication. These gap junctions consist of connexin proteins (CX40, CX43, CX45) responsible for the electrical coupling of CMs with cardiac fibroblasts (CFs)³⁶. Mutations and aberrant function of these gap junctions are associated with several cardiovascular diseases and arrhythmogenesis³⁷. Although CMs are the

ideal cell type for investigating cardiac tissue functions, isolated CMs result in inadequate cell yield and inconsistent quality. CMs are also very difficult to be isolated, maintained in cell culture, and produced in a large scale^{38,39}.

Therefore, *in-vitro* experiments, especially for evaluating biomaterial scaffolds, often employ alternative cell models for CM, such as H9c2 and HL-1 cell lines. HL-1 is an adult immortalized cardiomyocyte cell line derived from AT-1 mouse atrial cardiomyocyte tumor lineage. They can spontaneously contract and maintain a differentiated cardiac-specific phenotype^{40,41}. On the other hand, H9c2 is a cardiomyoblast cell line derived from embryonic rat ventricular heart tissue. H9c2 cells possess more resemblance to primary cardiomyocytes than HL-1 and have been extensively used in cardiovascular research as an alternative to primary cardiomyocytes^{42–44}. Additionally, H9c2 can also mature into cardiomyocyte-like cells under differentiation media containing retinoic acid^{45,46}.

In this thesis, H9c2 rat cardiac myoblasts procured from ATCC (p2-p9) were utilized for in-vitro evaluation of BC-Ppy composite films.

5.5. Material selection and pre-conditioning

The plain BC and BC-Ppy composites were evaluated in cardiac fibroblasts (CFs) for material biocompatibility through assays such as cell viability, cell proliferation, and attachment. Three materials were used for this purpose: **BC, BP2, and BP10**, i.e., BC-Ppy composites prepared with 2 mM and 10 mM pyrrole monomer. Subsequently, various assays were performed to investigate the behavior of BC and BC-Ppy materials in H9c2 cells. The cell viability, attachment, and morphological investigation upon culturing H9c2 on the materials were investigated for BC, and four concentrations of BC-Ppy composites: **BP1, BP3, BP5, and BP10**, derived from pyrrole concentrations of 1, 3, 5, and 10 mM, respectively. The total protein content of cells, cell-scaffold interaction, and ability of the scaffolds to differentiate H9c2 cardiomyoblasts to CM-like cells, with respect to the amount of Ppy in the scaffold, were scrutinized on BC and two BC-Ppy materials: **BP3 and BP5**.

The as-synthesized materials were dried at 60 °C in between Teflon plates with a 1 Kg weight on top. The dried scaffolds were then sterilized with UV light for 15 minutes on each side. The scaffolds were placed on low-adherent cell culture plates with poly(2-hydroxyethyl methacrylate) (PHEMA) coating and secured to the bottom of the well using Polytetrafluoroethylene (PTFE) rings. Following this, the scaffolds were incubated in culture media for 24 hours to promote solvent exchange and diffusion of the nutrients. The scaffolds were again sterilized by UV for 15-30 minutes on each side before cell seeding. In parallel, all

the cell culture experiments were carried out in plastic cell culture plates without BC or BC-Ppy materials as controls for comparative evaluation.

5.6 In-vitro cell culture assays

5.6.1 Cardiac Fibroblasts viability, attachment, and morphology

The CF cells were cultured in low-serum Fibroblast Growth Medium (FGM) at $\approx 15,000$ cells/cm² and maintained in a humidified atmosphere with 5% CO₂ at 37 °C for 72 hours. The culture media was changed every two days. The cell viability was estimated using LIVE/DEAD® assay, and cell attachment and proliferation were computed through the percentage of scaffold area coverage. All three parameters were measured at two-time points, 24 and 72 hours, to explore whether culture duration impacts material toxicity

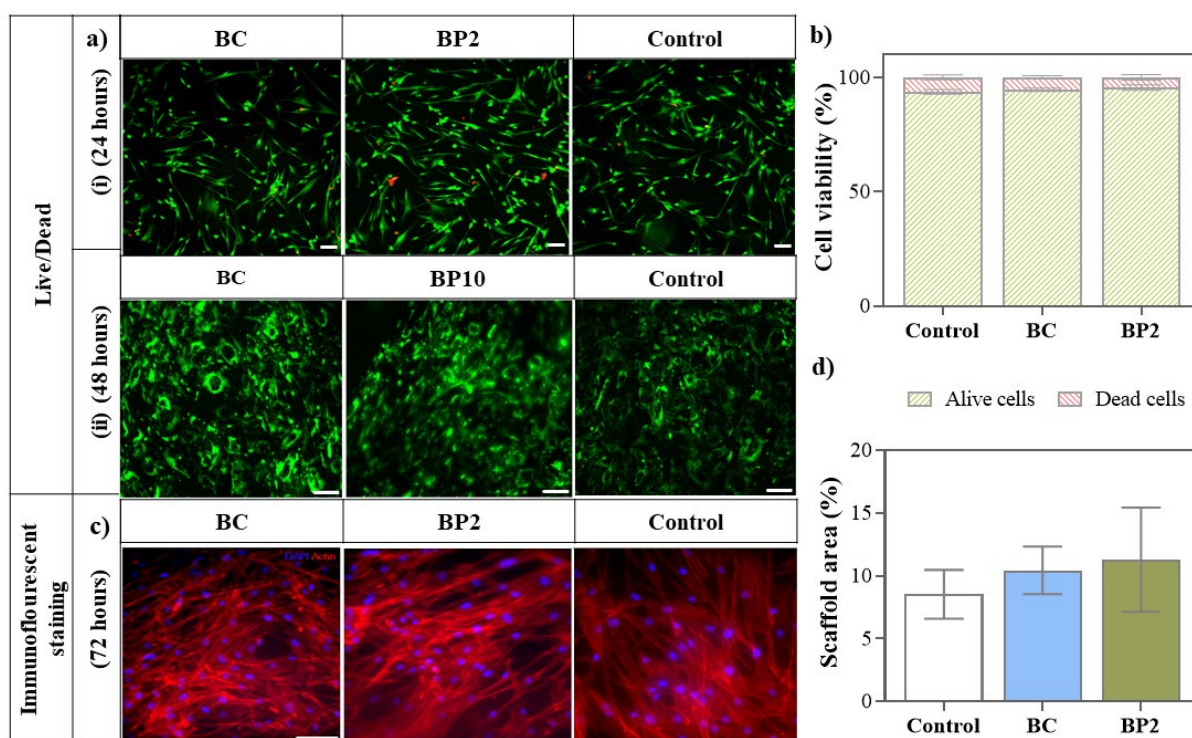


Figure 14. Cell viability of BC and BC-Ppy composites assessed by a) Live/Dead assay after 24 hours (i) and 48 hours (ii), b) Cell viability in the BC and BC-Ppy scaffolds compared with control (n=3), c) immunofluorescent images after 72 hours, and d) Scaffold area coverage by the cells (n=3). Scale bars: 100 μ m.

The cells showed good viability of $\approx 95\%$ in both BC and BC-Ppy after 24 hours (Figure 14a i, c). Even after 48 hours, the composite with the highest Ppy content, BP10, showed excellent cell viability similar to control and plain BC (Figure 14a ii). The immunofluorescent images (Figure 14c) revealed that BC and BC-Ppy scaffolds showed similar cell attachment, cell number, and morphology, with $\approx 10\%$ area coverage equivalent to cell culture plates

(Figure 14d). The behavior of hCFs on BC and BC-Ppy materials proved the biocompatibility and favorable material properties, encouraging further evaluation in H9c2 cardiomyoblasts.

5.6.2 By-product toxicity of scaffolds in H9c2 cell media

Two types of media were primarily used in this work for the culturing of H9c2 cells: growth medium (GM) (DMEM complete media) and differentiation medium (DM) (DMEM complete media with low serum (1% FBS) and Retinoic acid (RA)). We used GM to assess the viability, attachment, morphology, and DM to study the H9c2 maturation. The BC and Ppy might interact with the GM components or retinoic acid in the DM, releasing unwanted by-products that could potentially harm the cells⁴⁷. For this reason, we evaluated the by-product toxicity in GM and DM. The BC, BP3, and BP5 materials were incubated in both media overnight, and the supernatant was collected.

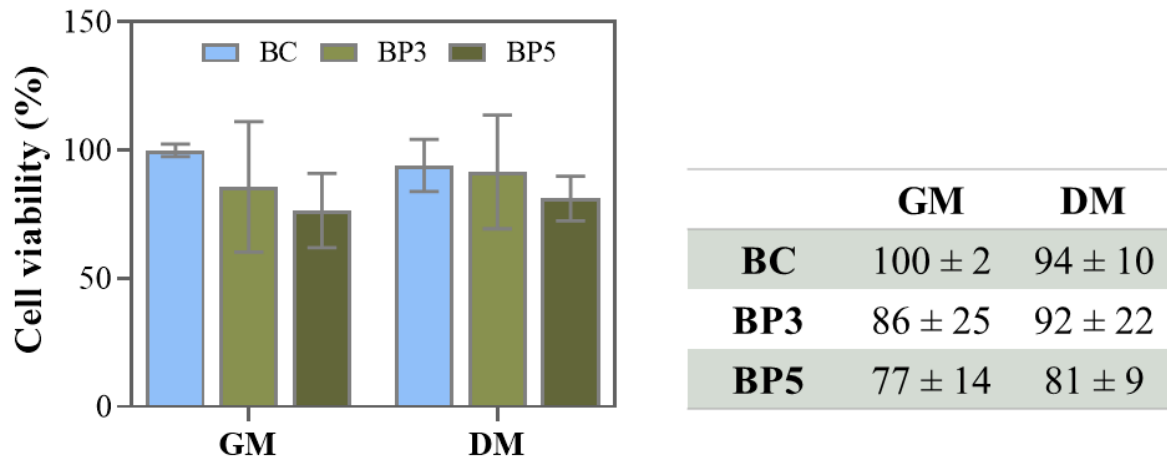


Figure 15. Cell viability analysis of BC and BC-Ppy materials' by-products incubated in growth medium (GM) and differentiation medium (DM).

The H9c2 cells were seeded on well plates in the presence of supernatant media, and viability was computed through MTT assay after 24 hours. None of the treatment groups showed any significant toxicity to the growth of H9c2 cells (Figure 15). Therefore, the incubation of materials in cell culture media does not lead to undesirable by-product release or cell-scaffold interactions, warranting the safety of our cell culture protocol.

5.6.3 H9c2 cell viability and attachment

The H9c2 cells were cultured at a cell count of $\approx 30,000$ cells/cm² onto the BC and BC-Ppy materials in the low-adherent 24-well cell culture plates in complete DMEM media. The viability of H9c2 cells was evaluated using LIVE/DEAD assay and MTT assay. The

LIVE/DEAD assay was performed using the stains calcein-AM for alive cells and propidium iodide for dead cells. The percentage of cell viability was computed from the fluorescent images using ImageJ software by counting the number of cells.

a) LIVE DEAD

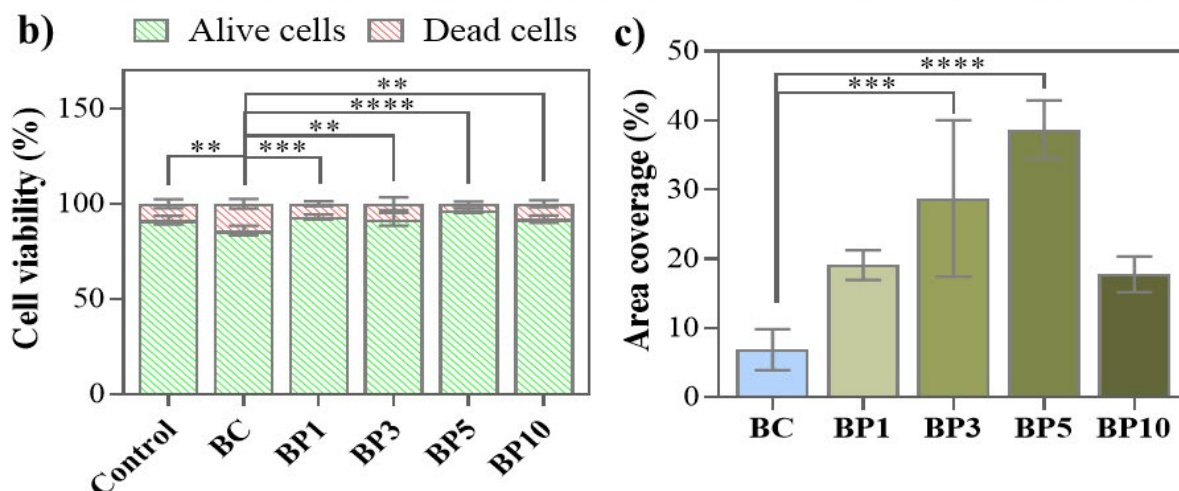
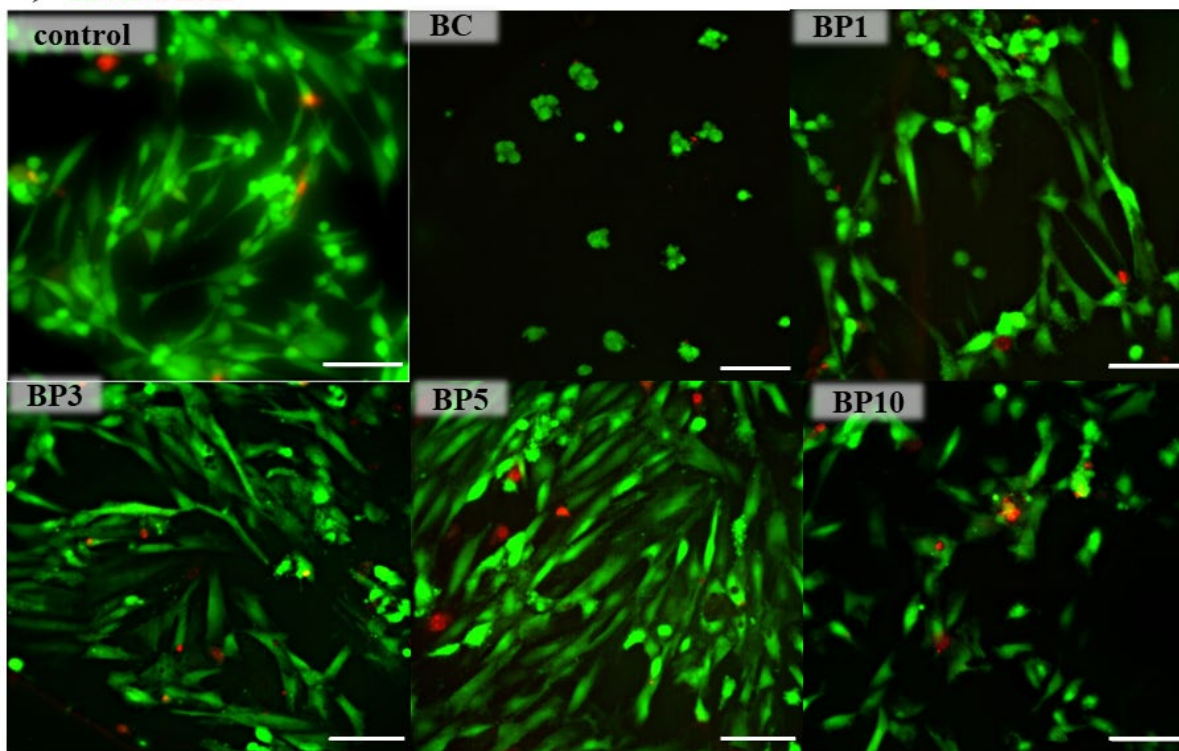


Figure 16. a) LIVE/DEAD images of H9c2 cells after 24 hours of culturing on the scaffolds, b) Cell viability computed from live/dead assay, c) Area of scaffolds covered by the cells after 24 hours. (n=4; scale bars = 100 μ m).

All five materials showed exceptional biocompatibility with H9c2 cells (Figure 16a). While the plain BC scaffolds presented $\approx 86\%$ cell viability, the presence of Ppy enhanced the percentage of alive cells considerably, with the highest cell viability of 96% exhibited by BP5 scaffolds. However, for the material BP10 with higher Ppy content, cell viability starts to

decrease and reach $\approx 92\%$ (Figure 16b). The cell attachment was also quantified by measuring the percentage of scaffold area covered by the cells. Similar to cell viability, cell attachment was also the highest for BP5 scaffolds, with $\approx 40\%$ area coverage, compared to BC scaffolds which showed only $\approx 7\%$ coverage (Figure 16c). In a nutshell, the healthy behavior of H9c2 cells on the BC-Ppy scaffold enhanced up to BP5. However, from BP10, the material exhibited a less favorable environment for the cells. Nevertheless, H9c2 cells still presented better viability and higher coverage on BP10 scaffolds over BC scaffolds. Previous reports on Ppy-containing scaffolds for tissue engineering also substantiate that Ppy NPs at very high concentrations are detrimental to biocompatibility, cell attachment, or their physiological behavior⁴⁸.

The cell viability and attachment were also evaluated by MTT assay on days 2, 3, and 6. The percentage of viable cells followed a bell-shaped pattern similar to the LIVE/DEAD assay, with cell attachment on materials up to BP5 surpassing the cell attachment in BC scaffolds (Figure 17). In contrast, the cell attachment in BP10 scaffolds was even lower than in BC scaffolds at all the time points. The materials until BP5 showed good cell viability even at day 6 of cell culture (BP5 $\approx 120\%$) (Figure 17a), indicating that the composites are highly biocompatible.

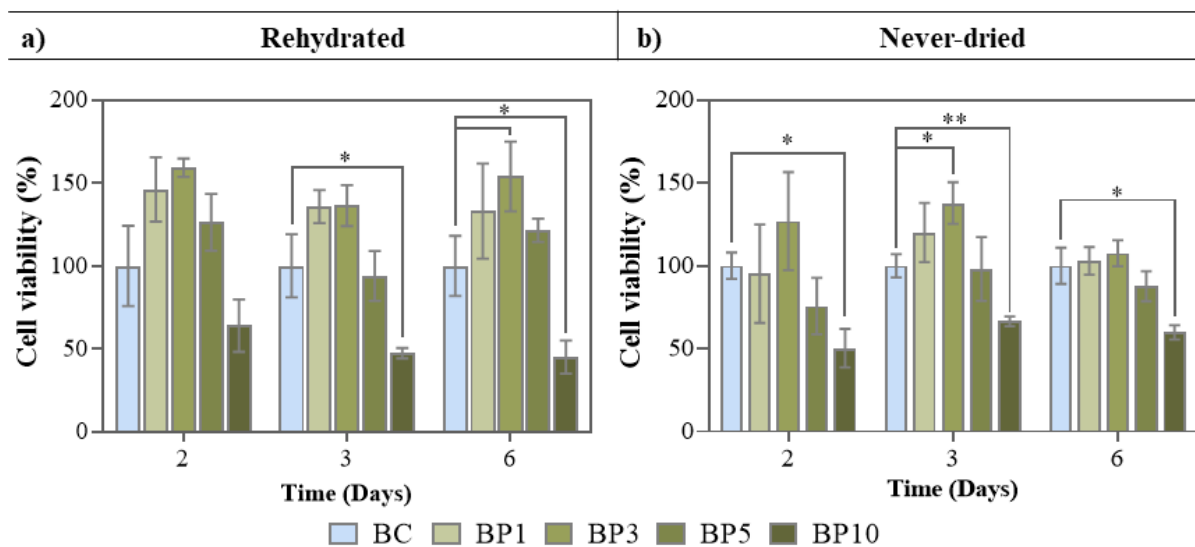


Figure 17. Cytotoxicity of H9c2 cells analyzed by MTT assay under two hydrating conditions of the scaffolds: a) Dried and rehydrated in the growth medium, b) never-dried and incubated in growth medium for solvent exchange.

In addition to dried and rehydrated scaffolds, the MTT assay was performed in never-dried scaffolds incubated in DMEM media. Both the never-dried and the rehydrated scaffolds showed similar behavior (Figure 17b), substantiating that the hydrating conditions of the material do not affect cell behavior. However, further experiments were only performed on dried and rehydrated scaffolds since these scaffolds are generally preferred at the commercialization level to facilitate packaging, maintaining sterility, and transport.

The live/dead assay of hCFs and H9c2 cells and the MTT assay of H9c2 cells on BC and BC-Ppy scaffolds led us to two main conclusions: 1) Presence of Ppy does not impact the viability, morphology, or attachment of fibroblasts (hCFs) to the scaffold surface irrespective of the Ppy content, and 2) While the BP10 scaffolds were safe for culturing hCFs and did not affect their cell viability, they were detrimental to the culturing of H9c2 cells, showing a significant reduction in cell viability and attachment.

The difference in behavior between the two cell types further endorses the need for evaluating different tissue cell types in biomaterials while designing tissue engineering scaffolds.

5.6.4 H9c2 cell Morphology

The morphology of H9c2 cells on BC and BC-Ppy composites was mainly studied through SEM imaging and immunostaining. The cells cultured on BC, BP1, BP3, BP5, and BP10 were visualized by phase contrast imaging through fluorescent microscopy on day 3 and day 7 of cell culture after immunostaining the cells with DAPI (for nucleus) and phalloidin (for actin filaments) stains. After 3 days of cell culture, cells on BC scaffolds rounded up and exhibited a reduced cell density, suggesting a lack of cell adhesion onto the surface. The cells on BC-Ppy composites showed better behavior, with BP5 presenting the best cell density, adhesion, and alignment on days 3 and 7 (Figure 18). The cells on BC-Ppy scaffolds displayed a characteristic elongated morphology as expected⁴⁹ (Figure 18, white arrow marks). However, cells on BP10 started to show signs of reduced adhesion, once again substantiating that while Ppy enhances cell viability and adhesion, suggesting higher concentrations of Ppy on materials can be counter-effective for cardiac cell culture.

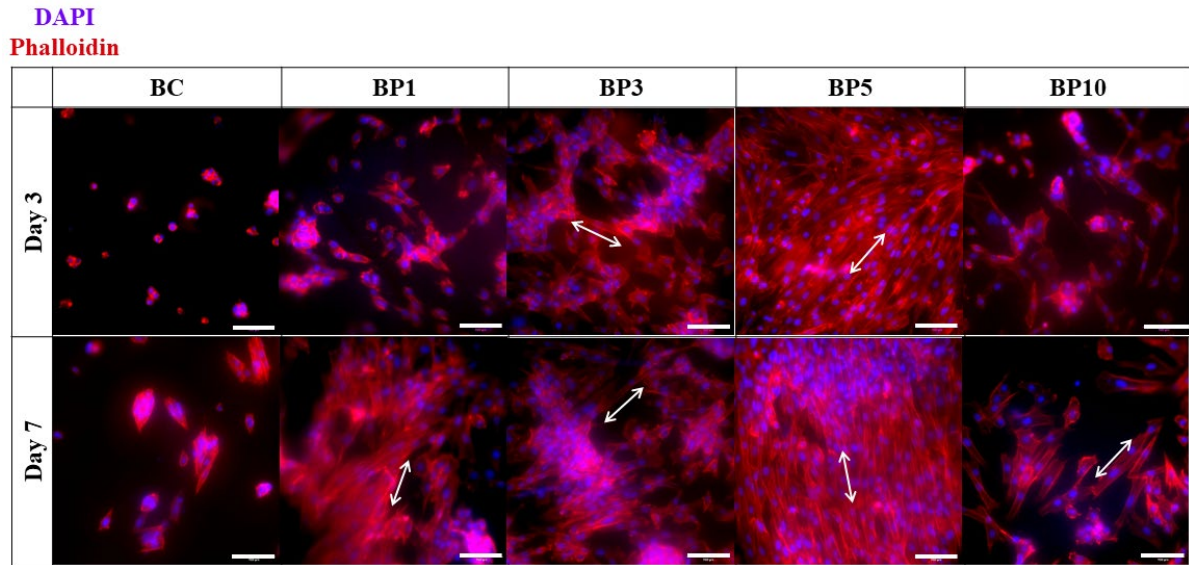


Figure 18. Immunofluorescent images of H9c2 cells attached to BC and BC-Ppy (BP1, BP3, BP5, and BP10) scaffolds at days 3 and 7 of cell culture. Scale bars: 100 μ m.

The cells cultured on BC, BP3, and BP5 scaffolds for 7 days were observed through SEM after fixation by glutaraldehyde, alcohol dehydration, and critical point drying. Upon encountering biomaterial scaffolds, adherent cells like H9c2 attach to the surfaces through interactions between the cell membrane and scaffold surfaces. This interaction is mediated by physical, chemical, electrical, and mechanical cues. The cells interact with scaffold surfaces through focal adhesion complexes consisting of membrane proteins, such as integrins, ligands, and receptors, present at membrane protrusions, called filopodia, which mediate the attachment of cells to ECM⁵⁰.

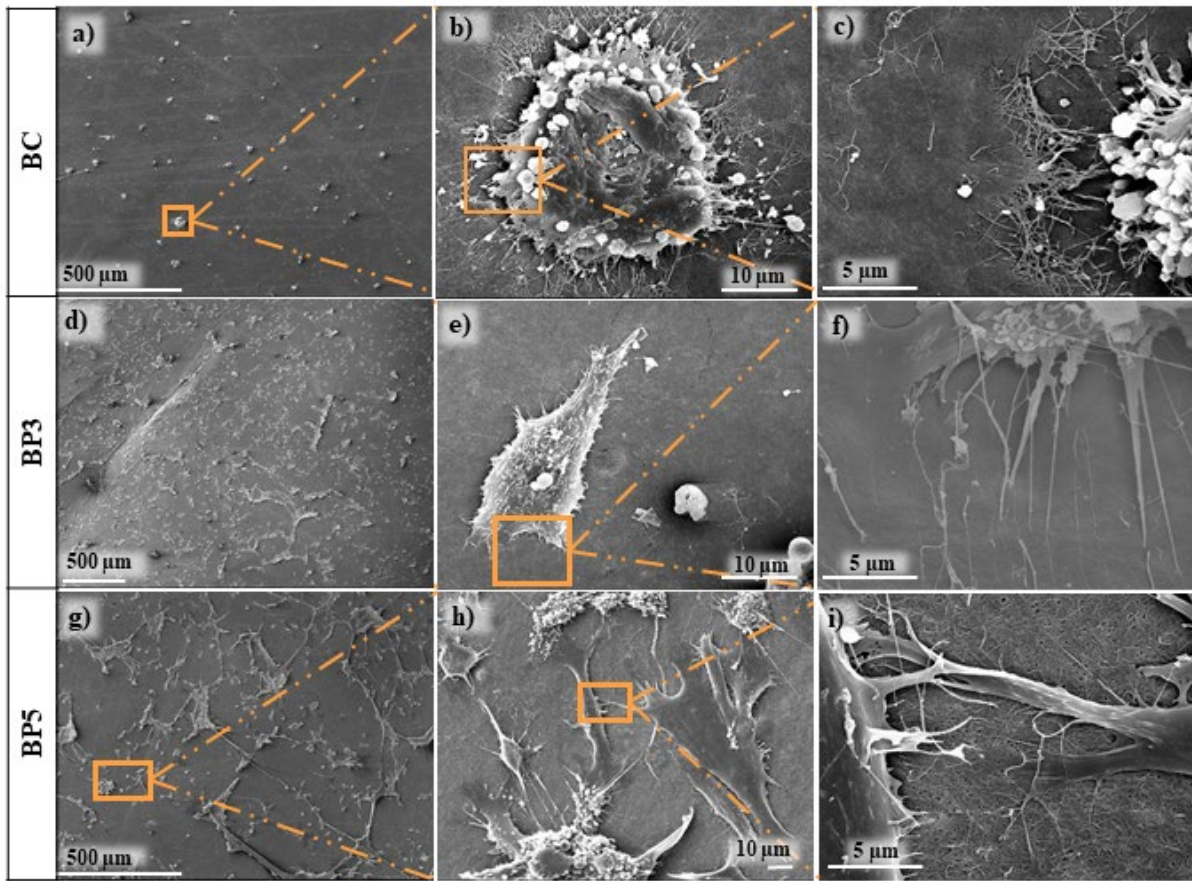


Figure 19. SEM images of H9c2 cells on BC and BC-Ppy scaffolds showing cell attachment and morphology through cell-scaffold interactions.

Filopodial structures (Figure 19d-i) protrude from the cell membrane attaching to the material surface, suggesting physical and mechanical interaction between the cell and the scaffold that promotes cell attachment, maturation, and spreading. However, cells cultured on the BC surface displayed spherical morphology, characteristic of immature/dead H9c2 cells. The BC cultured cells lack filopodial protrusions and association with the scaffold surface, corroborating with LIVE/DEAD and MTT assay results. The improvement in cell adhesion and morphology in BC-Ppy composites over plain BC scaffolds demonstrates that Ppy is essential for cell-scaffold interaction leading to cell migration and the characteristic H9c2 spindle-like cell morphology.

5.6.5 H9c2 maturation

The H9c2 cell line can be induced by retinoic acid (RA) to differentiate into a more mature cardiomyocyte-like phenotype^{45,46}. Evaluation of the scaffold material on the maturation of H9c2 is crucial for the future design of cell-laden BC-Ppy scaffolds and for comprehending the behavior of native cardiac tissue with cardiomyocytes towards the material.

Bearing this in mind, we first confirmed that the H9c2 cells could mature when cultured in a specific differentiation medium. Following this, we evaluated H9c2 cell maturation on the scaffold materials with and without adding differentiation media.

Maturation without scaffolds

Differentiation media (DM) containing 1% FBS with two concentrations of RA (0.01 μM and 1 μM) were utilized to assess the differentiation efficiency of the cells. The H9c2 cardiomyoblasts are proliferative and were cultured in growth media (GM) overnight at a cell density of 30000 cells/cm². GM was then exchanged with DM and cultured in the dark for 10 days, with new media change every 24 hours. The differentiation capacity of H9c2 cells was investigated through phase contrast microscopy to visualize cell morphology and proliferation. Immunostaining helped to understand morphology, adhesion, and bioactivity. Then we utilized western blotting to quantify the expression of cardiac marker Cardiac Troponin T (cTnT). Phase contrast images after 6 days revealed that the cells grown in DM (Figure 8a, bottom) demonstrated higher cell spreading and fusion, with larger cell size than cells grown in GM (Figure 20a, top). Upon computing the proliferation rate, we also found a marked decrease in proliferation for the cells cultured on DM (Figure 20b). The decreased proliferation, larger cells, and increased cell spreading indicate H9c2 maturation to a more cardiomyocyte-like phenotype.

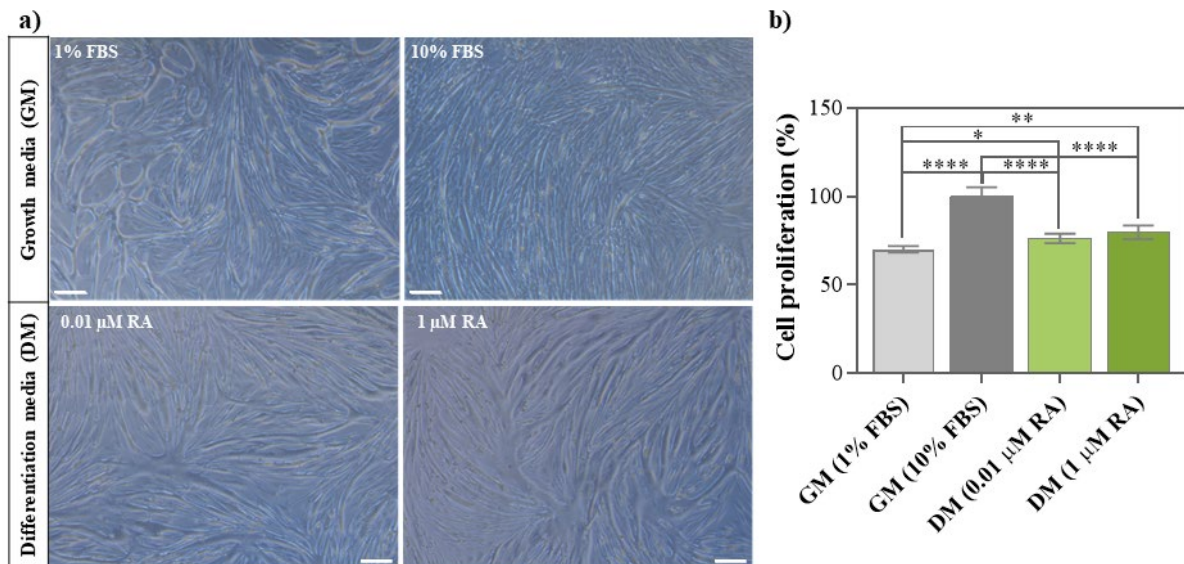


Figure 20. a) Phase contrast images of H9c2 cells cultured in growth medium (GM) (top) and differentiation medium (DM) for 6 days, b) Quantification of cell proliferation in GM and DM. (n=4; scale bars =100 μm).

For immunofluorescent imaging and quantitative estimation of protein markers, the cells were immunolabelled with primary antibodies against Ki67 (proliferative marker) and cTnT (cardiac marker) and stained with DAPI (nucleus) and phalloidin (actin filaments). We achieved successful H9c2 maturation with both the RA concentrations (Figure 21a, top). The immunofluorescence images reveal that the proliferative marker Ki67 is less expressed in the cells cultured on DM (Figure 21a, pink).

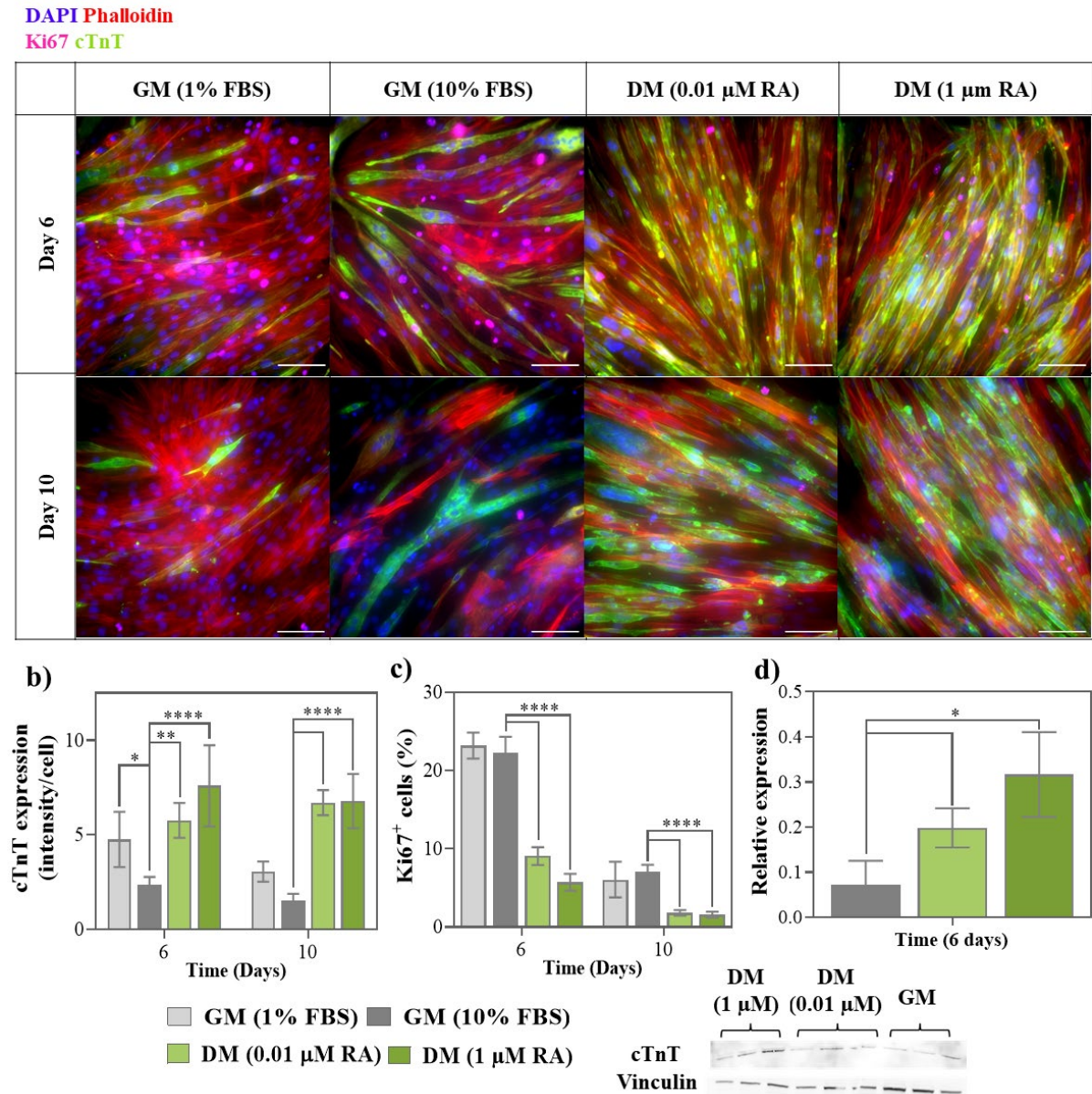


Figure 21. a) Immunofluorescent images of H9c2 cells in growth medium (GM) and differentiation medium (DM) at days 6 and 10, Quantification of b) cTnT expression, c) Ki67 expression (n=4), and d) Western blotting quantification of cTnT expression after 6 days (n=3).

On the other hand, the cardiac marker cTnT is higher in DM-cultured cells, indicating that the cells have attained a more cardiomyocyte-like phenotype (Figure 21a, green). The expression

of both the markers was also quantified, and we found that the expression is significantly different (higher for cTnT (Figure 21b) and lower for Ki67 (Figure 21c)) from the GM cultured cells at both day 6 and day 10 of cell culture.

Furthermore, western blotting to evaluate the relative expression level of cTnT with vinculin as the loading control also substantiates that the DM cultured cells expressed significantly higher cTnT protein (≈ 0.3) than GM cultured cells (≈ 0.07) after 6 days (Figure 21d). Therefore, we conclude that DM containing either concentration of RA can differentiate H9c2 cells to cardiomyocyte-like phenotype after just 6 days of cell culture. Next, we examined whether the presence of scaffold materials would promote further or attenuate the maturation of H9c2 cells.

Maturation of H9c2 cells on scaffolds

After confirming the ability of H9c2 cells to mature in the laboratory using DM containing lower RA concentration ($0.01 \mu\text{M}$), we utilized only this concentration and cell culture of 6 days for the subsequent experiments. The same experiments performed on H9c2 cells maturation without scaffolds were repeated with scaffolds. Additionally, we also carried out quantification of total protein content and other cardiac proteins through western blotting. The microscopic images revealed that H9c2 cells on the BC scaffold cultured in GM displayed rounded, detached morphology. However, the morphology of cells improved on BC scaffolds cultured in DM with a more elongated shape.

Interestingly, H9c2 cells seeded on top of the composite materials displayed an elongated morphology, with increased cell fusion and spreading typical of maturation in both GM and DM (Figure 22a). This suggests that the presence of Ppy could influence the maturation of H9c2 cells, even without any chemical stimulation using DM containing chemicals such as RA. Total protein content was estimated using a BCA assay to scrutinize cell growth and proliferation. Since decreased cell proliferation is a sign of cells progressing towards maturation, a reduced protein content would imply a more differentiated state of the cells. As expected, the total protein content of DM-cultured cells was lower than GM-cultured cells on the respective materials confirming the initiation of maturation (Figure 22b). Also, the total protein was higher in Ppy containing BP3 and BP5 than BC, indicating that Ppy promotes cell growth of mature cardiomyocyte-like H9c2 cells consistent with the previous results obtained in undifferentiated cardiomyoblast cells.

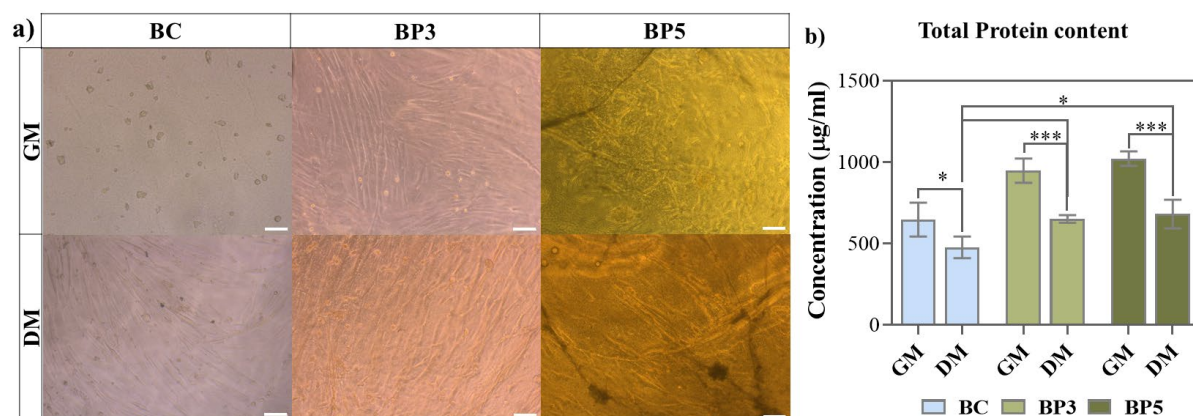


Figure 22. a) H9c2 cells grown on the scaffolds in the with and without differentiation medium, b) Total protein content of H9c2 cells grown on BC, BP3, and BP5 in GM and DM after 7 days estimated by BCA assay. Scale bars: 100 μ m.

Subsequently, we quantified the expression levels of specific cardiac protein markers cTnT, Heavy chain cardiac myosin (α -MHC), and Connexin-43 (Cx43)) through western blotting with specific antibodies, and GAPDH was used as the loading control. The DM considerably influenced the cardiac marker expression, especially cTnT and α -MHC. The supplementation of DM caused an increase in cTnT expression \approx threefold in the BP3 scaffolds and \approx twofold in the BP5 scaffolds (Figure 23a). Likewise, a two-fold rise in α -MHC expression was observed in cells from both BP3 and BP10 scaffolds in the presence of DM (Figure 23b).

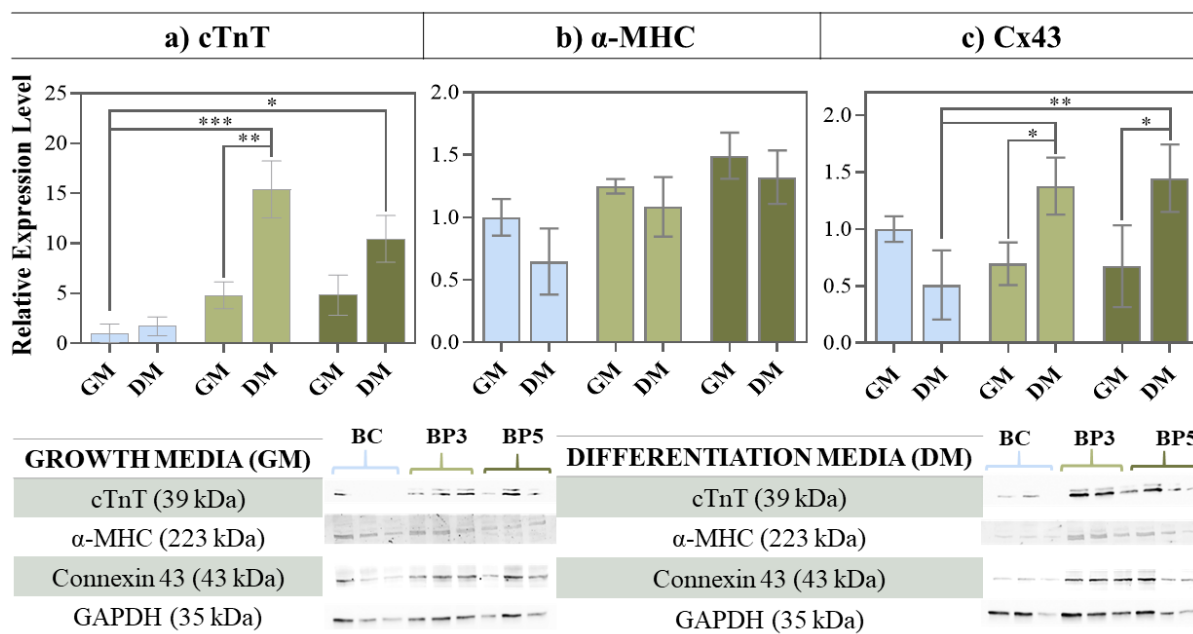


Figure 23. Quantification of cardiac-specific protein expression from western blot a) cTnT, b) α -MHC, and c) Cx43 expressions. N=3.

The presence of Ppy also played a crucial role in inducing maturation, as can be appreciated by comparing BC scaffolds with BP scaffolds, both in the presence and absence of DM. The cells cultured in GM on BP3 and BP5 displayed increased cTnT expression almost five times compared to BC scaffolds, even without any chemical stimulation of differentiation (Figure 23a). On the contrary, Ppy did not solely influence the α -MHC expression without differentiation-inducing media. But the combination of Ppy and DM showed almost three times increased α -MHC expression compared to BC scaffolds (BC-DM vs. BP3-DM and BP5-DM) (Figure 23b). Furthermore, the combined effect of Ppy and differentiation media resulted in a striking fifteen times increase of cTnT expression in BP3 and a ten times increase in the case of BP5 (BC-GM vs. BP3-DM and BP5-DM) (Figure 23a). While the use of DM did not impact the expression levels of Cx43, Ppy did show some influence. In both DM and GM cultured cells, the Cx43 expression was higher (although not significantly) with increasing Ppy concentration in the scaffold. In conclusion, Ppy and a chemical differentiation medium synergistically enhance the H9c2 maturation. Remarkably, Ppy alone has a strong positive influence in guiding the H9c2 cardiomyoblast cells toward cardiomyocyte-like maturation, even without external stimulation.

5.7 Conclusions

We successfully produced and characterized BC and BC-Ppy composite scaffolds. The final properties of BC-Ppy scaffolds were fine-tuned by modifying the initial monomer concentration to obtain a material with favorable material properties for cardiac cell culture. After carefully considering electrical conductivity, mechanical strength, surface wettability, and roughness, four BC-Ppy materials (BP1, BP3, BP5, BP10) were chosen for *in-vitro* evaluation. The plain BC scaffolds without any Ppy NPs were also examined to understand the influence of BC and Ppy NPs on cell behavior individually.

The BC-PPy composite scaffolds proved biocompatible to hCFs and H9c2 cells since cell viability was not affected as measured by the LIVE/DEAD assay and MTT assay. The presence of Ppy in the scaffold promoted cell attachment, migration, spreading, and morphology. The cells exhibited better attachment on scaffolds with higher Ppy content, with BP5 rendering the best results. However, each cell type behaves differently with biomaterial scaffolds. Consequently, while BP10 seems conducive to the adhesion and proliferation of hCFs, the same is not valid in the case of H9c2 cells.

The differential behavior of H9c2 cells on BP10 materials could be attributed to a change in material properties due to Ppy concentration. For instance, the tensile strength of BC-Ppy

scaffolds showed a marked decrease at BP10 (Chapter 2), suggesting that the BP10 scaffolds might not have provided enough material strength for the cells to anchor onto them. Similarly, other material properties of BP10, such as surface roughness and electrical conductivity, could have been hostile to H9c2 cells' attachment and growth.

Evaluation of specific cardiac phenotypes of H9c2 cells showed an interesting phenomenon. The BC-Ppy composites promoted maturation of H9c2 towards cardiomyocyte-like phenotypes such as an elongated morphology, increased cell spreading, reduced proliferation, and higher cardiac protein expressions, *even without any addition of differentiation media*. Both Ppy and media produce a synergistic effect in the presence of media, and H9c2 maturation is further enhanced.

The encouraging results of BC-Ppy composites as scaffold materials for culturing cardiac cells hCFs and H9c2 cells inspire further investigation of the material with other cardiac cell types. The role of Ppy in affecting cardiomyocyte beating is also an essential factor to be investigated. The potential of BC-Ppy NPs in promoting the maturation of H9c2 cells without any external intervention, such as an external electrical stimulus or chemical differentiation, has not been reported before and holds great value in designing multi-functional cardiac patches for myocardial infarction and cardiac arrhythmia.

References

1. Zhong, C. Industrial-Scale Production and Applications of Bacterial Cellulose. *Front. Bioeng. Biotechnol.*, 8 (2020).
2. Betlej, I., Krajewski, K. J., Boruszewski, P. & Zakaria, S. Bacterial cellulose-properties and its potential application. *Sains Malays* **50**, 493–505 (2021).
3. Zeng, M., Laromaine Sagué, A., Vallribera Massó, A., Roig Serra, A. Bacterial cellulose: fabrication, characterization and biocompatibility studies. *TDX (Tesis Doctorals en Xarxa)* 148 (2014).
4. Roig Sánchez, S. Novel bacterial cellulose materials: Structuration, functional nanocomposites and photocurable hydrogels. *TDX (Tesis Doctorals en Xarxa)* (2021).
5. Roig-Sanchez, S. *et al.* Nanocellulose films with multiple functional nanoparticles in confined spatial distribution. *Nanoscale Horiz* **4**, 634–641 (2019).
6. Anton-Sales, I., Koivusalo, L., Skottman, H., Laromaine, A. & Roig, A. Limbal Stem Cells on Bacterial Nanocellulose Carriers for Ocular Surface Regeneration. *Small* **17**, (2021).
7. Anton-Sales, I., Roig-Sanchez, S., Sánchez-Guisado, M. J., Laromaine, A. & Roig, A. Bacterial Nanocellulose and Titania Hybrids: Cytocompatible and Cryopreservable Cell Carriers. *ACS Biomater Sci Eng* **6**, 4893–4902 (2020).
8. Chen, Y. *et al.* Design and optimization of flexible polypyrrole/bacterial cellulose conductive nanocomposites using response surface methodology. *Polymers (Basel)* **11**, (2019).
9. Šeděnková, I., Taboubi, O., Paúrová, M., Hromádková, J. & Babič, M. Influence of the type and concentration of oxidant on the photoacoustic response of polypyrrole nanoparticles for potential bioimaging applications. *Synth Met* **292**, (2023).
10. Tikish, T. A., Kumar, A. & Kim, J. Y. Electrical and Optical Properties of Polypyrrole and Polyaniline Blends. *Polym Sci Ser A+* **62**, 680–690 (2020).
11. Muller, D., Rambo, C. R., Porto, L. M., Schreiner, W. H. & Barra, G. M. O. Structure and properties of polypyrrole/bacterial cellulose nanocomposites. *Carbohydr Polym* **94**, 655–662 (2013).
12. Kelly, F. M., Johnston, J. H., Borrmann, T. & Richardson, M. J. Functionalised hybrid materials of conducting polymers with individual fibres of cellulose. *Eur J Inorg Chem* 5571–5577 (2007).
13. Johnston, J. H., Moraes, J. & Borrmann, T. Conducting polymers on paper fibres. *Synth Met* **153**, 65–68 (2005).
14. Tang, L., Han, J., Jiang, Z., Chen, S. & Wang, H. Flexible conductive polypyrrole nanocomposite membranes based on bacterial cellulose with amphiphobicity. *Carbohydr Polym* **117**, 230–235 (2015).
15. Jakab, E., Mészáros, E. & Omastová, M. Thermal decomposition of polypyrroles. *J Therm Anal Calorim* **88**, 515–521 (2007).
16. Paajanen, A., Rinta-Paavola, A. & Vaari, J. High-temperature decomposition of amorphous and crystalline cellulose: reactive molecular simulations. *Cellulose* **28**, 8987–9005 (2021).
17. Guo, B., Glavas, L. & Albertsson, A. C. Biodegradable and electrically conducting polymers for biomedical applications. *Prog Polym Sci* **38**, 1263–1286 (2013).
18. Zeng, W. *et al.* Renal-Clearable Ultrasmall Polypyrrole Nanoparticles with Size-Regulated Property for Second Near-Infrared Light-Mediated Photothermal Therapy. *Adv Funct Mater* **31**, (2021).
19. Pauw, Lj. A method of measuring specific resistivity and Hall effect of discs of arbitrary shape. *Philips Res. Rep.* **13**, 1–9 (1958).
20. Huang, Y. *et al.* Effectively modulating thermal activated charge transport in organic semiconductors by precise potential barrier engineering. *Nat Commun* **12**, (2021).

21. Hasan, A. *et al.* Biomechanical properties of native and tissue engineered heart valve constructs. *J Biomech* **47**, 1949–1963 (2014).
22. Ennis, B. C. & Truong, V. T. Thermal and electrical stability of polypyrrole at elevated temperatures. *Synth Met* **59**, 387–399 (1993).
23. Kassim, A., Basar, Z. B. & Mahmud, H. N. M. E. Effects of preparation temperature on the conductivity of polypyrrole conducting polymer. *Proceedings of the Indian Academy of Sciences: Chemical Sciences* **114**, 155–162 (2002).
24. Otero, T. F., Márquez, M. & Suárez, I. J. Polypyrrole: Diffusion coefficients and degradation by overoxidation. *J. Phys. Chem. B* **108**, 15429–15433 (2004).
25. Holze, R. Overoxidation of Intrinsically Conducting Polymers. *Polymers (Basel)* **14**, (2022).
26. Ateh, D. D., Navsaria, H. A. & Vadgama, P. Polypyrrole-based conducting polymers and interactions with biological tissues. *J R Soc Interface* **3**, 741–752 (2006).
27. Ivey, M. J. & Tallquist, M. D. Defining the cardiac fibroblast. *Circ. J.* **80** 2269–2276 (2016).
28. Perbellini, F., Watson, S. A., Bardi, I. & Terracciano, C. M. Heterocellularity and Cellular Cross-Talk in the Cardiovascular System. *Front Cardiovasc Med* **5** (2018).
29. Doppler, S. A. *et al.* Cardiac fibroblasts: More than mechanical support. *J Thorac Dis* **9** S36–S51 (2017).
30. Fan, D., Takawale, A., Lee, J. & Kassiri, Z. Cardiac fibroblasts, fibrosis and extracellular matrix remodeling in heart disease. *Fibrogenesis Tissue Repair* **5** (2012).
31. Hall, C., Gehmlich, K., Denning, C. & Pavlovic, D. Complex relationship between cardiac fibroblasts and cardiomyocytes in health and disease. *J Am Heart Assoc* **10**, 1–15 (2021).
32. Chen, W., Bian, W., Zhou, Y. & Zhang, J. Cardiac Fibroblasts and Myocardial Regeneration. *Front. Bioeng. Biotechnol.* **9** (2021).
33. Camelliti, P., Borg, T. K. & Kohl, P. Structural and functional characterisation of cardiac fibroblasts. *Cardiovasc. Res.* **65** 40–51 (2005).
34. Dorn, G. W. Mitochondrial dynamics in heart disease. *Biochim. Biophys. Acta, Mol. Cell Res.* **1833** 233–241 (2013).
35. Li, A., Gao, M., Jiang, W., Qin, Y. & Gong, G. Mitochondrial Dynamics in Adult Cardiomyocytes and Heart Diseases. *Frontiers in Cell and Developmental Biology* **8** (2020).
36. Kanno, S. & Saffitz, J. E. The role of myocardial gap junctions in electrical conduction and arrhythmogenesis. *Cardiovasc Pathol.* **10** 169–177 (2001).
37. Severs, N. J. Gap junction remodeling and cardiac arrhythmogenesis: Cause or coincidence? *J Cell Mol Med* **5**, 355–366 (2001).
38. Zhou, B. *et al.* Functional isolation, culture and cryopreservation of adult human primary cardiomyocytes. *Signal Transduct Target Ther* **7**, (2022).
39. Bistola, V. *et al.* Long-term primary cultures of human adult atrial cardiac myocytes: Cell viability, structural properties and BNP secretion in vitro. *Int J Cardiol* **131**, 113–122 (2008).
40. Claycomb, W. C. *et al.* HL-1 cells: A cardiac muscle cell line that contracts and retains phenotypic characteristics of the adult cardiomyocyte. *Proc Natl Acad Sci U S A.* **95** 2979–2984 (1998).
41. White, S. M., Constantin, P. E. & Claycomb, W. C. Cardiac physiology at the cellular level: use of cultured HL-1 cardiomyocytes for studies of cardiac muscle cell structure and function. *Am J Physiol Heart Circ Physiol.* **286** H823–9 (2004).
42. Kuznetsov, A. v., Javadov, S., Sickinger, S., Frotschnig, S. & Grimm, M. H9c2 and HL-1 cells demonstrate distinct features of energy metabolism, mitochondrial function and sensitivity to hypoxia-reoxygenation. *Biochim Biophys Acta Mol Cell Res* **1853**, 276–284 (2015).
43. Onódi, Z. *et al.* Systematic transcriptomic and phenotypic characterization of human and murine cardiac myocyte cell lines and primary cardiomyocytes reveals serious

- limitations and low resemblances to adult cardiac phenotype. *J Mol Cell Cardiol* **165**, 19–30 (2022).
44. Abi-Gerges, N., Miller, P. E. & Ghetti, A. Human Heart Cardiomyocytes in Drug Discovery and Research: New Opportunities in Translational Sciences. *Curr Pharm Biotechnol* **21**, 787–806 (2020).
 45. Branco, A. F. *et al.* Gene expression profiling of H9c2 myoblast differentiation towards a cardiac-like phenotype. *PLoS One* **10**, (2015).
 46. Pereira, S. L. *et al.* Metabolic remodeling during H9c2 myoblast differentiation: Relevance for in vitro toxicity studies. *Cardiovasc Toxicol* **11**, 180–190 (2011).
 47. Ferraz, N. *et al.* In vitro and in vivo toxicity of rinsed and aged nanocellulose-polypyrrole composites. *J Biomed Mater Res A* **100 A**, 2128–2138 (2012).
 48. Kai, D., Prabhakaran, M. P., Jin, G. & Ramakrishna, S. Polypyrrole-contained electrospun conductive nanofibrous membranes for cardiac tissue engineering. *J Biomed Mater Res A* **99 A**, 376–385 (2011).
 49. Kobuszewska, A. *et al.* Heart-on-a-Chip: An Investigation of the Influence of Static and Perfusion Conditions on Cardiac (H9C2) Cell Proliferation, Morphology, and Alignment. *SLAS Technol* **22**, 536–546 (2017).
 50. Mattila, P. K. & Lappalainen, P. Filopodia: Molecular architecture and cellular functions. *Nat. Rev. Mol. Cell Biol.* **9** 446–454 (2008).

Annex

Arrhythmogenic mutations in *C. elegans* using CRISPR-Cas9 editing



SUMMARY

A wide number of genes are reported to be involved in the pathophysiology of cardiac arrhythmias. This study aimed to assess whether reproducing the same arrhythmic mutations in humans can result in rhythmic modifications of the *C. elegans* pharynx to employ the worms as models for specific types of arrhythmias. Following the results of calcium imaging in chapter 4 which suggested a strong role between the calcium signalling, pharynx pumping, and Ppy NPs, we chose to model three mutations of the calcium channel encoding gene *egl-19* in *C. elegans*. The CRISPR-Cas9 editing of *C. elegans* were performed during a research stay for a month with the guidance of Dr. Julián Cerón and Dr. Dmytro Kukhtar in the "Modelling Human Diseases in *C. elegans*" group at Instituto de Investigación Biomédica de Bellvitge (IDIBELL), Hospital Duran i Reynals, in Barcelona.

Index

6.1. Gene Mutations and Arrhythmias.....	171
6.2. CRISPR-Cas9	172
6.3. CRISPR-Cas9 in <i>C. elegans</i>.....	175
6.4. Arrhythmia specific mutations in <i>C. elegans</i>	177
6.5. CRISPR-Cas9 editing to produce mutant strains	179
6.6. Functional impact of the mutations	180
6.7. Conclusions	181

6.1. Gene mutations and Arrhythmias

Cardiac arrhythmias (CA) can be manifested by mutations in various genes within the heart. Based on whether the mutations occur in the developmental or functional components of the heart, the disorders are classified into "inherited arrhythmogenic disorders" or "ion channelopathies", respectively. The former group of disorders are characterized by structural abnormalities in the heart leading to conditions such as hypertrophic cardiomyopathy, arrhythmogenic right ventricular dysplasia (cardiomyopathy), and dilated cardiomyopathy. On the other hand, ion channelopathies involve mutations in the ion channels and transporter-associated proteins, causing conditions like congenital long QT syndrome (LQTS), short-QT syndrome, Brugada syndrome (BrS), and catecholaminergic polymorphic ventricular tachycardia (CPVT)²¹.

Loss-of-function mutations in genes encoding ion channels such as voltage-gated potassium channels *KCNQ1* and *KCNH2* have been associated with LQT1 and LQT2 syndromes, respectively²¹. On the other hand, mutations in voltage-gated calcium channels or mutations that affect Ca^{2+} homeostasis are found to be linked to arrhythmogenesis. Mutations in channels and receptors involved in calcium handling are also investigated for their influence in arrhythmias. *CACNA1* genes responsible for encoding L-type Ca^{2+} channels, ryanodine receptors (*Ryr2*) which mediate calcium-induced calcium release at the sarcoplasmic reticulum, and calsequestrins, have also been associated with arrhythmia, establishing the vital role of calcium signaling in regulating the cardiac rhythm²⁴.

Genome editing tools are useful in CA for 1) identifying the genes involved in CA pathology through knock-out studies, 2) designing mutation specific animal model for *in-vivo* evaluation of potential therapies, and 3) repairing the disease-causing mutations^{21,22}. Transgenic animal models of specific mutations are produced, and the molecular and electrophysiological functions of the mutants are compared with the wild-type animals to understand the impact of

those mutations in disease pathology. For example, mutations in hERG gene that encode voltage-gated potassium channels lead to LQT syndrome and can cause fatal ventricular arrhythmia²³. Repairing hERG gene mutations in cardiomyocytes using CRISPR technology can be an effective strategy to treat such LQTS.

6.2. CRISPR-Cas9

CRISPR-Cas9 is a natural immune defence system that protects bacteria against viral infections. When viruses infect bacteria, short segments of the viral DNA are integrated with the bacterial DNA, producing CRISPR sequences. Upon future virus attack, the bacteria produce RNA segments from the CRISPR sequences and attach them to the virus's DNA. The bacteria then use CRISPR-associated protein 9 (Cas9) endonuclease enzyme to cut the DNA, thus disabling the virus⁹.

In 2012, the CRISPR-Cas9 immune defense system was adapted by researchers to design the gene editing tool that has revolutionized genetic engineering¹⁰. In this technique, a guide RNA similar to the CRISPR sequence produced by bacteria is designed, that binds to the target sequence in the DNA of interest and to an enzyme called Cas9. When the Cas9-guide-RNA ribonucleoparticles identify complementary DNA to the spacer region of guide RNA, the enzyme cuts the sequence at the target site, leading to DSBs¹¹.

The CRISPR-Cas9 editing is more robust and versatile than other genome editing tools such as zinc finger nucleases and transcription activator-like (TAL) effector nucleases, because the endonucleases of the other two techniques need to be custom designed each time to complement the target sequence. Whereas the Cas9 protein is ubiquitous, with only the single-guide RNA (sgRNA) sequence being designed specifically for each target sequence in the DNA, making it a versatile DNA cutting tool¹³. CRISPR-Cas9 has also displayed higher

editing efficiency and is less expensive, making it the most popular genome editing technique to date^{1,12}.

The most commonly used CRISPR subtype is the type II CRISPR-Cas9 system, consisting of a single Cas9 protein from *Streptococcus pyogenes*. The CRISPR-Cas9 system comprises two components, a single-stranded guide RNA (sgRNA) and a Cas9 protein (Figure 1)¹⁴. The sgRNA is a duplex of a sequence of 17-20 base pairs (crRNA) and trans-activating crRNA (tracrRNA). The crRNA contains a spacer region complementary to the DNA target sequence and a region that allows pairing with tracrRNA which is needed for the activation of the Cas9. A "protospacer adjacent motif" (PAM) with "NGG" (any nucleotide-guanine-guanine) sequence upstream of the target site is essential for the recognition by the Cas9 protein. Upon binding the sgRNA with the target DNA, Cas9 cleaves the DNA at the target site to generate a DSB (Figure 2). As aforementioned, once DSBs are introduced in the DNA, the cell's repair mechanisms are activated, leading to insertion, deletion, or replacement with a customized sequence¹⁴.

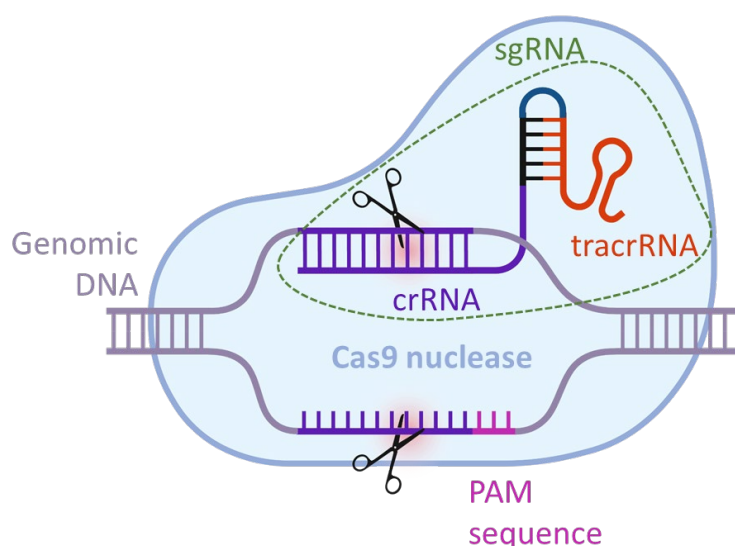


Figure 1. The components of a CRISPR-Cas9 system made of the guide RNA (sgRNA) containing the crRNA and tracrRNA, the adjacent protospacer motif (PAM) sequence, the Cas9 enzyme, and the target genomic DNA. The tracrRNA recognizes and binds Cas9 protein with the CRISPR system, crRNA interacts with the target DNA through base pairing, and the Cas9 enzyme cuts the DNA at the desired site.

Repair mechanisms

The DSBs induced by CRISPR-Cas9 are repaired through non-homologous end joining (NHEJ) or homology directed repair (HDR) (Figure 2)¹⁵. The NHEJ mechanism is activated without a repair template, where the machinery ligates the two nonhomologous ends, resulting in insertion and/or deletion mutations (indels). NHEJ is useful to produce gene knock-out models as the occurrence of indels through this error-prone mechanism does not hinder the outcome and even desirable when producing null mutants. On the other hand, HDR is a high-fidelity mechanism occurring less frequently than NHEJ, only when repair templates are available, and it helps create precise mutations at specific locations. The repair templates are usually double-stranded DNA sequences or single-stranded oligonucleotides (ssODNs). Point mutations, missense mutations, insertions/deletions, at a single nucleotide level can be achieved by using ssODNs as the repair template¹⁶.

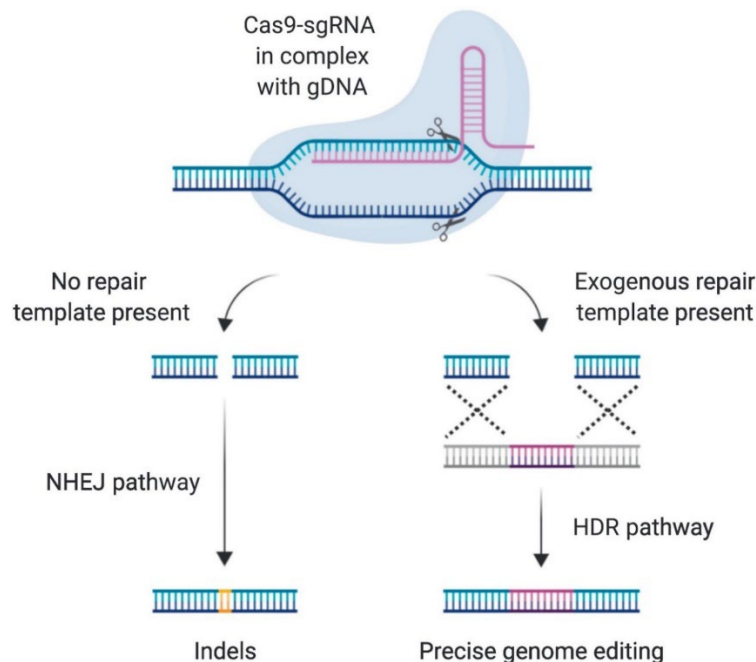


Figure 2. The two repair mechanisms to anneal the double stranded breaks introduced by CRISPR-Cas9. a) Non-homologous end joining (NHEJ) anneals the two open ends of the break, resulting in insertion and/or deletion mutations (mutant), b) Homology-directed repair (HDR) in the presence of a repair template with the desired sequence for replacement at the break site.

6.3. CRISPR-Cas9 in *Caenorhabditis elegans*

Mutated strains of *Caenorhabditis elegans* (*C. elegans*) are produced widely through CRISPR-Cas9 editing¹⁷ (Figure 3). The mixture of reagents is injected into *C. elegans*' germ line via microinjection. Mutation of the germ line cells allows the transfer of the mutation to the offspring, resulting in hundreds of mutant individuals at a time¹⁸. *C. elegans* are predominantly hermaphrodites, combined with the short life cycle facilitating the isolation of homozygous individuals in a short time (≈ 2 weeks)¹⁹. Methodologies such as co-CRISPR are employed to enhance the efficiency of screening and isolating homozygotes. co-CRISPR involves injecting the worms with another mutation that exhibits a visible phenotype such as dumpy/roller phenotypes, enabling rapid screening of the successfully mutated worms²⁰.

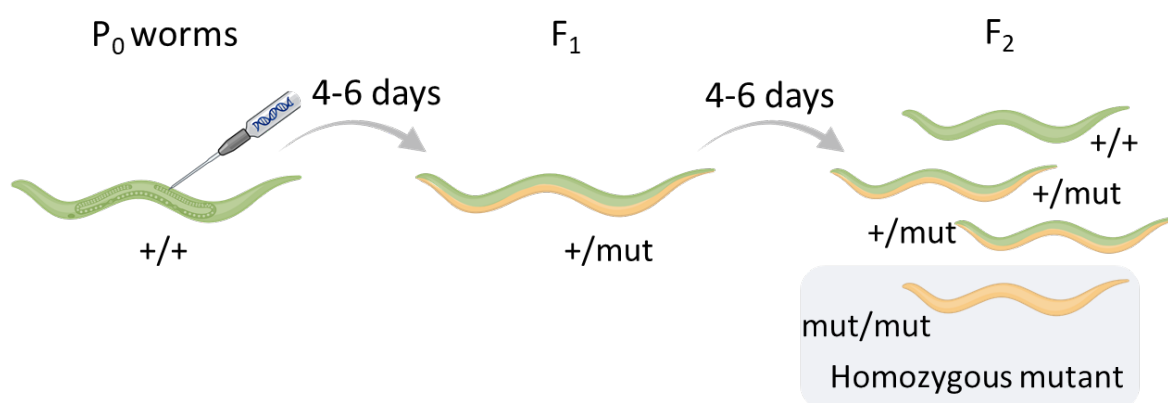


Figure 3. Schematic representation of CRISPR-Cas9 editing in *C. elegans* and isolation of homozygotes. After injection of P₀, heterozygous hermaphrodites are identified in F₁. By self-fertilization in the F₂, a quarter of the progeny segregates the mutation in homozygosity. The whole process can be achieved in less than a couple of weeks.

6.4. Arrhythmia specific mutations in *C. elegans*

Owing to the genetic homology between the voltage-gated ion channels of *C. elegans* pharynx and human heart, we focused ion channelopathies and their corresponding arrhythmic phenotypes²⁵. Significantly, the results of calcium imaging (Chapter 4) further emphasized the importance of voltage-gated calcium channels and the role of Ca²⁺ signalling on pharynx pumping, akin to human cardiac pumping. Therefore, we endeavoured to create mutations in

the calcium channels of *C. elegans* that are homologous to genes causing high-severity bradycardia mutations.

We employed the ClinVar database to identify arrhythmia causing mutations in humans and short-listed those mutations that affect Ca^{2+} homeostasis²⁶. Among those, missense mutations were prioritised since they are easier to model in *C. elegans* using CRISPR-Cas9. The main criteria for selecting a mutation to model is that it must be present in a highly conserved region in the *C. elegans* genome since genes from conserved regions show high functional relevance. Among the different genes listed in Table 1, *RYR2* and *CASQ2*, which are involved in calcium-induced calcium release from sarcoplasmic reticulum are identified in CPVT arrhythmias^{27,28}. The *unc-68* and *csq-1* genes of *C. elegans* are orthologous to human *RYR2* and *CASQ2*. Fischer *et. al.* exploited this orthology to reproduce the missense mutations in *unc-68* and *csq-1*, causing CPVT-like phenotypes in *C. elegans*²⁹.

Table1: The different arrhythmia types and associated genes and the channels the genes encode. The corresponding ortholog in *C. elegans* for each gene are also shown. Mutants of *unc-68* and *csq-1* genes in *C. elegans* (blue) have been reported to display arrhythmic phenotypes. The *egl-19* gene (maroon) is our gene of interest to create arrhythmogenic mutations.

Type of Arrhythmia	Human gene	Encoding channels & receptors	C. elegans ortholog
LQT4 / CPVT4	ANK2	Ankyrin-b	<i>unc-44</i>
LQT8/ Timothy and Brugada Syndromes/ SQT4	CACNA1C	Cav1.2	<i>egl-19</i>
LQT9	CAV3	Caveolin	<i>cav-1</i>
LQT12	SNTA1	α -1 Syntrophin	<i>stn-1</i>
CPVT	RyR2	RyR2	<i>unc-68</i> ^{29,30}
CPVT	CASQ2	Casequestrin	<i>csq-1</i> ^{29,30}
BrS4/SQT5	CACNB2b	Cav β 2b	<i>ccb-1</i>
Brs9/SQT6	CACNA2D1	Cav α 2 δ 1	<i>tag-180, unc-36</i>
Sinus bradycardia	CACNA1D	Cav1.3	<i>egl-19</i> ³¹
CPVT	CALM1	Calmodulin	<i>cmd-1</i>

Based on the required criteria and the existing literature, we chose the *egl-19* gene which is highly homologous to human *CACNA1C/D* genes, as our target gene to model arrhythmogenic mutations in *C. elegans*. In addition to genetic orthology, the two genes also share functional similarity; while *CACNA1* genes play an essential role in regulating cardiac pumping through Ca^{2+} signalling, *egl-19* gene also regulates pharyngeal pumping in *C. elegans* by mediating the Ca^{2+} dynamics. The mutations in *egl-19* genes were selected according to the homologous mutations for arrhythmia found in the human genome in the identical residues (Table2).

Table 2: Three missense mutations in *CACNA1* genes associated with long QT, timothy, and Brugada syndromes are listed: Glycine to Arginine at residue 406, Glycine to Serine at 402, and Isoleucine to threonine at 1186, along with the mutations in conserved regions of *C. elegans*.

Human <i>CACNA1</i> mutations	Associated arrhythmia	<i>C. elegans egl-19</i> mutations
Glycine406Arginine	Long QT, Timothy, Brugada syndrome ³²	Glycine369Arginine
Glycine402Serine	Long QT, Timothy syndrome ^{33,34}	Glycine365Serine
Isoleucine1186Threonine	Timothy syndrome ³⁵	Isoleucine1064Threonine

6.5. CRISPR-Cas9 editing to produce mutant strains

In this work, we utilized co-CRISPR technology to produce mutant strains of *C. elegans*, with dumpy (*dpy-10(cn64)*) allele as a co-CRISPR marker. The repair template ssODNs and the crRNA sequence were custom designed (Table 3) such that they contain the desired modification, silent mutations to avoid re-cutting by Cas9 and for genotyping, and homology arms of 35 bp to allow repair by recombination³⁶. The designed repair template sequence, crRNA sequence and other components of the injection mix were purchased from Integrated DNA technologies. The injection mix containing the Cas9 enzyme, tracrRNA sequence, crRNA for the target mutation, crRNA for *dpy-10* mutation and repair templates for both mutations (ssODN) was prepared in previously optimized ratios^{36,37} (Table 4).

Table 3: Summary of crRNAs and repair templates for missense mutations in the *egl-19* gene. **Red:** desired mutations, **green:** silent mutations.

Desired mutation	crRNA sequence	Repair template sequence
Gly369Arg	CTTGTCTTGGGAGTCT TGTC	GATCATTTTTCGTA CTCAATCTTG TCTTGGGAGTCTCTTCAAGAGAA TTCTCAAAAGAACGAGAAAAGG CAAGAGCG
Gly365Ser	CTTGTCTTGGGAGTCT TGTC	ACTCTTGTCAATCTTGGATCATT TTCGTA CTCAATCTTGTCTTGTCAG GTGCTTCTTCTGGAGAATTCTCAAA AGAACGA
Ile1064Thr	TTCATGATGAACATCT TCGT	ATCGCATTCTTCATGATGAACAT CTTGTAGGCTTGTG ACCGTTACATTCCAAAATGAAGG AGAACGTGAATACG

Table 4: The composition and corresponding volumes of each component in the injection mix with the total volume = 10 μ L.

	Volume (μ L)	Concentration (μ M)
Cas9 IDT	0.25	1.53
tracrRNA	0.50	1.60
crRNA <i>dpy-10</i>	0.40	0.40
crRNA edit	1.20	1.20
ssODN <i>dpy-10</i>	0.28	0.92
ssODN edit	0.22	2.20
RNase free water	7.15	
Total volume	10.00	

The prepared injection mix is stored in ice while preparing the microinjector setup. Briefly, ≈ 3 worms are placed on 2% agar pads containing halocarbane oil and gently immobilized using a thin filament. The microinjector is set up, the slide is placed on the platform, and the injection needle is aligned such that the needle is inclined at 45 °C to the worms' germline. The magnifications and x, y, and z-axes are adjusted to ensure that both the germline and the needle are visualized clearly in the same plane. The mix is injected while ensuring that the liquid has entered the nucleus of the germline cells, and the worms were placed individually on NGM plates.

The following day, worms with dumpy phenotypes were isolated from the pool of injected P₀ worms (F₁), to single out the successfully mutated worms and were genotyped by PCR using specific primers to confirm the mutation. ≈ 7 out of 28 injected worms showed the desired edit, yielding $\approx 25\%$ editing efficiency. After 48 hours, at least 10 progenies (F₂) of the successfully mutated worms were screened to identify and single out wild-type like worms and genotyped by PCR to select probable homozygotes containing the mutation and confirmed by Sangers sequencing. The homozygous mutated worms were verified whether the mutation resulted in lethal effects, and we found that out of the three mutations attempted, Gly369Arg mutated homozygous worms were not viable (Table 5).

Table 5: The three missense mutations produced using CRISPR-Cas9 in *C. elegans* and their homozygous viability. +/- = heterozygotes and -/- homozygous mutants.

Strain name	Viability	Phenotypes
Gly369Arg	Only +/-	Lethal
Gly365Ser	-/- viable	Pumping & other phenotypes
Ile1064Thr	-/- viable	Pumping & other phenotypes

6.6. Functional impact of the mutations

The Gly369Arg mutant was only viable in its heterozygous form, which did not exhibit any phenotypes suggesting that when both alleles of the gene are mutated, it causes lethality in worms. While in heterozygotes the wild-type allele is sufficient to compensate the phenotype. Therefore, only the mutations that resulted in viable homozygotes were considered for the evaluation of functional and physiological impacts in the worms. The Gly365Ser and Ile1064Thr mutant strains are denoted as CER696 and CER701, respectively. The worms from both the strains and wild-type were synchronized and grown to egg-bearing adult stage and imaged at adult day-1 age (AD1). The CER696 and CER701 strains attained adulthood with

eggs and other phenotypical identifications at 48 hours from L1 stage, similar to the wild-type worms (Figure 6).

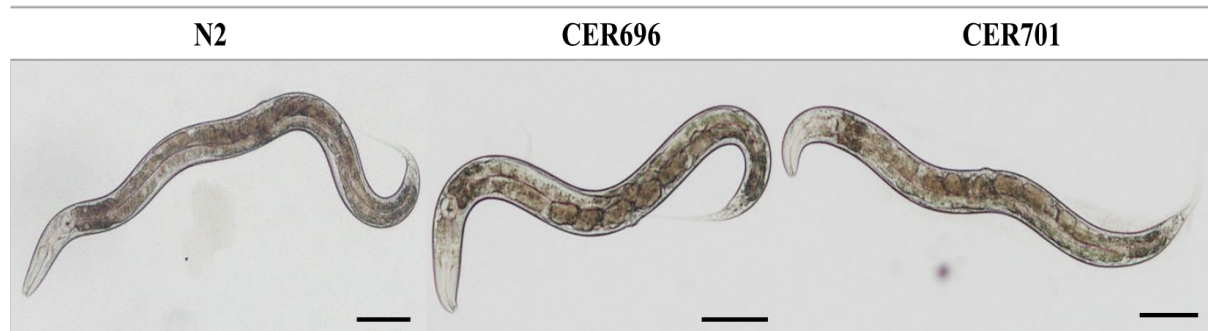


Figure 6: Representative optical microscopic images of CER696 and CER701 strain worms, compared with the wild-type N2 strain worms. Scale bar: 100 μm .

We computed the body lengths of all the three strains from the microscopic images of AD1 worms. The CER696 and CER701 worms displayed a shortened body length of an average of $\approx 950 \mu\text{m}$ and $\approx 870 \mu\text{m}$ respectively, compared to the wild-type worms which were of $\approx 1130 \mu\text{m}$ in length (Figure 7a). Notably, we found that the same mutations that cause bradycardiac effects in humans also reduced the basal pumping rate in *C. elegans*' pharynx. The CER696 and CER701 strains pump at a rate of ≈ 190 and 180 pumps/min respectively, whereas the average pumping rate of wild-type worms are ≈ 250 pumps/min (Figure 7b).

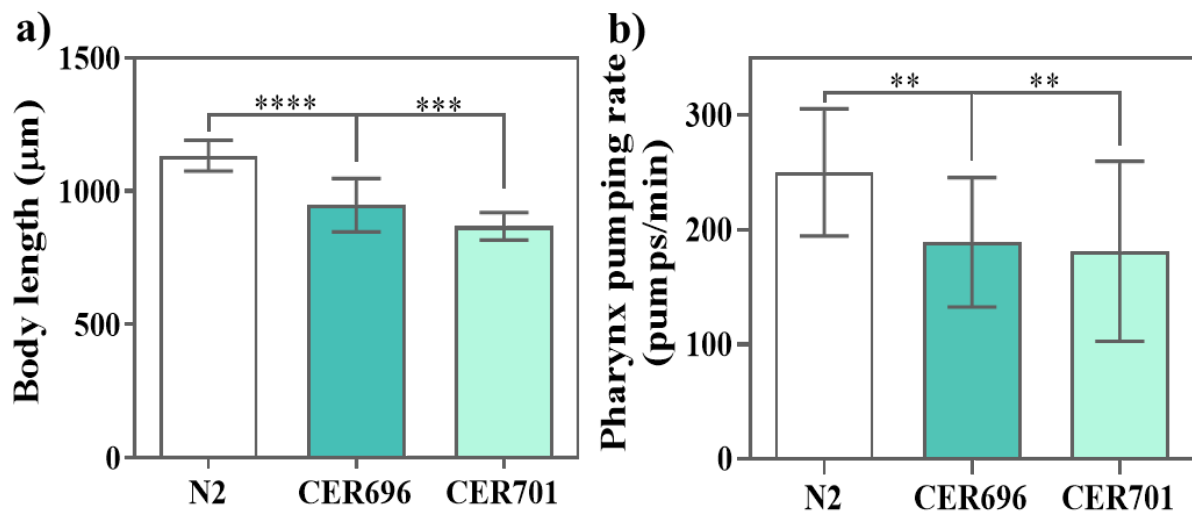


Figure 7: a) The body length of CER696 and CER701 strain worms at day-1 adult stage, in comparison with N2 strains ($N \approx 20$), b) The pharyngeal pumping rate of N2, CER696, and CER701 strain day-1 adult worms ($N \approx 30$).

The modification in pharyngeal function corroborates with the modification in cardiac function, showing us the versatility and functionality of *C. elegans* in using as arrhythmia models. Specific mutations of targets can be easily designed and utilised for evaluation of each drug, providing much more valuable information and deeper insights in to the physiological effects and mechanism of action of drugs, that is otherwise not possible with other animal models.

6.7. Conclusions

The opportunity of using *C. elegans* as arrhythmia models is emerging, with a handful of studies reporting successful incorporation of orthologous arrhythmogenic mutations in *C. elegans* resulting in arrhythmia-like phenotypes such as an impaired pumping rate^{29–31}. In this work, we showed the robustness and versatility of CRISPR-Cas9 technology and its use in *C. elegans* to produce any mutation of choice in *C. elegans* with ease. We shortlisted our mutations of interest through a literature study based on different parameters,

1. The mutations must be implicated to cause arrhythmia in humans,
2. Orthologous genes exist in *C. elegans* playing a similar functional role in the pharynx, and
3. The region containing the residue in the genome must be conserved with high functional relevance.

The three mutations we selected based on these criteria were successfully incorporated into the worms. However, the Gly369Arg mutation had critical effects on the worms, causing 100% lethality in homozygotes. Whereas for the other two mutations, we found that the worms exhibited reduced body length and a slower growth rate compared to the wild-type worms.

The reduced pumping rate was the most highlighted impact in the mutant worms. The same mutations that induce bradycardia in humans caused a reduced pumping rate in *C. elegans*. This marks the remarkable potential of exploiting *C. elegans* in arrhythmia genetics to identify genes and understand their mechanistic roles in regulating cardiac rhythm and to produce disease models for initial screening of drugs and nanoparticles. Bearing this in mind, our group is actively continuing our work in the mutant models, further evaluating other phenotypes such as life span, growth rate, aging, etc., and plan to employ these animal models to effectively assess anti-arrhythmic drugs and nanoparticles.

References

- (1) Mah, A. Genome Editing Techniques: The Tools That Enable Scientists to Alter the Genetic Code. *Synthego's The Bench Blog*, 2019, 1-12.
- (2) Li, H.; Yang, Y.; Hong, W.; Huang, M.; Wu, M.; Zhao, X. Applications of Genome Editing Technology in the Targeted Therapy of Human Diseases: Mechanisms, Advances and Prospects. *Signal Transduction and Targeted Therapy*, Springer Nature December 1, 2020.
- (3) Urnov, F. D.; Rebar, E. J.; Holmes, M. C.; Zhang, H. S.; Gregory, P. D. Genome Editing with Engineered Zinc Finger Nucleases. *Nature Reviews Genetics*, September 2010, 636–646.
- (4) Laity, J. H.; Lee, B. M.; Wright, P. E. Zinc Finger Proteins: New Insights into Structural and Functional Diversity. *Current Opinion in Structural Biology*, 2001, 11 (1), 39–46.
- (5) Carroll, D. Genome Engineering with Zinc-Finger Nucleases. *Genetics*, 2011, 188 (4), 773–782.
- (6) Joung, J. K.; Sander, J. D. TALENs: A Widely Applicable Technology for Targeted Genome Editing. *Nature Reviews Molecular Cell Biology*, January 2013, 49–55.
- (7) Bhardwaj, A.; Nain, V. TALENs—an Indispensable Tool in the Era of CRISPR: A Mini Review. *Journal of Genetic Engineering and Biotechnology*, 2021, 19(1).
- (8) Mussolino, C.; Alzubi, J.; Fine, E. J.; Morbitzer, R.; Cradick, T. J.; Lahaye, T.; Bao, G.; Cathomen, T. TALENs Facilitate Targeted Genome Editing in Human Cells with High Specificity and Low Cytotoxicity. *Nucleic Acids Research* 2014, 42 (10), 6762–6773.
- (9) Barrangou, R.; Fremaux, C.; Deveau, H.; Richards, M.; Boyaval, P.; Moineau, S.; Romero, D. A.; Horvath, P. CRISPR Provides Acquired Resistance against Viruses in Prokaryotes. *Science*, 2007, 315 (5819).
- (10) Jinek, M.; Chylinski, K.; Fonfara, I.; Hauer, M.; Doudna, J. A.; Charpentier, E. A Programmable Dual RNA-Guided DNA Endonuclease in Adaptive Bacterial Immunity. *Science*, 2012, 337 (6096), 816–821.
- (11) Jiang, W.; Bikard, D.; Cox, D.; Zhang, F.; Marraffini, L. A. RNA-Guided Editing of Bacterial Genomes Using CRISPR-Cas Systems. *Nature Biotechnology*, 2013, 31 (3), 233–239.
- (12) Loureiro, A.; Da Silva, G. J. Crispr-Cas: Converting a Bacterial Defence Mechanism into a State-of-the-Art Genetic Manipulation Tool. *Antibiotics*, 2019, 8 (1).
- (13) Hossain, M. A. CRISPR-Cas9: A Fascinating Journey from Bacterial Immune System to Human Gene Editing. In *Progress in Molecular Biology and Translational Science*, Elsevier B.V., 2021, 178, 63–83.
- (14) Dai, W. J.; Zhu, L. Y.; Yan, Z. Y.; Xu, Y.; Wang, Q. L.; Lu, X. J. CRISPR-Cas9 for in Vivo Gene Therapy: Promise and Hurdles. *Molecular Therapy - Nucleic Acids*, 2016, e349.
- (15) Ran, F. A.; Hsu, P. D.; Wright, J.; Agarwala, V.; Scott, D. A.; Zhang, F. Genome Engineering Using the CRISPR-Cas9 System. *Nature Protocols*, 2013, 8 (11), 2281–2308.
- (16) Tang, X. D.; Gao, F.; Liu, M. J.; Fan, Q. L.; Chen, D. K.; Ma, W. T. Methods for Enhancing Clustered Regularly Interspaced Short Palindromic Repeats/Cas9-Mediated Homology-Directed Repair Efficiency. *Frontiers in Genetics*, 2019, 10(JUN).

- (17) Dickinson, D. J.; Goldstein, B. CRISPR-Based Methods for *Caenorhabditis Elegans* Genome Engineering. *Genetics*, 2016, 202 (3), 885–901.
- (18) Kim, H. M.; Colaiácovo, M. P. CRISPR-Cas9-Guided Genome Engineering in *Caenorhabditis Elegans*. *Current Protocols in Molecular Biology* 2019, 129 (1).
- (19) Ceron, J.; Vicencio, J. A Living Organism in Your CRISPR Toolbox: *Caenorhabditis Elegans* Is a Rapid and Efficient Model for Developing CRISPR-Cas Technologies. *The CRISPR Journal*, 2021, 4 (1), 32–42.
- (20) Kim, H.; Ishidate, T.; Ghanta, K. S.; Seth, M.; Conte, D.; Shirayama, M.; Mello, C. C. A Co-CRISPR Strategy for Efficient Genome Editing in *Caenorhabditis Elegans*. *Genetics*, 2014, 197 (4), 1069–1080.
- (21) Hsiao, P. Y.; Tien, H. C.; Lo, C. P.; Juang, J. M. J.; Wang, Y. H.; Sung, R. J. Gene Mutations in Cardiac Arrhythmias: A Review of Recent Evidence in Ion Channelopathies. *Application of Clinical Genetics*, 2013, 6.
- (22) Moore, O. M.; Ho, K. S.; Copeland, J. S.; Parthasarathy, V.; Wehrens, X. H. T. Genome Editing and Cardiac Arrhythmias. *Cells*, 2023, 12 (10), 1363.
- (23) Curran, M. E.; Splawski, I.; Timothy, K. W.; Vincent, ~ G Michael; Green, E. D.; Keating, M. T. A Molecular Basis for Cardiac Arrhythmia: HERG Mutations Cause Long QT Syndrome, *Cell*, 1995, 80, 795-803.
- (24) Kistamás, K.; Veress, R.; Horváth, B.; Bányász, T.; Nánási, P. P.; Eisner, D. A. Calcium Handling Defects and Cardiac Arrhythmia Syndromes. *Frontiers in Pharmacology*, 2020, 11.
- (25) Shaye, D. D.; Greenwald, I. Ortholist: A Compendium of *C. Elegans* Genes with Human Orthologs. *PLoS One* 2011, 6 (5).
- (26) Landrum, M. J.; Lee, J. M.; Riley, G. R.; Jang, W.; Rubinstein, W. S.; Church, D. M.; Maglott, D. R. ClinVar: Public Archive of Relationships among Sequence Variation and Human Phenotype. *Nucleic Acids Research*, 2014, 42 (D1).
- (27) Dulhunty, A. F. Molecular Changes in the Cardiac RyR2 With Catecholaminergic Polymorphic Ventricular Tachycardia (CPVT). *Frontiers in Physiology*, 2022, 13.
- (28) Song, L.; Alcalai, R.; Arad, M.; Wolf, C. M.; Toka, O.; Conner, D. A.; Berul, C. I.; Eldar, M.; Seidman, C. E.; Seidman, J. G. Calsequestrin 2 (CASQ2) Mutations Increase Expression of Calreticulin and Ryanodine Receptors, Causing Catecholaminergic Polymorphic Ventricular Tachycardia. *Journal of Clinical Investigation*, 2007, 117 (7), 1814–1823.
- (29) Fischer, E.; Gottschalk, A.; Schüler, C. An Optogenetic Arrhythmia Model to Study Catecholaminergic Polymorphic Ventricular Tachycardia Mutations. *Scientific Reports*, 2017, 7 (1), 1–12.
- (30) Engel, M. A.; Wörmann, Y. R.; Kaestner, H.; Schüler, C. An Optogenetic Arrhythmia Model—Insertion of Several Catecholaminergic Polymorphic Ventricular Tachycardia Mutations into *Caenorhabditis Elegans* UNC-68 Disturbs Calstabin-Mediated Stabilization of the Ryanodine Receptor Homolog. *Frontiers in Physiology*, 2022, 13 (March).

- (31) Schüler, C.; Fischer, E.; Shaltiel, L.; Steuer Costa, W.; Gottschalk, A. Arrhythmogenic Effects of Mutated L-Type Ca²⁺-Channels on an Optogenetically Paced Muscular Pump in *Caenorhabditis Elegans*. *Scientific Reports*, 2015, 5 (May), 1–16.
- (32) Splawski, I.; Timothy, K. W.; Sharpe, L. M.; Decher, N.; Kumar, P.; Bloise, R.; Napolitano, C.; Schwartz, P. J.; Joseph, R. M.; Condouris, K.; Tager-Flusberg, H.; Priori, S. G.; Sanguinetti, M. C. *Ca V1.2 Calcium Channel Dysfunction Causes a Multisystem Disorder Including Arrhythmia and Autism*. 2004, 119, 19-31.
- (33) Depil, K.; Beyl, S.; Stary-Weinzinger, A.; Hohaus, A.; Timin, E.; Hering, S. Timothy Mutation Disrupts the Link between Activation and Inactivation in Ca V1.2 Protein. *Journal of Biological Chemistry*, 2011, 286 (36), 31557–31564.
- (34) Proost, D.; Saenen, J.; Vandeweyer, G.; Rotthier, A.; Alaerts, M.; Van Craenenbroeck, E. M.; Van Crombruggen, J.; Mortier, G.; Wuyts, W.; Vrints, C.; Del Favero, J.; Loeys, B.; Van Laer, L. Targeted Next-Generation Sequencing of 51 Genes Involved in Primary Electrical Disease. *Journal of Molecular Diagnostics*, 2017, 19 (3), 445–459.
- (35) Wemhöner, K.; Friedrich, C.; Stallmeyer, B.; Coffey, A. J.; Grace, A.; Zumhagen, S.; Seebohm, G.; Ortiz-Bonnin, B.; Rinné, S.; Sachse, F. B.; Schulze-Bahr, E.; Decher, N. Gain-of-Function Mutations in the Calcium Channel CACNA1C (Cav1.2) Cause Non-Syndromic Long-QT but Not Timothy Syndrome. *Journal of Molecular and Cellular Cardiology*, 2015, 80, 186–195.
- (36) Kukhtar Kukhtar, D. CRISPR-Cas9 to Model Retinitis Pigmentosa Caused by Mutations in Splicing Factors in *C. Elegans*,.Universitat de Barcelona, 2021.
- (37) Vicencio, J. Optimizing CRISPR-Cas Technologies in *Caenorhabditis Elegans*: Nested CRISPR and Expanded Targeting with Cas Variants. Universitat Pompeu Fabra, 2021.

Conclusions & Future Prospects

7.1. Conclusions

The research work presented in this thesis aimed to explore and expand the existing scientific knowledge on multiple aspects. The goal was achieved through a series of experiments that brings us to the main conclusions:

1. The synthesized polypyrrole nanoparticles (Ppy NPs) were spherical with a mean diameter of ≈ 130 nm. The polymeric NPs were made of repeating units of pyrrole, a conjugated pentose ring with aromatic secondary amines. The NPs possessed a strong and broad absorption in the entire near-infrared region, between 700-1200 nm. We also found that the nanoparticles were thermally stable, upto temperatures as high as 410 °C and conductivity of ≈ 0.8 S/cm, when synthesized from 0.1 M pyrrole monomer.
2. *Ppy NPs were biocompatible in C. elegans*, not inducing any lethal effects up to a concentration of 500 $\mu\text{g/mL}$. The growth and development were not affected by ingestion of Ppy NPs for 24 hours, as we found similar rate of development between untreated and treated worms from larval stage L4 to egg-bearing adult stage. Likewise, the NPs did not affect the reproductive system either, since the rate of reproduction and the growth and development of those progenies were also following same patterns as untreated worms.
3. At the molecular level, the NPs did not affect significantly on the lipid accumulation or oxidation, a reduction in lipid-to-protein content and enhanced lipid saturation compared to untreated worms were observed for Ppy NPs treated worms. We conclude that *Ppy NPs increases the lipid metabolism* due to a high energy and fuel consumption requirement; nevertheless, *they do not cause oxidative stress*.
4. In addition to employing *C. elegans* for toxicity evaluation of nanomaterials, we present the platform for using the worms to study cardiac rhythms with the help of pharynx, their muscular pumping organ. Two anti-arrhythmic drugs with established effects on heart rate were assessed in *C. elegans*. Propranolol (PL) reduced while Racepinephrine (RE) increased the pharynx pumping rate, similar to their effects observed in humans' cardiac pumping rate. Thus, *C. elegans can be a*

reliable and effective model to study cardiac-like effects of drugs and nanomaterials.

5. *Ppy NPs increases the pharynx pumping rate of C. elegans.* Worms with pumping impaired mutations, especially mutation in calcium channel showed more pronounced effect than wild-type worms. The simplicity and robustness of *C. elegans* allowed us to perform various experiments, such as the impact of treatment duration and post-excretion effects. We found that Ppy NPs affects the pumping rate in a *time-dependent manner*, and imparts a *moderate lasting impact* in worms, with the change in pumping rate sustaining upto 24 hours post excretion but reverting to basal rate by 72 hours.
6. Intracellular calcium levels in the pharynx were measured through calcium imaging, which suggested a strong interplay between calcium signaling, pharyngeal pumping, and the role of Ppy NPs in regulating these mechanisms. Ppy NPs caused an increase in calcium transient levels in wild-type worms, but not as much in a mutant strain with deletion mutation at the pharyngeal calcium channel. Therefore, we conclude that the *action of Ppy NPs is mediated through voltage-gated calcium channels in the pharynx*, that regulates calcium signaling and the concurring pharyngeal movements.
7. Scaffolds of Polypyrrole incorporated bacterial cellulose (BC-Ppy) were produced with tunable properties including mechanical strength, surface wettability, conductivity, and transparency, by modifying the monomer and precursor concentrations. The composites were made of continuous interconnected network of cellulose fibers of ≈ 65 nm, decorated throughout with Ppy NPs of ≈ 89 nm. We confirmed the hydrogen bonding interaction between BC and Ppy through FT-IR spectroscopy. Flexibility, transparency ductility, and surface wettability of the composite materials decreases while the surface roughness and conductivity increases with Ppy content.
8. Cell adhesion and behavior depends on all these parameters, therefore the Ppy content plays a major role. *BC-Ppy produced with 3- and 5-mM monomer concentrations (BP3 and BP5, respectively) possessed ideal characteristics for cardiac cell culturing*, with conductivities matching to native cardiac tissues, in the

order of 10^{-3} S/cm, in addition to acceptable surface wettability and tensile strength to facilitate cell viability and anchorage.

9. The immortalized cardiomyoblast cell type H9c2, displayed the *best adhesion and viability on BP5 scaffolds* with $\approx 96\%$ cell viability and 40% area coverage compared to only $\approx 85\%$ viability and 7% coverage on only BC scaffolds. The cell morphology was also strikingly different, *elongated and well spread on BP5 whereas rounded up and detached on BC surfaces*. This shows the indispensable role of Ppy NPs to promote cell adhesion.
10. The presence of Ppy NPs also highly influenced the differentiation of H9c2 towards cardiomyocyte-like phenotypes. The differentiation media containing retinoic acid facilitated maturation of the cells on both BC and BC-Ppy scaffolds. However, the BC-Ppy scaffolds were able to *promote the differentiation even without the chemical stimulation* using retinoic acid. Additionally, cells grown on the composite scaffolds expressed *elevated cardiac protein markers* compared to cells on BC scaffolds, further establishing the beneficial environment of BC-Ppy composite scaffolds for cardiac tissue engineering.

7.2. Future Prospects

The research work presented here opened up avenues that can be taken forward in two ways to accelerate the commercialization of an effective treatment for cardiac arrhythmia.

1. We tapped on the tremendous potential of the small yet powerful animal model *C. elegans* for cardiac rhythm assessments. As we can appreciate from the existing literature and the CRISPR-Cas9 editing, animals with specific types of arrhythmia can be created and drug candidates with those specific gene targets can be effectively tested. In addition to the drugs and nanoparticles reported here, other drugs in the market or nanoparticles under research can be investigated to identify unknown targets and mechanisms, and to provide extensive valuable information on parameters such as dosage, lethality, metabolic effects, genetic and molecular effects that has not been so straightforward with other animal models till date.

In our group, we are continuing this work and currently evaluating other phenotypical changes in the arrhythmia mutants, with plans to assess relevant drugs and nanomaterials in those specific strains.

2. Another possibility that this thesis has provided is the use of BC-Ppy scaffolds as effective cardiac patches. Careful designing of the material, cytocompatibility, and efficiency to promote cardiomyocyte-like behavior have been proven in this study. Having these results as foundation, evaluation of beating frequency on contractile cells such as primary cardiomyocytes, could be performed. The role of an external electrical stimulation in combination with Ppy NPs can be exploited as well. *C. elegans* are simple, small animals without a heart. They are highly useful in rapid and large-scale screening, and initial evaluations. However, the material must be subjected to further evaluation for the end application as cardiac patches.

The ideal way to take this work forward would be the evaluation of this material in multi-cellular environments, and animal models such as rodents.

Curriculum Vitae

Sumithra Yasaswini Srinivasan



Soon-to-be Ph.D. in Materials Science, from Universitat de Autonomia de Barcelona. Interested in nanomaterials and nanomedicine related research.



+34 651886427



sumithra.yasaswini@gmail.com



Barcelona, Spain



<https://www.linkedin.com/in/sumithrayasaswini/>

TECHNICAL SKILLS

- Nanoparticle synthesis
- Electron microscopy
- Spectroscopic techniques
- Caenorhabditis elegans
- Cell culture
- Microbiology

SOFT SKILLS

- Team work
- Problem-solving
- Scientific writing and communication
- Leadership

LANGUAGE

- English
- Tamil
- Hindi
- Spanish

RESEARCH EXPERIENCE

DOCTORAL RESEARCHER

Instituto de Ciencia de Materiales de Barcelona (ICMAB)

2018 - Present

Doctoral thesis entitled " Polypyrrole nanoparticles & composites: Cardiac arrhythmia treatment evaluated in cells & Caenorhabditis elegans" under the supervision of Dr. Anna Laromaine in the group of Nanoparticles & Nanocomposites.

JUNIOR RESEARCH FELLOW

Agharkar Research Institute, India

2016-2018

Nanoparticles for biomedical applications under Dr. Virendra Gajbhiye

- Mesoporous silica , iron oxide , cobalt ferrite, polypyrrole, gold, and silver nanoparticles synthesis & characterization.
- Magneto-electrical nanoparticles for sensing and purification of bacteria from liquid samples.
- Novel facile RNA/DNA isolation from fungal cells using magnetic nanoparticles.

JUNIOR RESEARCH FELLOW

Centre for Stem Cell Research, India

2015 - 2016

Identifying role of novel epigenetic regulators of erythroid differentiation and Chronic Myeloid Leukemia using third generation shRNA library lentiviral vectors with the guidance of Dr. Velayuthan Shaji.

MASTERS' THESIS STUDENT

Universitat de Barcelona, Spain

2014-2015

Thesis entitled "Interaction between GBV-C peptides and membrane lipids of nano-liposomal vesicles and their inhibitory action towards HIV-1 infection" under the supervision of Dr.Montserrat Pujol Cubelles.

EDUCATION

MASTER OF TECHNOLOGY, MEDICAL NANOTECHNOLOGY

SASTRA University, India

2014 - 2015

BACHELOR OF TECHNOLOGY IN BIOENGINEERING

SASTRA University, India

2010 - 2014

FELLOWSHIPS & GRANTS

MARIE-CURIE COFUND FELLOWSHIP

2018-2021, H2020-MSCA-DP-2016

DOctoral training programme in Functional Advanced Materials.

FRONTIER INTERDISCIPLINARY PROJECTS

2021-2023

FUNFUTURE PROGRAMME

NANOCONEXION TRAVEL GRANT

May, 2022

Travel grant to attend Nanospain 2022 conference

DESH-VIDESH SCHOLARSHIP

2014

Sponsorship by SASTRA University as a part of Semester Abroad Programme

CONFERENCES

SPANISH WORM MEETING 2019

The Institute of Photonic Sciences (ICFO, Barcelona)
March 2019

Contribution : Poster Presentation

4TH SCIENTIFIC MEETING OF BNC-B STUDENTS (JPHD2019)

Instituto de Ciencia de Materiales de Barcelona (ICMAB)
June, 2019

Contribution: Poster Presentation

3RD SPANISH CONFERENCE ON BIOMEDICAL APPLICATIONS OF NANOMATERIALS (SBAN)

Vitruual

September, 2020

Contribution: Poster Presentations

EMERGING 2021 SCHOOL: FUNCTIONAL ADVANCED MATERIALS FOR EMERGING APPLICATIONS

Instituto de Ciencia de Materiales de Barcelona (ICMAB)
June, 2021

Contribution: Oral Presentation

31ST CONFERENCE OF THE EUROPEAN SOCIETY FOR BIOMATERIALS (ESB)

Portugal (Virtual)

September, 2021

Contribution: Two poster presentations

6TH SCIENTIFIC MEETING OF BNC-B PHD STUDENTS, JPHD2021

Instituto de Ciencia de Materiales de Barcelona (ICMAB)
November 2021

Contribution: Oral presentation

PUBLICATIONS

1. S. Y. Srinivasan, P. Alvarez, D. Kukhtar, N. Benseny, J. Cerón, J. Alvarez, R. Fronteriz, M. Montero, A. Laromaine, **Arrhythmic Effects Evaluated on *Caenorhabditis elegans*: The Case of Polypyrrole Nanoparticles**. Submitted to ACS nano (ID nn-2023-033385).
2. S. Y. Srinivasan, M. Cler, O. Zapata-Arteaga, B. Dörling, M. Campoy-Quiles, E. Martinez, E. Engel, S. Perez-Amodio, A. Laromaine, **Conductive Bacterial Nanocellulose-Polypyrrole patches promote cardiomyocyte differentiation**. ACS Applied Bio Materials, Accepted: 30/05/2023.
3. Blasi, D., Gonzalez-Pato, N., Rodriguez Rodriguez, X., Diez-Zabala, I., Srinivasan, S. Y., Camarero, N., Esquivias, O., Roldán, M., Guasch, J., Laromaine, A., Gorostiza, P., Veciana, J., Ratera, I., **Ratiometric Nanothermometer Based on a Radical Excimer for In Vivo Sensing**. Small 2023, 2207806.
4. Kashyap, A., Jiménez-Jiménez, Á.L., Zhang, W., Capellades, M., Srinivasan, S., Laromaine, A., Serra, O., Figueras, M., Rencoret, J., Gutiérrez, A., Valls, M. and Coll, N.S. (2022), **Induced ligno-suberin vascular coating and tyramine-derived hydroxycinnamic acid amides restrict *Ralstonia solanacearum* colonization in resistant tomato**. New Phytol, 234: 1411-1429.
5. S. Y. Srinivasan, K. R. Gajbhiye, K. M. Paknikar, V. Gajbhiye, **Chapter 12 - Conjugated Polymer Nanoparticles as a Promising Tool for Anticancer Therapeutics**, In Polymeric Nanoparticles as a Promising Tool for Anticancer Therapeutics, Academic Press, 2019, Pages 257-280.
6. S. Y Srinivasan, K. M Paknikar, D. Bodas, and V. Gajbhiye. **Applications of cobalt ferrite nanoparticles in biomedical nanotechnology**, Nanomedicine 2018 13:10, 1221-1238
7. S. Y Srinivasan, V. Gajbhiye and D. Bodas. **Development of nano-immunosensor with magnetic separation and electrical detection of *Escherichia coli* using antibody conjugated Fe₃O₄@Ppy**, Nanotechnology, 2021, 32 085603
8. S. Y. Srinivasan, K. M. Paknikar, V. Gajbhiye, D. Bodas, **Magneto-Conducting Core/Shell Nanoparticles for Biomedical Applications**, ChemNanoMat 2018, 4, 151.

CONFERENCES

NANOSPAIN2022

Universidad Politecnica de Madrid, Madrid
May, 2022
Contribution: Oral presentation

5TH INTERNATIONAL SYMPOSIUM ON BACTERIAL CELLULOSE

Jena, Germany
September, 2022
Contribution: Oral presentation

VIII SPANISH WORM MEETING

LOGROÑO, SPAIN
October, 2022
Contribution: Oral presentation

RESEARCH STAYS

CALCIUM IMAGING IN C. ELEGANS

Institute of Biomedicine and Molecular Genetics (IBGM)
July, 2021
Calcium imaging to study difference in calcium levels upon nanoparticle treatment

GENOME EDITING IN C. ELEGANS

Institute of Biomedical Research of Bellvitge (IDIBELL)
July, 2021
Calcium imaging to study difference in calcium levels upon nanoparticle treatment

This document is confidential and is proprietary to the American Chemical Society and its authors. Do not copy or disclose without written permission. If you have received this item in error, notify the sender and delete all copies.

**Conductive Bacterial Nanocellulose-Polypyrrole patches
promote cardiomyocyte differentiation**

Journal:	<i>ACS Applied Bio Materials</i>
Manuscript ID	mt-2023-00303k.R1
Manuscript Type:	Article
Date Submitted by the Author:	26-May-2023
Complete List of Authors:	Srinivasan, Sumithra Yasaswini; Institut de Ciencia de Materials de Barcelona Cler, Marina; Institut de Bioenginyeria de Catalunya Zapata-Arteaga, Osnat; ICMAB, Nanostructured Materials Döring, Bernhard; Institut de Ciencia de Materials de Barcelona Campoy-Quiles, Mariano; Campus de la Universitat Autònoma de Barcelona , Institut de Ciència de Materials de Barcelona Martinez, Elena; Institut de Bioenginyeria de Catalunya, Biomimetic systems for cell engineering Engel, Elisabeth; IBEC Perez-Amodio, Soledad; Institute for Bioengineering in Catalonia Laromaine, Anna; Institut de Ciència de Materials de Barcelona, Institut de Ciencia de Materials de Barcelona

SCHOLARONE™
Manuscripts

Conductive Bacterial Nanocellulose-Polypyrrole patches promote cardiomyocyte differentiation

Sumithra Yaraswini Srinivasan ^{± 1}, Marina Cler ^{±2,3,4,5}, Osnat Zapata-Arteaga ¹, Bernhard Döring, Mariano Campoy-Quiles ¹, Elena Martínez ^{3,4,6}, Elisabeth Engel ^{2,4,5}, Soledad Pérez-Amodio ^{*2,4,5}, Anna Laromaine ^{*1}

*Email: sperez@ibecbarcelona.eu

*Email: alaromaine@icmab.es

¹ Institute of Material Science of Barcelona (ICMAB), CSIC, Campus UAB, 08193 Bellaterra, Spain

² IMEM-BRT group, Departament de Ciència i Enginyeria de Materials, Universitat Politècnica de Catalunya, 08028 Barcelona, Spain

³ Biomimetic Systems for Cell Engineering, Institute for Bioengineering of Catalonia (IBEC), The Barcelona Institute of Science and Technology, 08028 Barcelona, Spain

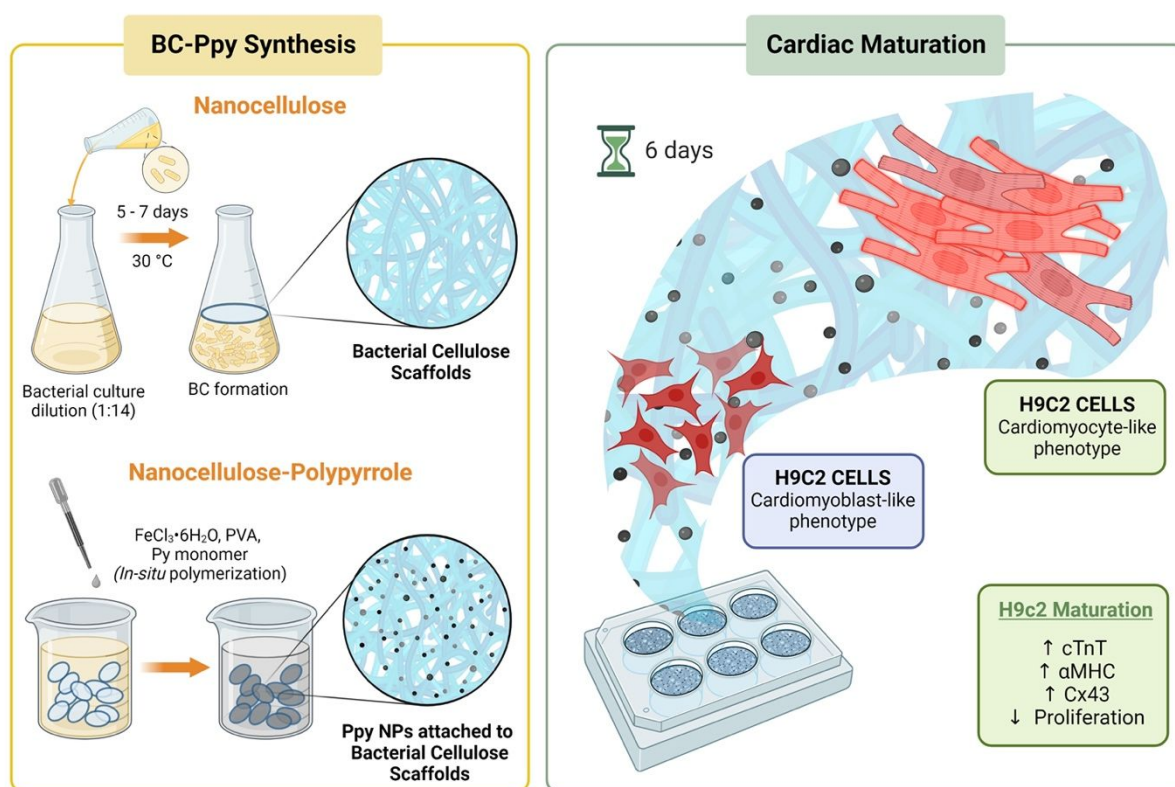
⁴ CIBER en Bioingeniería, Biomateriales y Nanomedicina, CIBER-BBN, 28029 Madrid, Spain

⁵ Biomaterials for Regenerative Therapies, Institute of Bioengineering Catalunya (IBEC), The Barcelona Institute of Science and Technology, 08028 Barcelona, Spain

⁶ Department of Electronics and Biomedical Engineering, University of Barcelona (UB), 08028 Barcelona, Spain

± Those authors contributed equally to the work *corresponding authors

Graphical Abstract



Keywords: Bacterial nanocellulose, Polypyrrole, Conducting polymers, Tissue Engineering, Cardiac patches

Abstract

The low endogenous regenerative capacity of the heart, added to the prevalence of cardiovascular diseases, triggered the advent of cardiac tissue engineering in the last decades. The myocardial niche plays a critical role in directing the function and fate of cardiomyocytes; therefore, engineering a biomimetic scaffold holds excellent promise. We produced an electroconductive cardiac patch of bacterial nanocellulose (BC) with polypyrrole nanoparticles (Ppy NPs) to mimic the natural myocardial microenvironment. BC offers a 3D interconnected fiber structure with high flexibility, which is ideal for hosting Ppy nanoparticles. BC-Ppy composites were produced by decorating the network of BC fibers (65 ± 12 nm) with conductive Ppy nanoparticles (83 ± 8 nm). Ppy NPs effectively augment the conductivity, surface roughness, and thickness of BC composites despite reducing scaffolds' transparency. BC-Ppy composites were flexible (up to 10mM Ppy), maintained their intricate 3D ECM-like mesh structure in all Ppy concentrations tested, and displayed electrical conductivities in the range of native cardiac tissue. Furthermore, these novel materials exhibit tensile strength, surface roughness, and wettability values appropriate for their final use as cardiac patches. *In-vitro* experiments with cardiac fibroblasts and H9c2 cells confirmed the exceptional biocompatibility of BC-Ppy composites. BC-Ppy scaffolds improved cell viability and attachment, promoting a desirable cardiomyoblast morphology. Biochemical analyses revealed that H9c2 cells showed different cardiomyocyte phenotypes and distinct levels of maturity depending on the amount of Ppy in the substrate used. Specifically, the employment of BC-Ppy composites drives partial H9c2 differentiation towards a cardiomyocyte-like phenotype. The scaffolds increase the expression of functional cardiac markers in H9c2 cells, indicative of a higher differentiation efficiency, which is not observed with plain BC. Our results highlight the remarkable potential use of BC-Ppy scaffolds as a cardiac patch in tissue regenerative therapies.

Introduction

Cardiovascular diseases (CVD) are the leading cause of death globally, accounting for nearly 45% of all deaths in Europe^{1,2}. Cardiac arrhythmia (CA) is a prevalent condition occurring in as much as 90% of primary heart patients³. One of the primary causes of CA is myocardial infarction (MI), where a region of the cardiac muscle is damaged⁴. The heart has a limited regenerative ability⁵; consequently, cardiomyocytes lost due to MI cannot be replaced. Heart transplantation is currently the best available long-lasting treatment for severely damaged hearts. However, the lack of donor organs, compatibility requirements, the need for life-long immune suppression, and host immune rejection are still serious hurdles^{6,7}, which promoted the rise of cardiac tissue engineering (TE).

To regenerate damaged myocardial tissue, TE employs cells, scaffolds, and growth factors (or a combination of these)⁸. Researchers have investigated the possibility of injecting viable cells, such as stem or progenitor cells, into the infarcted myocardium to induce myocyte regeneration^{9,10}. However, this approach is limited by poor cell viability, low cell retention at the affected area, cell aggregation, and the inability to generate new functional cardiac tissues^{11–14}. The employment of scaffolds that can serve as delivery platforms have improved cell behavior *in-vivo* and *in-vitro* and enhanced the therapeutic effect of cell-based therapies^{10,15}. Inferred outcomes are directly dependent on the intrinsic properties of the engineered biomaterials; therefore, a proper design considering the requirements for its final application to the native tissue is crucial.

Topographical, biochemical, and electrical cues at the micro- and nanoscale are essential determinants of cardiac organization, morphology, and electrical and mechanical function. The heart is an electrically conducting organ, mediated by ionic diffusion at the neuromuscular junction and within the cardiomyocytes that generate action potentials and propagate electrical signals, leading to muscle contraction. Therefore, a scaffold for cardiac TE should mimic the native cardiac microenvironment, be cytocompatible, and possess appropriate mechanical and electrical properties to promote cell organization, survival, and function in the damaged host cardiac tissue^{16,17}. Chitosan, collagen, alginate, and extracellular matrix (ECM) from decellularized cardiac tissue are biomaterials explored in cardiac TE^{15–19}. However, none of these materials possess electrical conductivity and thus do not adequately mimic the intrinsic characteristics of the natural myocardial microenvironment. To tackle this, current approaches employing engineered cardiac scaffolds with electroconductive biomaterials, such as intrinsically conducting conjugated polymers (CPs), are being actively researched^{16,20–26}.

Among CPs, polypyrrole (Ppy) is a popular candidate since it can be synthesized using a simple oxidative polymerization method, it is dispersible in water with good aqueous stability, is biocompatible, possess tunable electrical conductivity, and can be combined with a large variety of biomaterials to form bio-nanocomposites^{22,27–29}. However, like most other CPs, PPy is insoluble and mechanically rigid on its own, which can affect its interaction with the elastic tissues of the heart. This work proposes a strategy combining Ppy with bacterial cellulose to produce cytocompatible, conductive, and flexible scaffolds for cardiac TE. Bacterial cellulose (BC) is a natural polymer with high purity compared to plant-derived cellulose, high porosity, and water retention capacity. BC is biocompatible³⁰, produced with low endotoxin levels (0.04 ± 0.01 endotoxin units (EU)/mL)³¹, non-immunogenic^{32–34}, and not bio-degradable, thus offering

longer residence time on the heart surface compared to natural hydrogel systems. BC films are highly flexible with excellent mechanical strength (up to 250 MPa) to withstand chronic shear stress and repeated contractile force. The fibrous mesh-like microstructure of BC highly resembles the extracellular matrix³⁰, mimicking the natural myocardial microenvironment, and incorporating Ppy in the BC films imparts electrical properties^{35–38}. Scaffolds combining plant-derived cellulose and Ppy have been reported for neuronal tissue engineering^{37,39} and cardiac applications^{40,41}; however, the use of bacterial cellulose, BC-Ppy, has not been evaluated for cardiac TE purposes.

BC-Ppy composites produced in this work are assessed using primary cardiac fibroblasts and H9c2 cells. We have highlighted the ability of BC-Ppy scaffolds to promote H9c2 differentiation to evaluate the materials in realistic environments resembling the adult cardiac tissue, which we believe is cardinal to ensure a high translational value of the cardiac patches.

Materials & Methods

BC films

A commercial *Komagataeibacter xylinus* strain (NCIMB 5346, CECT, Valencia, Spain) was used for BC production. The bacterial strain was maintained in agar plates with Hestrin-Schramm (HS) medium as the growth media containing peptone, agar, yeast, glucose (Condalab), citric acid, and Na₂HPO₄·12H₂O (Sigma-Aldrich). Bacterial solutions were diluted with fresh media (1:14 ratio) and were maintained for 5-7 days in culture well plates, as previously described⁴². BC films were carefully harvested and washed once in 50% ethanol (Panreac), twice in boiling 0.1 M NaOH (Sigma-Aldrich), and then rinsed with water to obtain neutral pH. BC films were stored at room temperature in water until use. For material characterization, BC films were dried at 60 °C for 2-3 days by placing them between Teflon plates under a 1Kg-weight.

BC-Ppy films

Ppy nanoparticles (NPs) were synthesized using *in-situ* oxidative polymerization in the presence of pre-synthesized BC films, as previously described⁴³. For the BC-Ppy synthesis, pyrrole (Sigma-Aldrich), polyvinyl alcohol (PVA) (average Mw: 30,000 – 70,000, 87-90% hydrolyzed, Sigma-Aldrich), and FeCl₃·6H₂O (Merck) were used. Wet BC films were added to an aqueous solution containing 7.5% PVA (wt/wt of monomer) as the surfactant and ferric chloride hexahydrate as the oxidant (2.4 times Py monomer concentration) and stirred slowly for 1 hour to allow absorption of the reactants into the BC films. Then, pyrrole monomer (1-100 mM) was added dropwise to it under slow stirring, and the polymerization was carried out for 4h at room temperature. The resulting BC-Ppy films were washed in distilled water until the supernatant was clear. The BC-Ppy films were dried at 60 °C for 2-3 days by placing them in between Teflon plates with a 1 Kg weight on top. *In-vitro* experiments were performed in dried BC composites to facilitate sterilization procedures before cell culture. Nevertheless, some cell culture experiments were conducted as well with BC composites prior to the drying process (referred to as “wet” materials). This was done to confirm akin behavior of the composites before and after drying treatment.

Scanning Electron Microscopy

BC-Ppy films were blended for 30 min and centrifuged at 9000 rpm for 15 min. The pellet was then dried at 60 °C and crushed using a pestle and mortar to yield powder. The powder was dispersed in water and sonicated for 5-10 min before sample preparation. The liquid was dropped on carbon tape mounted over an aluminum sample holder for SEM characterization and imaged in a Scanning Electron Microscope (QUANTA FEI 200 FEG-ESEM, voltage of 20kV, working distance of 8 mm, magnification levels of 10, 20, 40, and 100 kX).

Transmission Electron Microscopy

TEM samples were prepared in the same manner as SEM samples. A single drop of BC-Ppy aqueous dispersion was placed on top of a copper grid and dried at room temperature prior to imaging. Samples were imaged with a Transmission Electron Microscope (JEOL JEM-1210, voltage of 120 kV, magnification levels of 3, 6, 8, 10, and 20 kX). The size of BC fibers and Ppy NPs from TEM images were analyzed using ImageJ software.

Surface Roughness

The effect of Ppy on the surface roughness of the composites was studied using Atomic Force Microscopy (AFM). BC and BC-Ppy (1 mM) composites were prepared as usual and dried directly on top of a cover glass at room temperature. The films adhered strongly to the glass cover enabling scanning by the AFM probe on the surface. The scanning was performed in tapping mode, for a 30x30 μm area, and at least 3 regions per sample and 3 samples per concentration were scanned.

FTIR and UV-Vis-NIR Spectroscopy

The chemical structure and composition of the as-synthesized Ppy and BC-Ppy were characterized by Attenuated Total Reflectance-Fourier Transform Infrared (ATR-FTIR) spectroscopy (Spectrophotometer Jasco 4700) at a spectral range of 400-4000 cm^{-1} . The absorbance spectra of Ppy NPs and BC-Ppy were measured using a Cary 5000 UV-Vis-NIR spectrophotometer at a wavelength range of 200-1600 nm. Ppy NPs were dispersed in water by sonication and analyzed in liquid form, whereas BC-Ppy films were prepared at a 5 mM concentration to yield semi-translucent BC-Ppy films to allow light transmission.

Electrical Conductivity

The sheet resistance of dried BC-Ppy films was measured using an in-house 4-probe resistance measuring system using the Van der Pauw method⁴⁴. Film thickness was measured using a digital micrometer by choosing 5 points of contact on each film and taking the average. The electrical conductivity σ can then be calculated as follows:

$$\sigma = 1 / (R_{\text{sheet}} * t),$$

where, R_{sheet} is the sheet resistance of each film and t is its average thickness. The electrical conductivity of high-concentration materials (10, 50, and 100 mM) was measured as individual films. However, lower concentrations possessed conductivities below the range of our instruments. Consequently, at lower concentrations (1, 3, and 5 mM), five BC-Ppy films were stacked and dried together, forming a single thicker film with conductivity in the detectable range. Then, we computed the conductivity of the stacked films and extrapolated it to obtain the values of the individual films.

Stability of BC-Ppy

The stability of BC-Ppy materials was evaluated by visual observation, UV-Vis-NIR, and conductivity at different conditions. 0.1 M BC-Ppy nanocomposites, which had the highest concentration of Ppy tested, were employed for this analysis. First, the materials were evaluated over time: BC-Ppy was stored for six months at room temperature in sterile milli-Q water. The supernatant was collected, and UV-Vis-NIR scan was performed to analyze whether any Ppy-NPs had leached out from the composites into the supernatant. Further, the leaching of Ppy NPs into the supernatant was also assessed after 30 minutes of UV sterilization on each side of the films and after autoclaving at 121 $^{\circ}\text{C}$ for 20 minutes. The stability was also evaluated after incubation in the cell culture medium. BC-Ppy materials were incubated in Dulbecco's modified Eagle's medium (DMEM, GibcoTM, Invitrogen) medium for 24h at 37 $^{\circ}\text{C}$. Then, culture media was collected, and the presence of Ppy NPs in the supernatant was investigated. BC-Ppy scaffolds were then dried for 24h after being subjected to these four processes (water storage,

UV sterilization, autoclaving, and immersion in cell culture media). Following this, conductivity was measured and compared to the initial samples.

Mechanical Properties

The tensile strength and breaking strain of the materials were measured by cyclic uniaxial tensile and biaxial tensile tests. For both, Instron MicroTester 5548 (University of Zaragoza) at a test speed of 5 mm/min was used with a 5N and 10 N load cell for the uniaxial and biaxial tests, respectively. For uniaxial tests, BC and BC-Ppy at different concentrations were grown to dog-bone shapes using 3D-printed molds and were clamped at the two ends. Under submerged conditions, the material was pulled from both ends with a 60 mm distance between the clamps until the samples experienced a fracture and failed (Figure S1A). We measured the increase in the sample's length after elongation. Here, the measured length was the distance between two holding clamps and not the total length of the sample. Load vs. deformation data was obtained and then converted to stress vs. strain according to the formulae:

$$\text{Stress (MPa)} = \frac{\text{Load (N)}}{\text{Cross-sectional area (mm}^2\text{)}}$$

$$\text{Strain} = \frac{\text{Deformed length (mm)}}{\text{Original length (mm)}}$$

From the stress-strain curve, the maximum stress that a sample can withstand before failure is defined as its tensile strength. The strain at which sample fracture occurs is referred to as breaking strain, and the initial slope of the curve represents Young's modulus of a material. These properties together define the stiffness of a given material.

For the biaxial tensile test, the material was pulled at a uniform rate from all four directions. Therefore, two load-deformation curves were obtained from the two axes. The load-deformation was converted to stress vs. strain using the above formula, where the initial distance between the clamps was 9.5 mm (Figure S1B).

Surface wettability

The surface wettability was assessed through contact angle measurements for BC, and BP1, BP3, BP5, and BP10 composite materials. The films were dried and rewet in Milli-Q water for 24 hours. The rehydrated films were placed on top of a glass slide to facilitate adhesion of the films on the glass and provide a flat surface for a precise angle measurement. The adhered films were placed on the platform and a drop (4 μ L) of either DMEM or water is deposited at a rate of 1185 μ L/min on top to measure the DMEM/water contact angle, respectively. The solvent drop on the surface is captured and angles were measured, using a Drop Shape Analyzer DSA 100 (KRÜSS).

Cell culture

Low-adherent well plates were prepared by coating them with 5 mg/ml Poly (2-hydroxyethyl methacrylate) solution (Sigma) and stored sealed at 4°C until use. BC and BC-Ppy materials were sterilized with UV irradiation for 15 minutes on each side and secured by polytetrafluoroethylene rings at the bottom of each well. The scaffolds were immersed in DMEM containing 4.5 g/l glucose, 50% FBS (Gibco™, Invitrogen), and incubated overnight inside a

cell culture incubator at 37 °C with 5% CO₂. Scaffolds were coated with collagen (100 mg/ml, VitroCol®, Advanced Biomatrix) prior to myoblast seeding.

Thirty thousand cardiomyoblasts/cm² or fifteen thousand cardiac fibroblasts/cm² were seeded on top of each scaffold. Culture plastic wells (without scaffolds) were used as controls. Adult human cardiac fibroblasts (p5-p6, PromoCell®) were cultured in low-serum Fibroblast Growth Medium (PromoCell®), whereas H9c2 rat cardiac myoblasts (p2-p9, ATCC) were cultured with DMEM containing 4.5 g/l glucose, 10% FBS, 1% L-Glutamine (Gibco™, Thermo Fisher) and 1% penicillin/streptomycin (Gibco™, Invitrogen). Cultures were maintained in a humidified atmosphere with 5% CO₂ at 37 °C, and culture media was changed every two days.

Cell viability

The cytocompatibility of BC composites was examined through a LIFE/DEAD Assay. After culturing the cells onto the materials, these were washed in DPBS (Gibco™, Thermo Fisher) and incubated in a solution of 2 μM calcein-AM (Sigma) and 4 μM propidium iodide (Fluka) in DPBS for 20 minutes at 37 °C. Cells were then washed in DPBS and immediately imaged using a motorized wide-field microscope Leica Thunder 3D Live Cell. The number of alive and dead cells was quantified using ImageJ software. For analysis, a minimum of four pictures were quantified and averaged per sample.

Cellular viability was further validated by using the 3-(4,5-dimethylthiazol-2-yl)-2,5-diphenyltetrazolium Bromide (MTT) assay (ROCHE, Sigma Aldrich) according to the manufacturer's instructions. Briefly, MTT labeling reagent (final concentration 0.5 mg/ml) was added to each well and incubated for 4 hours in a humidified atmosphere (37 °C, 5% CO₂). Then, the solubilization buffer was added to the reaction and incubated overnight. After total solubilization of the purple formazan crystals, samples were collected in three replicates in a 96-well plate. The absorbance signal (wavelength: 580 nm, reference wavelength: 650nm) was measured in a TECAN Infinite M200 Pro microplate reader.

Cell adhesion and morphology

Cellular morphology and attachment were further monitored throughout the culture period, and phase contrast images were taken using a Leica DM IL LED Fluorescence microscope. Similarly, immunostaining images of cellular actin (Phalloidin-TRITC, Sigma Aldrich) were taken at different time points to observe cellular morphology using a wide-field microscope (Leica Thunder 3D Live Cell).

After 7 days of culture, cells were fixed with 2.5% glutaraldehyde in phosphate buffer. Fixed samples were then washed four times and dehydrated by immersion in increasing alcohol concentrations. Next, the specimens were dried by critical point drying and mounted on a metal stub using a sticky carbon disc tape to increase conductivity. Samples were then coated with an ultra-thin gold layer and observed in a Field Emission Scanning Electron Microscope (NOVA NanoSEM 230, FEI Company, IBEC).

H9c2 differentiation

H9c2 cells were seeded at a density of 30000 cells/cm² and maintained in a proliferative state overnight by culturing in growth media (high-glucose DMEM supplemented with 10% FBS, 1% L-Glutamine, and 1% penicillin/streptomycin) at 37 °C in a humidified atmosphere of 5% CO₂. Differentiation was performed by adapting previously described protocols^{45,46}. Briefly, cell growth media was changed to differentiation media (high-glucose DMEM (same

supplementation) using 1% FBS and 10 nM retinoic acid (Sigma) supplementation to improve cardiomyocyte yield). Culture in this media was continued for at least 6 days with daily media changes in the dark. All-trans-RA was prepared in DMSO and stored at -20°C in the dark to avoid degradation.

Western Blot

Protein expression of cardiomyocyte markers was studied by Western Blot. Protein samples were prepared by lysing cells with Pierce® RIPA Buffer (Thermo Fisher) supplemented with a protease inhibitor cocktail (Abcam) for 10 minutes shaking on ice. Then, samples were centrifuged for 10 minutes at 4 °C at 10,000G, and the supernatant was collected and stored at -80 °C until analysis. Total protein content was measured with a Pierce™ BCA Protein Assay Kit (Thermo Scientific) following the manufacturer's instructions. Equal protein amounts were mixed with Laemmli Sample Buffer (Bio-Rad) and denatured at 95 °C for 5 minutes. Samples were loaded in 10% Mini-PROTEAN® TGX™ Precast Protein Gels (Bio-Rad) and run at constant amperage (20mA/gel) for 1-2 hours. Protein samples were transferred onto a nitrocellulose membrane (Bio-Rad) by wet transfer at 100V for 1 hour at 4°C. Ponceau staining was used to assess a correct protein transfer. Membranes were blocked in Tris-buffered saline containing 0.1% Tween® 20 (TTBS) with 5% skim milk for 1 hour at room temperature and incubated overnight with primary antibodies at 4°C. Antibodies against Cardiac Troponin T (sc-20025 mouse monoclonal antibody, Santa Cruz, 1:1000), Connexin-43 (ab11370 rabbit polyclonal antibody, Abcam, 1:2000), and Heavy Chain Cardiac Myosin (ab50967 mouse monoclonal antibody, Abcam, 1:1000) were employed. GAPDH (PA1-987 rabbit polyclonal, Thermo Fisher, 1:2000) and Vinculin (V9131, Merck, 1:200) were used as loading controls to normalize the data. Horseradish peroxidase-conjugated antibodies against rabbit (ab97051, Abcam, 1:10000) or mouse (ab97023, Abcam, 1:5000) were used in TTBS-5% skim milk solution and incubated for 1 hour at room temperature. Membranes were developed using Clarity™ Western ECL Substrate (Bio-Rad), and the chemiluminescence was detected in a densitograph (AS4000 Imaging System, GE Healthcare Life Sciences). Quantitative analysis was performed using ImageJ software.

Immunostaining

Following culture, cells were washed in PBS and fixed in 4% formaldehyde solution (Electron Microscopy Sciences) for 10 min at room temperature. Fixed cells were then washed in cold PBS with 0.15% glycine (Sigma) three times, permeabilized in 0.05% Triton X-100 (Sigma) in PBS-0.15% Gly, and blocked in PBS-0.15% Gly-5% BSA solution for 45 minutes at room temperature. Cells were incubated with the corresponding primary antibody (Cardiac Troponin T (sc-20025 mouse monoclonal antibody, Santa Cruz, 1:100), Ki67 (ab16667 rabbit monoclonal antibody, Abcam, 1:250), Ryanodine R Receptor (ab219798 rabbit monoclonal antibody, Abcam, 1:100)) in PBS-0.15% Gly-1% BSA at 4°C overnight. Then, cells were washed three times for 5 minutes in PBS-0.15% Gly. Samples were then incubated with the corresponding secondary antibody in PBS-0.15% Gly-1% BSA for 1 hour at room temperature in the darkness (goat anti-mouse Alexa Fluor® 488 ab150113, 1:500 and donkey anti-rabbit Alexa Fluor® 647 ab150075, 1:500). Cells were then washed three times, counterstained with 4',6-diamidino-2-phenylindole (DAPI, Sigma, 1:500) and actin (Phalloidin-TRITC, Sigma Aldrich P1951, 3.5:500) for 30 min, washed three times again and stored in PBS at 4 °C until imaged. Immunolabelled samples were imaged using a wide-field microscope (Leica Thunder

3D Live Cell). At least four images per sample were analyzed. Quantitative image analysis was performed using ImageJ software.

Statistical Analysis

Data are presented as mean and error bars representing standard deviation (SD) from biological replicates. GraphPad Prism 9.4 was used as analysis and graphical software. Student's T-test (two-tailed distribution) was generally used to compare two samples, one-way ANOVA followed by post-hoc Tukey's test was used for multiple samples, and two-way ANOVA was used when two different categorical independent variables were tested for multiple samples. A p-value < 0.05 was considered statistically significant. Significance was represented as follows: * = $p < 0.05$, ** = $p < 0.01$, *** = $p < 0.001$, **** = $p < 0.0001$.

Results and Discussion

BC-Ppy synthesis

Bacterial cellulose (BC) films were naturally produced by *K. xylinus* bacteria, extracellularly, at the medium-air interface. In brief, the monomer (pyrrole) was added to a solution of PVA + FeCl₃·6H₂O in the presence of BC films. Here, the FeCl₃·6H₂O was used as an oxidant-cum-dopant providing the dopant anion Cl⁻, whereas PVA acts as a biocompatible surfactant controlling the size of Ppy NPs and preventing their aggregation (Figure S2A).

The composition and properties of BC-Ppy composites can be easily tuned by modifying the precursor concentration. Hence, we prepared BC-Ppy using different starting Py monomer concentrations from 1 mM to 100 mM. BC films changed color from white (transparent) to yellow – dark-green – black (opaque) color, reducing the transparency with increasing monomer concentrations (Figure 1). The thickness of the scaffolds also increased after Ppy functionalization, reaching up to ≈140 μm at the highest concentration (100 mM Py) in the dry state, whereas the initial dried BC films were ≈11 μm in thickness (Figure 1). BC-Ppy composites maintained the inherent flexibility of BC up to 50mM Py concentration. High Ppy content fragilized the composite and some breaks were observed upon bending (see Figure 1 and red arrows).

The BC-Ppy composites synthesis is simple and highly versatile. We used a commercial BC scaffold, cube of 1 cm, to incorporate Ppy and create a thick 3D structure. Ppy NPs were incorporated homogeneously within the 3D structure as the same color was observed in the exterior and the cross-section of the cube (Figure S2B), confirming the capability of extending to different BC structures.

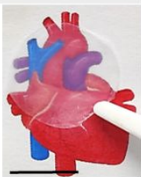
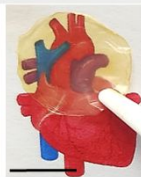

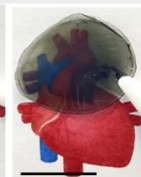
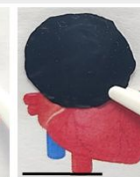

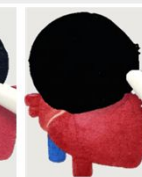





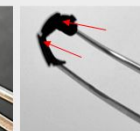
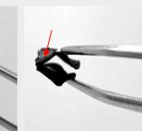
Sample	BC	BP1	BP3	BP5	BP10	BP50	BP100
[Py] (mM)	0	1	3	5	10	50	100
Thickness (μm)	11.0 ± 1.3	13 ± 2.6	17.9 ± 1.8	25.8 ± 5.1	44.9 ± 15.8	113.2 ± 25.7	139.8 ± 27.9
Conductivity (S/cm)	0	1.7 x 10 ⁻⁸	3.2 x 10 ⁻⁵	7.0 x 10 ⁻³	0.02±0.01	2±1	3±1
Color & Transparency							
Flexibility							

Figure 1 – Effect of Py concentration on scaffolds’ properties. Bacterial nanocellulose (BC) and Bacterial nanocellulose-Polypyrrole nanocomposites (BC-Ppy) at different concentrations of pyrrole (Py) and their change of properties. Scale bars: 1 cm.

Size and Morphology

At the micron scale, scanning electron microscopy (SEM) of BC-Ppy revealed that Ppy NPs had a spherical shape and were homogeneously distributed along the BC fibers (Figure 2A). The diameters of Ppy NPs and BC fibers were computed from TEM images and found to be 83 ± 8 and 65 ± 12 nm, respectively (Figure S3). Decoration of BC fibers with Ppy NPs does not affect the fiber diameter compared to plain BC. The composites exhibited fibers of uniform diameter throughout the films, possessing branches displaying a random mesh-like structure, similar to the ECM³⁰ (Figure 2A). It is also worth noting that, despite severe sample processing of the composites (involving blending, drying, and grinding), the NPs are still bound to the fibers, suggesting a strong interaction between the two components (Figure 2B).

Chemical Properties

The FTIR spectra of BC, Ppy NPs, and BC-Ppy composites are shown in Figure 2C. Spectra presented a peak around 3326 cm^{-1} corresponding to the -OH vibrations of BC, whereas the peak at 3249 cm^{-1} is assigned to the Ppy aromatic secondary amine (N-H) stretching. This latter peak shifted to 3345 cm^{-1} for the BC-Ppy composites, indicating a plausible hydrogen bonding between the -NH group of Ppy and the -OH group of cellulose³⁵ (Figure 2B). The peak at 2956 cm^{-1} corresponds to the aliphatic glycosidic CH bonds of cellulose BC-Ppy composites. PVA peaks at $\approx 1409\text{ cm}^{-1}$ assigned to C-H bending were not identified in the FTIR, indicating that the PVA amount is low and if any excess, was removed by the cleaning of the samples⁴⁷. On the other hand, the strong peak at 1635 cm^{-1} found in the composites confirmed the existence of N-H bending. The N-H bending peak also shifted to 1592 cm^{-1} in the composites, again pointing to hydrogen bond interactions. These observations are consistent with previously published reports on BC and Ppy composites^{35,48-51}. It is well known that BC has an abundant hydroxyl (-OH) group and Ppy has a secondary amine group in its repeating unit^{52,53} (Figure 2B). Therefore, based on the literature, we suggest that these groups form strong hydrogen bonds. The uniform distribution of -OH groups within BC and -NH groups within Ppy facilitated the homogenous synthesis of the NPs along the fibers as observed in the SEM and TEM images.

Atomic force microscopy (AFM) also confirms the presence of Ppy NPs and indicates that the surface roughness increased with the presence of Ppy NPs from 130 ± 31 nm for plain BC to 334 ± 257 nm for the BC-Ppy composites (Figure 2D). This effect is clearly related to the Ppy NPs attached to the fibers, which could also act as an anchoring point of cells as reported previously with BC-TiO₂ NPs³¹.

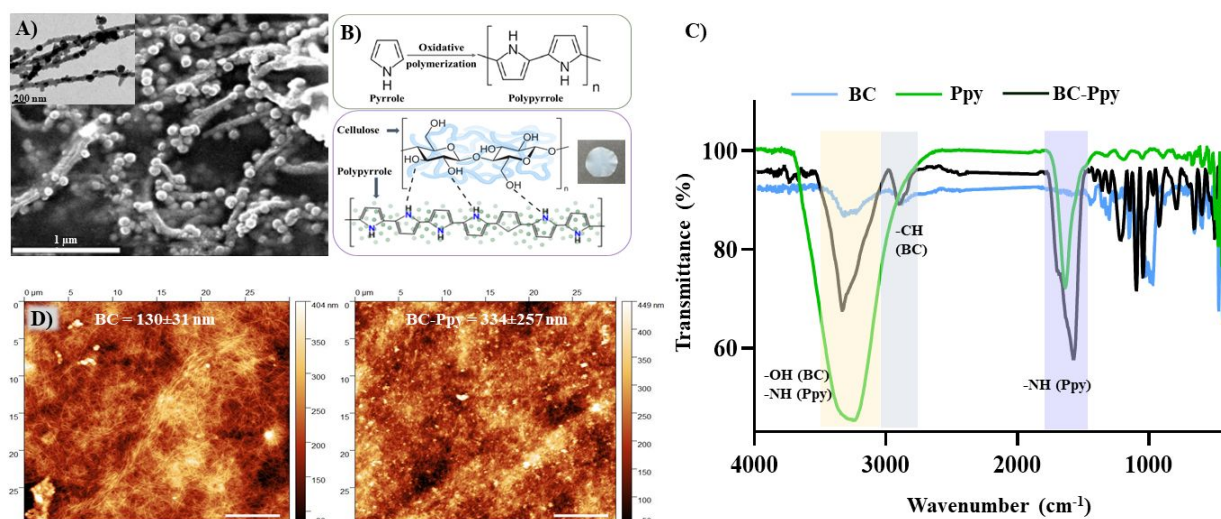


Figure 2 – Characterization of BC and BC-Ppy composites. A) SEM & TEM (inset) of BC-Ppy powders showing size, morphology, and distribution. B) Polypyrrole formation reaction and interaction between BC and Ppy. C) FTIR spectra. D) AFM images of BC and BC-Ppy showing surface roughness. Scale bar: 1 μ m.

Electrical Properties

BC-Ppy scaffolds were conductive, and we proved it using a simple LED setup, with the two probes placed on two ends of a dried BC-Ppy film. The LED bulb lights up upon contact with the surface (Figure 3A). Ppy exhibits a wide range of conductivity (from 10^{-10} to 10^4 S/cm) depending on its doping level, type of dopant, the extent of polymerization, etc.²⁹. Consequently, the electrical conductivity and thickness of BC-Ppy films as a function of Py monomer concentration were assessed. The thickness of BC-Ppy composites increased with pyrrole monomer concentration (Figure 3B), which can be attributed to the increased number of Ppy NPs attached to BC fibers improving the connectivity between Ppy domains. We prepared BC-Ppy with 1, 5, 10, 50, and 100 mM Py concentrations, and the average conductivity of BC-Ppy materials were 1.7×10^{-8} , 3.2×10^{-5} , 7×10^{-3} , 0.02 ± 0.01 , 1.7 ± 1.3 and 2.4 ± 1.5 S/cm respectively (Figure 3B, Figure 1). We evaluated the conductivity of BC-Ppy as a function of temperature and found that temperature increased the conductivity. For instance, at 100 mM monomer concentration, BC-Ppy showed 0.1 S/cm higher conductivity at 37 °C than at room temperature (Figure 3C), since in organic semiconductors, charge carrier transport occurs through hopping, which is a thermally activated mechanism⁵⁴. Therefore, when the scaffolds are employed for cell culture at 37 °C, they are expected to exhibit a slightly higher conductivity than what was measured at room temperature. Previous works reported Ppy materials reaching conductivities larger than 380 S/cm and applying them in purely electronic applications such as sensors, microelectronic devices, supercapacitors, etc.^{29,55,56}. The conductivity obtained in our BC-Ppy films, using $\text{FeCl}_3 \cdot 6\text{H}_2\text{O}$ as the oxidant and Cl^- anion doping, was higher than published reports of BC-Ppy composites (10^{-4} S/cm for 0.05M Py) using ammonium persulfate as the oxidant with sulfate ions as anionic dopant³⁷. Interestingly, the type of oxidant used for the dopant ion also plays a significant role in influencing conductivity. Another study of BC-Ppy composites with the same dopant anion (Cl^-) for neural tissue engineering by Thunberg *et al.* reported lower

conductivities (10^{-4} S/cm for 0.1M Py) than us for the same monomer concentrations³⁹. For the following evaluation of mechanical properties and cell experiments, we chose BC materials prepared with 1-10 mM Py concentrations {hereafter referred to as BP1 (1mM), BP3 (3mM), BP5 (5 mM), and BP10 (10 mM)} which exhibited conductivity between 10^{-8} to 10^{-2} S/cm since cardiac TE applications do not call for high conductivities^{38,57} given that the electrical conductivity of myocardial tissue is 10^{-5} - 10^{-3} S/cm^{58,59}.

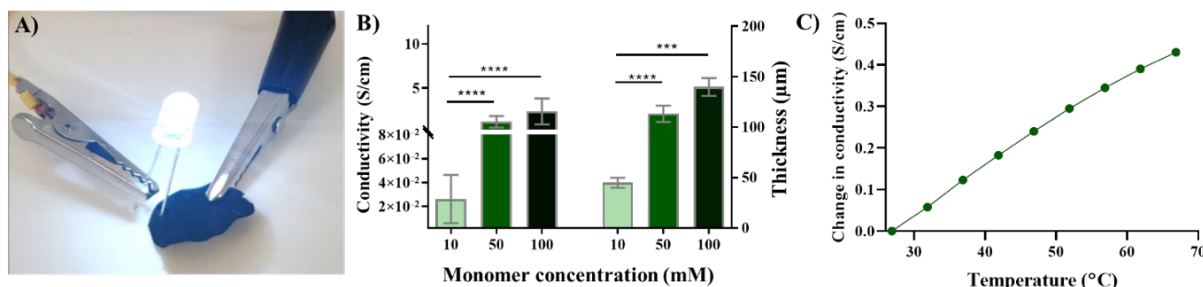


Figure 3 – Conductivity of BC-Ppy films. A) Conductivity of BC-Ppy films shown by a simple LED setup, B) Effect of initial monomer concentration in conductivity and thickness, C) Effect of temperature on conductivity.

Stability of BC-Ppy

Material's conductivity was not affected by UV sterilization, storage in water, nor incubation in cell culture media (Figure S4A). However, although non-significant, a decrease in conductivity could be observed after autoclaving (Figure S4A). This is possibly due to the over-oxidation of Ppy at higher temperatures and diffusion of the dopant Cl⁻ ions into the solution⁵⁷. Therefore, in this study, the composites were always sterilized by UV exposure prior to cell-culture experiments. We also evaluated any possible leaching of Ppy NPs into the solution upon storage in water, sterilization, and incubation in the cell-culture media by UV-Vis-NIR spectroscopy. No leaching of Ppy NPs was observed, indicating that the experimental conditions of the cell-culture studies do not cause any leaching from the scaffold (Figure S4B), and they are safe to be employed.

Mechanical Properties

Cardiac tissue withstands repetitive cyclic loading due to cardiac beating. Native myocardial tissue exhibits tensile strengths ranging from 0.4 (pulmonary artery) to 2.6 MPa (native circumferential heart valve) at 22% tensile strain under uniaxial cyclic tensile loading⁶⁰. We performed cyclic uniaxial tensile tests to reproduce the repetitive beating of the heart. The tensile strength of BC-Ppy materials increased slightly with the Ppy content, with a concomitant decrease in breaking strain. However, BP10 (with the highest Ppy content) possessed a tensile strength as low as ≈ 31 MPa and failed at $\approx 4\%$ strain (Figure 4A-C). This indicates that adding Ppy decreases the tensile strain of the composites, making them more brittle, especially pronounced at concentrations above 5 mM.

We also performed multi-axial tensile tests to get a deeper insight into the mechanical properties of our scaffolds (Figure 4D-F), BC, and BP5, and BP10 since myocardium is a tissue with anisotropic mechanical behavior^{61,62}. Tensile strength and breaking strain decreased with increasing polypyrrole concentration, similar to the uniaxial results (Figure 4F). Interestingly,

materials exhibited a more elastic behavior and higher tensile strength (108 MPa for BP5) and strain at failure (20% for BP5) under biaxial stress compared to uniaxial. This is possibly due to the material experience uniform strain from all directions, creating symmetrical force, and making it more difficult to reach a breaking strain in a particular direction, which is probably conferred by the BC scaffold. In both uniaxial and biaxial stress, BP10 has the lowest tensile strength, and ductility (Figure 4). Overall, the mechanical strength of BC-Ppy composites decreased compared to plain BC, substantiating the strong interaction via H-bonding which could influence the interaction with cells.

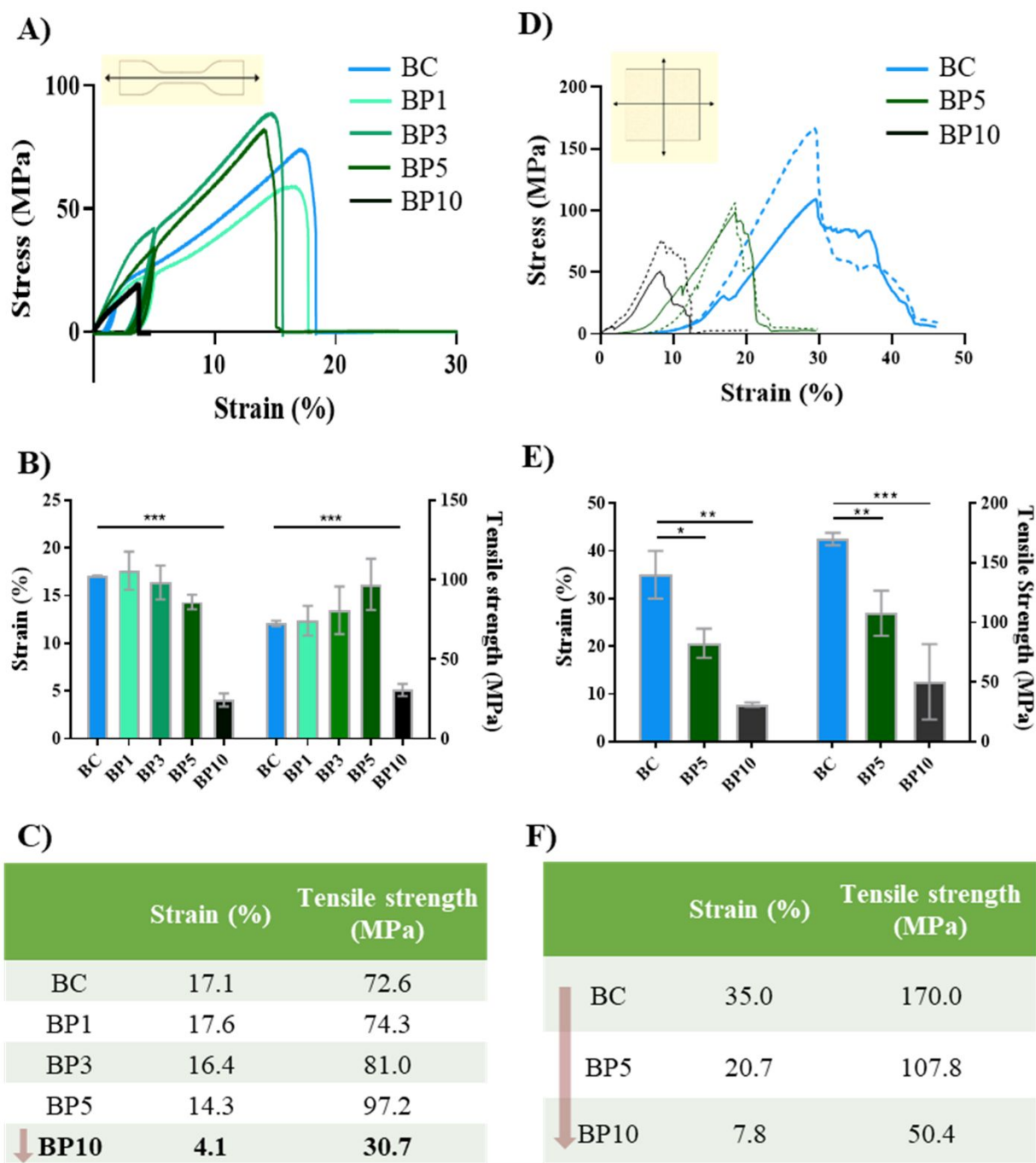


Figure 4 – Mechanical properties of BC and BC-Ppy scaffolds. A) uniaxial tensile test stress-strain curve, B & C) Breaking strain % and tensile strength from uniaxial tensile test, D) biaxial stress-strain curve (solid lines – force along x-axis; dashed lines – force along y-axis), and E & F) Breaking strain % and tensile strength from biaxial tensile test.

Surface Wettability

The surface wettability of materials influences cell adhesion and in turn biocompatibility. We measured the contact angle in water and the cell culture media DMEM for all scaffolds (BC, BP1-BP10). All the BC and BC-Ppy materials displayed hydrophilic behaviour, a contact angle < 90°, which increases at higher Ppy content, indicating a higher hydrophobicity (Figure 5). Beyond the BP5 in water and BP3 in DMEM, the contact angle starts to decrease. The lower contact angle with increased Ppy content can be attributed to a high doping level of hydrophilic Cl⁻ ions, and also to higher coverage of the BC-Ppy. In a nutshell, Ppy NPs on BC materials increase the hydrophobicity of the scaffolds, which is also substantiated by the increased surface roughness and amount of NPs in the materials.

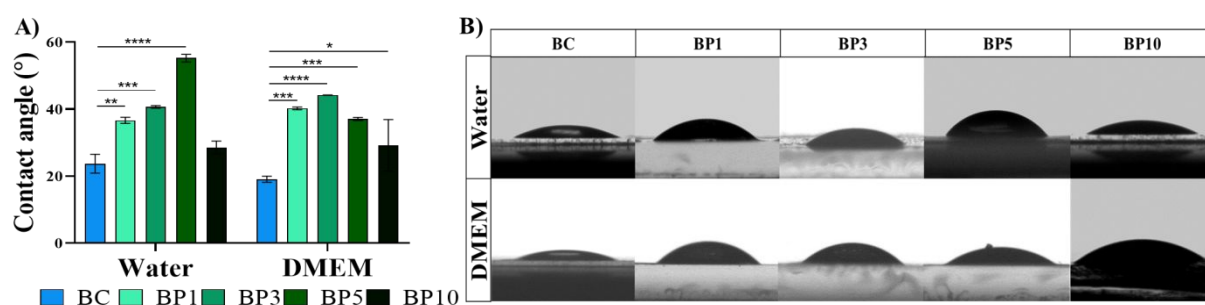


Figure 5 – Surface wettability of BC and BC-Ppy. A) DMEM and water contact angle measurements of BC and BC-Ppy composites. B) Sample pictures of water and DMEM droplets on the scaffold surfaces.

Viability of cardiac cells on BC-Ppy Scaffolds

Based on our characterization, we selected BC-Ppy scaffolds with low Ppy content (0, 1, 3, 5, and 10 mM) for the subsequent cellular studies since these concentrations have conductivities in the range of cardiac native tissue^{58,59}. The cytocompatibility of BC-Ppy composites was examined considering the most important cardiac cell types: cardiomyocytes, which generate contractile forces and regulate rhythmic heart beating⁶³, and cardiac fibroblasts, the largest cell population of the heart and key in the remodeling process occurring after heart injury⁶⁴. Consequently, the viability of H9c2 cardiomyoblasts and human adult cardiac fibroblasts (HCFs) on BC-Ppy scaffolds has been investigated.

The cytocompatibility of BC-Ppy composites was characterized by culturing H9c2 cells and evaluated by LIFE/DEAD staining. The number of live cells was quantified after 24 hours of culture, and all the scaffolds exhibited excellent cytocompatibility for H9c2 cells. Adding Ppy further increased the percentage of alive cells (Figure 6A-6B), suggesting that the electroconductive properties of BC-Ppy composites improve the cytocompatibility of BC scaffolds. In fact, Ppy has been previously blended with a wide variety of inert biomaterials, and the resulting Ppy-based constructs showed exceptional biocompatibility with cardiac cells^{65–70}. The presence of Ppy enhanced the adhesion of H9c2 cells onto the composites compared to plain BC scaffolds ($\approx 7\%$ cell area coverage), reinforcing the beneficial effect of Ppy (Figure 6A-6C). Among all tested BC-Ppy materials, BP5 rendered the best results in terms of cell attachment, reaching a cell coverage of $\approx 40\%$. BC-Ppy composites with higher Py concentrations (BP10) exhibited a decrease in the number of adhered cardiomyoblasts, even though they still outperformed plain BC scaffolds. The reduced H9c2 cells' density in BP10 can be attributed to the higher

concentration of Ppy in BP10 composites, which could be deleterious to H9c2 cells. Indeed, Ppy has been previously shown to be cytotoxic when used at elevated concentrations⁶⁸.

The bioactivity of H9c2 cells on BC and BC-Ppy scaffolds was further examined post-seeding at days 2, 3, and 6 by MTT assay. We found improved cell growth in the presence of Ppy (Figure 6D). BP1, BP3, and BP5 scaffolds outperformed BC with increased proliferation of H9c2 cells at all time points. The bioactivity of BC and BC-Ppy scaffolds was also evaluated when used in their “wet” form and rendered akin results (Figure S5). We confirmed this increase in H9c2 proliferation by quantifying total protein by Bicinchoninic Acid (BCA) assay after 7 days of culture (Figure 6E). The significant increment of total protein in BC-Ppy scaffolds suggests an increase in the total number of cells, which further confirms our previous findings: Ppy addition enhances cell adhesion to BC scaffolds.

Similarly, the cytocompatibility of our composites was tested with HCFs. Excellent viability and adhesion of HCFs onto both BC and BC-Ppy substrates were reported, even at higher concentrations of Ppy (see detailed information in Figure S6). All in all, BC-Ppy composites are cytocompatible with cardiac cells. Adding Ppy (up to 5 mM) to BC significantly enhances cell viability, growth, and adhesion of H9c2 cardiomyoblasts to the materials. On the other hand, HCFs grow and adhere better to plain BC substrates and can withstand higher concentrations of conductive Ppy in comparison to H9c2 cells, showing a less sensitive behavior than cardiomyoblasts. Previous work of Gelmi *et al.*⁷⁰ also described distinct sensitivities among different cardiac cell types. They tested endothelial progenitor cells (EPCs) and cardiac progenitor cells (CPCs) onto different Ppy-containing substrates. While all Ppy (dopant) materials were biocompatible for EPCs, CPCs showed sensitivity towards some of the biomaterials and displayed significantly decreased cell viability and density⁷⁰.

It has been reported that nanocellulose-Ppy composites need preconditioning (extensive rinsing and preincubation in a biological buffer for 48h) to obtain a noncytotoxic biomaterial⁷¹. Therefore, we lastly evaluated the potential cytotoxicity of non-preconditioned BC and BC-Ppy scaffolds. For this, BC / BC-Ppy composites were incubated overnight with cell media to allow leakage – if any – of materials’ components into the medium. Then, media was collected and added to H9c2 cells. No toxic effect was reported by any of our as-synthesized scaffolds (Figure S7), indicative of a superior methodology to obtain non-toxic nanocellulose-Ppy composites in comparison with previously described methods⁷¹ in which additional steps are needed to ensure good cell cytocompatibility.

H9c2 Cardiomyoblasts Attachment and Morphology on BC-Ppy Scaffolds

Cell morphology of H9c2 was examined on days 3 and 7 of culture. Cardiomyoblasts did not properly attach to plain BC. Indeed, a few cells adhered to BC materials displaying an atypical round shape and gathering in small clusters (Figure 7A i, vi). The addition of polypyrrole to BC scaffolds promoted the attachment of a higher number of cells, and adhered cells retained the characteristic H9c2 spread-out morphology⁴⁵ (Figure 7A ii-v, vii-x). In line with previous findings (Figure 6A-C), BP5 scaffolds were the best-performing ones. Cardiomyoblasts seeded on BP5 scaffolds showed similar cell density and morphology to controls (Figure S8). Other time points were imaged using phase contrast and showed the same trend (data not shown). Similarly, H9c2 cells grown onto “wet” BC-Ppy materials exhibited an identical behavior (Figure S9).

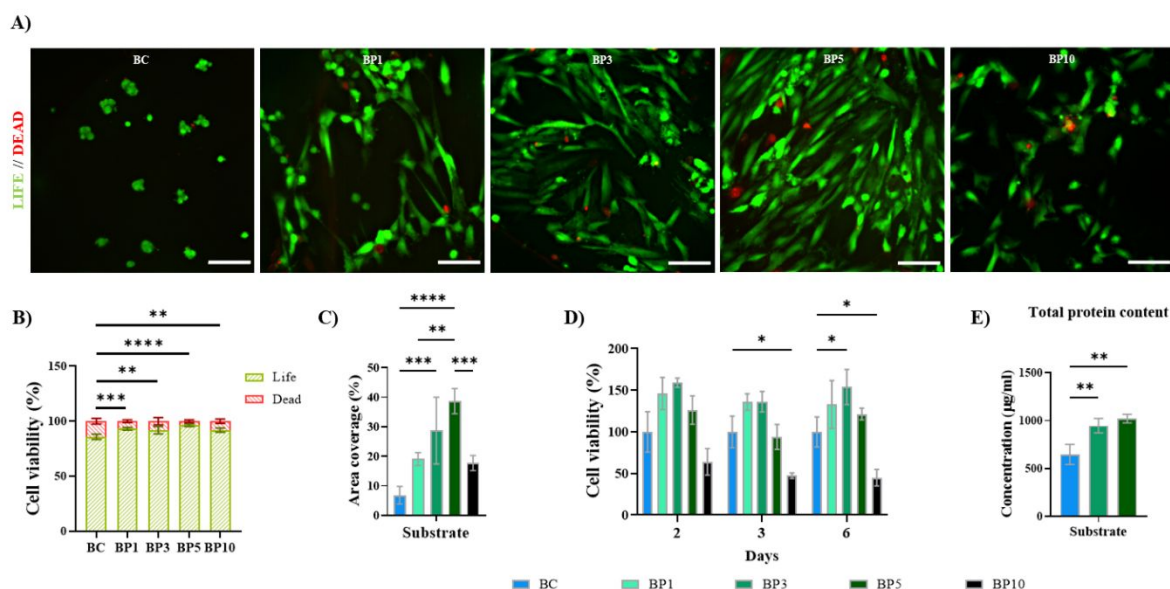


Figure 6 – Viability of H9c2 onto BC and BC-Ppy scaffolds. A) LIFE/DEAD Staining of H9c2 cells cultured for 24 hours onto BC and BC-Ppy scaffolds. B) Quantification of LIFE/DEAD images (n=4). C) Area coverage of cells adhered to BC and BC-Ppy scaffolds after 24h of culture (n=4). D) Cytotoxicity of H9c2 cardiomyoblasts after 2, 3, and 6 days of culture analyzed by MTT (n=3 at day 2 and n=4 at days 3 and 6; data normalized to the absorbance values obtained in plain BC materials at each time point). E) Quantification of the total protein content of H9c2 cells grown onto BC, BP3, and BP5 after 7 days of culture (n=4). Scale bars: 100 µm.

Cell-scaffold interactions were also examined after 7 days of culture by scanning electron microscopy (SEM). For this, only BP3 and BP5 were investigated as guided by previous experiments. SEM images showed that cells on BC-Ppy produce long filopodia that extend to the scaffolds, while cells on BC scaffolds exhibited limited filopodia. The lower H9c2 density and the uncharacteristic round cell shape of cardiomyoblasts on plain BC materials – which we reported previously by other methods – were confirmed. Cell bodies did not fuse well to BC scaffolds (Figure 7B i). Nevertheless, H9c2 cells elongated and attached to BC-Ppy materials with higher extension, adhesion, and cell density. The addition of Ppy to the BC scaffold allowed H9c2 cells to interact with the BC-Ppy nanofibers and cardiomyoblasts amalgamated with the BC-Ppy materials (Figure 7B ii-iii).

Cellular morphology serves as an indicator of cellular state and functionality⁷². In brief, H9c2 exhibited an abnormal cell shape when grown onto BC scaffolds, and the addition of Ppy allowed cells to retain their characteristic cell morphology. These results suggest that Ppy may promote a cardiac phenotype given its biomimetic conducting properties. Indeed, existing evidence shows a positive influence of electroconductive biomaterials *in-vitro*, including improved cytoskeletal organization, myocardial tissue maturation, or synchronization of cell beating, among others^{23,73}.

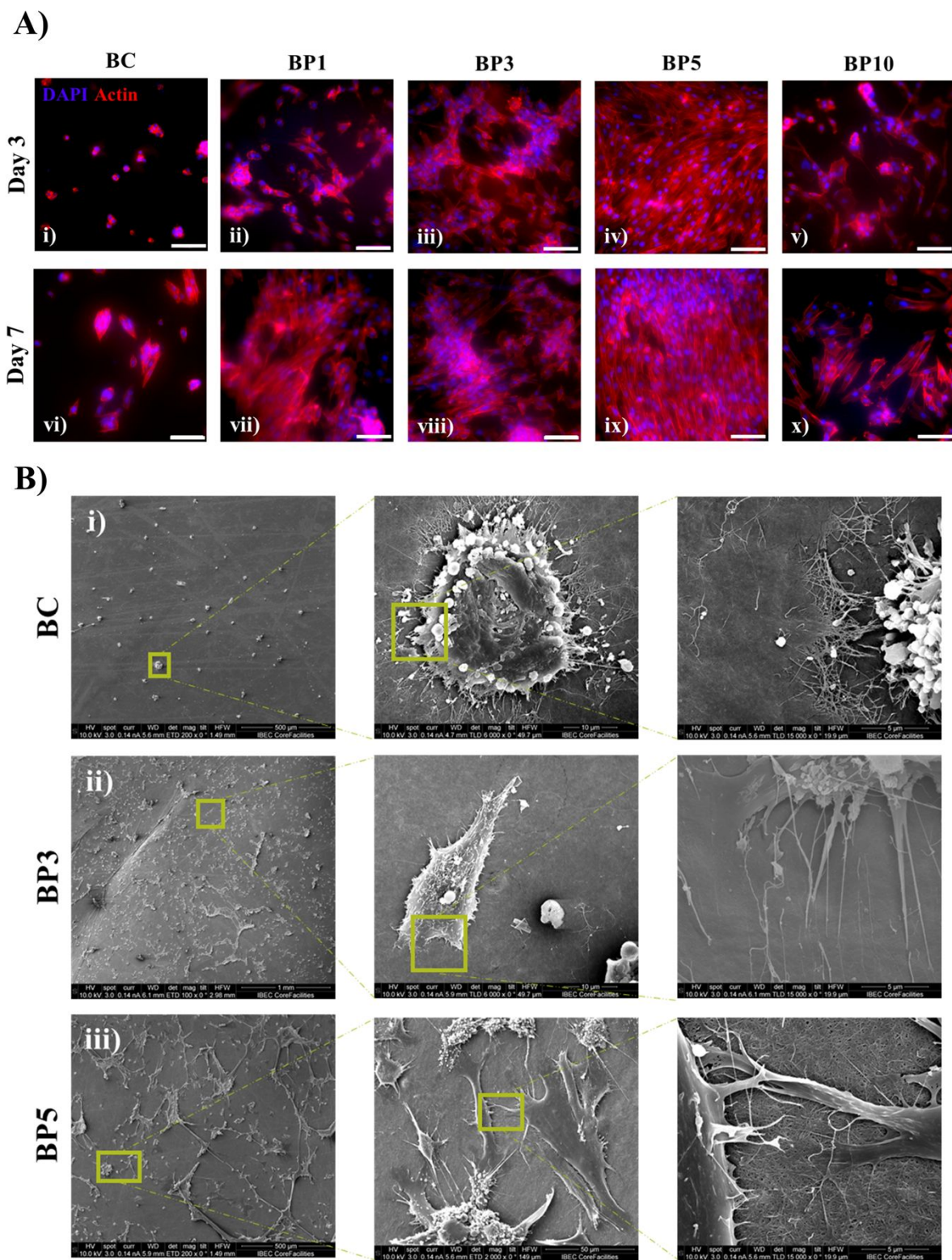


Figure 7 – H9c2 attachment to BC and BC-Ppy scaffolds. A) Fluorescence microscopy images of H9c2 cell populations seeded on nanocellulose composites after 3 and 7 days of culture. Scale bars: 100 μm . B) SEM images depicting H9c2 attachment and morphology after 7 days of culture onto BC, BP3, and BP5 materials.

Effects of conductive BC-Ppy scaffolds on H9c2 differentiation in-vitro

H9c2 is a myoblast cell line derived from embryonic rat ventricular heart tissue⁷⁴. H9c2 cells have been extensively used in cardiovascular research as an alternative for adult primary cardiomyocytes (PCMs)^{45,46,75}. PCMs are ideally the supreme cellular model for cardiovascular basic research^{76,77}, however, their use is extremely limited by the technical intricacies in their isolation, culture, and scale production⁷⁸. Despite the latest attempts to optimize PCM isolation, unstable quality and low cell yield are major hurdles that preclude the use of PCMs in non-acute *in-vitro* experiments^{78,79}. In this scenario, H9c2 surpasses other existing cardiac cell lines (e.g., HL-1, AC16)^{76,80} and can be further matured towards a cardiomyocyte-like phenotype when treated with retinoic acid (RA)^{45,46}. However, it was brought to our attention that recent studies using H9c2 cells to test distinct biomaterials for cardiac applications did not induce such a cardiomyocyte differentiation^{40,81–84}, suggesting plausible difficulties to mature H9c2 cells when grown onto engineered substrates. Additionally, other labs reported discrepancies when reproducing H9c2 maturation to cardiomyocytes^{76,85}, indicating some degree of resistance to differentiation. Nevertheless, H9c2 differentiation is imperative to achieve a better resemblance to adult cardiac tissue and perform investigations with higher translational value. Consequently, in the present study, we aim to characterize the behavior and differentiation capabilities of H9c2 cardiomyoblasts grown onto BC-Ppy composites.

We first confirmed the capabilities of H9c2 maturation to cardiomyocytes upon differentiation treatment. Two differentiation media were tested (containing 10 nM and 1 μ M RA) and efficiency was assessed after two treatment durations (6 and 10 days). H9c2 differentiation was confirmed at both time points by using any of the differentiation media (see detailed information in Figure S10). Six days of treatment and differentiation media containing 10 nM RA were employed henceforth.

Differentiation media contains RA; consequently, the possible combined toxicity of RA with the BC / BC-Ppy by-products was evaluated. Growth medium with and without 10nM RA was incubated with the BC / BC-Ppy composites. After overnight incubation, media was collected and added to H9c2 cells for 24h before checking cell viability by MTT. The combination of BC / BC-Ppy by-products with RA did not affect H9c2 cells viability (Figure 8A).

We then proceeded to chemically differentiate H9c2 cells onto BC-Ppy composites. H9c2 morphologic alterations were observed by phase contrast microscopy after differentiation treatment. H9c2 cells cultured in a growth medium retained their characteristic shape when grown onto BC-Ppy substrates, whereas they showed an atypical, rounded morphology when grown onto BC scaffolds, as previously described (Figure 8B, top panel). After culture with differentiation media, H9c2 myoblasts fused and showed an elongated shape in all conditions (Figure 8B, bottom panel). The acquisition of such a morphological signature evidences the successful chemical differentiation of H9c2 cells when grown onto bacterial cellulose composite substrates, which, to the best of our knowledge, was not reported until now.

As expected, inducing H9c2 differentiation onto the composites reduced cell proliferation (Figure 8C, left). Nevertheless, even under differentiation treatment, the presence of Ppy significantly increased cell growth as evidenced by the increment in total protein (Figure 8C, right). This is in line with our previous results (Figure 8) and suggests that the reported beneficial effects of Ppy in H9c2 cardiomyoblasts are preserved as well in differentiated cardiomyocyte-like H9c2 cells.

Given that functional assays are limited in H9c2 due to their inability to beat⁷⁵, differentiation of H9c2 cells onto the different substrates was further confirmed by the increased expression of

cardiac-specific markers, indicating a cardiomyocyte-like phenotype. Higher Cardiac Troponin T (cTnT) expression was observed when H9c2 were cultured with differentiation media (DM) in all conditions. Similarly, alpha Myosin Heavy Chain (α MHC) expression increased upon treatment, although exclusively when BC-Ppy composites were employed. No differences in the expression of the gap junction protein Connexin 43 (Cx43) were seen (Figure 8D, top graphs). Interestingly, H9c2 differentiation into cardiomyocytes was promoted by solely adding polypyrrole to the BC substrates (Figure 8D, bottom graphs). cTnT expression increased when H9c2 cells were grown onto BC-Ppy materials by using standard growth medium (GM) (i.e., without inducing myoblast differentiation chemically). Additionally, when H9c2 maturation was induced with differentiation media (DM), higher expression of cTnT was seen in cells grown onto BC-Ppy composites in comparison with plain BC scaffolds. α MHC expression only increased when H9c2 cells were cultured with differentiation media and grown onto Ppy-containing composites, suggesting a combined effect. In fact, α MHC content was also characterized in control cultures (material-free well plates) and its expression levels did not change by solely inducing differentiation chemically (Figure S11), reinforcing a possible synergistic effect of Ppy and the differentiation media. Lastly, Cx43 expression increased with Ppy concentration when BC-Ppy materials were used as substrates, regardless of the use of differentiation media or not.

In a nutshell, we found that adding the electrically conductive polymer polypyrrole to BC biomaterials fosters H9c2 differentiation *in-vitro*. Similarly, other polypyrrole-based conductive constructs have been reported to enhance the functional properties of cardiac cells, reinforcing our findings to a greater extent. Spearman *et. al* reported enhanced Cx43 expression and improved Ca^{2+} transients in cardiomyocytes when Ppy was added to their polycaprolactone matrix⁶⁶. Tsui *et. al* showed enhanced cellular organization, sarcomere development, and improved expression of cardiac markers (Cx43, Myh7, SCN5A, cTnT) when conjugating Ppy to acid-modified silk fibroin cardiac scaffolds⁶⁹. Comparably, Gelmi *et. al* proposed a novel Ppy-containing electromechanically active composite to promote differentiation of hiPSCs to cardiomyocytes⁸⁶. Coating their fibrous scaffolds with Ppy increased the expression of cardiomyocyte-specific genes (Actinin, Myh6) and regulators of cardiac differentiation (NKX2.5, GATA4). Nevertheless, they used pre-conditioned hiPSCs (3-days culture with differentiation medium prior to cell seeding onto their materials) and stimulated the cells electromechanically (0,05 Hz biphasic stimulation). Furthermore, they continued using this specialized differentiation medium with their materials, making it difficult to faithfully attribute such a cell maturation to the materials or the external cell stimulation. Au contraire, we can see a partial differentiation of H9c2 cells by solely using BC-Ppy composites as cellular substrates, undoubtedly highlighting the beneficial effect of these conductive biocomposites on cardiac maturation.

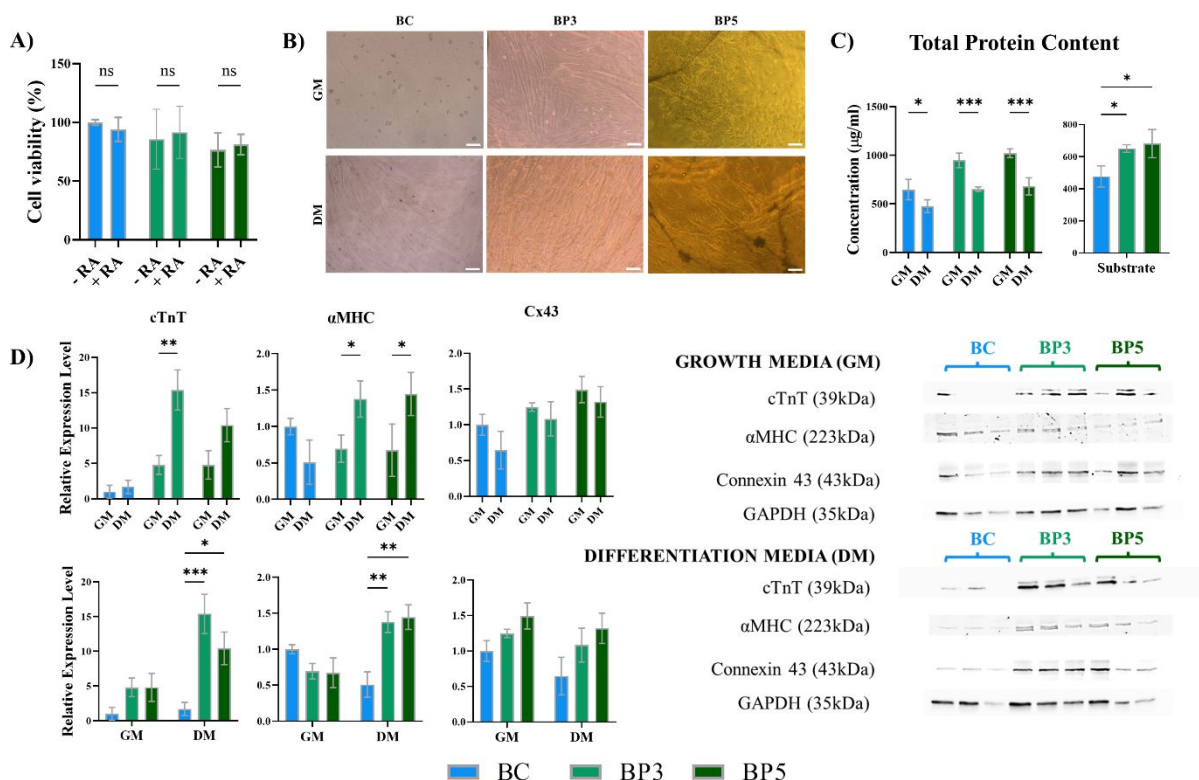


Figure 8 – H9c2 Differentiation onto BC / BC-PPy scaffolds. A) Combined toxicity of RA with BC/BC-PPy by-products on cardiomyoblasts (n=4, data normalized by viability of H9c2 cells incubated with growth medium (without RA) from plain BC scaffolds). B) Morphological change of cardiomyoblasts grown onto BC / BC-PPy materials upon differentiation treatment. C) Left: Total protein content of H9c2 grown onto different substrates with growth and differentiation media after 7 days of culture (n=3). Right: Quantification of total protein content of H9c2 cells grown onto BC, BP3, and BP5 with differentiation treatment (n=3). D) Protein expression of specific cardiac markers cTnT, α MHC, and Connexin 43; GAPDH was used as the loading control (n=3, protein expression data normalized to intensity values of cells grown onto plain BC materials with growth medium). GM= Growth Medium; DM= Differentiation Medium. Scale bars: 100 μ m.

Conclusions

Cardiac tissue engineering quests for biocompatible, mechanically robust, and flexible scaffolds that allow cell attachment and proliferation with adequate conductivity for the transmission of electrical signals to the entire myocardium. In this study, we created electroconductive nanofibrous scaffolds by incorporating Ppy NPs through in-situ synthesis into the 3D interconnected bacterial cellulose fiber network. We investigated their use as cardiac tissue scaffolds. Polypyrrole NPs efficiently impart conductive properties to BC, increase surface roughness and thickness, and decrease transparency. BC-Ppy composites maintained flexibility up to 10mM concentration and the 3D mesh- like structure in the entire range of concentrations.

The excellent cytocompatibility of BC-Ppy composites was confirmed with both primary human cardiac fibroblasts and H9c2 cardiomyoblasts. We demonstrated that the addition of polypyrrole improved the biocompatibility of BC materials since cardiomyoblasts showed enhanced cell viability, adhesion, morphology, and proliferation. H9c2 cells seeded on BC-Ppy showed an

increased degree of differentiation to cardiomyocytes when combined with current chemical differentiation protocols, suggesting a synergistic effect of Ppy with the differentiation medium. Moreover, our results indicate that BC-Ppy materials alone (i.e., without chemical induction of maturation) may drive partial H9c2 differentiation, as evidenced by an enhanced expression of cardiac-specific proteins.

This work suggests that BC-Ppy nanofibrous scaffolds hold exceptional potential to be used as an *in-vitro* platform for the differentiation of immature cardiac cells *in-vitro* and encourages further investigations of the use of electroconductive BC-Ppy substrates in cardiac tissue engineering.

Supporting information: Schematic representations of experimental setup of mechanical testing and methodology of BC and BC-Ppy synthesis; further characterization of BC-Ppy materials (size distribution of BC nanofibers and Ppy NPs and stability of BC-Ppy); cytotoxicity of materials in “wet” format (viability and immunolabelled images); biocompatibility of BC-Ppy scaffolds with cardiac fibroblasts; toxicity of BC and BC-Ppy by-products; comparison of H9c2 attachment on BC-Ppy nanocomposites and control culture plates; successful H9c2 maturation *in-vitro*; expression of α MHC after differentiation treatment in control substrates.

Acknowledgments

This work was supported by the Spanish Ministry of Science and Innovation (MICINN) through the National Research Agency (AEI) and European Regional Development Funds (ERDF/FEDER), project BIOCARDIO ref. RTI2018-096320-B-C21, project BIOSOFT-REGE ref. PID2021-122645OB-I00, the CERCA Program/Generalitat de Catalunya, the 'Severo Ochoa' Programme for Center of Excellence in R&D (CEX2019-000917), the Programme/Generalitat de Catalunya (2017-SGR-359), the Severo Ochoa Programme of the Spanish Ministry of Science and Innovation (MICINN—Grant SEV-2014–0425, 2015–2019 and CEX2018–000,789-S, 2019–2023) and the projects FIP-PALOMA, FIP-BEAT, and the PDC2022-133755-I00/AEI/10.13039/501100011033 European Union NextGeneration EU/PRTR. This research was also supported by the European Union's Horizon 2020 research and innovation program H2020-MSCA-COFUND-2016 (DOC-FAM, grant agreement Nr. 754397). This project also received the support of a La Caixa INPhINIT Fellowship (ID 100010434) with project code LCF/BQ/DR19/11740025. SYS is enrolled in the Materials Science Ph.D. program of the UAB. SYS and AL participate in the Spanish National Research Council (CSIC) interdisciplinary platform for sustainable plastics towards a circular economy (SusPlast), in the Aerogels COST ACTION (CA 18125), and in CSIC-Conexión Nanomedicine, EPNOE network, and Red Nanocare 2.0. The authors acknowledge the use of Biorender.com.

References

- (1) Wilkins, E.; Wilson, L.; Wickramasinghe, K.; Bhatnagar, P.; Leal, J.; Luengo-Fernandez, R.; Burns, R.; Rayner, M.; Townsend, N. European Cardiovascular Disease Statistics 2017 Edition. *European Heart Network* **2017**, 1–192.
- (2) Townsend, N.; Wilson, L.; Bhatnagar, P.; Wickramasinghe, K.; Rayner, M.; Nichols, M. Cardiovascular Disease in Europe: Epidemiological Update 2016. *Eur Heart J* **2016**, 37 (42), 3232–3245. <https://doi.org/10.1093/eurheartj/ehw334>.
- (3) Artucio, H., & Pereira, M. Cardiac Arrhythmias in Critically Ill Patients: Epidemiologic Study. *Crit Care Med* **1990**, 18 (12), 1383–1388.
- (4) Granrud, G. A.; Vatterott, P. J. Arrhythmias and Acute Myocardial Infarction. *Postgrad Med* **1991**, 90 (6), 85–96. <https://doi.org/10.1080/00325481.1991.11701102>.
- (5) Laflamme, M. A.; Murry, C. E. Heart Regeneration. *Nature* **2011**, 473 (7347), 326–335. <https://doi.org/10.1038/nature10147>.
- (6) Balì, I.; Tiso, L.; Barzon, E.; Turato, M.; Vida, V.; Tessari, C. Heart Transplantation: The Challenging Journey of an ACHD. In *Guide for Advanced Nursing Care of the Adult with Congenital Heart Disease*; Flocco, S. F., Habibi, H., Dellafiore, F., Sillman, C., Eds.; Springer International Publishing: Cham, 2022; pp 167–184. https://doi.org/10.1007/978-3-031-07598-8_11.
- (7) Kittleson, M. M.; Kobashigawa, J. A. Cardiac Transplantation. *JACC Heart Fail* **2017**, 5 (12), 857–868. <https://doi.org/10.1016/j.jchf.2017.08.021>.
- (8) Ikada, Y. Challenges in Tissue Engineering. *J R Soc Interface* **2006**, 3 (10), 589–601. <https://doi.org/10.1098/rsif.2006.0124>.
- (9) Gage, F. H. Cell Therapy. *Nature* **1998**, 392 (6679 Suppl), 18–24.
- (10) Braunwald, E. Cell-Based Therapy in Cardiac Regeneration. *Circ Res* **2018**, 123 (2), 132–137. <https://doi.org/10.1161/CIRCRESAHA.118.313484>.
- (11) Caplice, N. M.; Gersh, B. J.; Alegria, J. R. Cell Therapy for Cardiovascular Disease: What Cells, What Diseases and for Whom? *Nat Clin Pract Cardiovasc Med* **2005**, 2 (1), 37–43. <https://doi.org/10.1038/ncpcardio0073>.
- (12) Segers, V. F. M.; Lee, R. T. Stem-Cell Therapy for Cardiac Disease. *Nature* **2008**, 451 (7181), 937–942. <https://doi.org/10.1038/nature06800>.
- (13) Dib, N.; Khawaja, H.; Varner, S.; McCarthy, M.; Campbell, A. Cell Therapy for Cardiovascular Disease: A Comparison of Methods of Delivery. *J Cardiovasc Transl Res* **2011**, 4 (2), 177–181. <https://doi.org/10.1007/s12265-010-9253-z>.
- (14) Haraguchi, Y.; Shimizu, T.; Yamato, M.; Okano, T. Concise Review: Cell Therapy and Tissue Engineering for Cardiovascular Disease. *Stem Cells Transl Med* **2012**, 1 (2), 136–141. <https://doi.org/10.5966/sctm.2012-0030>.
- (15) Mu, L.; Dong, R.; Guo, B. Biomaterials-Based Cell Therapy for Myocardial Tissue Regeneration. *Adv Healthc Mater* **2023**, 12 (10). <https://doi.org/10.1002/adhm.202202699>.
- (16) Chen, Q.-Z.; Harding, S. E.; Ali, N. N.; Lyon, A. R.; Boccaccini, A. R. Biomaterials in Cardiac Tissue Engineering: Ten Years of Research Survey. *Materials Science and Engineering: R: Reports* **2008**, 59 (1–6), 1–37. <https://doi.org/10.1016/j.mser.2007.08.001>.

- (17) Nguyen, A. H.; Marsh, P.; Schmiess-Heine, L.; Burke, P. J.; Lee, A.; Lee, J.; Cao, H. Cardiac Tissue Engineering: State-of-the-Art Methods and Outlook. *J Biol Eng* **2019**, *13* (1), 57. <https://doi.org/10.1186/s13036-019-0185-0>.
- (18) Christman, K. L.; Lee, R. J. Biomaterials for the Treatment of Myocardial Infarction. *J Am Coll Cardiol* **2006**, *48* (5), 907–913. <https://doi.org/10.1016/j.jacc.2006.06.005>.
- (19) Cui, Z.; Yang, B.; Li, R.-K. Application of Biomaterials in Cardiac Repair and Regeneration. *Engineering* **2016**, *2* (1), 141–148. <https://doi.org/10.1016/J.ENG.2016.01.028>.
- (20) Yang, B.; Yao, F.; Hao, T.; Fang, W.; Ye, L.; Zhang, Y.; Wang, Y.; Li, J.; Wang, C. Development of Electrically Conductive Double-Network Hydrogels via One-Step Facile Strategy for Cardiac Tissue Engineering. *Adv Healthc Mater* **2016**, *5* (4), 474–488. <https://doi.org/10.1002/adhm.201500520>.
- (21) Bidez, P. R.; Li, S.; MacDiarmid, A. G.; Venancio, E. C.; Wei, Y.; Lelkes, P. I. Polyaniline, an Electroactive Polymer, Supports Adhesion and Proliferation of Cardiac Myoblasts. *J Biomater Sci Polym Ed* **2006**, *17* (1–2), 199–212. <https://doi.org/10.1163/156856206774879180>.
- (22) Guo, B.; Ma, P. X. Conducting Polymers for Tissue Engineering. *Biomacromolecules* **2018**, *19* (6), 1764–1782. <https://doi.org/10.1021/acs.biomac.8b00276>.
- (23) Solazzo, M.; O'Brien, F. J.; Nicolosi, V.; Monaghan, M. G. The Rationale and Emergence of Electroconductive Biomaterial Scaffolds in Cardiac Tissue Engineering. *APL Bioeng* **2019**, *3* (4), 041501. <https://doi.org/10.1063/1.5116579>.
- (24) Esmaeili, H.; Patino-Guerrero, A.; Hasany, M.; Ansari, M. O.; Memic, A.; Dolatshahi-Pirouz, A.; Nikkhah, M. Electroconductive Biomaterials for Cardiac Tissue Engineering. *Acta Biomater* **2022**, *139*, 118–140. <https://doi.org/10.1016/j.actbio.2021.08.031>.
- (25) Sun, H.; Zhou, J.; Huang, Z.; Qu, L.; Lin, N.; Liang, C.; Dai, R.; Tang, L.; Tian, F. Carbon Nanotube-Incorporated Collagen Hydrogels Improve Cell Alignment and the Performance of Cardiac Constructs. *Int J Nanomedicine* **2017**, *Volume 12*, 3109–3120. <https://doi.org/10.2147/IJN.S128030>.
- (26) Puiggali-Jou, A.; Ordoño, J.; del Valle, L. J.; Pérez-Amodio, S.; Engel, E.; Alemán, C. Tuning Multilayered Polymeric Self-Standing Films for Controlled Release of L-Lactate by Electrical Stimulation. *Journal of Controlled Release* **2021**, *330*, 669–683. <https://doi.org/10.1016/j.jconrel.2020.12.049>.
- (27) Guo, B.; Glavas, L.; Albertsson, A.-C. Biodegradable and Electrically Conducting Polymers for Biomedical Applications. *Prog Polym Sci* **2013**, *38* (9), 1263–1286. <https://doi.org/10.1016/j.progpolymsci.2013.06.003>.
- (28) Park, Y.; Jung, J.; Chang, M. Research Progress on Conducting Polymer-Based Biomedical Applications. *Applied Sciences* **2019**, *9* (6), 1070. <https://doi.org/10.3390/app9061070>.
- (29) Huang, Y.; Li, H.; Wang, Z.; Zhu, M.; Pei, Z.; Xue, Q.; Huang, Y.; Zhi, C. Nanostructured Polypyrrole as a Flexible Electrode Material of Supercapacitor. *Nano Energy* **2016**, *22*, 422–438. <https://doi.org/10.1016/j.nanoen.2016.02.047>.
- (30) Petersen, N.; Gatenholm, P. Bacterial Cellulose-Based Materials and Medical Devices: Current State and Perspectives. *Appl Microbiol Biotechnol* **2011**, *91* (5), 1277–1286. <https://doi.org/10.1007/s00253-011-3432-y>.

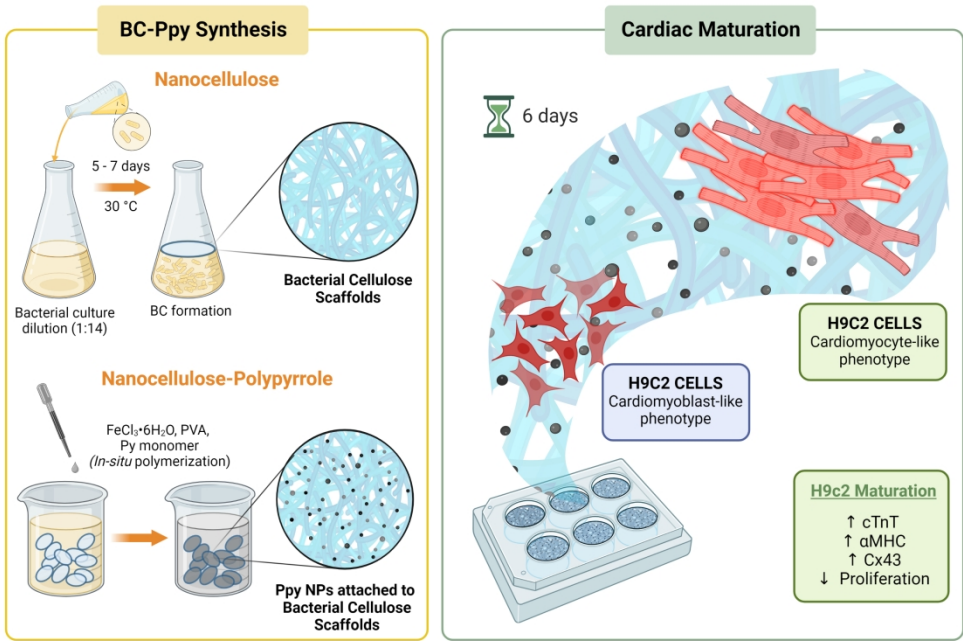
- (31) Anton-Sales, I.; Roig-Sanchez, S.; Sánchez-Guisado, M. J.; Laromaine, A.; Roig, A. Bacterial Nanocellulose and Titania Hybrids: Cytocompatible and Cryopreservable Cell Carriers. *ACS Biomater Sci Eng* **2020**, *6* (9), 4893–4902. <https://doi.org/10.1021/acsbiomaterials.0c00492>.
- (32) Yang, X.; Huang, J.; Chen, C.; Zhou, L.; Ren, H.; Sun, D. Biomimetic Design of Double-Sided Functionalized Silver Nanoparticle/Bacterial Cellulose/Hydroxyapatite Hydrogel Mesh for Temporary Cranioplasty. *ACS Appl Mater Interfaces* **2023**, *15* (8), 10506–10519. <https://doi.org/10.1021/acsami.2c22771>.
- (33) Barjasteh, M.; Dehnavi, S. M.; Ahmadi Seyedkhani, S.; Rahnamaee, S. Y.; Golizadeh, M. Improved Biological Activities of Dual Nanofibrous Chitosan/Bacterial Cellulose Wound Dressing by a Novel Silver-Based Metal-Organic Framework. *Surfaces and Interfaces* **2023**, *36*, 102631. <https://doi.org/10.1016/j.surfin.2023.102631>.
- (34) Kim, G.-D.; Yang, H.; Park, H. R.; Park, C.-S.; Park, Y. S.; Lee, S. E. Evaluation of Immunoreactivity of in Vitro and in Vivo Models against Bacterial Synthesized Cellulose to Be Used as a Prosthetic Biomaterial. *Biochip J* **2013**, *7* (3), 201–209. <https://doi.org/10.1007/s13206-013-7302-9>.
- (35) Chen, Y.; Wang, F.; Dong, L.; Li, Z.; Chen, L.; He, X.; Gong, J.; Zhang, J.; Li, Q. Design and Optimization of Flexible Polypyrrole/Bacterial Cellulose Conductive Nanocomposites Using Response Surface Methodology. *Polymers (Basel)* **2019**, *11* (6), 960. <https://doi.org/10.3390/polym11060960>.
- (36) Müller, D.; Rambo, C. R.; D.O.S.Recouvreux; Porto, L. M.; Barra, G. M. O. Chemical in Situ Polymerization of Polypyrrole on Bacterial Cellulose Nanofibers. *Synth Met* **2011**, *161* (1–2), 106–111. <https://doi.org/10.1016/j.synthmet.2010.11.005>.
- (37) Muller, D.; Silva, J. P.; Rambo, C. R.; Barra, G. M. O.; Dourado, F.; Gama, F. M. Neuronal Cells Behavior on Polypyrrole Coated Bacterial Nanocellulose Three-Dimensional (3D) Scaffolds. *J Biomater Sci Polym Ed* **2013**, *24* (11), 1368–1377. <https://doi.org/10.1080/09205063.2012.761058>.
- (38) Huang, Z.-B.; Yin, G.-F.; Liao, X.-M.; Gu, J.-W. Conducting Polypyrrole in Tissue Engineering Applications. *Front Mater Sci* **2014**, *8* (1), 39–45. <https://doi.org/10.1007/s11706-014-0238-8>.
- (39) Thunberg, J.; Kalogeropoulos, T.; Kuzmenko, V.; Hägg, D.; Johannesson, S.; Westman, G.; Gatenholm, P. In Situ Synthesis of Conductive Polypyrrole on Electrospun Cellulose Nanofibers: Scaffold for Neural Tissue Engineering. *Cellulose* **2015**, *22* (3), 1459–1467. <https://doi.org/10.1007/s10570-015-0591-5>.
- (40) Ajdary, R.; Ezazi, N. Z.; Correia, A.; Kemell, M.; Huan, S.; Ruskoaho, H. J.; Hirvonen, J.; Santos, H. A.; Rojas, O. J. Multifunctional 3D-Printed Patches for Long-Term Drug Release Therapies after Myocardial Infarction. *Adv Funct Mater* **2020**, *30* (34). <https://doi.org/10.1002/adfm.202003440>.
- (41) He, Y.; Hou, H.; Wang, S.; Lin, R.; Wang, L.; Yu, L.; Qiu, X. From Waste of Marine Culture to Natural Patch in Cardiac Tissue Engineering. *Bioact Mater* **2021**, *6* (7), 2000–2010. <https://doi.org/10.1016/j.bioactmat.2020.12.011>.
- (42) Roig Sánchez, S. Novel Bacterial Cellulose Materials: Structuration, Functional Nanocomposites and Photocurable Hydrogels, 2021. <http://www.tdx.cat/handle/10803/673852>.

- (43) Srinivasan, S. Y.; Gajbhiye, V.; Bodas, D. Development of Nano-Immunosensor with Magnetic Separation and Electrical Detection of Escherichia Coli Using Antibody Conjugated Fe₃O₄@Ppy. *Nanotechnology* **2020**, 32 (8). <https://doi.org/10.1088/1361-6528/abc8b1/meta>.
- (44) Pauw, Lj. A Method of Measuring Specific Resistivity and Hall Effect of Discs of Arbitrary Shape. *Philips Research Reports* **1958**, 13 (1), 1–9.
- (45) Branco, A. F.; Pereira, S. P.; Gonzalez, S.; Gusev, O.; Rizvanov, A. A.; Oliveira, P. J. Gene Expression Profiling of H9c2 Myoblast Differentiation towards a Cardiac-Like Phenotype. *PLoS One* **2015**, 10 (6), e0129303. <https://doi.org/10.1371/journal.pone.0129303>.
- (46) Pereira, S. L.; Ramalho-Santos, J.; Branco, A. F.; Sardão, V. A.; Oliveira, P. J.; Carvalho, R. A. Metabolic Remodeling during H9c2 Myoblast Differentiation: Relevance for in Vitro Toxicity Studies. *Cardiovasc Toxicol* **2011**, 11 (2), 180–190. <https://doi.org/10.1007/s12012-011-9112-4>.
- (47) Krishna, A.; Kumar, A.; Singh, R. K. Effect of Polyvinyl Alcohol on the Growth, Structure, Morphology, and Electrical Conductivity of Polypyrrole Nanoparticles Synthesized via Microemulsion Polymerization. *ISRN Nanomater* **2012**, 2012, 1–6. <https://doi.org/10.5402/2012/809063>.
- (48) Muller, D.; Rambo, C. R.; Porto, Luismar. M.; Schreiner, W. H.; Barra, G. M. O. Structure and Properties of Polypyrrole/Bacterial Cellulose Nanocomposites. *Carbohydr Polym* **2013**, 94 (1), 655–662. <https://doi.org/10.1016/j.carbpol.2013.01.041>.
- (49) Kelly, F. M.; Johnston, J. H.; Borrmann, T.; Richardson, M. J. Functionalised Hybrid Materials of Conducting Polymers with Individual Fibres of Cellulose. *Eur J Inorg Chem* **2007**, 2007 (35), 5571–5577. <https://doi.org/10.1002/ejic.200700608>.
- (50) Johnston, J. H.; Moraes, J.; Borrmann, T. Conducting Polymers on Paper Fibres. *Synth Met* **2005**, 153 (1–3), 65–68. <https://doi.org/10.1016/j.synthmet.2005.07.138>.
- (51) Tang, L.; Han, J.; Jiang, Z.; Chen, S.; Wang, H. Flexible Conductive Polypyrrole Nanocomposite Membranes Based on Bacterial Cellulose with Amphiphobicity. *Carbohydr Polym* **2015**, 117, 230–235. <https://doi.org/10.1016/j.carbpol.2014.09.049>.
- (52) Razak, S. I. A.; Azmi, N. S.; Fakhruddin, K.; Dahli, F. N.; Wahab, I. F.; Sharif, N. F. A.; Yusof, A. H. M.; Nayan, N. H. M. Coating of Conducting Polymers on Natural Cellulosic Fibers. In *Conducting Polymers*; InTech, 2016. <https://doi.org/10.5772/63304>.
- (53) Bideau, B.; Loranger, E.; Daneault, C. Comparison of Three Polypyrrole-Cellulose Nanocomposites Synthesis. *Journal of Advances in Nanomaterials* **2016**, 1 (2). <https://doi.org/10.22606/jan.2016.12007>.
- (54) Huang, Y.; Gong, X.; Meng, Y.; Wang, Z.; Chen, X.; Li, J.; Ji, D.; Wei, Z.; Li, L.; Hu, W. Effectively Modulating Thermal Activated Charge Transport in Organic Semiconductors by Precise Potential Barrier Engineering. *Nat Commun* **2021**, 12 (1), 21. <https://doi.org/10.1038/s41467-020-20209-w>.
- (55) Pang, A. L.; Arsad, A.; Ahmadipour, M. Synthesis and Factor Affecting on the Conductivity of Polypyrrole: A Short Review. *Polym Adv Technol* **2021**, 32 (4), 1428–1454. <https://doi.org/10.1002/pat.5201>.
- (56) Li, Y.; Gao, Y.; Lan, L.; Zhang, Q.; Wei, L.; Shan, M.; Guo, L.; Wang, F.; Mao, J.; Zhang, Z.; Wang, L. Ultrastretchable and Wearable Conductive Multifilament Enabled by Buckled Polypyrrole

- Structure in Parallel. *npj Flexible Electronics* **2022**, 6 (1), 42. <https://doi.org/10.1038/s41528-022-00176-6>.
- (57) Ateh, D. D.; Navsaria, H. A.; Vadgama, P. Polypyrrole-Based Conducting Polymers and Interactions with Biological Tissues. *J R Soc Interface* **2006**, 3 (11), 741–752. <https://doi.org/10.1098/rsif.2006.0141>.
- (58) Pedrotty, D. M.; Kuzmenko, V.; Karabulut, E.; Sugrue, A. M.; Livia, C.; Vaidya, V. R.; McLeod, C. J.; Asirvatham, S. J.; Gatenholm, P.; Kapa, S. Three-Dimensional Printed Biopatches With Conductive Ink Facilitate Cardiac Conduction When Applied to Disrupted Myocardium. *Circ Arrhythm Electrophysiol* **2019**, 12 (3), 1–11. <https://doi.org/10.1161/CIRCEP.118.006920>.
- (59) Gabriel, C.; Peyman, A.; Grant, E. H. Electrical Conductivity of Tissue at Frequencies below 1 MHz. *Phys Med Biol* **2009**, 54 (16), 4863–4878. <https://doi.org/10.1088/0031-9155/54/16/002>.
- (60) Hasan, A.; Ragaert, K.; Swieszkowski, W.; Selimović, Š.; Paul, A.; Camci-Unal, G.; Mofrad, M. R. K.; Khademhosseini, A. Biomechanical Properties of Native and Tissue Engineered Heart Valve Constructs. *J Biomech* **2014**, 47 (9), 1949–1963. <https://doi.org/10.1016/j.jbiomech.2013.09.023>.
- (61) Courtney, T.; Sacks, M. S.; Stankus, J.; Guan, J.; Wagner, W. R. Design and Analysis of Tissue Engineering Scaffolds That Mimic Soft Tissue Mechanical Anisotropy. *Biomaterials* **2006**, 27 (19), 3631–3638. <https://doi.org/10.1016/j.biomaterials.2006.02.024>.
- (62) Kaiser, N. J.; Coulombe, K. L. K. Physiologically Inspired Cardiac Scaffolds for Tailored in Vivo Function and Heart Regeneration. *Biomedical Materials (Bristol)*. Institute of Physics Publishing June 1, 2015. <https://doi.org/10.1088/1748-6041/10/3/034003>.
- (63) Woodcock, E. A.; Matkovich, S. J. Cardiomyocytes Structure, Function and Associated Pathologies. *Int J Biochem Cell Biol* **2005**, 37 (9), 1746–1751. <https://doi.org/10.1016/j.biocel.2005.04.011>.
- (64) Deb, A.; Ubil, E. Cardiac Fibroblast in Development and Wound Healing. *J Mol Cell Cardiol* **2014**, 70, 47–55. <https://doi.org/10.1016/j.yjmcc.2014.02.017>.
- (65) Mihic, A.; Cui, Z.; Wu, J.; Vlacic, G.; Miyagi, Y.; Li, S.-H.; Lu, S.; Sung, H.-W.; Weisel, R. D.; Li, R.-K. A Conductive Polymer Hydrogel Supports Cell Electrical Signaling and Improves Cardiac Function After Implantation into Myocardial Infarct. *Circulation* **2015**, 132 (8), 772–784. <https://doi.org/10.1161/CIRCULATIONAHA.114.014937>.
- (66) Spearman, B. S.; Hodge, A. J.; Porter, J. L.; Hardy, J. G.; Davis, Z. D.; Xu, T.; Zhang, X.; Schmidt, C. E.; Hamilton, M. C.; Lipke, E. A. Conductive Interpenetrating Networks of Polypyrrole and Polycaprolactone Encourage Electrophysiological Development of Cardiac Cells. *Acta Biomater* **2015**, 28, 109–120. <https://doi.org/10.1016/j.actbio.2015.09.025>.
- (67) Parchehbaf-Kashani, M.; Sepantafar, M.; Talkhabi, M.; Sayahpour, F. A.; Baharvand, H.; Pahlavan, S.; Rajabi, S. Design and Characterization of an Electroconductive Scaffold for Cardiomyocytes Based Biomedical Assays. *Materials Science and Engineering: C* **2020**, 109 (December 2019), 110603. <https://doi.org/10.1016/j.msec.2019.110603>.
- (68) Kai, D.; Prabhakaran, M. P.; Jin, G.; Ramakrishna, S. Polypyrrole-Contained Electrospun Conductive Nanofibrous Membranes for Cardiac Tissue Engineering. *J Biomed Mater Res A* **2011**, 99A (3), 376–385. <https://doi.org/10.1002/jbm.a.33200>.

- (69) Tsui, J. H.; Ostrovsky-Snider, N. A.; Yama, D. M. P.; Donohue, J. D.; Choi, J. S.; Chavanachat, R.; Larson, J. D.; Murphy, A. R.; Kim, D.-H. Conductive Silk–Polypyrrole Composite Scaffolds with Bioinspired Nanotopographic Cues for Cardiac Tissue Engineering. *J Mater Chem B* **2018**, *6* (44), 7185–7196. <https://doi.org/10.1039/C8TB01116H>.
- (70) Gelmi, A.; Ljunggren, M. K.; Rafat, M.; Jager, E. W. H. Influence of Conductive Polymer Doping on the Viability of Cardiac Progenitor Cells. *J. Mater. Chem. B* **2014**, *2* (24), 3860–3867. <https://doi.org/10.1039/C4TB00142G>.
- (71) Ferraz, N.; Straømme, M.; Fellström, B.; Pradhan, S.; Nyholm, L.; Mihranyan, A. In Vitro and in Vivo Toxicity of Rinsed and Aged Nanocellulose–Polypyrrole Composites. *J Biomed Mater Res A* **2012**, *100 A* (8), 2128–2138. <https://doi.org/10.1002/jbm.a.34070>.
- (72) Prasad, A.; Alizadeh, E. Cell Form and Function: Interpreting and Controlling the Shape of Adherent Cells. *Trends Biotechnol* **2019**, *37* (4), 347–357. <https://doi.org/10.1016/j.tibtech.2018.09.007>.
- (73) Ul Haq, A.; Carotenuto, F.; De Matteis, F.; Proposito, P.; Francini, R.; Teodori, L.; Pasquo, A.; Di Nardo, P. Intrinsically Conductive Polymers for Striated Cardiac Muscle Repair. *Int J Mol Sci* **2021**, *22* (16), 8550. <https://doi.org/10.3390/ijms22168550>.
- (74) Kimes, B.; Brandt, B. Properties of a Clonal Muscle Cell Line from Rat Heart. *Exp Cell Res* **1976**, *98* (2), 367–381. [https://doi.org/10.1016/0014-4827\(76\)90447-X](https://doi.org/10.1016/0014-4827(76)90447-X).
- (75) Watkins, S. J.; Borthwick, G. M.; Arthur, H. M. The H9C2 Cell Line and Primary Neonatal Cardiomyocyte Cells Show Similar Hypertrophic Responses in Vitro. *In Vitro Cell Dev Biol Anim* **2011**, *47* (2), 125–131. <https://doi.org/10.1007/s11626-010-9368-1>.
- (76) Onódi, Z.; Visnovitz, T.; Kiss, B.; Hambalkó, S.; Koncz, A.; Ágg, B.; Váradi, B.; Tóth, V. É.; Nagy, R. N.; Gergely, T. G.; Gergő, D.; Makkos, A.; Pelyhe, C.; Varga, N.; Reé, D.; Apáti, Á.; Leszek, P.; Kovács, T.; Nagy, N.; Ferdinandy, P.; Buzás, E. I.; Görbe, A.; Gircz, Z.; Varga, Z. V. Systematic Transcriptomic and Phenotypic Characterization of Human and Murine Cardiac Myocyte Cell Lines and Primary Cardiomyocytes Reveals Serious Limitations and Low Resemblances to Adult Cardiac Phenotype. *J Mol Cell Cardiol* **2022**, *165*, 19–30. <https://doi.org/10.1016/j.yjmcc.2021.12.007>.
- (77) Abi-Gerges, N.; Miller, P. E.; Ghetti, A. Human Heart Cardiomyocytes in Drug Discovery and Research: New Opportunities in Translational Sciences. *Curr Pharm Biotechnol* **2020**, *21* (9), 787–806. <https://doi.org/10.2174/1389201021666191210142023>.
- (78) Zhou, B.; Shi, X.; Tang, X.; Zhao, Q.; Wang, L.; Yao, F.; Hou, Y.; Wang, X.; Feng, W.; Wang, L.; Sun, X.; Wang, L.; Hu, S. Functional Isolation, Culture and Cryopreservation of Adult Human Primary Cardiomyocytes. *Signal Transduct Target Ther* **2022**, *7* (1), 254. <https://doi.org/10.1038/s41392-022-01044-5>.
- (79) Bistola, V.; Nikolopoulou, M.; Derventzi, A.; Katakaki, A.; Sfyras, N.; Nikou, N.; Toutouza, M.; Toutouzas, P.; Stefanadis, C.; Konstadoulakis, M. M. Long-Term Primary Cultures of Human Adult Atrial Cardiac Myocytes: Cell Viability, Structural Properties and BNP Secretion in Vitro. *Int J Cardiol* **2008**, *131* (1), 113–122. <https://doi.org/10.1016/j.ijcard.2007.10.058>.
- (80) Kuznetsov, A. V.; Javadov, S.; Sickinger, S.; Frotschnig, S.; Grimm, M. H9c2 and HL-1 Cells Demonstrate Distinct Features of Energy Metabolism, Mitochondrial Function and Sensitivity to Hypoxia-Reoxygenation. *Biochimica et Biophysica Acta (BBA) - Molecular Cell Research* **2015**, *1853* (2), 276–284. <https://doi.org/10.1016/j.bbamcr.2014.11.015>.

- (81) Ho, C. M. B.; Mishra, A.; Lin, P. T. P.; Ng, S. H.; Yeong, W. Y.; Kim, Y.-J.; Yoon, Y.-J. 3D Printed Polycaprolactone Carbon Nanotube Composite Scaffolds for Cardiac Tissue Engineering. *Macromol Biosci* **2017**, *17* (4), 1600250. <https://doi.org/10.1002/mabi.201600250>.
- (82) Zanzanizadeh Ezazi, N.; Ajdary, R.; Correia, A.; Mäkilä, E.; Salonen, J.; Kemell, M.; Hirvonen, J.; Rojas, O. J.; Ruskoaho, H. J.; Santos, H. A. Fabrication and Characterization of Drug-Loaded Conductive Poly(Glycerol Sebacate)/Nanoparticle-Based Composite Patch for Myocardial Infarction Applications. *ACS Appl Mater Interfaces* **2020**, *12* (6), 6899–6909. <https://doi.org/10.1021/acsami.9b21066>.
- (83) Ajdary, R.; Huan, S.; Zanzanizadeh Ezazi, N.; Xiang, W.; Grande, R.; Santos, H. A.; Rojas, O. J. Acetylated Nanocellulose for Single-Component Bioinks and Cell Proliferation on 3D-Printed Scaffolds. *Biomacromolecules* **2019**, *20* (7), 2770–2778. <https://doi.org/10.1021/acs.biomac.9b00527>.
- (84) Chen, P.-H.; Liao, H.-C.; Hsu, S.-H.; Chen, R.-S.; Wu, M.-C.; Yang, Y.-F.; Wu, C.-C.; Chen, M.-H.; Su, W.-F. A Novel Polyurethane/Cellulose Fibrous Scaffold for Cardiac Tissue Engineering. *RSC Adv* **2015**, *5* (9), 6932–6939. <https://doi.org/10.1039/C4RA12486C>.
- (85) Patten, V.; Chabaesele, I.; Sishi, B. J. N.; van Vuuren, D. Cardiomyocyte Differentiation: Experience and Observations from 2 Laboratories. *Journal of the South African Heart Association (SA Heart)* **2017**, *14*, 96–107. <https://doi.org/10.24170/14-2-2498>.
- (86) Gelmi, A.; Cieslar-Pobuda, A.; de Muinck, E.; Los, M.; Rafat, M.; Jager, E. W. H. Direct Mechanical Stimulation of Stem Cells: A Beating Electromechanically Active Scaffold for Cardiac Tissue Engineering. *Adv Healthc Mater* **2016**, *5* (12), 1471–1480. <https://doi.org/10.1002/adhm.201600307>.



254x177mm (300 x 300 DPI)

Ratiometric Nanothermometer Based on a Radical Excimer for In Vivo Sensing

Davide Blasi, Nerea Gonzalez-Pato, Xavier Rodriguez Rodriguez, Iñigo Diez-Zabala, Sumithra Yasaswini Srinivasan, Núria Camarero, Oriol Esquivias, Mònica Roldán, Judith Guasch, Anna Laromaine, Pau Gorostiza, Jaume Veciana,* and Imma Ratera*

Ratiometric fluorescent nanothermometers with near-infrared emission play an important role in in vivo sensing since they can be used as intracellular thermal sensing probes with high spatial resolution and high sensitivity, to investigate cellular functions of interest in diagnosis and therapy, where current approaches are not effective. Herein, the temperature-dependent fluorescence of organic nanoparticles is designed, synthesized, and studied based on the dual emission, generated by monomer and excimer species, of the tris(2,4,6-trichlorophenyl) methyl radical (TTM) doping organic nanoparticles (TTMd-ONPs), made of optically neutral tris(2,4,6-trichlorophenyl)methane (TTM- α H), acting as a matrix. The excimer emission intensity of TTMd-ONPs decreases with increasing temperatures whereas the monomer emission is almost independent and can be used as an internal reference. TTMd-ONPs show a great temperature sensitivity (3.4% K⁻¹ at 328 K) and a wide temperature response at ambient conditions with excellent reversibility and high colloidal stability. In addition, TTMd-ONPs are not cytotoxic and their ratiometric outputs are unaffected by changes in the environment. Individual TTMd-ONPs are able to sense temperature changes at the nano-micro-scale. In vivo thermometry experiments in *Caenorhabditis elegans* (*C. elegans*) worms show that TTMd-ONPs can locally monitor internal body temperature changes with spatio-temporal resolution and high sensitivity, offering multiple applications in the biological nanothermometry field.

1. Introduction

Nanothermometry is becoming a fundamental topic in several technological and scientific fields like electronics and biology.^[1–6] Indeed, the miniaturization and the increment in power density in micro and optoelectronic devices require accurate temperature determination with high spatial resolution of the thermal effects (self-heating, heat dissipation, etc.) to optimize device performance.^[1–4] In biology, during the last years a rising interest in intracellular thermal sensing has appeared,^[5–7] for instance in diagnosis (sensing the heat production in cancer and inflammatory processes)^[8,9] and in hyperthermia therapy, where monitoring the temperature during the treatment is fundamental to avoid an over-generation of heat that can burn the surrounding tumor's tissue.^[10–12] Nanothermometry for biology is still challenging since bio-sensors should exhibit high sensitivity, accuracy, and spatial resolution, together with

D. Blasi, N. Gonzalez-Pato, X. Rodriguez Rodriguez, I. Diez-Zabala, S. Y. Srinivasan, O. Esquivias, J. Guasch, A. Laromaine, J. Veciana, I. Ratera
Institut de Ciència de Materials de Barcelona (ICMAB-CSIC)
Bellaterra 08193, Spain
E-mail: veciana.j@icmab.es; iratera@icmab.es

D. Blasi
Dipartimento di Chimica
Università degli Studi di Bari "Aldo Moro"
Bari 70125, Italy

N. Gonzalez-Pato, X. Rodriguez Rodriguez, J. Guasch, P. Gorostiza, J. Veciana, I. Ratera
Networking Research Center on Bioengineering
Biomaterials and Nanomedicine (CIBER-BBN)
Campus UAB
Bellaterra 08193, Spain

N. Camarero, P. Gorostiza
Institute for Bioengineering of Catalonia (IBEC)
The Barcelona Institute of Science and Technology
Clúster, Baldiri Reixac 10-12, Barcelona 08028, Spain

M. Roldán
Unitat de Microscòpia Confocal i Imatge Cel·lular
Servei de Medicina Genètica i Molecular
Institut Pediàtric de Malalties Rares (IPER)
Hospital Sant Joan de Déu
Esplugues de Llobregat 08950, Spain

J. Guasch
Dynamic Biomimetics for Cancer Immunotherapy
Max Planck Partner Group
ICMAB-CSIC
Campus UAB
Bellaterra 08193, Spain

P. Gorostiza
Catalan Institution for Research and Advanced Studies (ICREA)
Barcelona 08010, Spain

 The ORCID identification number(s) for the author(s) of this article can be found under <https://doi.org/10.1002/smll.202207806>.

© 2023 The Authors. Small published by Wiley-VCH GmbH. This is an open access article under the terms of the Creative Commons Attribution License, which permits use, distribution and reproduction in any medium, provided the original work is properly cited.

DOI: 10.1002/smll.202207806

no cytotoxicity and optical and colloidal stabilities being such properties unaffected by changes in pH, concentration, ionic strength, and viscosity typical affecting biological media.^[13] Several systems have been explored as nanothermometers meeting all these requirements, such as organic molecular dyes,^[14,15] quantum dots (QDs),^[16] Ln³⁺ doped systems,^[10,17,18] polymers, and hybrid organic-inorganic systems.^[19–22] All these luminescent sensors exploit the thermal dependence of a fluorophore emission for determining the temperature. These changes can be observed as variations in luminescence intensity, emission band shape, polarization, lifetime, or broadening of the emission bandwidth.^[23]

Intensity-based sensors offer the possibility to work with a simple set-up,^[24] reducing costs and time for data analysis.^[25] Despite its simplicity, an absolute emission intensity measurement can lead to errors due to fluctuations in the active fluorophore concentration inside the cell or tissue due to aggregation or photodegradation. To overcome these problems, a ratiometric output with a dual emission sensing system is needed, also called luminescent intensity ratio (LIR). The simplest strategy, in order to have a dual emission, is to bind together two different emitting species with different thermal quenching of the emission, or exploit different states of aggregation of the same fluorophore, like in the case of excimers.^[12,15,24,26,27]

Recently, organic nanoparticles (ONPs)^[28] and radical-based ONPs have been proposed as fluorescence probes for in vitro bioimaging.^[29] Indeed, polyhalogenated trityl radicals can achieve long-wavelength emission without the need of an extended conjugated system.^[30,31] In addition, it is possible to further red-shift radical emission into the biological transparency window (650 – 950 nm) through the formation of excimers. These excimers, obtained by dispersing radical species in rigid hosts (generally the closed-shell radical precursor) have been studied during the last years due to the possibility to modulate their association/dissociation via the application of an external magnetic field at liquid helium temperature.^[32,33] However, tuning the radical excimer association/dissociation by varying the external temperature has never been reported.

In this work, we propose a highly sensitive full-organic contactless nanothermometer based on organic radical nanoparticles (TTMd-ONPs) consisting of the optically neutral tris(2,4,6-trichlorophenyl)methane (TTM- α H) as a matrix and the tris(2,4,6-trichlorophenyl)methyl radical (TTM) as dopant (Figure 1). These nanoparticles exhibit a dual emission due to the presence of radical monomers and excimers inside the par-

ticle. Increasing temperatures cause a decrease in the excimer emission intensity without a significant alteration of the monomer emission, which allows to use it as an internal reference. This system offers a simple and reproducible nanoscopic sensor, entirely based on two small metal-free molecules, the open-shell TTM radical and its close-shell precursor, the TTM- α H, which are processed as TTMd-ONPs in a single-step self-assembly process, using the re-precipitation method. Achieving a ratiometric output using excimers instead of two different emitting species simplifies and optimizes the preparation of the nano-sensor as well as the thermal sensing, since both emissions come from the same compound and thus, a single wavelength can excite both emitting species. Thus, no correction for different bleaching rates is needed as in the case of hybrid systems. Moreover, excimers of the TTMd-ONPs emit in the region of deep-red/near infrared (NIR) (the first transparency windows of biological tissues), offering the opportunity to penetrate in the deep-tissue for in vivo applications.^[34] In addition, TTMd-ONPs, owing to their metal-free formulation, are non-cytotoxic and their ratiometric outputs are unaffected by changes in pH and ionic strength that may occur under physiological conditions. Moreover, thanks to the magnetic properties of the TTMd-ONPs, could also be used as dual-mode bio-imaging, coupling luminescence, and magnetic resonance.^[35]

2. Results and Discussion

In previous works, we reported, for the first time, that TTM radical was able to form excimers when dispersed in rigid matrices (polymers or ONPs), like in TTMd-ONPs.^[36,37] Radical excimers in ONPs are extremely promising since they are efficient emitters in the NIR, constituting an attractive system for optoelectronics.^[32,33] These TTMd-ONPs were characterized by an average size distribution of ≈ 100 nm, spherical shape, and high colloidal stability in water. In addition, these radical doped systems can also play a relevant role in bio-imaging and bio-sensing since they are water dispersible and present unique optical properties. Indeed, they show a huge Stock's shift and an efficient emission in the first biological transparency window (650 – 950 nm), which minimizes self-absorption effects and shows better tissue penetration compared to UV-visible wavelengths,^[38] together with microsecond lifetimes that allow filtering self-fluorescence signals simply applying a delay between excitation and detection. Therefore, the optical

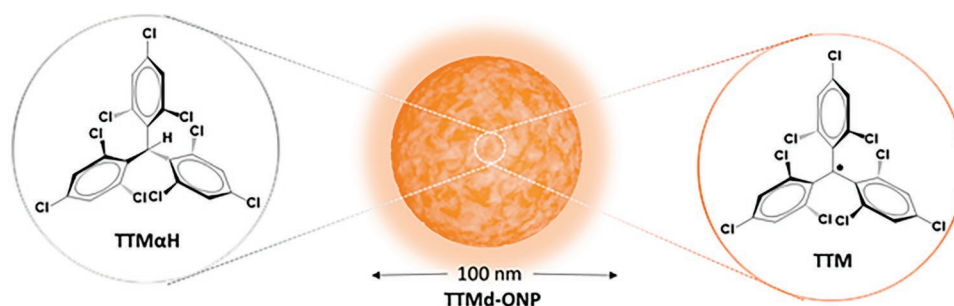


Figure 1. Molecular structures of TTM- α H and the TTM radical molecules and idealized representation of TTMd-ONPs made of a blend of TTM- α H, acting as a matrix and the optically active TTM radical.

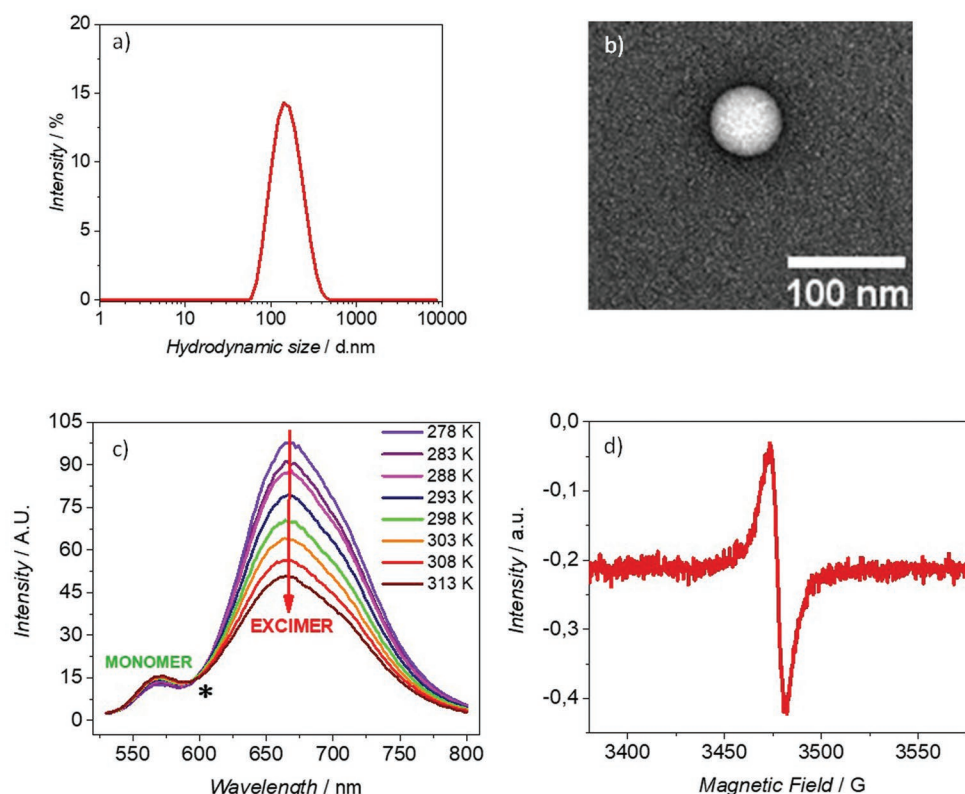


Figure 2. TTMd-ONPs 20% water suspension (with 5% in vol of THF); a) dynamic light scattering (DLS) size distribution at RT and b) representative TEM image of one TTMd-ONP; c) fluorescence emission spectra changing the temperature in the range 278 – 313 K (step 5 K). The isostilbic point is marked with an asterisk. d) EPR signal at RT.

properties of TTM radical doped ONPs offer outstanding opportunities as contactless nanothermometer. To accomplish such objective, we started investigating the TTMd-ONPs composed of 20% w/w of TTM radical dispersed in the TTM- α H matrix. These ONPs were prepared by slow dropping of a THF solution of the two mixed molecules into MilliQ water as reported.^[36,37] The resulting water suspension of ONPs (with 5% in vol of THF), showed an average hydrodynamic diameter of 100 nm with negative Z-potentials close to –45 mV (**Figure 2a**). **Figure 2** shows the emission spectra of these particles as a function of temperature in the 278–313 K range. The excimer emission at 665 nm is strongly quenched upon increasing the temperature, while the monomer emission at 572 nm is weakly affected by the thermal variation. The system exhibits an isostilbic point at 594 nm clearly indicating a temperature-controlled equilibrium between monomers and excimers (**Figure S1a**, Supporting Information). Moreover, electron paramagnetic resonance (EPR) measurements of TTMd-ONPs (**Figure 2d**) demonstrate that the radical magnetic properties are preserved inside the nanoparticles.

Figure 3a,b shows the absorption spectra of water suspension of TTMd-ONPs and the temperature-dependence of the excimer (orange) and monomer (blue) maximum emission intensities. Interestingly, as it can be seen following the temperature-dependence of the luminescent intensity ratio, $LIR = I_M/I_E$, the process is completely reversible (**Figure 3c**; **Figure S1b**, Supporting Information), so collections of

TTMd-ONPs can be used to monitor real-time temperature variations of their suspensions. We already observed in our previous work that changing the TTM doping concentration in ONPs, allows tuning both the monomer/excimer fluorescence intensity ratio and the maximum wavelength of the excimer emission band, which is red-shifted upon increasing the radical concentration.^[25,36,37] For this reason, ONPs with different % of doping were prepared (15, 20, 25% w/w of TTM) and the resulting suspensions of ONPs in water with a 5% of THF showed average sizes and Z-potentials values of 100 nm, with narrow size distribution, and –45 mV, respectively.

The thermometric parameter I_M/I_E at different temperatures were fitted with the empirical Equation (1).^[25,39,40]

$$LIR = \frac{I_M}{I_E} = a + b \exp(cT) \quad (1)$$

where I_M and I_E correspond to the maximum intensity of fluorescence emission of the monomer and excimer respectively, and a , b , and c are constants.

To determine the performance of the nanothermometric system we evaluated the luminescent intensity ratio (LIR) and compare the results with other reported sensors determining the absolute sensitivity (S_a), using Equation S1 (Supporting Information).

However, to compare LIR of systems, that are different in nature, it is preferable to use the relative sensitivity (S_r)

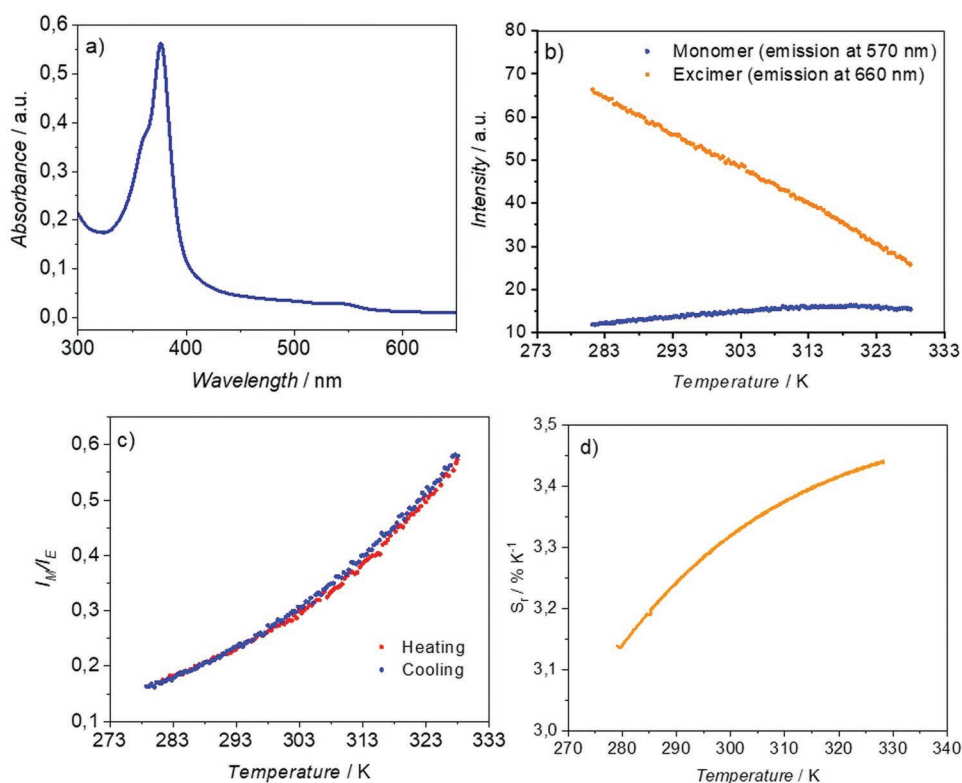


Figure 3. TTMD-ONPs 20% water suspension (with a 5% of THF); a) absorption spectrum, b) temperature-dependent excimer (orange) and monomer (blue) maximum emission intensities, c) luminescent intensity ratio of monomer over excimer in one cycle heating/cooling showing the high reversibility of temperature sensing of the ONPs and d) relative sensitivity of the particles with increasing temperature.

parameter and not the absolute sensitivity (S_a) value, given by Equation (2).^[25,39,40]

$$S_r = \left| \frac{\partial Q / \partial T}{Q} \right| \times 100\%, [\% \cdot K^{-1}] \quad (2)$$

Temperature dependence of ratiometric output $Q(T)$ was obtained by fitting the experimental I_M/I_E ratio with the empirical Equation (1), for the three TTMD-ONPs samples (Figure S2, Supporting Information). Afterwards, to evaluate the performance of every sample as nanothermometer, it was calculated the values of the absolute and relative sensitivity, using Equations S1 (Supporting Information) and 2, respectively (Figure S2, Supporting Information). TTMD-ONPs with 20% of TTM exhibited the best relative sensitivity all along the investigated temperature range, showing a thermal relative sensitivity at RT of $S_r = 3.3\%K^{-1}$ ($T = 298$ K); one of the highest values reported for nanothermometers based on small fluorescent metal-free organic molecules using an intensity-based method for the thermal detection.^[41] The smallest detectable temperature change or minimum temperature resolution was estimated, using Equation S2 (Supporting Information), as $\Delta T_{\min} = 0.3$ degree, which is very good compared with other reported systems.^[8,42] Hence, 20% TTMD-ONPs suspension was chosen as the optimal suspension for further studies (Figure 3).

To use the TTMD-ONPs as contactless nanothermometers for bio-sensing, the suspension was dialyzed to remove the remaining organic solvent (THF), present due to particle

preparation. Dialysis caused a small reduction of the relative sensitivity since ONPs dispersed in pure MilliQ water showed a $S_r = 2.3\% K^{-1}$ ($T = 298$ K) (Figure S3, Supporting Information). This sensitivity change is attributed to the elimination of THF traces that may be trapped into the ONPs during the self-assembly process. It is remarkable, that above 283 K the sensitivity remains above $2\% K^{-1}$, which is a very promising result considering the generally accepted value of $0.5\% K^{-1}$ quality threshold for useful biosensing nanothermometers,^[25] which is exceeded by our ONPs in the whole temperature range. The effect of the dialysis did not affect the ONPs morphology, size, or size distribution. Thus, ONPs presented a uniform monomodal size distribution, with an average diameter of 106 ± 21 nm (Figure S4, Supporting Information), a Z-potential of -42 mV and a spherical shape, exactly as observed for samples after preparation.^[37]

To move on toward biological applications of 20% TTMD-ONPs as nanothermometers, their spectroscopic and colloidal properties were tested in conditions more similar to those of intracellular and biological environments. First, we verified that the ratiometric output or LIR thermometric parameter of TTMD-ONPs suspensions is independent of concentration fluctuations because this issue is fundamental in bio-imaging since ONPs could accumulate differently in specific areas of the analyzed cells or tissues. With this aim, the thermometric parameter of 20% TTMD-ONPs in pure MilliQ water was compared with the 1:3 dilution (20% TTMD-ONPs dil). Results in Figure S5 (Supporting Information) demonstrate that both

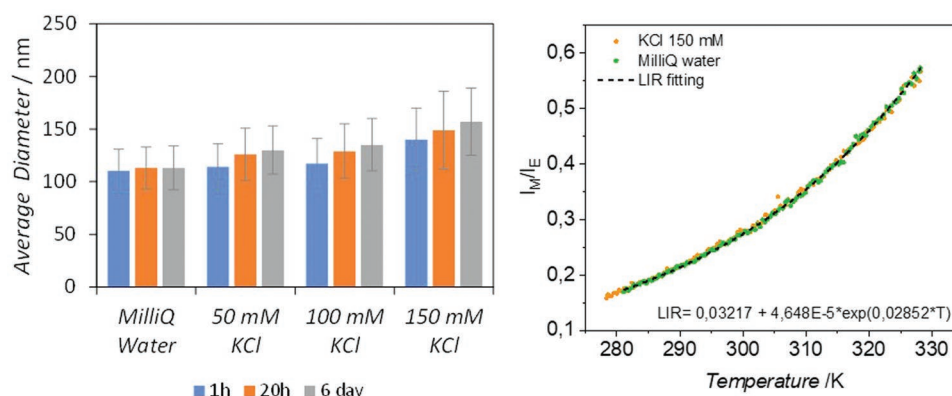


Figure 4. Effect of the ionic strength on the optical and colloidal properties of 20% TTMD-ONPs water suspensions. KCl was added in three concentrations: 50, 100, and 150 mM. Left) Size stability by DLS; right) stability of fluorescence intensity ratios as a function of temperature.

suspensions exhibit the same ratiometric output and sensitivity. The effect of the ionic strength on the optical and colloidal properties was also analyzed because it is well known that the presence of salts can affect the colloidal stability of the suspensions enhancing aggregation of ONPs with concomitant optical changes. The most abundant ion in the cytoplasm is potassium, with a concentration of ≈ 139 mM.^[27] Thus, in order to evaluate the effect of the K^+ ion on the optical properties and the colloidal stability of 20% TTMD-ONPs suspensions, KCl was added in a fresh-dialyzed sample in three different concentrations: 50, 100, and 150 mM. The three resulting suspensions and the suspension in pure MilliQ water were analyzed by dynamic light scattering (DLS) technique at 1 h, 20 h, and 6 days after the addition of the potassium salt, and the results are reported in **Figure 4**. In pure water, the system is extremely stable and no appreciable changes occur during six days; a result that can be ascribed to the highly negative values of the Z-potential of ONPs preventing their aggregation. Adding higher amounts of KCl salt slightly destabilizes the suspensions, but small signals of aggregation can be observed only after six days with the largest salt concentration of 150 mM assayed. Nevertheless, no changes in the optical response of the ONPs were associated with this aggregation since the fluorescence intensity ratios of the sample in MilliQ water and the one with KCl at 150 mM, after six days are not significantly different (Figure 4). This result shows that suspensions of a collection of isolated ONPs and those with some degree of aggregation exhibit the same emissive properties.

Another key parameter to consider for biosensing applications of ONPs is the pH. The regulation of the pH is a fundamental process for cell's correct growth and function. Indeed, cellular metabolic activities, with CO_2 and lactic acid production, can modify the intracellular pH-inducing complex H_3O^+ transporting processes.^[43–45] Consequently, the optical properties and colloidal stability of 20% TTMD-ONPs suspensions were tested in the range of pH 5–8 using phosphate-buffered saline (PBS) solutions (Table S1, Supporting Information). Analyzing the DLS data of suspensions at three different pH values during 4 days (Figure S6, Supporting Information), shows that the most acidic media (pH 5) promotes a small aggregation of the particles after 4 days, while the suspension at pH 8 does not show any signal of aggregation. This result is consistent with

the fact that ONPs present a negative value of Z-potential. Also, in this case, the I_M/I_E luminescent intensity ratios of the three suspensions are not significantly different.

As the last physicochemical characterization, we checked the colloidal and emission stability of the 20% TTMD-ONPs suspensions after prolonged thermal stress in order to evaluate the possibility to use such nanoparticles also as nanothermometers in hyperthermia therapy. PBS was added to a fresh dialyzed sample to buffer the pH at 5.0, 6.5, and 8.0, with an ionic strength of 150 mM (Table S2, Supporting Information). The resulting suspensions together with the nanoparticles in MilliQ water were heated for 2 h at 323 K and DLS analysis was performed before heating, and after 1 h and 2 h of heating (Figure S7, Supporting Information). In MilliQ water the heating process does not induce any growth of particles while in the presence of PBS there is a slight tendency to increase particle size which is almost independent of the pH. Prolonged heating at 323 K did not induce any precipitation or drastic aggregation; thus, the 20% TTMD-ONPs is a robust system to be considered as a fluorescent nanothermometer suitable also for sensing in different environmental conditions relevant for in vivo applications, i.e., hyperthermia therapy.

To use TTMD-ONPs as nanothermometers for cellular biosensing we performed a viability assay^[46] evaluating the metabolic activity of cells in the presence of 20% TTMD-ONPs suspensions using the 3-(4,5-dimethylthiazol-2-yl)-2,5-diphenyltetrazolium bromide (MTT) colorimetric assay. The obtained cell viability results with COS-7 cells, a kidney fibroblast-like cell line (Figure S8, Supporting Information), indicate that such cells are viable in all tested concentrations of ONPs. Additionally, tsA201 embryonic adherent cells, a transformed human kidney cell line, were incubated with the ONPs suspension. Fluorescence microscopy images showed healthy cell morphologies which support the good biocompatibility of the ONPs (Figure S9, Supporting Information).

Once we have demonstrated that suspensions of TTMD-ONPs are not cytotoxic and permit us to sense the temperature of their aqueous surrounding media with high sensitivity, we addressed if isolated nanoparticles might sense the local temperature at the nanoscale. We incubated 20% TTMD-ONPs suspensions at a given concentration on top of a small glass coverslip treated with poly-L-Lys for ONP attachment, which

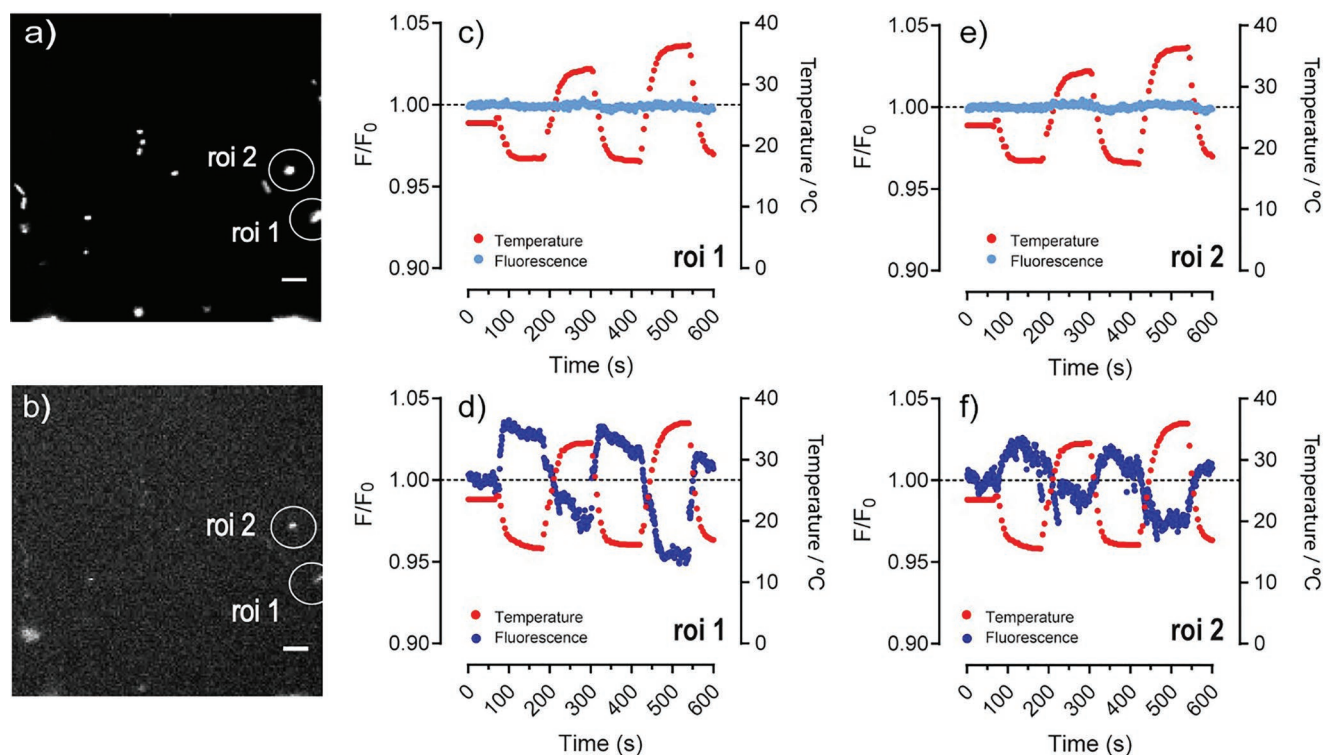


Figure 5. Representative images and fluorescence intensity versus time traces of 20% TTMD-ONPs in response to sequential temperature gradients. Images and emissive signals for ROIs #1 and #2 were recorded with a fluorescence inverted microscope exciting at $\lambda_{\text{exc}} = 377$ nm and detecting the emission with a 510–560 nm filter for the monomers (a) and with a 595–670 nm filter for the excimers (b). Scale bar 1 μm . Variation of the fluorescence intensity ratio (F/F_0) emitted by the monomers (c,e) and by the excimers (d,f) in a temperature interval of ≈ 20 degrees.

was connected to a fluidic system. We placed under the coverslip a system to cool down and warm up the sample with a temperature amplitude of ± 20 degrees. To test for reversibility and homogeneity, we performed two cold-hot cycles in each measurement, choosing different regions of interest (ROIs) whose fluorescence signals were analyzed separately (Figure 5). To record the TTMD-ONPs fluorescence signals, we employed an inverted fluorescence microscope exciting at $\lambda_{\text{exc}} = 377$ nm (using a monochromatic light source based on a xenon lamp) and reading the emissions with two different dichroic filters: the first one at 510–560 nm recording the emission of monomers and the second one at 595–670 nm for the excimer's emission (Figure 5a,b). Interestingly, the monomer fluorescence intensities of nanoparticles in two ROIs remained almost constant in a temperature interval of ≈ 20 degrees (Figure 5c,e), while the excimer signals were inversely proportional to it (Figure 5d,f). This result demonstrates that TTMD-ONPs can sense temperature changes locally at the nanoscale, and behave as ratiometric temperature nanoprobess. For statistical analysis of fluorescence emission signals, see Figure S10 (Supporting Information).

After demonstrating the temperature sensing capability of 20% TTMD-ONPs at the submicron scale, we measured the temperature in living *Caenorhabditis elegans* (*C. elegans*) worms as an in vivo model system. *C. elegans* is a 1 mm long nematodes, with a short life cycle, rapid reproduction, optical transparency, and physiological similarity with humans.^[47] Therefore, *C. elegans* offer experimental simplicity and valuable infor-

mation as an animal model to test bioimaging probes,^[42,48] for nanothermometry experiments using nanoparticles.^[42,49,50]

Before using our ONPs in *C. elegans*, we carried out several control experiments of the ONPs' behavior in the environment of *C. elegans*. First, we checked if the M9 buffer, the saline medium commonly used to maintain and expose ONPs to *C. elegans*, affected the hydrodynamic sizes and size distributions of the 20% TTMD-ONPs over time. During the first 24 h (time of ONPs exposure to *C. elegans*) no significant changes in the average hydrodynamic size and size distributions of ONPs occurred (Figure S11, Supporting Information). So, the nanoparticles preserve their original average diameter of ≈ 100 nm, which is an appropriate size to be ingested by the worms. The L4 larval stage worms were treated with $55 \mu\text{g mL}^{-1}$ suspension of 20% TTMD-ONPs in liquid M9 buffer for 24 h (Figure 6; Figure S12, Supporting Information). After 24 h of exposure 97% of worms were alive with no significant difference from the control group, which demonstrates that ONPs are not lethal for the worms. Similarly, we also measured body length after exposure to examine the growth and development of *C. elegans* from the L4 to the egg-bearing adult stage during the 24 h, and found that the ONPs did not affect the rate of development significantly. The survival and development assays confirm that the TTMD-ONPs do not show any biological toxicity in *C. elegans*. A third control experiment was employed to determine the survival rate of *C. elegans* at different temperatures. This test helped to identify at which temperature the worms died to determine the temperature range to use the worms as

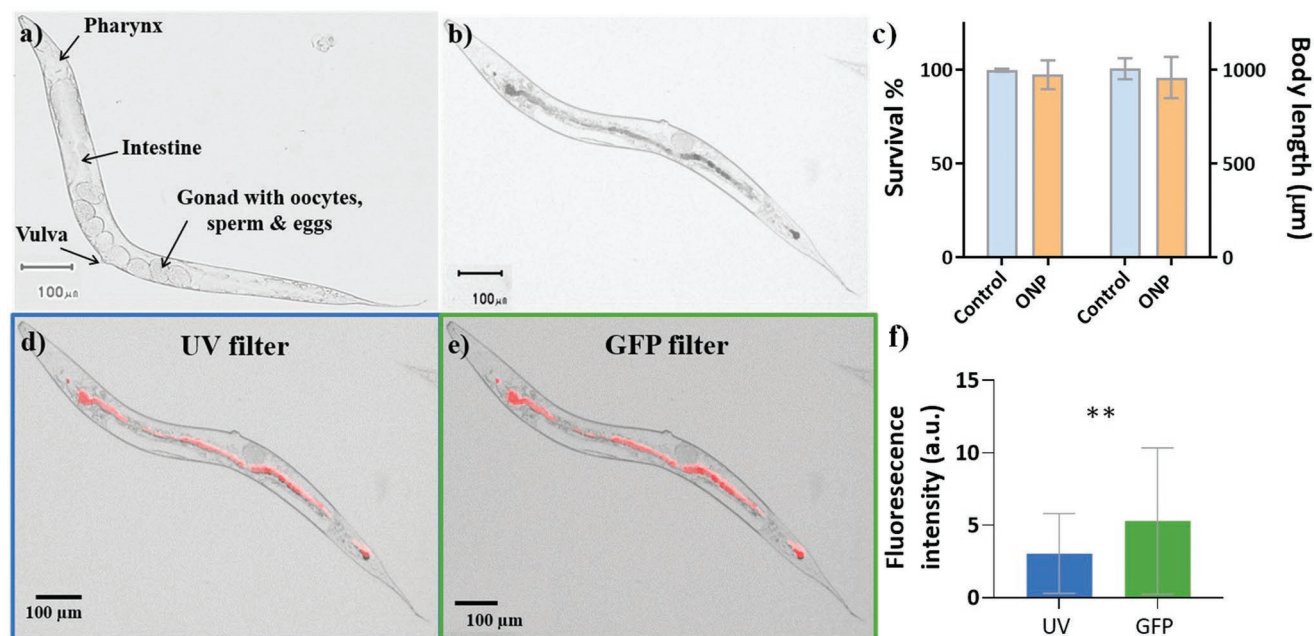


Figure 6. a) Untreated control *C. elegans* where some anatomical parts of the worm are described; b) *C. elegans* treated with ONPs. c) Survival rate and body length of *C. elegans* with and without ONPs. Treated worms under d) UV filter (>510 nm), e) GFP filter (>590 nm), where the TTM-ONPs are visualized in the intestine; f) comparative fluorescence intensity of ONPs under the two filters.

a model system to test the TTMd-ONPs as nanothermometers. *C. elegans* were heated up with steps of 5 K starting from 293 until 328 K. For each temperature, after two minutes of stabilization, a few drops of the worms' suspension were observed under the microscope to count the dead and alive worms. The survival rate at 293 K was considered as the positive control since some worms could have died for other reasons. Table S3 (Supporting Information) shows survival rates obtained in the studied temperature range, showing that, at 308 K, 72% of worms were still alive which declined drastically at temperatures higher than 313 K (Figure S13, Supporting Information). This result indicates that *C. elegans* can be used as an in vivo model system for validating ONPs as nanothermometers but only at temperatures below 313 K.

Then, we proceeded to observe the *C. elegans* exposed to 55 $\mu\text{g mL}^{-1}$ of the 20% TTMd-ONPs with a fluorescence microscope using UV (> 510 nm) and Green (> 590 nm) long pass filters at RT to visualize ingested ONPs (Figure 6). The ONPs were ingested orally and passed through the pharynx to the intestines. Higher accumulation of ONPs can be observed near the pharynx since it acts as a filter-grinder and ONPs might concentrate there.^[51]

After visualizing the nanoparticles within the worms, the output emission intensity of the ONPs was measured to check the validity of the luminescent ONPs as an in vivo nanothermometer. Taking advantage of the transparency of the worms, we proceeded in the same way as with the 20% TTMd-ONPs aqueous suspensions, measuring the emission of a suspension of *C. elegans* exposed to ONPs and control *C. elegans* in a cuvette. We compared the emission spectra of a suspension of *C. elegans* with a suspension of *C. elegans* exposed to ONPs at 278 and 298 K (Figure S14, Supporting Information).

Interestingly, in the untreated *C. elegans* suspension, an emission band at 523 nm appears when the worms are alive which is attributed to their tissue autofluorescence, that overlaps with the monomer band of the ONPs.^[52] The intensity of this band increases significantly when the sample is heated at 328 K and remains intense when the suspension was cooled down to 278 K. Indeed, the increase of this band has been attributed to the death of the worms with the temperature and the denaturation of proteins.^[53] In the literature, a model predicts that 1% of the *C. elegans* proteome should be denatured at 320 K and 50% of their proteome is denatured at 326 K.^[54] These results indicate that *C. elegans* cannot be used as model systems for evaluating in vivo the performances of ONPs as nanothermometers at temperatures higher than 313 K.

Finally, to determine the sensitivity of 20% TTMd-ONPs inside the worms as nanothermometers and to compare it with the free nanoparticles, further emission spectra were performed. For both suspensions, an emission scan was performed at 278 K with an excitation wavelength of 377 nm to obtain the maxima of the monomer and excimer emission bands of the TTMd-ONPs in the two samples. Then, a thermal scan was performed, recording only the maximum intensity for the excimer and monomer bands, every 0.5 K, from 278 K until 313 K with a heating rate of 0.8 K min^{-1} . Finally, to check the reversibility of the system the inverse thermal scan was carried out, from 313 to 278 K. The luminescence intensity ratio (Q) between the maximum of the monomer, corrected by subtracting the emission of the worms due to its autofluorescence at 523 nm, and the maximum of excimer was plotted and fitted using the LIR empirical Equation (1) through data points at different temperatures. Then, deriving the LIR function of Q with respect to temperature, the thermal absolute sensitivity

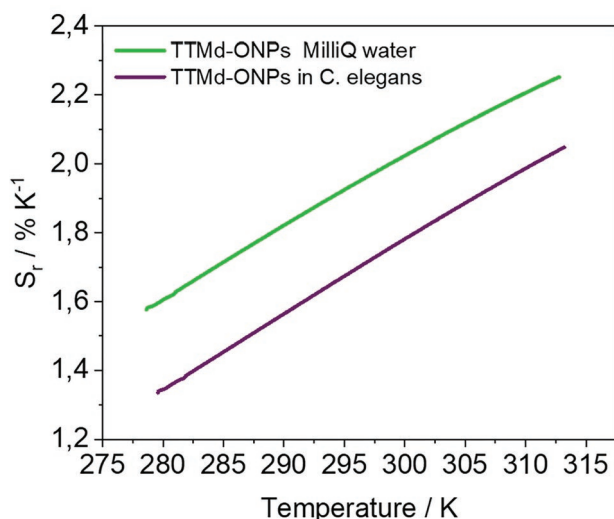


Figure 7. Relative sensitivity of TTMD-ONP as nanothermometer at different temperatures in water suspension (green) and inside *C. elegans* (violet).

values for both samples were obtained using Equation S1, and the relative sensitivity was determined using Equation (2). As observed in **Figure 7**, the sensitivity of the ONPs ingested in *C. elegans* (TTMD-ONP *C. elegans*) was successfully measured and found to be very significant, $S_r = 1.7\% K^{-1}$ ($T = 298 K$). The relative temperature sensitivity is always higher than $1\% K^{-1}$ in the whole evaluated temperature range, which is twice the threshold quality value of $0.5\% K^{-1}$ set in the literature for nanothermometry applications.^[25] In addition we also estimated a minimum temperature resolution of $\Delta T_{min} = 0.6$ degrees, using Equation S2 (Supporting Information), which is also a very promising result for future applications of TTMD-ONPs as in vivo fluorescent nanothermometers.

The possibility to measure changes of temperature dependent fluorescence emission, of organic nanoparticles in a live organism is very promising, but to use them in practical applications, it is necessary to show the performance of this nanothermometer locally at the submicron scale. Hence, we have measured temperature changes inside individual *C. elegans* in a localized area of their intestine, using a confocal microscope. For confocal measurements, *C. elegans* were immobilized using NemaGel, and changes in temperature were recorded by tracking the fluorescence emission intensity at two wavelength ranges, 420–570 and 620–720 nm to record the emission associated with the monomer and the excimer, respectively. A 3D representation of the *C. elegans* intestine with the ingested TTMD-ONPs is represented in Figure S15 (Supporting Information) with also a zoom of a small area showing emission of monomer (green) and excimer (red) of a single TTMD-ONPs particle/aggregate.

Three different temperature ranges were studied starting from 290–293 K by cooling the microscope cage with dry ice, then increasing it to 297–300 K and finally to 307–308 K, by using a heater coupled to the confocal. For each temperature at least 6 measurements were recorded to have statistical data. In **Figure 8a** is represented the ratio between monomer and excimer emission in the bottom region of the intestine

of the *C. elegans*, the data for the top region is represented in Figure S16 (Supporting Information).

As demonstrated above, with increasing temperature, the ratio between the monomer and excimer emissions bands (Q) increases and the same behavior is shown locally inside an individual *C. elegans*. These results demonstrate that these ONPs can be used to measure the temperature in a small localized area of a single animal.

Even though the deviation for each temperature range is broad because every *C. elegans* is different and can metabolize the TTMD-ONPs in different ways, similar ratiometric behavior to that obtained in vitro is observed. When increasing the temperature, the fluorescence emission intensity decreases for the red frame (420–570 nm) and keeps constant for the green one (620–720 nm). For a better understanding of the data, Figure 8b shows the same *C. elegans* animal at two different temperatures. At higher temperature a decrease of fluorescence intensity of the nanoparticles at higher wavelengths is observed, supporting the reported data.

3. Conclusion

We have developed organic radical TTMD-ONPs, as ratiometric nanothermometers based on a radical excimer for in vivo sensing with excellent temperature sensitivity $3.4\% K^{-1}$ (at 328 K), reversibility and high colloidal stability. One of the advantages of the described system is its simplicity since both the host and guest molecules forming the nanoparticles are small metal-free organic molecules which allow higher control on the molecular structure, higher reproducibility of the synthesis, and easier purification than polymers. Moreover, both the host and the guest molecules, the TTM- αH and TTM radical, respectively, are processed as nanoparticles by the self-assembly of the two molecules in a simple single-step process using the re-precipitation method. Thanks to the simplicity of the synthesis of the two molecules and their self-assembly properties, TTMD-ONPs constitute an example of a cost-effective thermal sensor. In pure water the suspension of TTMD-ONPs is colloidal stable offering the possibility to be stored for a long time without aggregation or radical-leaking phenomena. The colloidal properties are preserved even increasing the ionic strength and varying the pH in the range of 5–8. Furthermore, TTMD-ONPs show two emission bands with a ratiometric output or LIR thermometric parameter, that is independent of dilution, particle aggregation, ionic strength, and pH, while was strongly affected by changes in temperature, showing a completely reversible behavior without any hysteresis. The second strength of TTMD-ONPs is provided by the open-shell electronic configuration of the TTM radical emitter molecule, present as a monomer or as an excimer, which ensures better optical performances than close-shell fluorophores. Indeed, sensors based on organic closed-shell fluorophores show low values of Stokes shift and short lifetimes ($\approx ns$), which make these systems subjected to use inner-filter effects and showing scattering problems. Thanks to the large Stokes shift and their large emission lifetime (for both the monomer and the excimer emission) TTMD-ONPs can avoid problems related to the autofluorescence of the biological tissue or the scattering of the

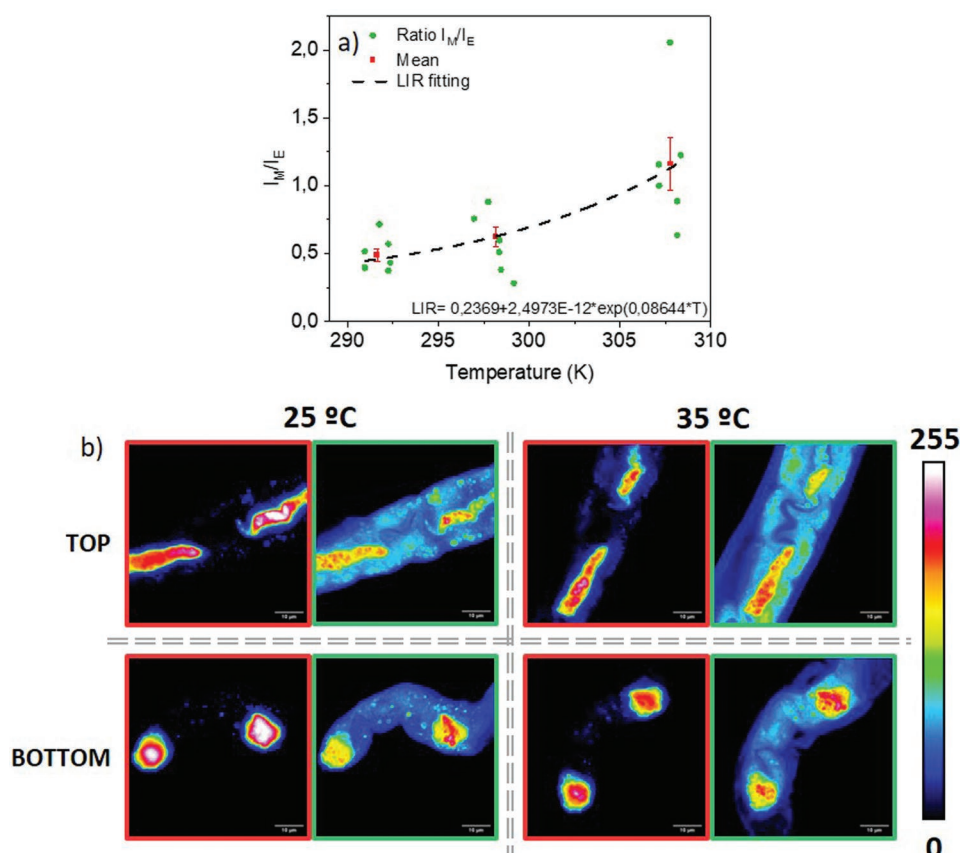


Figure 8. a) Local measurement of the ratio (Q) I_M/I_E between monomer and excimer maxima fluorescence emission at increasing temperature of the TTMD-ONPs inside *C. elegans*, from a region of the bottom of the body. Red points represent the average of the ratios and the error bars are the standard errors caused by different worms for the same temperature range, for $n = 6$ and $p = 0.9917$, 0.9994 , and 0.9959 , respectively; b) representative confocal images of the top and bottom parts from the same *C. elegans* with TTMD-ONPs inside the intestine at two different temperatures, 298 K (left) and 308 K (right). The green frame represents the 420–570 nm detection wavelength and the red frame the 620–720 nm wavelength. Scale bar 10 μm. The color scale shows pixels with the lowest intensity (0) to the highest intensity (4095).

excitation light. Since simply applying a delay between the excitation and the detection it is possible to considerably increase the signal to noise ratio. Therefore, TTMD-ONPs constitute a small-molecule-based luminescence ratiometric sensor able to join the strengths of both organic and inorganic sensors but being all-organic. TTMD-ONPs emit in the region of deep-red/NIR (i.e., the first transparency windows of biological tissues), offering the opportunity to obtain a deep-tissue penetration for in vivo applications. In addition, TTMD-ONPs are not cytotoxic and their ratiometric outputs are unaffected by changes of small aggregations, pH or ionic strength that may occur under physiological conditions. Finally, in vivo thermometry experiments made with *Caenorhabditis elegans* worms indicated that TTMD-ONPs could monitor locally in vivo the temperature changes at the sub-micron scale from 278 to 313 K, with a high sensitivity indicating the considerable potential applications of TTMD-ONPs in the biological thermometry field. In addition, thanks to the chiroptical and magnetic properties of polyhalogenated trityl radicals,^[55,56] new nanothermometers are being designed, enhancing the optical outputs and versatility of these systems for biological and clinical research.^[57] Moreover, to use these systems in a biological environment, both, the excitation and the emission wavelength are required to be in the biological

window. In a work in progress we are studying the use of TTMD-ONPs as two-photon microscopy probe to increase the excitation wavelength in order to have both the excitation and the emission wavelengths in the biological window increasing its penetration capacity into tissues and cells without damage.

Supporting Information

Supporting Information is available from the Wiley Online Library or from the author.

Acknowledgements

D.B. and N.G.-P. contributed equally to this work. The authors are grateful for the financial support received from the Spanish Government (PID2020-115296RA-I00, PID2019-105622RB-I00, PDI2021-122645OB-I00, RTI2018-096273-B-I00 and PID2019-111493RB-I00) funded by MICIN and the “Ramón y Cajal” program (RYC-2017-22614), the Generalitat de Catalunya (SGR-918, 2017SGR765, SGR Cat 2021-00438, 2017-SGR-1442, and 2021-SGR-1410, 2021-SGR-00446), and the Networking Research Center on Bioengineering, Biomaterials, and Nanomedicine (CIBER-BBN). DB gratefully acknowledges the REFIN (Return for Future

Innovation) action for funding, an initiative co-funded by European Union through the POR Puglia 2014 - 2020 (ID grant: 2455F798). This research was also supported by the European Union's Horizon 2020 research and innovation program H2020-MSCA-COFUND-2016 (DOC-FAM, grant agreement Nr. 754397), Human Brain Project WaveScaES (SGA2-785907 and SGA3-945539), DEEPER (ICT36-2020-101016787), and the Marie Skłodowska-Curie grant agreement Nr. 101007804 (Micro4Nano). Support from Fundaluce and CaixaHealth (ID 100010434) are also acknowledged. The work was supported as well by the Max Planck Society through the Max Planck Partner Group "Dynamic Biomimetics for Cancer Immunotherapy" in collaboration with the Max Planck for Medical Research (Heidelberg, Germany). ICMAB-CSIC acknowledges support from the Severo Ochoa Programme for Centres of Excellence in R&D (FUNFUTURE, CEX2019-000917-S). IBEC acknowledges support from the CERCA programme of AGAUR/Generalitat de Catalunya and the Severo Ochoa Programme. This work had been developed inside the "Biochemistry, Molecular Biology and Biomedicine" and "Materials Science" Ph.D. programs of UAB. Nerea Gonzalez-Pato acknowledges the financial support from the FPU fellowship (FPU17/02551) from the Spanish Ministry.

Conflict of Interest

The authors declare no conflict of interest.

Data Availability Statement

The data that support the findings of this study are available from the corresponding author upon reasonable request.

Keywords

Caenorhabditis elegans, excimer emission, in vivo sensing, luminescence, organic radical nanoparticles, ratiometric nanothermometers, trityl radicals

Received: December 13, 2022













Revised: March 24, 2023

Published online:

- [1] A. Majumdar, *Annu. Rev. Mater. Sci.* **1999**, 29, 505.
- [2] D. Halbental, J. Cuppens, M. B. Shalom, L. Embon, N. Shadmi, Y. Anahory, H. R. Naren, J. Sarkar, A. Uri, Y. Ronen, Y. Myasoedov, L. S. Levitov, E. Joselevich, A. K. Geim, E. Zeldov, *Nature* **2016**, 539, 407.
- [3] M. Tzur, B. Desiatov, I. Goykhman, M. Grajower, U. Levy, *Opt. Express* **2013**, 21, 29195.
- [4] O. Yarimaga, S. Lee, D. Y. Ham, J. M. Choi, S. G. Kwon, M. Im, S. Kim, J. M. Kim, Y. K. Choi, *Macromol. Chem. Phys.* **2011**, 212, 1211.
- [5] K. Okabe, N. Inada, C. Gota, Y. Harada, T. Funatsu, S. Uchiyama, *Nat. Commun.* **2012**, 3, 705.
- [6] G. Kucsko, P. C. Maurer, N. Y. Yao, M. Kubo, H. J. Noh, P. K. Lo, H. Park, M. D. Lukin, *Nature* **2013**, 500, 54.
- [7] K. Okabe, R. Sakaguchi, B. Shi, S. Kiyonaka, *Pflugers Arch. Eur. J. Physiol.* **2018**, 470, 717.
- [8] J. Zhou, B. del Rosal, D. Jaque, S. Uchiyama, D. Jin, *Nat. Methods* **2020**, 17, 967.
- [9] M. Monti, L. Brandt, J. Ikomi-Kumm, H. Olsson, *Scand. J. Haematol.* **1986**, 36, 353.
- [10] E. N. Cerón, D. H. Ortgies, B. Del Rosal, F. Ren, A. Benayas, F. Vetrone, D. Ma, F. Sanz-Rodríguez, J. G. Solé, D. Jaque, E. M. Rodríguez, *Adv. Mater.* **2015**, 27, 4781.
- [11] L. Meng, S. Jiang, M. Song, F. Yan, W. Zhang, B. Xu, W. Tian, *ACS Appl. Mater. Interfaces* **2020**, 12, 26842.
- [12] H. Zhou, M. Sharma, O. Berezin, D. Zuckerman, M. Y. Berezin, *ChemPhysChem* **2016**, 17, 27.
- [13] M. Quintanilla, M. Henriksen-Lacey, C. Rennero-Lecuna, L. M. Liz-Marzán, *Chem. Soc. Rev.* **2022**, 51, 4223.
- [14] J. M. Lupton, *Appl. Phys. Lett.* **2002**, 81, 2478.
- [15] N. Chandrasekharan, L. A. Kelly, *J. Am. Chem. Soc.* **2001**, 123, 9898.
- [16] V. A. Vlaskin, N. Janssen, J. Van Rijssel, R. Beaulac, D. R. Gamelin, *Nano Lett.* **2010**, 10, 3670.
- [17] S. Rohani, M. Quintanilla, S. Tuccio, F. De Angelis, E. Cantelar, A. O. Govorov, L. Razzari, F. Vetrone, *Adv. Opt. Mater.* **2015**, 3, 1606.
- [18] X. Wang, Q. Liu, Y. Bu, C. S. Liu, T. Liu, X. Yan, *RSC Adv.* **2015**, 5, 86219.
- [19] J. Li, C. Sun, R. Shen, X. Cao, B. Zhou, D. Bai, H. Zhang, *J. Am. Chem. Soc.* **2014**, 136, 11050.
- [20] A. A. Tseng, K. Chen, C. D. Chen, K. J. Ma, *IEEE Trans. Electron. Packag. Manuf.* **2003**, 26, 141.
- [21] C.-W. Tseng, D.-C. Huang, Y.-T. Tao, *ACS Appl. Mater. Interfaces* **2012**, 4, 5483.
- [22] H. Zhang, J. Jiang, P. Gao, T. Yang, K. Y. Zhang, Z. Chen, S. Liu, W. Huang, Q. Zhao, *ACS Appl. Mater. Interfaces* **2018**, 10, 17542.
- [23] J. Daniel, F. Vetrone, *Nanoscale* **2012**, 4, 4301.
- [24] T. Barilero, T. L. Saux, C. Gosse, L. Jullien, *Anal. Chem.* **2009**, 81, 7988.
- [25] C. D. S. Brites, P. P. Lima, N. J. O. Silva, A. Millán, V. S. Amaral, F. Palacio, L. D. Carlos, *Nanoscale* **2012**, 4, 4799.
- [26] L. Jethi, M. M. Krause, P. Kambhampati, *J. Phys. Chem. Lett.* **2015**, 6, 718.
- [27] C. Gota, K. Okabe, T. Funatsu, Y. Harada, S. Uchiyama, *J. Am. Chem. Soc.* **2009**, 131, 2766.
- [28] S. Sinha, Z. Kelemen, E. Hümpfner, I. Ratera, J. P. Malval, J. P. Jurado, C. Viñas, F. Teixidor, R. Núñez, *Chem. Commun.* **2022**, 58, 4016.
- [29] X. Bai, W. Tan, A. Abdurahman, X. Li, F. Li, *Dyes Pigm.* **2022**, 202, 110260.
- [30] D. Mesto, Y. Dai, C. N. Dibenedetto, A. Punzi, J. Krajčovič, M. Striccoli, F. Negri, D. Blasi, *Euro. J. Org. Chem.* **2023**, 26, 202201030.
- [31] I. Ratera, J. Vidal-Gancedo, D. Maspoch, S. T. Bromley, N. Crivillers, M. Mas-Torrent, *J. Mater. Chem. C* **2021**, 9, 10610.
- [32] K. Kato, S. Kimura, T. Kusamoto, H. Nishihara, Y. Teki, *Angew. Chem., Int. Ed.* **2019**, 58, 2606.
- [33] S. Kimura, T. Kusamoto, S. Kimura, K. Kato, Y. Teki, H. Nishihara, *Angew. Chem., Int. Ed.* **2018**, 57, 12711.
- [34] A. Jana, L. Bai, X. Li, H. Ågren, Y. Zhao, *ACS Appl. Mater. Interfaces* **2016**, 8, 2336.
- [35] X. He, X. Shen, D. Li, Y. Liu, K. Jia, X. Liu, *ACS Appl. Bio Mater.* **2018**, 1, 520.
- [36] D. Blasi, *Molecular and Supramolecular Strategies for Highly Luminescent Trityl Radicals and Their Sensing Applications*, **2017**.
- [37] D. Blasi, D. M. Nikolaidou, F. Terenziani, I. Ratera, J. Veciana, *Phys. Chem. Chem. Phys.* **2017**, 19, 9313.
- [38] J. Mérian, J. Gravier, F. Navarro, I. Texier, *Molecules* **2012**, 17, 5564.
- [39] M. Jia, Z. Sun, M. Zhang, H. Xu, Z. Fu, *Nanoscale* **2020**, 12, 20776.
- [40] H. Xu, M. Jia, Z. Wang, Y. Wei, Z. Fu, *ACS Appl. Mater. Interfaces* **2021**, 13, 61506.
- [41] Y. Sun, M. Fu, M. Bian, Q. Zhu, *Biotechnol. Bioeng.* **2023**, 120, 7.
- [42] M. Fujiwara, S. Sun, A. Dohms, Y. Nishimura, K. Suto, Y. Takezawa, K. Oshimi, L. Zhao, N. Sadzak, Y. Umehara, Y. Teki, N. Komatsu, O. Benson, Y. Shikano, E. Kage-Nakada, *Sci. Adv.* **2020**, 6, eaba9636.
- [43] J. Kurkdjian, A. Guern, *Annu. Rev. Plant Physiol. Plant Mol. Biol.* **1989**, 40, 271.

- [44] A. Hulikova, A. L. Harris, R. D. Vaughan-Jones, P. Swietach, *J. Cell. Physiol.* **2013**, 228, 743.
- [45] T. Bagar, K. Altenbach, N. D. Read, M. Benčina, *Eukaryotic Cell* **2009**, 8, 703.
- [46] Ö. S. Aslantürk, in *Genotoxicity – A Predictable Risk to Our Actual World*, (Eds: M. L. Larramendy, S. Soloneski) IntechOpen, London **2018**, <https://doi.org/10.5772/interopen.69556>.
- [47] L. Gonzalez-Moragas, A. Roig, A. Laromaine, *Adv. Colloid Interface Sci.* **2015**, 219, 10.
- [48] J. Chen, C. Guo, M. Wang, L. Huang, L. Wang, C. Mi, J. Li, X. Fang, C. Mao, S. Xu, *J. Mater. Chem.* **2011**, 21, 2632.
- [49] T. Kimata, H. Sasakura, N. Ohnishi, N. Nishio, I. Mori, *Worm* **2012**, 1, 31.
- [50] J. S. Donner, S. A. Thompson, C. Alonso-Ortega, J. Morales, L. G. Rico, S. I. C. O. Santos, R. Quidant, *ACS Nano* **2013**, 7, 8666.
- [51] Z. F. Altun, D. Hall, *Alimentary System, Pharynx, in Worm Atlas* **2009**, <http://dx.doi.org/doi:10.3908/wormatlas.1.3>.
- [52] Z. Pincus, T. C. Mazer, F. J. Slack, *Aging* **2016**, 8, 889.
- [53] D. Jones, E. P. M. Candido, *J. Exp. Zool.* **1999**, 284, 147.
- [54] K. Ghosh, K. Dill, *Biophys. J.* **2010**, 99, 3996.
- [55] P. Mayorga-Burrezo, V. G. Jiménez, D. Blasi, T. Parella, I. Ratera, A. G. Campaña, J. Veciana, *Chem. – Eur. J.* **2020**, 26, 3776.
- [56] P. Mayorga Burrezo, V. G. Jiménez, D. Blasi, I. Ratera, A. G. Campaña, J. Veciana, *Angew. Chem., Int. Ed.* **2019**, 58, 16282.
- [57] C. He, H. He, J. Chang, B. Chen, H. Ma, M. J. Booth, *Light: Sci. Appl.* **2021**, 10, 194.

Induced ligno-suberin vascular coating and tyramine-derived hydroxycinnamic acid amides restrict *Ralstonia solanacearum* colonization in resistant tomato

Anurag Kashyap¹ , Álvaro Luis Jiménez-Jiménez^{1*} , Weiqi Zhang^{1*} , Montserrat Capellades^{1,2} ,
Sumithra Srinivasan³ , Anna Laromaine³ , Olga Serra⁴ , Mercè Figueras⁴ , Jorge Rencoret⁵ ,
Ana Gutiérrez⁵ , Marc Valls^{1,6}  and Nuria S. Coll^{1,2} 

¹Centre for Research in Agricultural Genomics (CRAG), CSIC-IRTA-UAB-UB, Campus UAB, 08193 Bellaterra, Spain; ²Consejo Superior de Investigaciones Científicas (CSIC), 08001 Barcelona, Spain; ³Institute of Material Science of Barcelona (ICMAB), CSIC, Campus UAB, 08193 Bellaterra, Spain; ⁴Laboratori del Suro, Biology Department, University of Girona, Campus Montilivi, 17003 Girona, Spain; ⁵Institute of Natural Resources and Agrobiology of Seville (IRNAS), CSIC, 41012 Seville, Spain; ⁶Department of Genetics, University of Barcelona, 08028 Barcelona, Spain

Summary

Author for correspondence:

Nuria S. Coll

Email: nuria.sanchez-coll@cragenomica.es

Received: 17 November 2021

Accepted: 3 January 2022

New Phytologist (2022) 234: 1411–1429

doi: 10.1111/nph.17982

Key words: bacterial wilt, feruloyltyramine, HCAAs, lignin, *Ralstonia solanacearum*, suberin, tomato, vascular coating.

- Tomato varieties resistant to the bacterial wilt pathogen *Ralstonia solanacearum* have the ability to restrict bacterial movement in the plant. Inducible vascular cell wall reinforcements seem to play a key role in confining *R. solanacearum* into the xylem vasculature of resistant tomato. However, the type of compounds involved in such vascular physico-chemical barriers remain understudied, while being a key component of resistance.
- Here we use a combination of histological and live-imaging techniques, together with spectroscopy and gene expression analysis to understand the nature of *R. solanacearum*-induced formation of vascular coatings in resistant tomato.
- We describe that resistant tomato specifically responds to infection by assembling a vascular structural barrier formed by a ligno-suberin coating and tyramine-derived hydroxycinnamic acid amides. Further, we show that overexpressing genes of the ligno-suberin pathway in a commercial susceptible variety of tomato restricts *R. solanacearum* movement inside the plant and slows disease progression, enhancing resistance to the pathogen.
- We propose that the induced barrier in resistant plants does not only restrict the movement of the pathogen, but may also prevent cell wall degradation by the pathogen and confer antimicrobial properties, effectively contributing to resistance.

Introduction

In natural environments plants are constantly exposed to diverse microbiota, including pathogenic organisms. In addition to pre-existing structural cell barriers that act as a first line of defense (Serrano *et al.*, 2014; Falter *et al.*, 2015), pathogen perception results in activation of a complex, multi-layered immune system in plants (Jones & Dangl, 2006). As part of the suite of inducible defenses, *de novo* formation of physico-chemical barriers prevents pathogen colonization and spread inside the plant. Despite their importance, the exact composition of these barriers, as well as the mechanisms that lead to their formation in the plant upon pathogen invasion remain largely unknown.

The interaction between the soil-borne bacterial wilt pathogen *Ralstonia solanacearum* and tomato offers a paradigmatic scenario to study inducible physico-chemical barriers, because of its agro-

economic impact, and the well-developed genetic and molecular tools available in both organisms. *Ralstonia solanacearum* enters the root system through wounds or at the points of emergence of lateral roots, where the epidermal and endodermal barriers may be compromised (Vasse *et al.*, 1995; Álvarez *et al.*, 2010; Ursache *et al.*, 2021). After entering the root, the bacterium moves centripetally towards the vasculature and once it reaches the xylem, it multiplies and spreads vertically within the vessels and horizontally to other vessels and the surrounding tissues (Dignonnet *et al.*, 2012).

The xylem tissue is a major battleground for the interaction between vascular wilt pathogens and their hosts, where the outcome of the infection is at stake (Yadeta & Thomma, 2013). To prevent the spread of pathogenic propagules, the xylem vasculature of resistant plants undergoes intense structural and metabolic modifications, such as reinforcing the walls of xylem vessels, pit membranes and surrounding xylem parenchyma cells in response to pathogens (Street *et al.*, 1986; Benhamou, 1995). This prevents pathogen colonization of the surrounding parenchyma

*These authors contributed equally to this work.

cells, nearby vessels and inter-cellular spaces through degeneration of the vessel pit membranes or cell walls by the pathogen (Nakaho *et al.*, 2000; Liu *et al.*, 2005; Pérez-Donoso *et al.*, 2010; Dignonnet *et al.*, 2012; Lowe-Power *et al.*, 2018). This vascular confinement is an effective strategy commonly found among plants resistant to vascular wilt pathogens such as *R. solanacearum*, which otherwise spread systemically and eventually kill the plant (McGarvey *et al.*, 1999; Vasse *et al.*, 2000; Potter *et al.*, 2011; Caldwell *et al.*, 2017; Scortichini, 2020; Kashyap *et al.*, 2021).

Among the various tomato germplasms, the cultivar Hawaii 7996 (H7996) is the most effective natural source of resistance against *R. solanacearum* (Grimault *et al.*, 1994; Nakaho *et al.*, 2004). In this cultivar, resistance to *R. solanacearum* is a complex polygenic trait (2000; Thoquet *et al.*, 1996; Mangin *et al.*, 1999; Wang *et al.*, 2013). Our previous study identified the bottlenecks through which H7996 is able to limit *R. solanacearum* spread *in planta* (Planas-Marquès *et al.*, 2019), namely: (1) root colonization, (2) vertical movement from roots to shoots, (3) circular invasion of the vascular bundle and (4) radial apoplastic spread from the vessels into the cortex. Vascular cell wall reinforcements seem to play a key role in confining *R. solanacearum* into the xylem vascular bundles of resistant tomato H7996. Ultra-microscopic studies in resistant tomato showed that the pit membranes, as well as xylem vessel walls and parenchyma cells form a conspicuously thick coating in the form of an electron dense amorphous layer, as part of the defense response against *R. solanacearum* (Nakaho *et al.*, 2000; Kim *et al.*, 2016).

Among the polymers constituting vascular coating structures, lignin is the most typically found, constituting an integral part of the secondary cell wall of the xylem vasculature. Lignin is well documented as a common structural defense against vascular wilt pathogens (Novo *et al.*, 2017; Zeiss *et al.*, 2019; Kashyap *et al.*, 2021) and it is also emerging as an important inducible defense component in other diseases/pests affecting the vasculature (Jhu *et al.*, 2021; Joo *et al.*, 2021). Suberin has also been reported to be deposited in vascular coatings as a defense response (Kashyap *et al.*, 2021), although the mechanisms regulating its synthesis, spatio-temporal dynamics and inducibility remain elusive. Interestingly, root microbiota has been recently shown to shape suberin deposits in the plant, highlighting its central role in plant–microbe interactions (Salas-González *et al.*, 2021). Suberin is a polyester containing long and very long chain fatty acids and derivatives and also some aromatics, mainly ferulic acid. Cells that accumulate suberin also accumulate lignin, whose deposition has been described to precede that of suberin in phellem cells (Lulai & Corsini, 1998). This lignin is also known as a lignin-like polymer, which consists of hydroxycinnamates and monolignols (Graça, 2015). The ligno-suberin heteropolymer formed by the lignin-like polymer and suberin has been also referred to as the poly(aromatic) and poly(aliphatic) domains of suberin, respectively. Commonly, suberized cell walls also comprise soluble phenolic compounds, which share biosynthetic pathways with suberin and lignin (Bernards, 2002).

Ferulic acid present in the suberin and lignin-like fractions is proposed to link both polymers (Graça, 2010) and its continuous

production has been demonstrated essential for suberin deposition (Andersen *et al.*, 2021). Ferulic acid amides, such as feruloyl-tyramine and feruloyloctopamine, have been described as structural components of the lignin-like polymer and in the phenolic soluble fraction of suberizing wound-healing potato tuber (Negrel *et al.*, 1996; Razem & Bernards, 2002). Ferulic acid amides belong to the hydroxycinnamic acid amide (HCAA) family, which present antimicrobial activity and are considered biomarkers during plant–pathogen interactions (Zeiss *et al.*, 2021). However, the precise role of HCAs in plant defense remains to be elucidated (Macoy *et al.*, 2015a,b). Besides their direct antimicrobial activity as soluble phenols, HCAs have also been proposed to crosslink to cell wall structural polymers during infection, potentially contributing towards the formation of a phenolic barrier that can make the cell wall resilient to pathogenic degradation (Zeiss *et al.*, 2021).

In the present study, we conducted a detailed investigation of the inducibility, structure and composition of the xylem vascular wall reinforcements that restrict *R. solanacearum* colonization in resistant tomato. Using a combination of histological and live-imaging techniques, together with spectroscopy and gene expression analysis we provide important new insights into the pathogen-induced formation of vascular coatings. In particular, we show that a ligno-suberin vascular coating and tyramine-derived HCAs contribute to restriction of *R. solanacearum* in resistant tomato. In addition, we demonstrate that genes in the ligno-suberin-associated pathways can be explored to engineer resistance against *R. solanacearum* into commercial susceptible varieties of tomato.

Materials and Methods

Plant materials and growth conditions

Tomato (*Solanum lycopersicum*) varieties Marmande, Hawaii 7996 (H7996) and Moneymaker (wild-type and 35S::THT 1-3, generated by Campos *et al.* (2014)), were used. Plants were grown in controlled growth chambers at 60% humidity, 12 h : 12 h, day : night and 27°C (light-emitting diode (LED) lighting) or 25°C (fluorescent lighting).

Ralstonia solanacearum strains and growth conditions

Ralstonia solanacearum GMI1000 strain (Phylotype I, race 1 bio-var 3) was used, including luminescent and fluorescent reporter strains of *R. solanacearum* GMI1000 described in Cruz *et al.* (2014) and Planas-Marquès *et al.* (2019).

Cloning and stable transformation in tomato

For generation of the 35S::FHT-HA construct the FHT (Soly-c03g097500) coding sequence was amplified from tomato H7996 complementary DNA (cDNA) using the forward and reverse primers part7FHTF1 and part7FHTHAR1, respectively (Supporting Information Table S1). The amplified product was cloned into the pJET1.2/blunt cloning vector using a CloneJet

PCR cloning kit (ThermoFisher, Waltham, MA, USA) and then digested by *Sma*I and *Bam*HI. The digested products were purified using NZYGelpure (Nzytech, Lisbon, Portugal) followed by ligation into the pART7 and later to pART27 vector (Gleave, 1992). pART27 containing *35S::FHT-HA* was transformed into *Marmande*. For this, the construct was transformed into *Agrobacterium tumefaciens* strain C58C1. Cotyledon explant preparation, selection, and regeneration followed the methods described by Mazier *et al.* (2011). Transformants were selected on kanamycin-containing medium. Accumulation of FHT-HA protein was assayed by immunoblot with a monoclonal HA antibody (GenScript, Piscataway, NJ, USA).

Bacterial inoculation in plants

Four- to five-week-old tomato plants were inoculated through roots with *R. solanacearum* using the soil drenching method with a 1×10^7 colony-forming unit (CFU) ml^{-1} suspension of bacteria as described in Planas-Marquès *et al.* (2018). Inoculated plants were kept in a growth chamber at 27°C. For tomato leaf infiltration, plants were vacuum-infiltrated by submerging the whole aerial part in a $c. 10^5$ CFU ml^{-1} bacterial suspension as described in Planas-Marquès *et al.* (2018). For inoculation directly onto the stem vasculature, 10 μl (5 μl at a time) of 10^5 CFU ml^{-1} bacterial suspension was placed at the node of the petiole and pin-inoculated using a sterile needle (30G \times 1/2", BD Microlance; Becton Dickinson, Franklin Lakes, NJ, USA).

Ralstonia solanacearum pathogenicity assays and quantification of bacterial growth *in planta*

Infected plants were scored for wilting symptoms using a scale from 0 to 4: 0 = healthy plant with no wilt, 1 = 25%, 2 = 50%, 3 = 75%, and 4 = 100% of the canopy wilted as described by Planas-Marquès *et al.* (2019). The relative light units per second (RLU s^{-1}) readings were converted to CFU g^{-1} tissue as described in Planas-Marquès *et al.* (2019). For bacterial colonization assays using green fluorescent protein (GFP) reporter strain, transverse stem cross-sections were made at the inoculation point and at a distance of 0.5, 1, 2 and 3 cm in both upward and downward direction, using a sterile razor blade. Quantification of mean green fluorescence was done using IMAGEJ software (Planas-Marquès *et al.*, 2019). For leaf *in planta* multiplication assays, three leaf discs of 0.8 cm^2 were homogenized in 200 μl of sterile distilled water. CFU cm^{-2} leaf tissue were calculated after dilution plating of samples with appropriate selection antibiotics and CFU counting 24 h later.

Histological methods

Thin ($c. 150 \mu\text{m}$) transverse cross-sections were obtained with a sterile razor blade from a 1.5 cm area of the taproot-to-hypocotyl transition zone located immediately below the soil line (Fig. S1a). Inoculated plants were sectioned when bacterial colonization level reached 10^5 CFU g^{-1} taproot-to-hypocotyl transition zone tissue. This corresponded to 4 d post-inoculation (dpi) in

Marmande and 9 dpi in *H7996*, at which stage only *H7996* sections showed a localized browning at one xylem pole indicative of infection. Sections were kept in 70% ethanol at room temperature for 5 d and examined using fluorescence microscopy using a Leica DM6B-Z microscope under ultraviolet (UV) illumination (340–380 nm excitation and 410–450 nm barrier filters). Autofluorescence emitted from phenolic deposits was recorded using a Leica-DFC9000GT-VSC07341 camera and the signal was pseudo-colored green. Sections were also stained with phloroglucinol-HCl for the detection of lignin and observed under bright field (Pomar *et al.*, 2004). Photographs were taken with a DP71 Olympus digital camera. Cross-sections were also observed under UV with a Leica-DM6B-Z microscope (340–380 nm excitation and 410–450 nm barrier filters). To detect the autofluorescent blue-to-green pH-dependent color conversion of wall-bound ferulic acid cross-sections were initially mounted in 70% ethanol (neutral pH) and then in 1N potassium hydroxide (KOH) (pH above 10) adapting the protocol from Carnachan & Harris (2000), Harris & Trethewey (2010) and Donaldson & Williams (2018). A Leica DM6B-Z microscope was used to observe autofluorescence (340–380 nm excitation and 410–450 nm barrier filters). Images were recorded using a Leica MC190-HD-0518131623 digital camera. To visualize suberin aliphatics, sections were treated with 5% Sudan IV, dissolved in 70% ethanol and illuminated with UV light. These sections were subsequently treated with 1N KOH to detect ferulic acid as described earlier. For both ferulic acid and suberin, the HC PL APO or HC PL FLUOTAR objectives of the Leica DM6B-Z microscope were used and images were captured using a Leica MC190-HD-0518131623 color digital camera. The UV autofluorescence signal from xylem vessel walls and surrounding layers was measured using the LAS X Leica software and changes in ferulate accumulation were quantified using IMAGEJ software by selecting the area of xylem vessel walls showing autofluorescence. Quantifications of fluorescence intensity were normalized per micrometer of region of interest (ROI), which corresponded to a particular area of the vascular bundles, where main vessels concentrate (represented in Fig. 1b). Basically, the line is drawn at each of the four corners in the whole image and then the fluorescence is normalized by the length of the lines.

Two-dimensional nuclear magnetic resonance (2D-NMR)

The samples of a pool of 15 tomato plants (taproot-to-hypocotyl region), water treated or having a bacterial load of 10^5 CFU g^{-1} were milled and extracted sequentially with water, 80% ethanol, and with acetone, by sonicating in an ultrasonic bath during 30 min each time, centrifuging and eliminating the supernatant. Then, lignin/suberin fraction was enzymatically isolated by hydrolyzing the carbohydrates fraction with Cellulysin (Calbiochem, San Diego, CA, USA), as previously described (Rico *et al.*, 2014). Approximately 20 mg of enzymatic lignin/suberin preparation was dissolved in 0.6 ml of deuterated dimethyl sulfoxide ($\text{DMSO}-d_6$). Heteronuclear single quantum coherence (HSQC) spectra were acquired on a Bruker Advance III 500 MHz spectrometer (Bruker, Karlsruhe, Germany) equipped

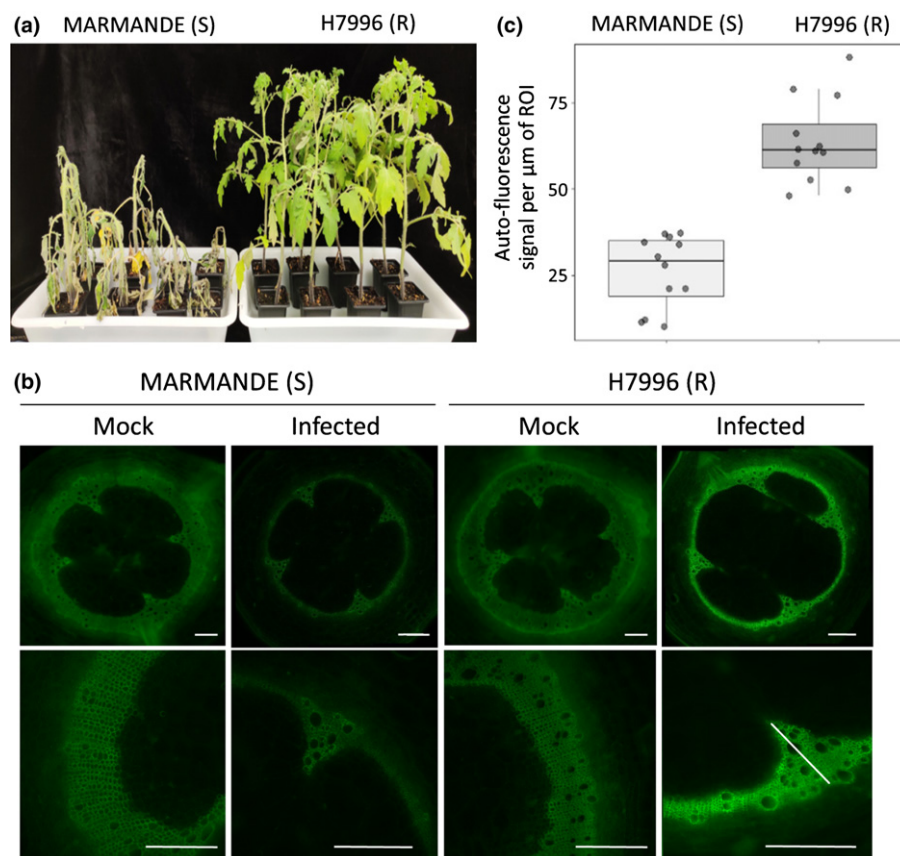


Fig. 1 Resistant H7996 tomato restricts *Ralstonia solanacearum* colonization and induces a vascular coating response with wall bound phenolics. Susceptible (Marmande) and resistant (H7996), 5-wk-old tomato plants were inoculated through roots by soil-soak with $c. 1 \times 10^7$ colony-forming unit (CFU) ml^{-1} of *R. solanacearum* GMI1000 and incubated at 28°C. (a) At 12 d post-inoculation (dpi) most Marmande plants showed severe wilting symptoms, whereas H7996 remained mostly symptomless. (b) Cross-sections of the taproot-to-hypocotyl area containing 10^5 CFU g^{-1} of *R. solanacearum* were analyzed by ultraviolet (UV) microscopy. To focus on cell wall-deposited phenolic compounds, soluble phenolic compounds were removed with ethanol prior to observation. A strong autofluorescence signal emitted from the walls of vessels and surrounding parenchyma cells in infected H7996 plants compared to Marmande or the mock controls, can be observed. Fluorescence signal in white was green colored. Images from a representative experiment out of three with $n = 5$ plants per cultivar. Bar, 500 μm . (c) The UV autofluorescence signal in (b) was measured using the Leica APPLICATION SUITE X (LAS X) software. A representative region of interest (ROI) is highlighted in (b) and corresponded to a line traversing the selected vascular bundles. Data are represented with box and whiskers plots: whiskers indicate variability outside the upper and lower quartiles and boxes indicate second quartile, median and third quartile. Different letters indicate statistically significant differences ($\alpha = 0.05$, Fisher's least significant difference test).

with a 5 mm TCI cryoprobe, using the experimental conditions previously described (Rico *et al.*, 2014). HSQC cross-signals were assigned and quantified as described (del Río *et al.*, 2018; Rencoret *et al.*, 2018; Mahmoud *et al.*, 2020). In the aromatic region, the correlation signals of G_2 and $S_{2,6}$ were used to estimate the content of the respective G- and S-lignin units. The C_α/H_α signals of the $\beta-O-4'$ ethers (A_α), phenylcoumarans (B_α), and resinols (C_α) in the linkages region were used to estimate their relative abundances, whereas the C_γ/H_γ signal was used in the case of cinnamyl alcohol end-units (I_γ).

RNA extraction, cDNA synthesis and quantitative RT-PCR analysis

Taproot-to-hypocotyl transition zone sections of $c. 0.5$ mm thickness were obtained and the xylem vascular tissues (vascular bundles and surrounding parenchyma cells) were collected and kept in liquid nitrogen. Each sample comprised taproot-to-hypocotyl transition

zone xylem tissues of six plants. RNA was extracted using the Maxwell RSC Plant RNA Kit (Promega, Madison, WI, USA). Complementary DNA was synthesized from 2 μg RNA using High Capacity cDNA Reverse Transcription Kit (Applied Biosystems, Foster City, CA, USA). Complementary DNA amplification and analysis was performed using the LightCycler 480 System (Roche, Basel, Switzerland). The Elongation Factor 1 alpha housekeeping gene (*eEF1 α* , *Solyc06g005060*) was used as a reference. All reactions were run in triplicate for each biological replicates. Melting curves and relative quantification of target genes were determined using the software LIGHTCYCLER v.1.5 (Roche). The level of expression relative to the reference gene was calculated using the formula $2^{-\Delta\text{CT}}$, where $\Delta\text{CT} = (\text{CT RNA target} - \text{CT reference RNA})$.

Statistical analysis

Statistical analyses were performed using STATGRAPHICS software. All statistical tests are indicated in the respective figure legends.

Results

Resistant H7996 tomato restricts *R. solanacearum* colonization and induces a vascular coating response involving wall-bound phenolics

In order to understand the mechanisms underscoring restriction of *R. solanacearum* spread in resistant tomato varieties we used the resistant variety H7996 and compared it to the susceptible cultivar Marmande. In our assay conditions, most Marmande plants were wilted 10 d after inoculation with *R. solanacearum* GMI1000, while H7996 plants remained largely asymptomatic (Figs 1a, S2a; Planas-Marquès *et al.*, 2019). Accordingly, bacterial loads in the taproot-to-hypocotyl region were drastically reduced in H7996 compared to Marmande, confirming the remarkable bacterial restriction ability of this cultivar (Fig. S1b; Planas-Marquès *et al.*, 2019).

To identify defense-associated anatomical and physico-chemical modifications in H7996 after infection with *R. solanacearum* compared to Marmande we performed histochemical, spectroscopic and gene expression analysis. For this, plants were infected with a 10^7 *R. solanacearum* solution or mock through their roots using the soil-drench method and then we collected tissue containing 10^5 CFU g⁻¹ tissue of bacteria at the taproot-to-hypocotyl transition area, located c. 1 cm below-ground (Fig. S1a). Marmande reached 10^5 CFU g⁻¹ tissue at around 4 dpi, while the resistant H7996 took approximately 9 d to do so (Fig. S2). We have previously observed that the root-to-hypocotyl area constitutes a key bottleneck for bacterial progression inside the plant (Zuluaga *et al.*, 2015; Puigvert *et al.*, 2017; Planas-Marquès *et al.*, 2019), being thus an ideal target zone for analysis of structural defense responses.

We initially analyzed UV autofluorescence of transverse cross-sections of the taproot-to-hypocotyl region, indicative of phenolic compounds (Donaldson, 2020). To focus on cell wall-deposited phenolic compounds, soluble phenolic compounds were removed with ethanol prior to observation as reported (Pouzoulet *et al.*, 2013; Araujo *et al.*, 2014). Infection with *R. solanacearum* induced a strong UV signal emitted from the walls of the vessels, and also from surrounding xylem parenchyma cells and tracheids in resistant H7996 (Fig. 1b,c). This enhanced autofluorescence was not observed in the susceptible variety Marmande nor in mock-treated samples (Fig. 1b, c). In tissues outside the vascular area, inoculation resulted in a decrease of autofluorescence in both susceptible and resistant tomato lines.

Spectroscopic analysis reveals *R. solanacearum*-induced deposition of suberin and accumulation of tyramine-derived amides in resistant H7996 tomato and lignin structural modifications in susceptible Marmande tomato

In order to decipher the composition of the cell wall-deposited compounds we used two-dimensional (2D) HSQC nuclear magnetic resonance (NMR), one of the most powerful tools for plant cell wall structural analysis providing

information on the composition and linkages in lignin/suberin polymers (Ralph & Landucci, 2010; Correia *et al.*, 2020). The 2D-HSQC spectra of infected or mock-treated taproot-to-hypocotyl transition zones of H7996 and Marmande tomato plants were obtained and the main lignin and suberin substructures identified are shown in Fig. 2, while the chemical shifts of the assigned cross-signals are detailed in Table S2. Importantly, the aliphatic region of the 2D-HSQC spectra revealed that H7996 infected plants were more enriched in poly-aliphatic structures characteristic of suberin (magenta-colored signals), compared to its mock control (Fig. 2a). Related to this, an olefinic cross-signal of unsaturated fatty acid structures (UF, δ_C/δ_H 129.4/5.31), typical of suberin, was also found to be increased in the HSQC spectrum of the infected H7996 tomato. A rough estimate based on the integration of lignin and suberin HSQC signals, revealed that the suberin/lignin ratio in *R. solanacearum*-infected H7996 plants was doubled compared to mock-treated plants, evidencing an increase in suberin deposition as a consequence of the bacterial infection. Interestingly, signals compatible with feruloylamides (FAM₇; δ_C/δ_H 138.6/7.31) and with tyramine-derived amides (Ty in orange; δ_C/δ_H 129.3/6.92, 114.8/6.64, 40.5/3.29 and 34.2/2.62) were exclusively found in the spectrum of infected H7996 plants, suggesting the presence of feruloyltyramine exclusively in these samples (Fig. 2a). Since tyramines have been found as structural components co-occurring with suberin (Bernards *et al.*, 1995; Bernards & Lewis, 1998), which generates physically and chemically resistant barriers (He & Ding, 2020), our results substantiate the hypothesis of suberin as an important defense element against *R. solanacearum* infection in resistant tomato plants. On the contrary, the 2D-HSQC spectra from the Marmande variety did not display notable variations between mock and infected plants in the signals corresponding to suberin, tyramine-related structures nor feruloylamides (Fig. 2a).

Interestingly, 2D-HSQC-NMR spectra also revealed significant structural modifications in the composition of lignin and the distribution of linkages in tomato plants after infection. Lignins with lower S : G ratios are more branched (condensed) and recalcitrant towards pathogen attack (Iiyama *et al.*, 2020). Therefore, lignin in inoculated H7996, with an S : G ratio of 1.0 should be, a priori, more resistant than the lignin in inoculated Marmande plants (S : G ratio of 1.5). The 2D-HSQC analysis revealed that the infection of susceptible Marmande plants resulted in an increase of the S : G ratio and a clear reduction of all major lignin linkages (β -O-4', β -5' and β - β' ; reduction in roughly 9%, 43% and 46%, respectively), evidencing that a lignin depolymerization process took place (Fig. 2a). In contrast, infected H7996 tomato displayed a slight decrease of the S : G ratio, and only β -O-4' linkages (the easiest to degrade in the lignin polymer) were significantly reduced, while the β -5' and β - β' were not so affected as in the case of Marmande plants. In this context, the major reduction in lignin linkages observed in Marmande after infection could explain, at least in part, its higher susceptibility to the pathogen.

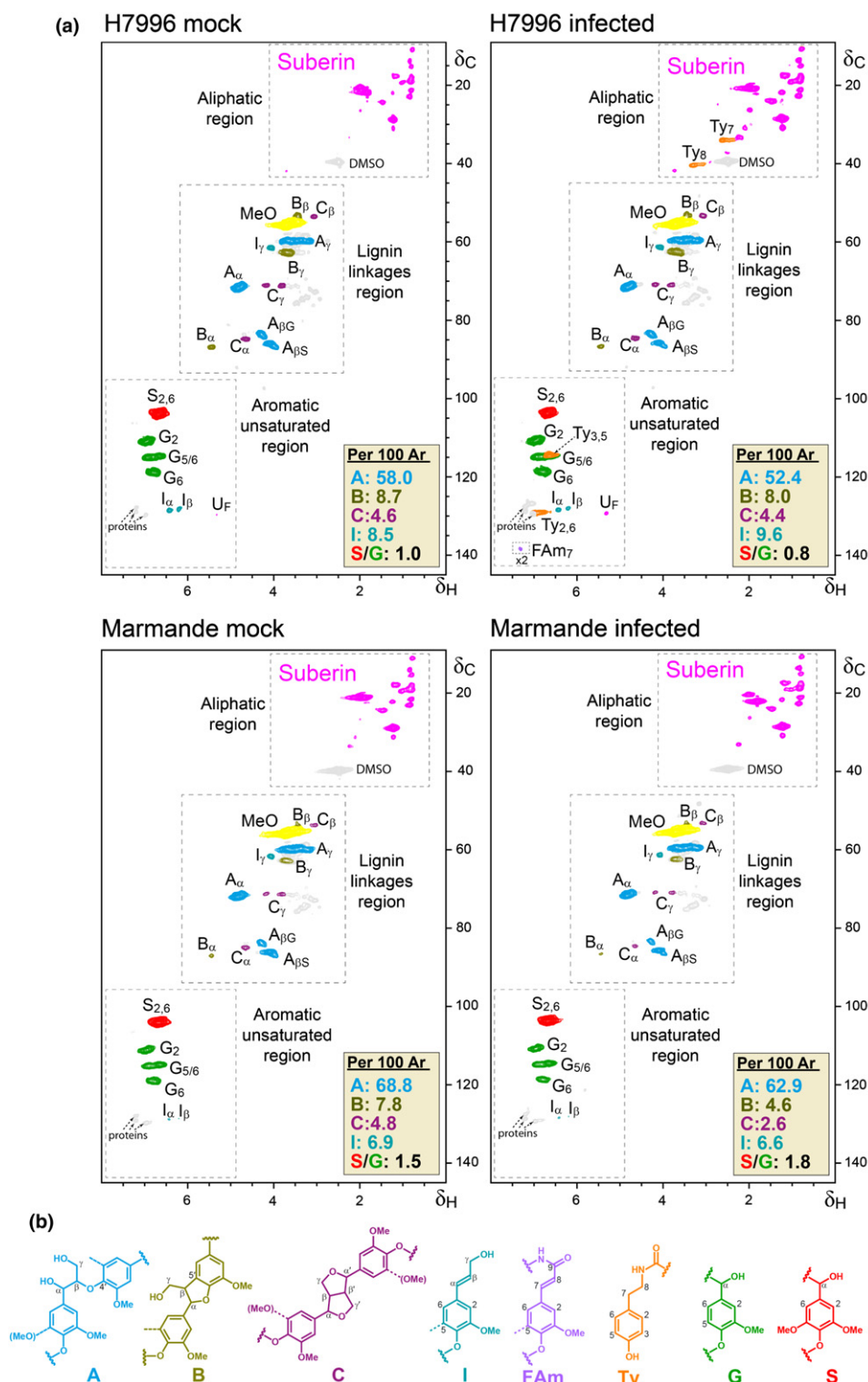


Fig. 2 Feruloylamides, tyramine-derived amides and suberin-compatible compounds are specifically enriched in resistant H7996 tomato after infection with *Ralstonia solanacearum*. (a) Two-dimensional heteronuclear single quantum correlation-nuclear magnetic resonance (2D-HSQC-NMR) spectra of enzymatically isolated lignin/suberin fractions from mock-treated and *R. solanacearum*-infected taproots (containing 10^5 colony-forming unit (CFU) g^{-1} taproot-to-hypocotyl transition tissue) of H7996 and Marmande tomato plants. The experiment was performed twice with similar results. (b) Main lignin/suberin structures identified: β -O-4' alkyl aryl ethers (A), β -5' phenylcoumarans (B), β - β' resinols (C), cinnamyl alcohols end-groups (I), feruloylamides (FAm), tyramine-derived amides (Ty), guaiacyl lignin units (G), syringyl lignin units (S), as well as unassigned aliphatic signals from suberin. The structures and contours of the HSQC signals are color coded to aid interpretation. Proton (1H) and carbon-13 (^{13}C) NMR chemical shifts of the assigned signals are detailed in Supporting Information Table S2. To detect FAM₇ signal, the spectrum scaled-up to 2-fold ($\times 2$) intensity. The abundances of the main lignin linkages (A, B and C) and cinnamyl alcohol end-groups (I) are referred to as a percentage of the total lignin units ($S + G = 100\%$).

Histochemical analysis reveals the formation of structural vascular coatings containing suberin and ferulate/feruloylamide in resistant H7996 tomato in response to *R. solanacearum* infection

To confirm our spectroscopic data, we histochemically analyzed taproot-to-hypocotyl transition zone samples of mock and infected H7996 and Marmande tomato plants. Observation of Phloroglucinol-HCl stained sections under brightfield microscopy (Wiesner staining) (Pomar *et al.*, 2002; Pradhan Mitra & Loqué, 2014), showed that mock and infected H7976 (resistant) as well as mock Marmande (susceptible) samples showed a red-purple color characteristic of the reaction of phloroglucinol-HCl in vessels and fibers, indicative of lignin (Fig. 3a). In contrast, infected Marmande sections exhibited reduced phloroglucinol-HCl staining, suggesting a change in composition of xylem lignin upon infection (Fig. 3a). This observation is in agreement with the structural changes specifically detected in the lignin structure of infected Marmande plants by 2D-HSQC-NMR (Fig. 2a), which suggest lignin depolymerization and may partly underscore the high susceptibility of this tomato variety.

UV illumination of phloroglucinol-HCl-stained samples allows quenching the autofluorescence from lignin and hence detect residual cell wall autofluorescence, which has been associated with suberin deposits (Baayen & Elgersma, 1985; Rioux *et al.*, 1998; Pouzoulet *et al.*, 2013). Under these conditions, the increased autofluorescence observed in the vascular coating regions of infected H7996 tomato plants was not quenched in phloroglucinol-HCl stained samples (Fig. 3a,b). A more detailed observation revealed that this nonquenched autofluorescence was localized in specific regions compatible with (1) intervessel and vessel-parenchyma pit membranes or pit chamber walls and (2) parenchyma coatings with fluorescent signals enriched in intracellular spaces (Fig. 3c).

Next, we analyzed whether the pathogen-induced coating of vessels observed in H7996 correlated also with an increase in ferulates, a major suberin component. We performed KOH treatment of plant tissues, which specifically shifts the UV fluorescence of ferulate/feruloylamide to green, allowing its detection (Carnachan & Harris, 2000; Harris & Trethewey, 2010; Donaldson & Williams, 2018). UV autofluorescence of vascular coatings in response to *R. solanacearum* infection in resistant H7996 shifted from blue to a strong green color upon treatment with alkali (1N KOH) (Fig. S3a). This indicated that the *R. solanacearum*-induced xylem vasculature feruloylation was specific to resistant H7996, as the fainter blue autofluorescence observed in mock-treated resistant H7996 or susceptible Marmande tissues did not change to green at high pH in either early (Fig. S3a,b) or late (Fig. S3c) stages of infection.

To corroborate that the ferulate/feruloylamide accumulation in infected H7996 tomato was related with vascular suberization, we combined the ferulate-specific UV-alkali treatment described earlier with Sudan IV staining, which binds aliphatic components of suberin to produce a reddish-brown coloration. This revealed suberization in the taproot-to-hypocotyl area of *R. solanacearum*-infected H7996 plants, xylem vessel walls as well as the layers of

vessels, parenchyma cells and tracheids in the immediate vicinity (Fig. 4). In the periphery of suberized cells, a green signal from UV-alkali was observed (Fig. 4), which may indicate ferulate/feruloylamide deposition indicative of a preceding stage towards suberization in this cell layer. In comparison, no positive Sudan IV or UV-alkali staining was detected in infected Marmande or mock-treated tomato plants. Together, suberized and feruloylated layers of parenchyma cells, vessels and tracheids might form a 'suberization zone' creating a strong physico-chemical barrier to limit *R. solanacearum* spread from the colonized xylem vessel lumen.

Ralstonia solanacearum infection activates the biosynthesis of aliphatic suberin precursors and feruloylamide, and aliphatic esterification of ferulic acid in the vasculature of resistant H7996

Since a differential accumulation of suberin-compatible compounds was specifically observed in infected H7996, we surmised that genes related to suberin and feruloylamide synthesis, as well as ferulic acid esterification to aliphatics may be upregulated in resistant tomato in response to *R. solanacearum* invasion. To test this hypothesis, we analyzed: (1) expression of genes in the phenylpropanoid and suberin biosynthesis pathways, which provide the necessary precursors for the ligno-suberin heteropolymer; (2) the feruloyl transferase FHT (ASFT/HHT in Arabidopsis), which is involved in the formation of ferulate esters of fatty acyl compounds necessary to form suberin and soluble waxes (Gou *et al.*, 2009; Molina *et al.*, 2009; Serra *et al.*, 2010); and (3) N-hydroxycinnamoyl transferases (*THT*), which are involved in the synthesis of HCAAs such as feruloyltyramine, which is found on the lignin-like polymer and in the soluble phenolic fraction of some suberized tissues (Negrel *et al.*, 1993; Schmidt *et al.*, 1999).

Quantitative reverse transcription polymerase chain reaction (RT-PCR) from xylem vascular tissue obtained from the taproot-to-hypocotyl zone in *R. solanacearum*- or mock-treated H7996 and Marmande plants showed specific upregulation of all genes analyzed from the suberin biosynthetic pathway in H7996 infected plants compared to the mock controls (Figs 5, S4). These included essential suberin biosynthesis genes such as *CYP86A1* and *CYP86B1* (fatty acid oxidation), *FAR* (primary alcohol generation), *KCSs* (fatty acid elongases) and *GPAT5* (acylglycerol formation). In addition, feruloyl transferase *FHT* (*ASFT/HHT* in Arabidopsis), was also strongly upregulated in infected H7996 plants (Figs 5, S5b). Regarding *THT*, in tomato we identified five putative homologs (Fig. S6a), all induced by infection in the vascular tissue of H7996 (Figs 5, S6b). Among them, *SlTHT1-3* showed the strongest upregulation in H7996 after infection (Figs 5, S6b). In comparison, *R. solanacearum* infection had only a modest effect on genes related to phenylpropanoid pathway as only upregulation was detected in the first enzyme of the pathway (*PAL*) (Figs 5, S7).

Together, these data indicate that upregulation of genes involved in the formation of aliphatic suberin precursors, ferulic acid esterification to aliphatics (*FHT*) and production of HCAAs, such as feruloyltyramine (*THT*), constitute a very specific response of H7996 plants that takes place in the vasculature

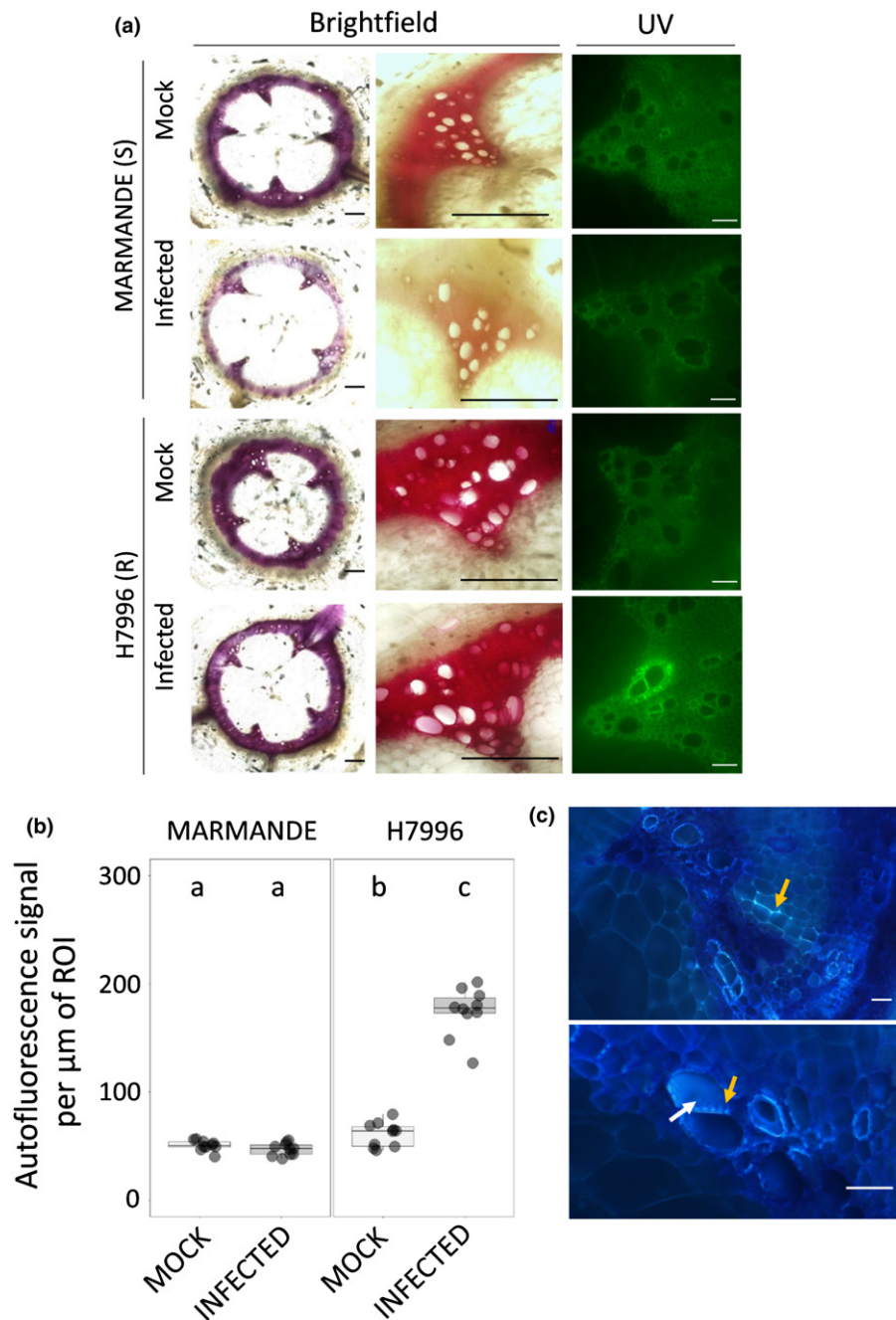


Fig. 3 Resistant H7996 tomato shows vascular autofluorescence not-quenched with phloroglucinol and susceptible Marmande shows a decrease in phloroglucinol-HCl lignin signal. Susceptible (Marmande) and resistant (H7996) 5-wk-old tomato plants were root-inoculated with a *Ralstonia solanacearum* GMI1000 strain at a concentration of $c. 1 \times 10^7$ colony-forming unit (CFU) ml^{-1} or water mock. (a) Cross-sections of the taproot-to-hypocotyl area containing 10^5 CFU g^{-1} of *R. solanacearum* were stained with phloroglucinol-HCl and observed under ultraviolet (UV) to visualize other autofluorescent compounds different from lignin (not quenched with phloroglucinol-HCl) (right) and under brightfield to visualize lignin deposition (left). In infected H7996 strong UV autofluorescence could be observed in the walls of xylem vessels surrounding xylem parenchyma cells and tracheids, indicating reinforcement of walls of vascular tissue with phenolics formed *de novo* upon infection. In infected Marmande the red phloroglucinol stain was reduced especially in the intervessel areas. (b) The UV autofluorescence signal in (a) was measured using the LAS X Leica software after the phloroglucinol-HCl treatment. Data are represented with box and whiskers plots: whiskers indicate variability outside the upper and lower quartiles and boxes indicate second quartile, median and third quartile. (c) Detailed observation of infected H7996 xylem after the phloroglucinol-HCl treatment shows the strong UV fluorescence concentrated in specific areas possibly corresponding to intervessel and vessel-parenchyma bordered pit membranes and/or pit chambers (yellow and white arrows, respectively). Fluorescence was also observed in parenchyma cells, specially enriched at intercellular cell corners (green arrow). Panel (b) correspond to a representative experiment out of three each with $n = 6$ plants per variety. Different letters indicate statistically significant differences ($\alpha = 0.05$, Fisher's least significant difference test). Panels (a) and (c) were representative images. Bars: (a, left), 100 μm ; (a, right) 500 μm ; (c) 50 μm .

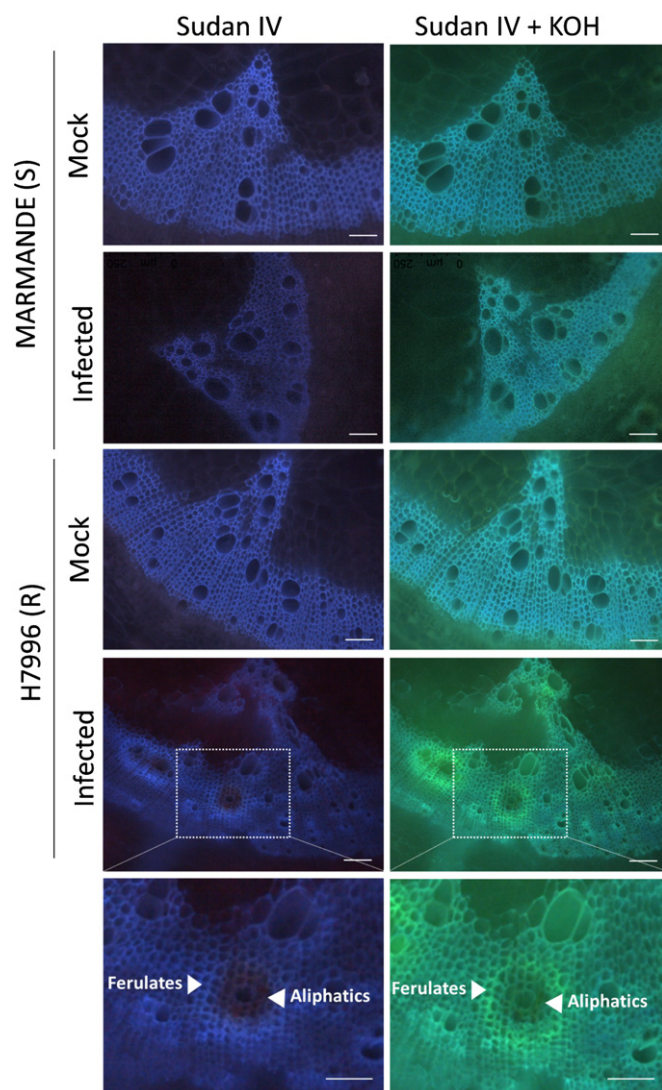


Fig. 4 Resistant H7996 tomato shows cell wall ferulate/feruloylamide and suberin deposition in restricted zones of vascular tissue upon *Ralstonia solanacearum* infection. Susceptible Marmande or resistant H7996 tomato plants were soil-inoculated with a c. 1×10^7 colony-forming unit (CFU) ml^{-1} suspension of *R. solanacearum* GMI1000 or mock-inoculated with water and incubated at 28°C. Cross-sections were obtained from taproot-to-hypocotyl transition tissue containing 10^5 CFU g^{-1} of *R. solanacearum*. Sections were stained with Sudan IV to visualize suberin aliphatics and subsequently treated with 1N potassium hydroxide (KOH) (pH above 10) to visualize ferulic acid bound to cell wall. Sudan IV positive staining (reddish-brown coloration) was observed around xylem vessels specifically in infected H7996, indicating accumulation of suberin aliphatics. Accumulation of ferulic acid bound to cell wall (blue-green coloration) appears also specifically in infected H7996 resistant tomato, surrounding Sudan IV-stained areas. White arrowheads indicate the sites of accumulation of ferulates and aliphatic compounds. Representative images from one experiment out of three with $n = 6$ plants each were taken. Bar, 100 μm .

upon *R. solanacearum* infection. Further, these data are in agreement with NMR data of infected H7996, which showed a specific increase in insoluble fatty acid structures typical of suberin as well as the appearance of signals from structural tyramine-derived amides and feruloylamides (Fig. 2a).

Overexpression of *S1THT1-3* in a susceptible tomato cultivar confers resistance to *R. solanacearum*

Based on our results, we set to determine whether overexpressing genes involved in ferulic acid esterification to suberin aliphatics and feruloylamide biosynthesis, such as *S1FHT* and *S1THT1-3*, respectively, would increase resistance against *R. solanacearum* in a susceptible tomato background. Initially, we obtained transgenic tomato lines stably overexpressing *S1FHT* on a susceptible Marmande background (Fig. S8). Under normal growth conditions these lines are morphologically undistinguishable from wild-type (Wt), although they display a subtle increase in fresh weight (Fig. S9). We analyzed symptom progression and bacterial colonization. *S1FHT* overexpression lines showed a slight delay in disease progression (Fig. 6a) and moderately milder symptoms. The taproot-to-hypocotyl of *S1FHT* overexpressors displayed a slight reduction in bacterial loads after soil-soak inoculation in comparison to Wt tomato (Fig. 6b).

Regarding *S1THT1-3*, the corresponding tomato overexpressing line was readily available on a Moneymaker background (Campos *et al.*, 2014). This line has been shown to overaccumulate soluble HCAA such as feruloyltyramine and also the hormone salicylic acid (SA) upon infection with *Pseudomonas syringae* pv. tomato (Campos *et al.*, 2014). It is worth noting that tomato plants overexpressing *S1THT1-3* display a slight decrease in fresh weight compared to wild-type plants, although with the naked eye they appear undistinguishable (Fig. S10). As expected, the Moneymaker tomato cultivar showed similar susceptibility to *R. solanacearum* as Marmande (Fig. 7a,b). In contrast, overexpression of *S1THT1-3* resulted in a dramatic increase of resistance against *R. solanacearum*, with disease progressing remarkably slower in this line compared to wild-type (Fig. 7a,b). Importantly, bacterial loads were significantly lower in the taproot-to-hypocotyl and hypocotyl of the *S1THT1-3* overexpressor after soil inoculation in comparison to Wt tomato (Fig. 7c). Similarly, direct leaf inoculation also showed severe bacterial growth restriction in the *THT1-3* overexpressing line (Fig. S11a). Further, we monitored the colonization patterns of a *R. solanacearum* GFP reporter strain after stem inoculation of the *S1THT1-3* overexpressing line compared to Wt. In transverse stem cross-sections of 6 dpi plants, bacteria stayed confined near the inoculation point in the *35S::S1THT1-3* line whereas they spread unrestrictedly in susceptible wild-type stems from the inoculation point and at least 3 cm up and downwards (Fig. 7d,e, S11b).

Concomitant with the observed restriction of *R. solanacearum* colonization, an increase in autofluorescence around the vasculature was observed in the *S1THT1-3* overexpressor (Fig. 8a). At similar bacterial loads, Wt did not display such enhanced vascular fluorescence. Phloroglucinol-HCl staining did not quench the paravascular autofluorescence in *S1THT1-3* (Fig. 8a,d), indicating that similar to what was previously observed for H7996, the observed increase in wall-bound phenolic deposits did not only correspond to lignin. To gain a deeper insight into the composition of the *R. solanacearum*-induced vascular deposits in *S1THT1-3* overexpressing plants we performed combined Sudan IV-alkali staining (Fig. 8b,c,e). Treatment with alkali resulted in a clear

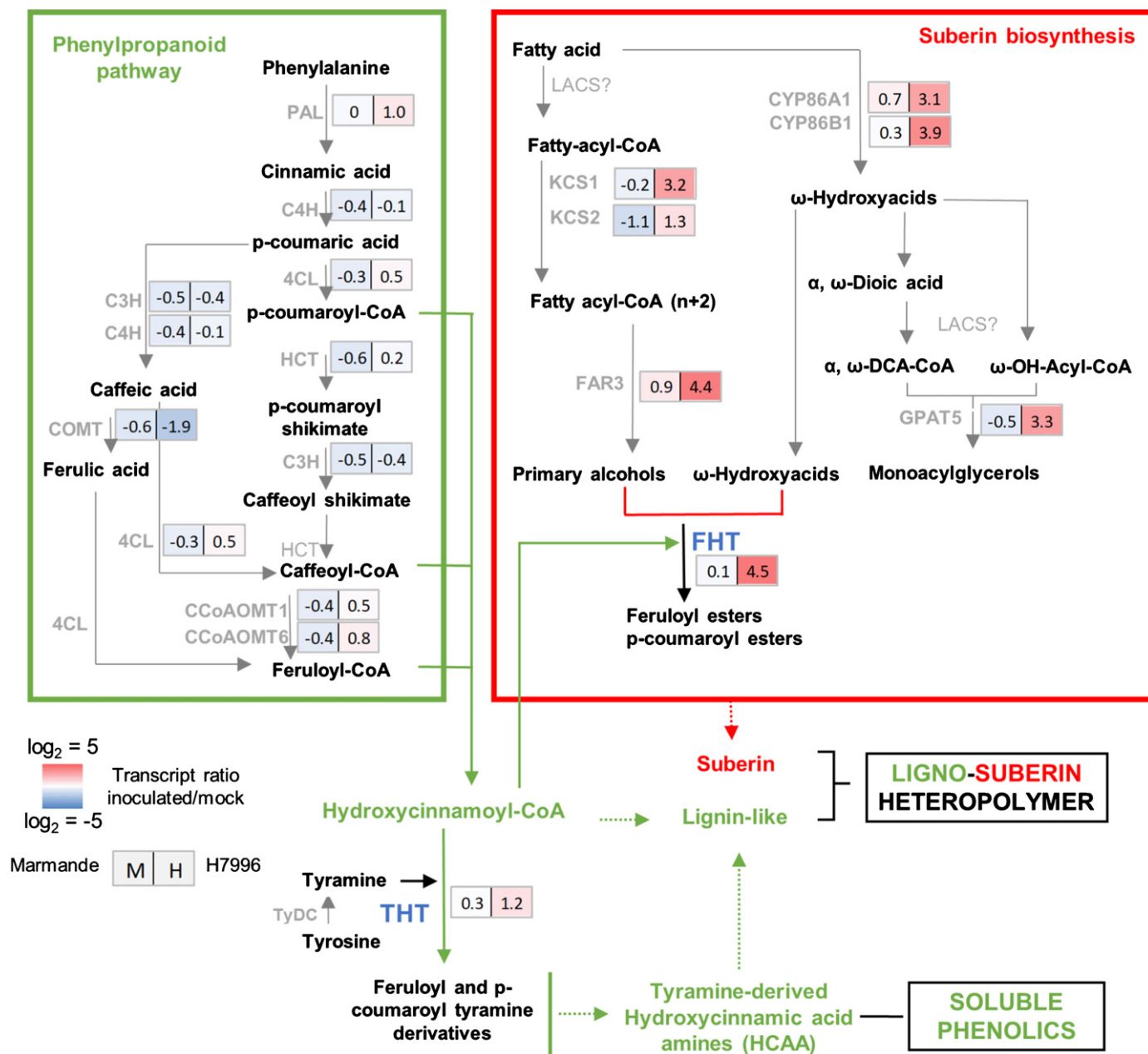


Fig. 5 Genes of the ligno-suberin heteropolymer biosynthesis pathway are specifically induced in the xylem vasculature of resistant H7996 tomato upon *Ralstonia solanacearum* infection. The levels of expression of genes belonging to metabolic pathways relevant for suberin, lignin and feruloyltyramine and related amides biosynthesis were analyzed by quantitative polymerase chain reaction (qPCR) of taproot vascular tissue in infected or mock-treated H7996 or Marmande tomato plants. Plants containing an *R. solanacearum* inoculum of 10^5 colony-forming unit (CFU) g^{-1} were selected and xylem vascular tissue from the taproot-to-hypocotyl transition zone, comprising of metaxylems and surrounding parenchyma cells was collected for RNA extraction and complementary DNA (cDNA) synthesis. In parallel, xylem tissue was collected from mock plants. Heatmaps show \log_2 fold change RTA (relative transcript abundance) values of infected vs mock for Marmande (left) and Hawaii (right). The tomato gene encoding for the alpha-subunit of the translation elongation factor 1 (*SleEF1* α) was used as endogenous reference. Three biological replicates ($n = 3$) were used, and taproots of six plants were used in each replicate. All the original qPCR results can be found in Supporting Information Figs S3–S6. The scheme represents the phenylpropanoid and suberin biosynthesis pathways providing lignin-like and suberin precursors for the ligno-suberin heteropolymer. Abbreviations: PAL, phenylalanine ammonia-lyase; C4H, cinnamate-4-hydroxylase; C3H, coumarate 3-hydroxylase; 4CL, 4-coumarate-CoA ligase; HCT, hydroxycinnamoyl-CoA shikimate/quinic hydroxycinnamoyl transferase; COMT, caffeic acid 3-O-methyltransferase; CCaOAMT, caffeoyl CoA 3-O-methyltransferase; CYP86A1 and CYP86B1, cytochrome P450 fatty acid ω -hydroxylases; KCS1/2, 3-ketoacyl-CoA synthase; FAR 1/3/4, fatty acyl-CoA reductase; GPAT5, glycerol-3-phosphate acyltransferase 5; THT, tyramine hydroxycinnamoyl transferase; TyDC, tyrosine decarboxylase; FHT, feruloyl transferase. The question mark (?) denotes a hypothetical reaction.

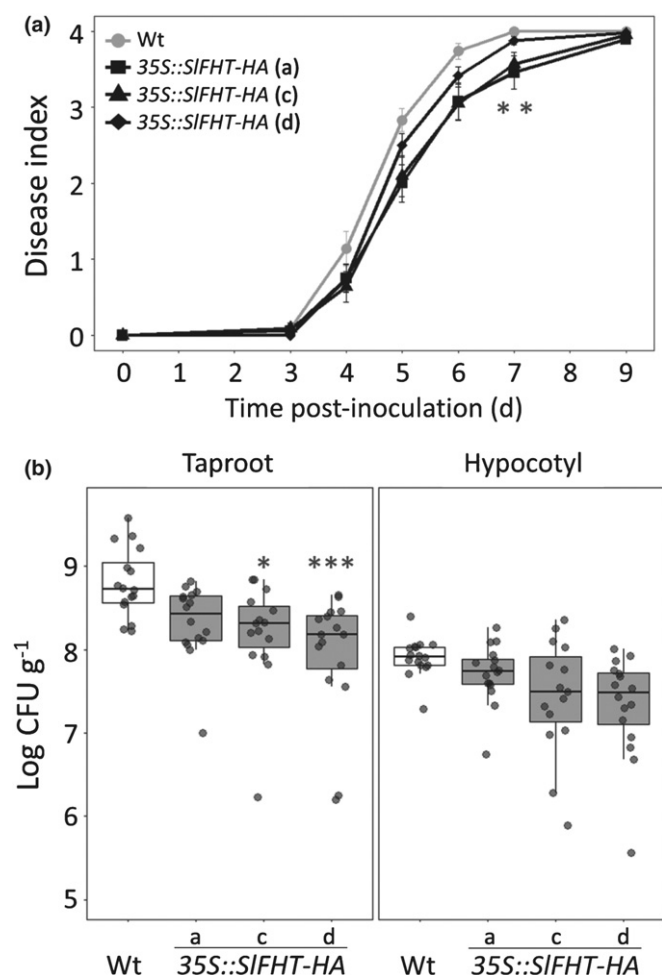


Fig. 6 Overexpression of *SIFHT-HA* in susceptible tomato slightly restricts colonization by *Ralstonia solanacearum*. (a, b) A pathogenicity assay was performed comparing wild-type (Wt) and three independent *35S::SIFHT-HA* Marmande tomato lines (a, c and d) after infection with *R. solanacearum* GMI1000 lux reporter strain. Five-wk-old plants were soil-soak inoculated with $c. 1 \times 10^7$ colony-forming unit (CFU) ml^{-1} or mock and grown at 28°C. (a) Wilting progress was monitored by rating plants daily on a 0 to 4 disease index scale where 0 = healthy and 4 = 100% wilted. Plotted values correspond to means \pm standard error of 24 independent plants ($n = 24$) from a representative experiment out of a total of three. Asterisks indicate statistically significant differences between Wt and each of the *35S::SIFHT-HA* analyzed using a paired Student's *t*-test (*, $P < 0.05$). (b) The level of *R. solanacearum* colonization in the taproot and hypocotyl was calculated as colony forming units per gram of fresh taproot tissue (CFU g^{-1}) at 12 d post infection (dpi). Data are represented with box and whiskers plots: whiskers indicate variability outside the upper and lower quartiles and boxes indicate second quartile, median and third quartile. Data presented are of a representative experiment out of a total of three experiments. In (a) a Kruskal–Wallis test at each dpi was conducted to examine differences in disease index among different genotypes. Significant differences among genotypes were confirmed by applying a pairwise Wilcoxon test. Asterisks indicate statistically significant differences between wild-type and *35S::SIFHT-HA* tomato lines in (a) (*, $P < 0.05$).

blue-to-green shift of UV autofluorescence around xylem vessels occurring specifically in the *S1THT1-3* overexpressor upon infection, which reveals the presence of ferulates/feruloylamides as part of the observed vascular deposits. In contrast, no positive

Sudan IV staining was detected, indicating that a canonical suberin polyester does not seem to be part of vascular coatings in *S1THT1-3* overexpressing plants. Since Sudan IV only stains specific moieties of the complex suberin heteropolymer, we cannot rule out that the observed vascular deposits in *S1THT1-3* are formed by a noncanonical ligno-suberin heteropolymer that does not react with Sudan IV. Further investigation will be needed in order to ascertain the exact nature of the *R. solanacearum*-induced vascular deposits in the *S1THT1-3* overexpressor. In conclusion, our data clearly show that *StTHT1-3* ectopic expression provides a very effective resistance mechanism against *R. solanacearum* – potentially mediated by accumulation of elevated amounts of HCAs such as feruloyltyramine, which drastically restricts vascular colonization, preventing bacterial spread and blocking the onset of disease.

Discussion

Ligno-suberin deposits in vascular cell walls and feruloyltyramine accumulation acts as a resistance mechanism restricting *R. solanacearum* colonization in resistant tomato

In our study, resistant tomato (H7996) was observed to react aggressively to *R. solanacearum* infection by reinforcing the walls of vessels and the surrounding parenchyma cells with UV autofluorescent phenolic deposits (Fig. 1). An increase in autofluorescence had been previously reported in another resistant tomato variety, LS-89, although its composition was not precisely defined (Ishihara *et al.*, 2012). Histochemical analysis of vascular coatings in resistant tomato upon *R. solanacearum* infection showed that suberin-associated autofluorescence was prominent in the vasculature, in line with previous reports using transmission electron microscopy (TEM) that showed thickening of the pit membranes accumulating electron-dense material in tomato plants resistant to *R. solanacearum* (Nakaho *et al.*, 2000, 2004). The suberin nature of these coatings was further supported by the positive Sudan IV staining of vessels and surrounding parenchyma cells of H7996 taproot-to-hypocotyl transition zone upon infection (Fig. 4). These results are in agreement with coatings detected in tomato plants resistant to *Verticillium albo-atrum* (Robb *et al.*, 1991), where suberin and lignin were both deposited in intercellular spaces between parenchyma cells adjoining a xylem vessel or infusing and occluding pit membranes coatings (Street *et al.*, 1986; Robb *et al.*, 1991). Besides, inhibition of the phenylpropanoid pathway inhibited the formation of both lignin and suberin coatings (Street *et al.*, 1986), in agreement with the ferulic acid requirement to correctly deposit suberin (Andersen *et al.*, 2021) and reinforcing our observations of the presence of a ferulate/feruloylamide-derived polymer detected in H7996 *R. solanacearum* (Fig. 4). In line with this, NMR data of resistant H7996 tomato vascular tissue revealed the presence of tyramine-derived amides and feruloylamides incorporated into the cell wall and also an enrichment in poly-aliphatic structures characteristic of suberin (Fig. 2) (Graça, 2015; Legay *et al.*, 2016; Figueiredo *et al.*, 2020).

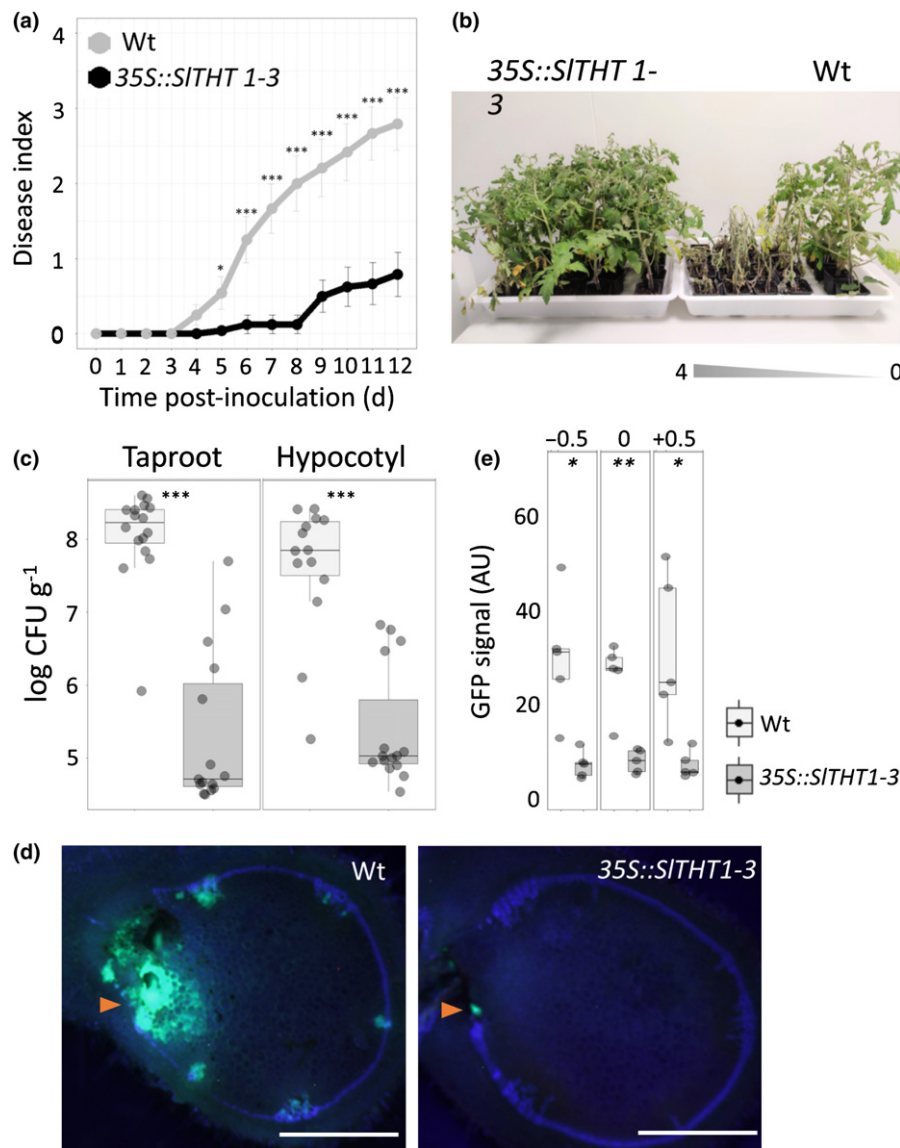


Fig. 7 Overexpression of *SITH1-3* in susceptible tomato confers resistance to *Ralstonia solanacearum*. (a, b) A pathogenicity assay was performed comparing wild-type (Wt) and 35S::SITH1-3 tomato lines (Moneymaker background) after infection with *R. solanacearum* lux reporter GMI1000 strain. Five-wk-old plants were soil-soak inoculated with c. 1×10^7 colony-forming units (CFU) ml⁻¹ and grown at 28°C. (a) Wilting progress was monitored by rating plants daily on a 0 to 4 disease index scale where 0 = healthy and 4 = 100% wilted. Plotted values correspond to means \pm standard error of 24 independent plants ($n = 24$) from a representative experiment out of a total of three. Asterisks indicate statistically significant differences between Wt and 35S::SITH1-3 using a Kruskal–Wallis test at each day post infection (dpi) was conducted to examine differences in disease index among different genotypes. Significant differences among genotypes were confirmed by applying a pairwise Wilcoxon test (*, $P < 0.05$; ***, $P < 0.0001$). (b) Pictures were taken 12 dpi. Wt plants were arranged according to the degree of symptom severity (from 4 to 0). (c) Transgenic 35S::SITH1-3 tomato significantly restricted *R. solanacearum* colonization in both the taproot-to-hypocotyl transition zone and hypocotyl compared to Wt. Five-wk-old tomato plants were root-inoculated with a *R. solanacearum* GMI1000 luciferase reporter strain at a concentration of c. 1×10^7 CFU ml⁻¹ or water mock. The level of *in planta* colonization by *R. solanacearum* was calculated as colony forming units per gram of fresh taproot tissue (CFU g⁻¹) at 12 dpi. Data are represented with box and whiskers plots: whiskers indicate variability outside the upper and lower quartiles and boxes indicate second quartile, median and third quartile. Box-and-whisker plots show data from a representative experiment out of three ($n = 14$ –16) (***, $P < 0.0001$). (d) Transverse stem cross-sections of Wt and transgenic 35S::SITH1-3 tomato lines were imaged under a confocal microscope 6 d after infection with a *R. solanacearum* GMI1000 green fluorescent protein (GFP) reporter strain. *Ralstonia solanacearum* at a concentration of 10^5 CFU ml⁻¹ was injected directly into the xylem vasculature of the first internode thorough the petiole. Orange arrow points the site of inoculation. Representative images of *R. solanacearum* colonization progress at the point of inoculation are shown. Bar, 2 mm. (e) Mean green fluorescence of the GFP signal emitted from *R. solanacearum* at cross-sections obtained as described in (d) at the point of inoculation (0), below the point of inoculation (–0.5 cm) and above the point of inoculation (+0.5 cm) was measured using IMAGEJ. Data are represented with box and whiskers plots: whiskers indicate variability outside the upper and lower quartiles and boxes indicate second quartile, median and third quartile. Data from a representative experiment out of a total of three, with $n = 5$ plants per condition. In (a) a Kruskal–Wallis test at each dpi was conducted to examine differences in disease index among different genotypes. Significant differences among genotypes were confirmed by applying a pairwise Wilcoxon test. Asterisks indicate statistically significant differences between wild-type and 35S::SITH1-3 tomato lines in (a) (*, $P < 0.05$; **, $P < 0.001$).

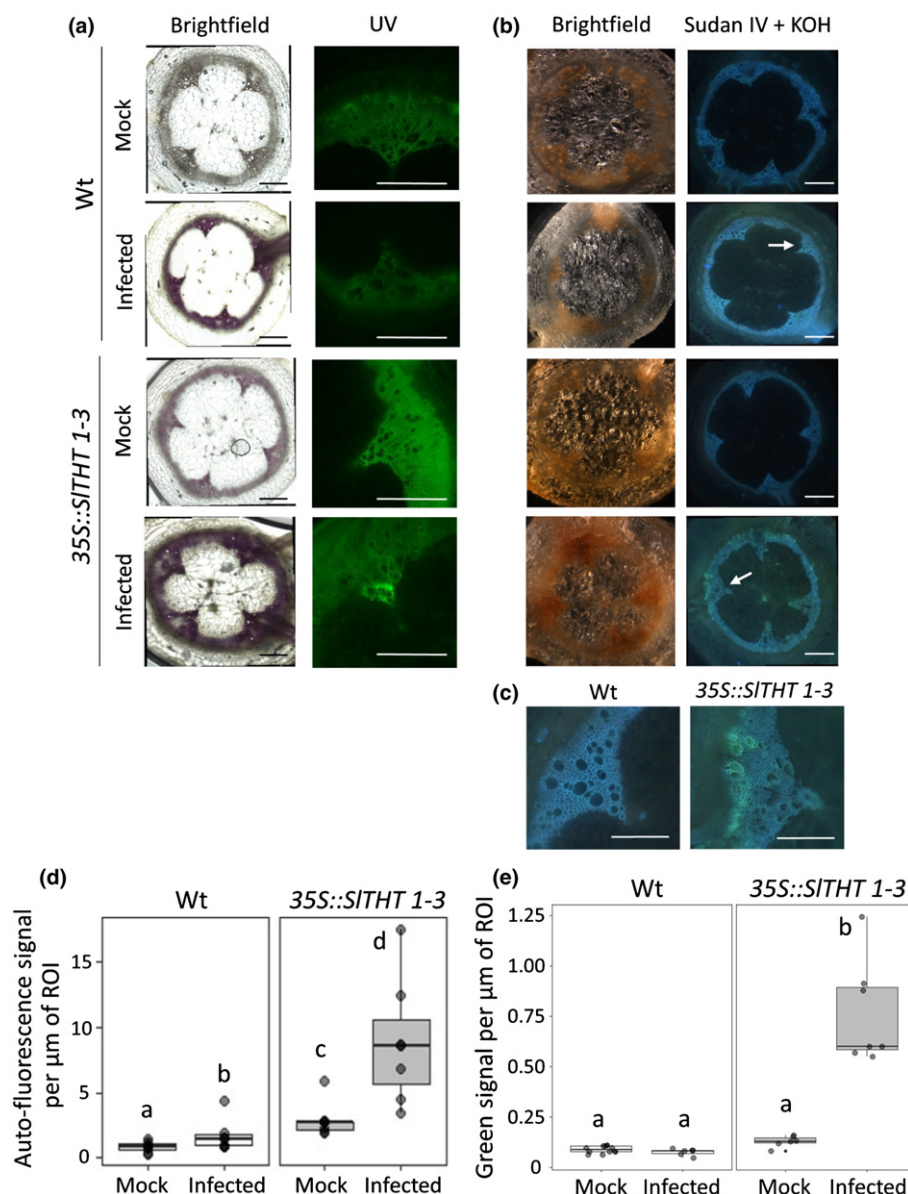


Fig. 8 Overexpression of *S1THT1-3* in susceptible tomato results in vascular autofluorescence not-quenched with phloroglucinol and cell wall ferulate/feruloylamide deposition in restricted zones of vascular tissue upon *Ralstonia solanacearum* infection. Susceptible wild-type Moneymaker (Wt) or resistant 35S::S1THT1-3 overexpressing tomato plants were soil-inoculated with a c. 1×10^7 colony-forming unit (CFU) ml^{-1} suspension of *R. solanacearum* GMI1000 lux reporter strain. Cross-sections were obtained from taproot-to-hypocotyl of both genotypes tissue containing 10^5 CFU g^{-1} of *R. solanacearum*. (a) Cross-sections were stained with phloroglucinol-HCl and observed under brightfield to visualize lignin deposition (left) and under ultraviolet (UV) to visualize other autofluorescent compounds different from lignin (not quenched with phloroglucinol-HCl) (right). (b) Combined Sudan IV+KOH treatment showed no positive suberin aliphatic signal in *S1THT1-3*, but a significant increase in ferulate/feruloylamide accumulation upon infection. (c) Close-ups (10×) of the vascular bundles of Wt and 35S::S1THT1-3 infected plants pointed with a white arrow in (b) are also shown. Images from a representative experiment out of three with $n = 6$ plants per cultivar. (d) Quantification of UV fluorescence after phloroglucinol-HCl staining as shown in (a, right) were performed with Las X software by selecting the vascular areas surrounding main vessels with strong localized fluorescence or green signal. (e) Quantification of UV green fluorescence from ferulate deposits after Sudan IV+KOH staining as shown in (a, right) were performed with Las X software by selecting the vascular areas surrounding main vessels with strong localized fluorescence or green signal. Data in (d, e) are represented with box and whiskers plots: whiskers indicate variability outside the upper and lower quartiles and boxes indicate second quartile, median and third quartile. Different letters indicate statistically significant differences ($\alpha = 0.05$, Fisher's least significant difference test). Bar, 500 μm .

Beyond histochemistry and spectroscopic signature detections, further evidence supporting the nature of these ligno-suberin coatings as responsible of the resistance observed in H7796 to *R. solanacearum* was unequivocally provided transcriptionally using gene markers. Tissues undergoing suberization have to go

through a complex reprogramming involving a network of metabolic pathways, in order to produce the precursors of the polymer and their polymerization into the matrix (Lashbrooke *et al.*, 2016). Transcriptional reprogramming associated to suberin biosynthesis was clearly observed in the taproot-to-

hypocotyl transition zone vascular tissue of resistant H7996 tomato upon infection with *R. solanacearum* (Fig. 5). Interestingly, PAL, which showed modest upregulation in resistant H7996, had been previously defined as a rate-limiting enzyme of phenylpropanoid pathway (Faragher & Brohier, 1984; Howles *et al.*, 1996). Considering this, the observed upregulation could provide more tyramine and feruloyl-CoA, which together with the upregulation of *THT* would be in agreement with the increased presence of feruloyltyramine detected by 2D-HSQC-NMR (Fig. 2a).

The 2D-HSQC-NMR also revealed differences in the composition and structure of lignin between resistant and susceptible tomato cultivars after infection (Fig. 2). The amounts and the level of lignin of a particular tissue affect wall strength, degradability and pathogen resistance (Cho *et al.*, 2012; Mnich *et al.*, 2020). However, its role in resistance/susceptibility responses is not fully understood. Part of the challenge lies in the fact that its composition seems to be less static than what was previously established. A large variety of lignin-like polymers may co-exist in plants depending on the developmental or environmental context. This becomes particularly relevant in plant–pathogen interactions, where a large variety of compounds linked to lignin differentially accumulate upon infection (Cho *et al.*, 2012; Zeiss *et al.*, 2019). The observed lignin structural differences after infection indicate that (1) under basal conditions the two tomato varieties display differences in the composition and structure of lignin and (2) *R. solanacearum* infection affects very differently the lignin fraction in the two varieties: resistant tomato shows only a slight decrease in the S : G ratio that may be linked to an accumulation of the ligno-suberin heteropolymer, while susceptible Marmande undergoes pronounced depolymerization that correlates with a decrease in ferulate/feruloylamide (Fig. 3a). Although *R. solanacearum* has not been shown to be able to specifically depolymerize lignin, the pathogen secretes enzymes that can degrade cell wall polysaccharides and could participate in the observed Marmande stem collapse phenotype (Fig. 1a). In resistant H7996, however, vascular ligno-suberin-containing coatings would allow to create a hydrophobic barrier to prevent enzymes from accessing the cell wall substrates and at the same time create reinforcements, contributing to resistance to the pathogen. The fact that these reinforcements are rich in tyramine/feruloyltyramine, may further reinforce the structural barrier, providing rigidity and hampering cell wall digestibility by the pathogen's hydrolytic enzymes (Macoy *et al.*, 2015a,b; Zeiss *et al.*, 2021). In addition to that, resistant H7996 may have evolved yet undiscovered mechanisms that directly prevent lignin degradation by the pathogen.

Overall, our data indicate that vascular coating with wall-bound ligno-suberized compounds may restrict horizontal spread of the bacterium (Fig. 1). In comparison, susceptible tomato is either not able to induce such vascular coating upon *R. solanacearum* infection or induces a very weak response (Figs 1, 3), potentially predisposing its vascular walls to disruption by the pathogen's cell wall degrading enzymes. Considering that both varieties seem to possess the metabolic components to build such barriers, the difference in response may be a direct effect of the

differential transcriptional activation of the pathway in vascular tissue of H7996 compared to Marmande. The fact that varieties with moderate resistance to *R. solanacearum* show intermediate restriction of colonization (Planas-Marquès *et al.*, 2019), indicate that the formation of these barriers may be a quantitative trait. However, this also opens the possibility that the differential transcriptional activation of the ligno-suberin pathway observed in resistant tomato may have evolved as an effective mechanism to execute defense responses triggered by activation of an immune receptor upon *R. solanacearum* recognition. Very few immune receptors involved in perception of vascular wilt pathogens have been identified so far, and the mechanisms involved in translating this recognition into effective defense responses in the vasculature remain vastly unknown. Considering that the xylem is a dead tissue, it is expected that the surrounding parenchyma cells will have a pivotal role in perception of the pathogen as well as the signaling leading to the synthesis and wall-binding of the metabolites involved in vascular coating structures, such as the one described here. In fact, xylem parenchyma cells have been shown to synthesize vascular coating components in response to the wilt pathogen *V. albo-atrum* (Street *et al.*, 1986). However, how suberin is synthesized and deposited in the xylem is still poorly defined. Exciting research currently ongoing in this area will certainly help understanding the origin and transport of ligno-suberin components to form inducible vascular deposits in response to pathogens. This will also help determine the exact point of perception of the pathogen (at a cell type or tissular level). Identification of pathogen-inducible pathways specifically occurring in resistant varieties such as the one presented here open new avenues of research to shed light on this biologically and agronomically relevant question.

Based on the earlier observations, we propose the following model (Fig. 9). When reaching the xylem vessels of resistant H7996, *R. solanacearum* multiplies and tries to invade the surrounding healthy vessels and parenchyma cells by degradation of the xylem pit membranes and walls. Resistant tomato plants respond to *R. solanacearum* vascular invasion depositing feruloyltyramine and other HCAA-tyramine derived compounds, and suberin. These deposits would block the pit membrane access and serve as coatings of the vessel walls and parenchyma cells present in the immediate vicinity of colonized vessels, compartmentalizing the infection. These ligno-suberized layers together form a 'zone of ligno-suberization' creating a strong physico-chemical barrier to limit *R. solanacearum* spread.

Engineering tomato resistance against *R. solanacearum* by inducing the tyramine-HCAA pathway

Considering the observed accumulation of ligno-suberin and cell wall-linked feruloyltyramine in resistant H7996 tomato in response to *R. solanacearum* infection, we sought to understand the implications of overexpressing genes involved in the synthesis of these compounds in susceptible tomato cultivars upon *R. solanacearum* infection. We focused on *FHT* and *THT* and because their corresponding transcripts are upregulated in the xylem vasculature of resistant tomato upon *R. solanacearum*

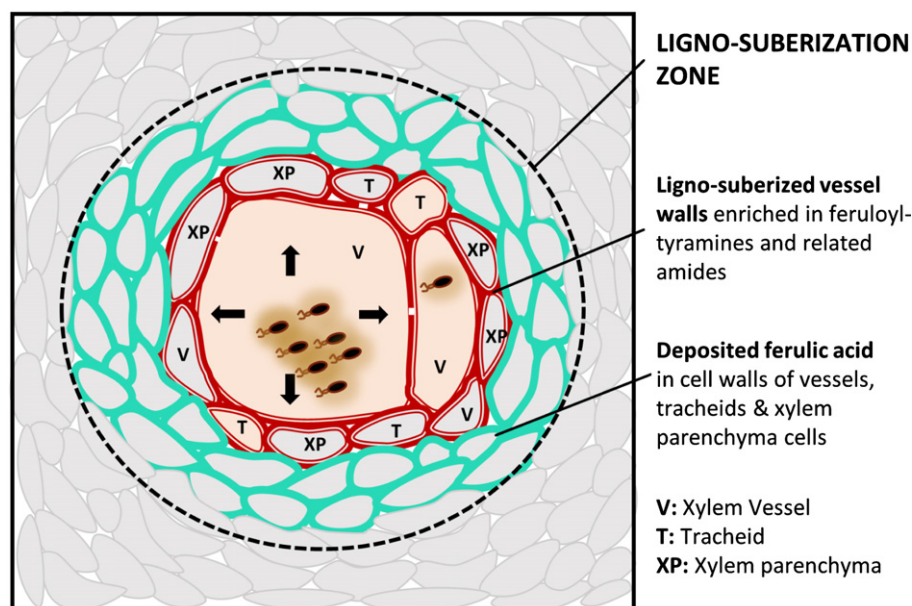


Fig. 9 Schematic representation of the vascular ligno-suberization process potentially taking place in infected vessels of resistant H7996 tomato upon *Ralstonia solanacearum* infection. Colonization of the vasculature by *R. solanacearum* in resistant tomato plants induces a ligno-suberization process in the walls of the infected vessel (V) and of the adjacent tracheids (T) and parenchyma cells (XP) (red). The lignin-like polymer accompanying suberin would be enriched in structural feruloyltyramine and related amides. The signal of structural ferulic acid (ester or as amide) would extend to the walls of peripheral parenchyma cells, vessels and tracheids (green), indicating a stage preceding suberization or a final layered pattern, still to be resolved. Together, the red and green areas, would form a 'zone of ligno-suberization' (black dashed line) potentially creating a physico-chemical barrier to limit *R. solanacearum* spread from the colonized xylem vessel lumen.

infection (Fig. 5) and they are the enzymes related with the synthesis of suberin ferulates and ether linked feruloyltyramine, respectively.

SIFHT overexpression had a small effect on the responses of susceptible tomato against *R. solanacearum*, showing a slight delay in wilting symptoms together with a slight decrease of bacterial loads in the plant (Fig. 6). The fact that increasing the levels of FHT in Marmande does only result in a marginal increase in resistance might be linked to a shortfall of aliphatic precursors in this variety (Fig. 5), which constrain a subsequent increase in suberin synthesis. In contrast, transgenic tomato overexpressing *S1THT1-3* on a susceptible background was highly resistant to *R. solanacearum* (Fig. 7). Importantly, this transgenic line was previously shown to accumulate elevated amounts of soluble HCAAs such as feruloyltyramine and also SA upon infection with the bacteria *Pseudomonas syringae* pv. *tomato* (Pto) and to slightly but significantly restrict bacterial growth (Campos *et al.*, 2014). Since SA does not seem to play a major role in defense responses against *R. solanacearum* (Hirsch *et al.*, 2002; Hernández-Blanco *et al.*, 2007; Hanemian *et al.*, 2016), accumulation of this hormone in *S1THT1-3* overexpressing line may not be the major underlying cause of the observed increase in resistance in this line. Alternatively, enhanced production of tyramine-derived HCAAs may constitute an important defense strategy against *R. solanacearum*. Feruloyltyramines exhibit antimicrobial activity (Fattorusso *et al.*, 1999; Novo *et al.*, 2017) and that they can be involved in plant priming or an adaptive strategy where plants are in a physiological state with improved defensive capacity (Zeiss *et al.*, 2021). These tyramine-derived

HCAAs overproduced in *S1THT1-3* overexpressing plants may interfere with *R. solanacearum* colonization by becoming incorporated into the vascular and perivascular cell walls, providing a stronger crosslinking and restricting the movement of the pathogen inside the plant (Fig. 8) but also partly by remaining soluble and acting as direct antimicrobial agents against the pathogen. *Ralstonia solanacearum* possesses a hydroxycinnamic acid degradation pathway and it has been shown that mutants that cannot degrade hydroxycinnamic acids are less virulent on tomato (Lowe-Power *et al.*, 2015; Zhang *et al.*, 2019), which clearly underscores the importance of HCAAs in the arms race taking place in this pathosystem. Considering that the ligno-suberin pathway and HCAAs are well-conserved across the plant kingdom (Philippe *et al.*, 2020; Kashyap *et al.*, 2021; Zeiss *et al.*, 2021), these findings open the possibility to engineer disease resistance in other *R. solanacearum* hosts by manipulating these pathways. Interestingly, ligno-suberin deposits and accumulation of HCAAs have been reported in response to drought (Macoy *et al.*, 2015a,b; Zhang *et al.*, 2020). Therefore, engineering these pathways could have a double impact both on biotic and abiotic stress responses, improving plant performance in the field under adverse conditions.

In conclusion, we have provided evidence of the formation of a 'ligno-suberization zone' enriched in ether-linked feruloyltyramine and possibly related amides as an effective strategy to confine *R. solanacearum* into infected vessels of resistant tomato plants, preventing horizontal spread of the pathogen into healthy tissues and delaying disease symptoms. Resistance against *R. solanacearum* can be attained in susceptible tomato

background by stably overexpressing *THT* potentially contributing. In the future, it will be interesting to investigate the contribution of HCAs and suberin to resistance against the pathogen, the mechanisms whereby *R. solanacearum* perception leads to the formation of a ligno-suberin coatings around the vasculature in resistant tomato varieties. Increasing the spatio-temporal resolution of the tomato–*R. solanacearum* interaction will be instrumental to reach a deeper insight into structural resistance mechanisms. Also, since vascular confinement has been reported in different plant species as a means of resistance against various vascular wilt pathogens (De Ascensao & Dubery, 2000; Martín *et al.*, 2008; Xu *et al.*, 2011; Sabella *et al.*, 2018), the level of conservation of vascular ligno-suberin deposition and HCAs as a constituent of vascular coatings and part of a resistance mechanism remains to be determined.

Acknowledgements


The authors would like to thank Gabriel Castrillo and Nico Geldner for inspiring discussions. The authors also thank Marc Planas-Marqués for helpful comments and María Pilar López Gresa (IBMCP-UPV) for kindly sharing the tomato THT seeds. Research is funded by MCIN/AEI/10.13039/501100011033 (NSC, MV), MCIN/AEI/PID2019-110330GB-C21 (MF, OS), MCIN/AEI/PID2020-118968RB-I00 (JR), through the 'Severo Ochoa Programme for Centres of Excellence in R&D' (SEV-2015-0533, CEX2019-000917 and CEX2019-000902-S funded by MCIN/AEI/ 10.13039/501100011033), and by the Spanish National Research Council (CISC) pie-201620E081 (JR, AG) and the Generalitat de Catalunya (2017SGR765 grant). AK is the recipient of a Netaji Subhas – Indian Council of Agricultural Research International Fellowship. SS acknowledges financial support from DOC-FAM, European Union's Horizon 2020 research and innovation programme under the Marie Skłodowska-Curie grant agreement no. 754397. This work was also supported by the CERCA Program/Generalitat de Catalunya.


Author contributions


AK designed and performed experiments, interpreted data and wrote the manuscript. ÁLJ-J performed the experiments required for the second submission of the manuscript. WZ performed experiments. MC performed experiments, interpreted data and reviewed the manuscript. SS conducted preliminary spectroscopy experiments and reviewed the manuscript. JR isolated the lignin/suberin fractions and conducted the 2D-HSQC-NMR analysis, including data interpretation. AG isolated the lignin/suberin fractions and conducted the 2D-HSQC-NMR analysis, including data interpretation. AL conducted preliminary spectroscopy experiments and reviewed the manuscript. OS conducted histopathology staining experiments, interpreted data and reviewed the manuscript. MF interpreted data and reviewed the manuscript. MV designed experiments, interpreted data and reviewed the manuscript. NSC conceptualized the research, designed experiments,


interpreted data and wrote the manuscript. ÁLJ-J and WZ contributed equally to this work.

ORCID


Montserrat Capellades  <https://orcid.org/0000-0001-9514-2885>


Nuria S. Coll  <https://orcid.org/0000-0002-8889-0399>


Mercè Figueras  <https://orcid.org/0000-0002-6288-1830>

Ana Gutiérrez  <https://orcid.org/0000-0002-8823-9029>


Álvaro Luis Jiménez-Jiménez  <https://orcid.org/0000-0002-9406-4595>


Anurag Kashyap  <https://orcid.org/0000-0003-2622-8209>

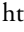
Anna Laromaine  <https://orcid.org/0000-0002-4764-0780>

Jorge Rencoret  <https://orcid.org/0000-0003-2728-7331>

Olga Serra  <https://orcid.org/0000-0002-1678-0932>

Sumithra Srinivasan  <https://orcid.org/0000-0002-0473-9801>

Marc Valls  <https://orcid.org/0000-0003-2312-0091>

Weiqi Zhang  <https://orcid.org/0000-0002-2535-1398>

Data availability

The data that support the findings of this study are available from the corresponding author upon reasonable request.

References

- Álvarez B, Biosca EG, López MM. 2010. On the life of *Ralstonia solanacearum*, a destructive bacterial plant pathogen. In: Méndez-Vilas A, ed. *Technology and education topics in applied microbiology and microbial biotechnology*. Badajoz, Spain: Formatex, 267–279.
- Andersen TG, Molina D, Kilian J, Franke RB, Ragni L, Geldner N. 2021. Tissue-autonomous phenylpropanoid production is essential for establishment of root barriers. *Current Biology* 31: 965–977.
- Araujo L, Bispo WMS, Cacique IS, Moreira WR, Rodrigues FA. 2014. Resistance in mango against infection by *Ceratocystis fimbriata*. *Phytopathology* 104: 820–833.
- Baayen RP, Elgersma DM. 1985. Colonization and histopathology of susceptible and resistant carnation cultivars infected with *Fusarium oxysporum* f. sp. *dianthi*. *Netherlands Journal of Plant Pathology* 91: 119–135.
- Benhamou N. 1995. Ultrastructural and cytochemical aspects of the response of eggplant parenchyma cells in direct contact with *Verticillium*-infected xylem vessels. *Physiological and Molecular Plant Pathology* 46: 321–338.
- Bernards MA. 2002. Demystifying suberin. *Canadian Journal of Botany* 80: 227–240.
- Bernards MA, Lewis NG. 1998. The macromolecular aromatic domain in suberized tissue: a changing paradigm. *Phytochemistry* 47: 915–933.
- Bernards M, Lopez M, Zajicek J, Lewis N. 1995. Hydroxycinnamic acid-derived polymers constitute the polyaromatic domain of suberin. *Journal of Biological Chemistry* 270: 7382–7386.
- Caldwell D, Kim B, Iyer-Pascuzzi AS. 2017. *Ralstonia solanacearum* differentially colonizes roots of resistant and susceptible tomato plants. *Phytopathology* 107: 528–536.
- Campos L, Lisón P, López-Gresa MP, Rodrigo I, Zacarés L, Conejero V, Bellés JM. 2014. Transgenic tomato plants overexpressing tyramine N-hydroxycinnamoyltransferase exhibit elevated hydroxycinnamic acid amide levels and enhanced resistance to *Pseudomonas syringae*. *Molecular Plant-Microbe Interactions* 27: 1159–1169.
- Carnachan SM, Harris PJ. 2000. Ferulic acid is bound to the primary cell walls of all gymnosperm families. *Biochemical Systematics and Ecology* 28: 865–879.
- Cho K, Kim Y, Wi SJ, Seo JB, Kwon J, Chung JH, Park KY, Nam MH. 2012. Nontargeted metabolite profiling in compatible pathogen-inoculated tobacco

- (*Nicotiana tabacum* L. cv. Wisconsin 38) using UPLC-Q-TOF/MS. *Journal of Agriculture and Food Chemistry* 60: 11015–11028.
- Correia VG, Bento A, Pais J, Rodrigues R, Haliński P, Frydrych M, Greenhalgh A, Stepnowski P, Vollrath F, King AWT *et al.* 2020. The molecular structure and multifunctionality of the cryptic plant polymer suberin. *Materials Today Bio* 5: 100039.
- Cruz APZ, Ferreira V, Pianzola MJ, Siri MI, Coll NS, Valls M. 2014. A novel, sensitive method to evaluate potato germplasm for bacterial wilt resistance using a luminescent *Ralstonia solanacearum* reporter strain. *Molecular Plant–Microbe Interactions* 27: 277–285.
- De Ascensao ARDCF, Dubery IA. 2000. Panama disease: cell wall reinforcement in banana roots in response to elicitors from *Fusarium oxysporum* f. sp. *cubense* race four. *Phytopathology* 90: 1173–1180.
- Digonnet C, Martinez Y, Denancé N, Chasseray M, Dabos P, Ranocha P, Marco Y, Jauneau A, Goffner D. 2012. Deciphering the route of *Ralstonia solanacearum* colonization in *Arabidopsis thaliana* roots during a compatible interaction: focus at the plant cell wall. *Planta* 236: 1419–1431.
- Donaldson L. 2020. Autofluorescence in plants. *Molecules* 25: 2393.
- Donaldson L, Williams N. 2018. Imaging and spectroscopy of natural fluorophores in pine needles. *Plants* 7: 10.
- Falter C, Ellinger D, Von Hulsen B, Heim R, Voigt CA. 2015. Simple preparation of plant epidermal tissue for laser microdissection and downstream quantitative proteome and carbohydrate analysis. *Frontiers in Plant Science* 6: 194.
- Faragher JD, Brohier RL. 1984. Anthocyanin accumulation in apple skin during ripening: regulation by ethylene and phenylalanine ammonia-lyase. *Scientia Horticulturae* 22: 89–96.
- Fattorusso E, Lanzotti V, Taglialatela-Scafati O. 1999. Antifungal N-feruloylamides from roots of two *Allium* species. *Plant Biosystems* 133: 199–203.
- Figueiredo R, Portilla Llerena JP, Kiyota E, Ferreira SS, Cardeli BR, de Souza SCR, dos Santos Brito M, Sodek L, Cesarino I, Mazzafera P. 2020. The sugarcane ShMYB78 transcription factor activates suberin biosynthesis in *Nicotiana benthamiana*. *Plant Molecular Biology* 104: 411–427.
- Gleave AP. 1992. A versatile binary vector system with a T-DNA organisational structure conducive to efficient integration of cloned DNA into the plant genome. *Plant Molecular Biology* 20: 1203–1207.
- Gou J-Y, Yu X-H, Liu C-J. 2009. A hydroxycinnamoyltransferase responsible for synthesizing suberin aromatics in Arabidopsis. *Proceedings of the National Academy of Sciences, USA* 106: 18855–18860.
- Graça J. 2010. Hydroxycinnamates in suberin formation. *Phytochemistry Reviews* 9: 85–91.
- Graça J. 2015. Suberin: the biopolyester at the frontier of plants. *Frontiers in Chemistry* 3: 62.
- Grimault V, Anais G, Prior P. 1994. Distribution of *Pseudomonas solanacearum* in the stem tissues of tomato plants with different levels of resistance to bacterial wilt. *Plant Pathology* 43: 663–668.
- Hanemian M, Barlet X, Sorin C, Yadeta KA, Keller H, Favory B, Simon R, Thomma BPHJ, Hartmann C, Crespi M *et al.* 2016. Arabidopsis CLAVATA1 and CLAVATA2 receptors contribute to *Ralstonia solanacearum* pathogenicity through a miR169-dependent pathway. *New Phytologist* 211: 502–515.
- Harris PJ, Trethewey JAK. 2010. The distribution of ester-linked ferulic acid in the cell walls of angiosperms. *Phytochemistry Reviews* 9: 19–33.
- He M, Ding N. 2020. Plant unsaturated fatty acids: multiple roles in stress response. *Frontiers in Plant Science* 11: 562785.
- Hernández-Blanco C, Feng DX, Hu J, Sánchez-Vallet A, Deslandes L, Llorente F, Berrocal-Lobo M, Keller H, Barlet X, Sánchez-Rodríguez C *et al.* 2007. Impairment of cellulose synthases required for Arabidopsis secondary cell wall formation enhances disease resistance. *Plant Cell* 19: 890–903.
- Hirsch J, Deslandes L, Feng DX, Balagué C, Marco Y. 2002. Delayed symptom development in ein2-1, an Arabidopsis ethylene-insensitive mutant, in response to bacterial wilt caused by *Ralstonia solanacearum*. *Phytopathology* 92: 1142–1148.
- Howles PA, Sewalt VJH, Paiva NL, Elkind Y, Bate NJ, Lamb C, Dixon RA. 1996. Overexpression of L-phenylalanine ammonia-lyase in transgenic tobacco plants reveals control points for flux into phenylpropanoid biosynthesis. *Plant Physiology* 112: 1617–1624.
- Iiyama K, Lam TBT, Stone B. 2020. Covalent cross-links in the cell wall. *Plant Physiology* 104: 315–320.
- Ishihara T, Mitsuhashi I, Takahashi H, Nakaho K. 2012. Transcriptome analysis of quantitative resistance-specific response upon *Ralstonia solanacearum* infection in tomato. *PLoS ONE* 7: e46763.
- Jhu M, Farhi M, Wang L, Philbrook RN, Belcher MS, Nakayama H, Zumstein KS, Rowland SD, Ron M, Shih PM *et al.* (2021). Lignin-based resistance to *Cuscuta campestris* parasitism in Heinz resistant tomato cultivars. *bioRxiv*. doi: 10.1101/706861.
- Jones JDG, Dangl JL. 2006. The plant immune system. *Nature* 444: 323–329.
- Joo Y, Kim H, Kang M, Lee G, Choung S, Kaur H, Oh S, Choi JW, Ralph J, Baldwin IT *et al.* 2021. Pith-specific lignification in *Nicotiana attenuata* as a defense against a stem-boring herbivore. *New Phytologist* 232: 332–344.
- Kashyap A, Planas-marquès M, Capellades M, Valls M, Coll NS. 2021. Blocking intruders: inducible physico-chemical barriers against plant vascular wilt pathogens. *Journal of Experimental Botany* 72: 184–198.
- Kim SG, Hur OS, Ro NY, Ko HC, Rhee JH, Sung JS, Ryu KY, Lee SY, Baek HJ. 2016. Evaluation of resistance to *Ralstonia solanacearum* in tomato genetic resources at seedling stage. *Plant Pathology Journal* 32: 58–64.
- Lashbrooke J, Cohen H, Levy-Samocha D, Tzfadia O, Panizel I, Zeisler V, Massalha H, Stern A, Trainotti L, Schreiber L *et al.* 2016. MYB107 and MYB9 homologs regulate suberin deposition in angiosperms. *Plant Cell* 28: 2097–2116.
- Legay S, Guerriero G, André C, Guignard C, Cocco E, Charton S, Boutry M, Rowland O, Hausman JF. 2016. MdMyb93 is a regulator of suberin deposition in russeted apple fruit skins. *New Phytologist* 212: 977–991.
- Liu H, Zhang S, Schell MA, Denny TP. 2005. Pyramiding unmarked deletions in *Ralstonia solanacearum* shows that secreted proteins in addition to plant cell-wall-degrading enzymes contribute to virulence. *Molecular Plant–Microbe Interactions* 18: 1296–1305.
- Lowe-Power TM, Ailloud F, Allen C. 2015. Hydroxycinnamic acid degradation, a broadly conserved trait, protects *Ralstonia solanacearum* from chemical plant defenses and contributes to root colonization and virulence. *Molecular Plant–Microbe Interactions* 28: 286–297.
- Lowe-Power TM, Khokhani D, Allen C. 2018. How *Ralstonia solanacearum* exploits and thrives in the flowing plant xylem environment. *Trends in Microbiology* 26: 929–942.
- Lulaj EC, Corsini DL. 1998. Differential deposition of suberin phenolic and aliphatic domains and their roles in resistance to infection during potato tuber (*Solanum tuberosum* L.) wound-healing. *Physiological and Molecular Plant Pathology* 53: 209–222.
- Macoy DM, Kim WY, Lee SY, Kim MG. 2015a. Biosynthesis, physiology, and functions of hydroxycinnamic acid amides in plants. *Plant Biotechnology Reports* 9: 269–278.
- Macoy DM, Kim WY, Lee SY, Kim MG. 2015b. Biotic stress related functions of hydroxycinnamic acid amide in plants. *Journal of Plant Biology* 58: 156–163.
- Mahmoud AB, Danton O, Kaiser M, Han S, Moreno A, Algaffar SA, Khalid S, Oh WK, Hamburger M, Mäser P. 2020. Lignans, amides, and saponins from *Haplophyllum tuberculatum* and their antiprotozoal activity. *Molecules* 25: 2825.
- Mangin B, Thoquet P, Olivier J, Grimsley NH. 1999. Temporal and multiple quantitative trait loci analyses of resistance to bacterial wilt in tomato permit the resolution of linked loci. *Genetics* 151: 1165–1172.
- Martín JA, Solla A, Domingues MR, Coimbra MA, Gil L. 2008. Exogenous phenol increase resistance of *Ulmus minor* to Dutch elm disease through formation of suberin-like compounds on xylem tissues. *Environmental and Experimental Botany* 64: 97–104.
- Mazier M, Flamain F, Nicolai M, Sarnette V, Caranta C. 2011. Knock-down of both eIF4E1 and eIF4E2 genes confers broad-spectrum resistance against potyviruses in tomato. *PLoS ONE* 6: e29595.
- McGarvey JA, Denny TP, Schell MA. 1999. Spatial-temporal and quantitative analysis of growth and EPS I production by *Ralstonia solanacearum* in resistant and susceptible tomato cultivars. *Phytopathology* 89: 1233–1239.
- Mnich E, Bjarnholt N, Eudes A, Harholt J, Holland C, Jørgensen B, Larsen FH, Liu M, Manat R, Meyer AS *et al.* 2020. Phenolic cross-links: building and deconstructing the plant cell wall. *Natural Products Reports* 37: 919–961.

- Molina I, Li-Beisson Y, Beisson F, Ohlrogge JB, Pollard M. 2009. Identification of an Arabidopsis feruloyl-coenzyme a transferase required for suberin synthesis. *Plant Physiology* 151: 1317–1328.
- Nakaho K, Hibino H, Miyagawa H. 2000. Possible mechanisms limiting movement of *Ralstonia solanacearum* in resistant tomato tissues. *Journal of Phytopathology* 148: 181–190.
- Nakaho K, Inoue H, Takayama T, Miyagawa H. 2004. Distribution and multiplication of *Ralstonia solanacearum* in tomato plants with resistance derived from different origins. *Journal of General Plant Pathology* 70: 115–119.
- Negrel J, Javelle F, Paynot M. 1993. Wound-induced tyramine hydroxycinnamoyl transferase in Potato (*Solanum tuberosum*) tuber discs. *Journal of Plant Physiology* 142: 518–524.
- Negrel J, Pollet B, Lapierre C. 1996. Ether-linked ferulic acid amides in natural and wound periderms of potato tuber. *Phytochemistry* 43: 1195–1199.
- Novo M, Silvar C, Merino F, Martínez-Cortés T, Lu F, Ralph J, Pomar F. 2017. Deciphering the role of the phenylpropanoid metabolism in the tolerance of *Capsicum annuum* L. to *Verticillium dahliae* Kleb. *Plant Science* 258: 12–20.
- Pérez-Donoso AG, Sun Q, Caroline Roper M, Carl Greve L, Kirkpatrick B, Labavitch JM. 2010. Cell wall-degrading enzymes enlarge the pore size of intervessel pit membranes in healthy and *Xylella fastidiosa*-infected grapevines. *Plant Physiology* 152: 1748–1759.
- Philippe G, Sørensen I, Jiao C, Sun X, Fei Z, Domozych DS, Rose JK. 2020. Cutin and suberin: assembly and origins of specialized lipidic cell wall scaffolds. *Current Opinion in Plant Biology* 55: 11–20.
- Planas-Marqués M, Bernardo-Faura M, Paulus J, Kaschani F, Kaiser M, Valls M, Van Der Hoorn RAL, Coll NS. 2018. Protease activities triggered by *Ralstonia solanacearum* infection in susceptible and tolerant tomato lines. *Molecular & Cellular Proteomics* 17: 1112–1125.
- Planas-Marqués M, Kressin JP, Kashyap A, Panthee DR, Louws FJ, Coll NS, Valls M. 2019. Four bottlenecks restrict colonization and invasion by the pathogen *Ralstonia solanacearum* in resistant tomato. *Journal of Experimental Botany* 71: 2157–2171.
- Pomar F, Merino F, Barceló AR. 2002. O-4-linked coniferyl and sinapyl aldehydes in lignifying cell walls are the main targets of the Wiesner (phloroglucinol-HCl) reaction. *Protoplasma* 220: 17–28.
- Pomar F, Novo M, Bernal MA, Merino F, Barceló AR, Barceló AR. 2004. Changes in stem lignins (monomer composition and crosslinking) and peroxidase are related with the maintenance of leaf photosynthetic integrity during *Verticillium* wilt in *Capsicum annuum*. *New Phytologist* 163: 111–123.
- Potter C, Harwood T, Knight J, Tomlinson I. 2011. Learning from history, predicting the future: the UK Dutch elm disease outbreak in relation to contemporary tree disease threats. *Philosophical Transactions of the Royal Society of London. Series B: Biological Sciences* 366: 1966–1974.
- Pouzoulet J, Jacques A, Besson X, Dayde J, Mailhac N. 2013. Histopathological study of response of *Vitis vinifera* cv. Cabernet Sauvignon to bark and wood injury with and without inoculation by *Phaeomonniella chlamydospora*. *Phytopathologia Mediterranea* 52: 313–323.
- Pradhan Mitra P, Loqué D. 2014. Histochemical staining of *Arabidopsis thaliana* secondary cell wall elements. *Journal of Visualized Experiments* 87: e51381.
- Puigvert M, Guarischi-Sousa R, Zuluaga P, Coll NS, Macho AP, Setubal JC, Valls M. 2017. Transcriptomes of *Ralstonia solanacearum* during root colonization of *Solanum commersonii*. *Frontiers in Plant Science* 8: 370.
- Ralph J, Landucci L. (2010). NMR of lignins. In: Heitner JA, Dimmel C, Schmidt DR, eds. *Lignin and lignans: advances in chemistry*. Boca Raton, FL, USA: CRC Press, Taylor & Francis, 137–243.
- Razem FA, Bernards MA. 2002. Hydrogen peroxide is required for poly (phenolic) domain formation during wound-induced suberization. *Journal of Agriculture and Food Chemistry* 50: 1009–1015.
- Rencoret J, Kim H, Evaristo AB, Gutiérrez A, Ralph J, Del Río JC. 2018. Variability in lignin composition and structure in cell walls of different parts of macaúba (*Acrocomia aculeata*) Palm Fruit. *Journal of Agriculture and Food Chemistry* 66: 138–153.
- Rico A, Rencoret J, Del Río JC, Martínez AT, Gutiérrez A. 2014. Pretreatment with laccase and a phenolic mediator degrades lignin and enhances saccharification of *Eucalyptus* feedstock. *Biotechnology for Biofuels* 7: 6.
- del Río JC, Rencoret J, Gutiérrez A, Kim H, Ralph J. 2018. Structural characterization of lignin from Maize (*Zea mays* L.) fibers: evidence for diferuloylputrescine incorporated into the lignin polymer in Maize kernels. *Journal of Agriculture and Food Chemistry* 66: 4402–4413.
- Rioux D, Nicole M, Simard M, Ouellette GB. 1998. Immunocytochemical evidence that secretion of pectin occurs during gel (gum) and tylosis formation in trees. *Phytopathology* 88: 494–505.
- Robb J, Lee SW, Mohan R, Kolattukudy PE. 1991. Chemical characterization of stress-induced vascular coating in tomato. *Plant Physiology* 97: 528–536.
- Sabella E, Luvisi A, Aprile A, Negro C, Vergine M, Nicoli F, Miceli A, De Bellis L. 2018. *Xylella fastidiosa* induces differential expression of lignification related-genes and lignin accumulation in tolerant olive trees cv. Leccino. *Journal of Plant Physiology* 220: 60–68.
- Salas-González I, Rey G, Flis P, Custódio V, Gopaulchan D, Bakhoun N, Dew TP, Suresh K, Franke RB, Dangl JL *et al.* 2021. Coordination between microbiota and root endodermis supports plant mineral nutrient homeostasis. *Science* 371: eabd0695.
- Schmidt A, Grimm R, Schmidt J, Scheel D, Strack D. 1999. Cloning and expression of a potato cDNA encoding hydroxycinnamoyl-CoA:tyramine N-(hydroxycinnamoyl)transferase. *Journal of Biological Chemistry* 274: 4273–4280.
- Scortichini M. 2020. The multi-millennial olive agroecosystem of salento (Apulia, Italy) threatened by *Xylella fastidiosa* subsp. Pauca: a working possibility of restoration. *Sustain* 12: 6700.
- Serra O, Figueras M, Franke R, Prat S, Molinas M. 2010. Unraveling ferulate role in suberin and periderm biology by reverse genetics. *Plant Signaling & Behavior* 5: 953–958.
- Serrano M, Coluccia F, Torres M, L'Haridon F, Métraux JP. 2014. The cuticle and plant defense to pathogens. *Frontiers in Plant Science* 5: 274.
- Street PFS, Robb J, Ellis BE. 1986. Secretion of vascular coating components by xylem parenchyma cells of tomatoes infected with *Verticillium albo-atrum*. *Protoplasma* 132: 1–11.
- Thoquet P, Olivier J, Sperisen C, Rogowsky P, Laterrot H, Grimsley N. 1996. Quantitative trait loci determining resistance to bacterial wilt in tomato cultivar Hawaii 7996. *Molecular Plant-Microbe Interactions* 9: 826–836.
- Ursache R, Vieira Teixeira CDJ, Tendon VD, Gully K, Bellis DD, Schmid-Siebert E, Andersen TG, Shekhar V, Calderon S, Pradervand S *et al.* 2021. GDLS-domain proteins have key roles in suberin polymerization and degradation. *Nature Plants* 7: 353–364.
- Vasse J, Frey P, Trigalet A. 1995. Microscopic studies of intercellular infection and protoxylem invasion of tomato roots by *Pseudomonas solanacearum*. *Molecular Plant-Microbe Interactions* 8: 241–251.
- Vasse J, Genin S, Frey P, Boucher C, Brito B. 2000. The hrpB and hrpG regulatory genes of *Ralstonia solanacearum* are required for different stages of the tomato root infection process. *Molecular Plant-Microbe Interactions* 13: 259–267.
- Wang JF, Ho FI, Truong HTH, Huang SM, Balatero CH, Dittapongpich V, Hidayati N. 2013. Identification of major QTLs associated with stable resistance of tomato cultivar “Hawaii 7996” to *Ralstonia solanacearum*. *Euphytica* 190: 241–252.
- Xu L, Zhu L, Tu L, Liu L, Yuan D, Jin L, Long L, Zhang X. 2011. Lignin metabolism has a central role in the resistance of cotton to the wilt fungus *Verticillium dahliae* as revealed by RNA-seq-dependent transcriptional analysis and histochemistry. *Journal of Experimental Botany* 62: 5607–5621.
- Yadeta KA, Thomma BPHJ. 2013. The xylem as battleground for plant hosts and vascular wilt pathogens. *Frontiers in Plant Science* 4: 97.
- Zeiss DR, Mhlongo MI, Tugizimana F, Steenkamp PA, Dubery IA. 2019. Metabolomic profiling of the host response of tomato (*Solanum lycopersicum*) following infection by *Ralstonia solanacearum*. *International Journal of Molecular Sciences* 20: 3945.
- Zeiss DR, Piater IA, Dubery IA. 2021. Hydroxycinnamate amides: intriguing conjugates of plant protective metabolites. *Trends in Plant Science* 26: 184–195.
- Zhang L, Merlin I, Pascal S, Bert PF, Domergue F, Gambetta GA. 2020. Drought activates MYB41 orthologs and induces suberization of grapevine fine roots. *Plant Direct* 4: 278.
- Zhang Y, Zhang W, Han L, Li J, Shi X, Hikichi Y, Ohnishi K. 2019. Involvement of a PadR regulator PrhP on virulence of *Ralstonia solanacearum* by controlling detoxification of phenolic acids and type III secretion system. *Molecular Plant Pathology* 20: 1477–1490.

Zuluaga AP, Solé M, Lu H, Góngora-Castillo E, Vaillancourt B, Coll N, Buell CR, Valls M. 2015. Transcriptome responses to *Ralstonia solanacearum* infection in the roots of the wild potato *Solanum commersonii*. *BMC Genomics* 16: 246.

Supporting Information

Additional Supporting Information may be found online in the Supporting Information section at the end of the article.

Fig. S1 Tissue used for analysis and bacterial dynamics.

Fig. S2 H7996 plants show mild symptoms upon challenge inoculation of *Ralstonia solanacearum*.

Fig. S3 Vascular coating response to *Ralstonia solanacearum* infection with wall bound phenolics.

Fig. S4 Expression of suberin biosynthetic genes in xylem vasculature of taproots upon infection of *Ralstonia solanacearum*.

Fig. S5 Phylogeny of feruloyl transferase (FHT) orthologs in different plant species and expression of the putative tomato FHT ortholog in response to *Ralstonia solanacearum* infection.

Fig. S6 Phylogeny of tyramine hydroxycinnamoyl transferase (THT) orthologs in different plant species and expression of the

tomato THT gene family members in response to *Ralstonia solanacearum* infection.

Fig. S7 Expression of phenylpropanoid pathway genes in xylem vasculature of taproots upon invasion of *Ralstonia solanacearum*.

Fig. S8 Immunoblot of 35S::*SlFHT-HA* in independent Marmande tomato lines expressing 35S::*SlFHT-HA* (Marmande).

Fig. S9 Fresh weight of 35S::*SlFHT-HA* plants.

Fig. S10 Fresh weight of 35S::*SlTHT1-3* plants.

Fig. S11 Overexpression of *SlTHT1-3* in tomato results in restricted colonization by *Ralstonia solanacearum*.

Table S1 List of primers used in this study.

Table S2 Assignments of the correlation signals in the two-dimensional heteronuclear single quantum coherence (2D HSQC) spectra.

Please note: Wiley Blackwell are not responsible for the content or functionality of any Supporting Information supplied by the authors. Any queries (other than missing material) should be directed to the *New Phytologist* Central Office.